UNIVERSITÀ
DEGLI STUDI
DI PADOVA

Sede Amministrativa: Università degli Studi di Padova

Dipartimento di
Ingegneria Industriale - DII

CORSO DI DOTTORATO DI RICERCA IN: ***Ingegneria Industriale***
CURRICOLO: *Ingegneria chimica, dei materiali e meccanica*
29° CICLO

ADDITIVE MANUFACTURING THROUGH MICRO DIRECT LASER METAL DEPOSITION TECHNOLOGY: INFLUENCE OF THE MATERIAL AND PROCESS PARAMETERS ON THE PRODUCT QUALITY

Tesi redatta con il contributo finanziario da Fondazione Cassa di Risparmio di Padova e Rovigo per l'ambito di ricerca: Ingegneria di precisione e micro-fabbricazione

Coordinatore: Paolo Colombo
Supervisore: Paolo Francesco Bariani

Dottorando: Federico Mazzucato

Abstract

Direct Laser Metal Deposition is a laser based Additive Manufacturing technology that is finding a growing employment and industrial application in sectors such as aerospace, automotive, biomedical, and electronics. Its great success is mainly related to its great capability to manufacture a wide range of material (both metals and ceramics) and its potentiality to confer a high degree of geometrical complexity to the realized artefacts. Part of its wide industrial diffusion is related to its great flexibility and versatility, which allow different process operations at time such as coating, repairing, and additively manufacturing new components as well. Research works, patents and developments of new Direct Laser Metal Deposition systems applied at the macro-scale represent a relevant part of the current State of the Art in metal Additive Manufacturing technologies. Nevertheless, to the best of Author's knowledge, no research activities were carried out on the feasibility of Direct Laser Metal Deposition process applied at the micro-scale.

This Ph.D. research work deals with the application of the Direct Laser Metal Deposition process at the micro-scale. The feasibility and the technical issues in downscaling the technology from macro to micro are discussed and analysed. The main parameters affecting the process are identified and their influence on the dimensional accuracy, structural integrity, surface roughness, and internal porosity of realized micro artefacts is investigated.

The experimental results show the feasibility in applying the Direct Laser Metal Deposition process at the micro-scale thanks to the assumption of a new building approach for the artefact realization. The deposition of 3D full dense artefacts with very low surface roughness and a limited "stepwise" effect is demonstrated. Moreover, it is underlined the need of a new deposition nozzle concepts to increase the powder deposition efficiency and to ensure a high powder particle mass concentration in correspondence to the molten pool.

This Ph.D. thesis is the first research work investigating the feasibility and application of the Direct Laser Metal Deposition technology at the micro-scale, representing a significant step forward in the development of the Manudirect ® MSL50 machine and providing a great contribution in terms of research activities in the field of Additive Manufacturing.

Sommario

Direct Laser Metal Deposition è una tecnologia additiva appartenente alla famiglia delle Direct Laser Deposition Technologies, dove il componente viene realizzato in modo additivo, strato dopo strato e senza l'utilizzo di utensili da taglio, attraverso l'impiego di una sorgente laser che localmente interagisce con polvere metallica depositata in modo diretto.

L'interesse attorno a questa tecnologia è cresciuto in modo sostanziale negli ultimi anni, trovando sempre maggiore impiego in settori industriali quali l'aerospaziale, l'automobilistico, il biomedicale e l'elettronico. Grazie alle sue caratteristiche tecnologiche non convenzionali e alle sue uniche potenzialità, il processo di Direct Laser Metal Deposition combina l'elevata complessità geometrica conferita al prodotto alla possibilità di processare un'ampia gamma di materiali metallici, spaziando dalle leghe di Titanio a quelle di Nickel, dalle leghe di Rame ai Cermet. Un ulteriore aspetto e vantaggio tecnologico correlato con questa tecnologia riguarda la sua forte flessibilità e versatilità nel prestarsi ad essere impiegata in diversi processi tecnologici quali: coating, repairing e, non per ultimo, Additive Manufacturing.

Ad oggi, l'attività scientifica in ambito Additive Manufacturing di metalli si focalizza principalmente sull'analisi dell'applicazione del processo di Direct Laser Metal Deposition su scala macro-metrica, in quanto, assieme alla tecnologia di Selective Laser Melting, risulta essere la tecnologia che riscuote maggior interesse in ambito scientifico-industriale. Tuttavia, ad oggi, poca attenzione è stata rivolta nell'analizzare l'applicabilità di tale processo su scala micro-metrica. La possibilità di produrre parti dall'elevata complessità geometrica e dal costo relativamente contenuto, attraverso la deposizione di materiali innovativi e difficilmente lavorabili per le tecnologie tradizionali (quali fresatura e tornitura per esempio), aprirebbe nuovi fronti applicativi e tecnologici a forte vantaggio di settori quali il biomedicale o l'elettronico dove la produzione di micro-componenti ad oggi trova forti limitazioni in termini di costi di produzione e fattibilità del componente.

Questo lavoro di ricerca, quindi, si prefigge l'obiettivo di analizzare l'applicabilità della tecnologia di Direct Laser Metal Deposition su scala micro-metrica. La fattibilità e le problematiche tecnico-processuali legate allo "down-scaling" di tale processo da una scala macro ad una micro vengono trattate ed analizzate, investigando come i parametri di processo influenzino l'accuratezza dimensionale, la finitura superficiale e l'integrità strutturale della parte realizzata per Additive Manufacturing. Inoltre, tale attività ha lo scopo di dimostrare la fattibilità nel realizzare micro-strutture massive full-dense con un ottima rugosità superficiale, identificando le maggiori problematiche a livello processuale e proponendo nuovi futuri sviluppi miranti al miglioramento di tale tecnologia in ambito micro.

Il lavoro di ricerca qui presentato rappresenta una forte spinta motivazionale ed innovativa all' esplorazione della tecnologia di Direct Laser Metal Deposition applicata nel micro Additive Manufacturing di metalli, in particolare nel motivare futuri ricercatori nello sviluppare e migliorare le performance sistemi già esistenti come quello impiegato in questo progetto (sistema per micro-lavorazioni additive Manudirect ® MSL50).

Acknowledgements

Innanzitutto, vorrei ringraziare la mia splendida famiglia: papà Daniele, mamma Tiziana e le sorelline Michela e Rossella che, nonostante le dure prove e difficoltà affrontate in questi anni, non mi hanno mai fatto mancare il loro supporto morale ed economico, ritrovandoci più forti ed uniti.

Inoltre, un ringraziamento va ad Alice che con le sue “paranoie” e “complessità morali” si dimostra essere invece un valido, costante e felice supporto sia nella vita privata che in quella professionale.

Un ringraziamento particolare va al Prof. Paolo F. Bariani che mi ha permesso di vivere e compiere una bellissima esperienza nell’ambito delle tecnologie additive, mettendo a disposizione grandi risorse materiali e non, da impiegare nel campo della ricerca.

Infine (ma non per ultimi), vorrei ringraziare gli amici se non colleghi d’avventura che ho avuto la fortuna di conoscere ed incontrare in questi anni trascorsi al laboratorio Te.Si. Un sentito ringraziamento quindi a: Riccardo, Luca, Marco, Filippo, Ruggero e Davide, facendo loro i miei migliori auguri professionali e non.

“you gain strength, courage and confidence
by every experience in which you stop
to look fear in the face”

Eleanor Roosevelt

Contents

Glossary of terms

2D = two dimensional
3D = three dimensional
AM = Additive Manufacturing
ASTM = American Society for Testing and Material
BSE = Backscattered electrons detector
CAD = Computer Aided Design
CFD = Computational Fluid Dynamics
CNC = Computer Numerically Controlled
CT = Computed Tomography
d = laser spot diameter
d_{LF} = laser focus distance
d_{WP} = working-plane distance
DED = Direct Energy Deposition
DLD = Direct Laser Deposition
DLMD = Direct Laser Metal Deposition
DOE = Design of Experiments
E_d = energy density
EBSD = diffracted backscattered electrons detector
EDS = energy dispersive X-ray spectrometry detector
f = powder feed rate
F = laser scan speed
FDM = Fused Deposition Modelling
FGM = Functionally Graded Material
FGS = Functionally Graded Structure
HAZ = Heat Affected Zone
I = specific energy
LBAM = Laser Based Additive Manufacturing
MPL = Multi Passes per Layer
n°p = number of passes
OPL = One Pass per Layer
P = laser power
PBF = Powder Bed Fusion
SEM = Scanning Electron Microscope
SLM = Selective Laser Sintering
T = temperature
Δz = vertical displacement

List of figures

List of tables

List of publications

KHADEMZADEH S, PARVIN N, MAZZUCATO F, BARIANI P F (2014). Geometrical characterization of thin walls produced by micro laser sintering. In: iCAT2014 Proceedings of 5° International Conference on Additive Manufacturing. p. 137-141, Vienna, 16-17 October 2014

MAZZUCATO F, BARIANI P (2015). Analysis of balling phenomenon in micro direct laser metal deposition. In: Proceedings of the 4M/ICOMM2015 Conference. 108, Milan, Italy

MAZZUCATO F, BARIANI P (2015). Dimensional accuracy of AISI 316L micro-features in Direct Laser Metal Deposition. In: Proceedings XII A.I.Te.M. Conference. P. 137-140, Palermo, 7/09/2015

Khademzadeh S, Parvin N, Bariani PF, Mazzucato F (2015). Effects of Micro Laser Sintering Process Parameters on Quality of Nickel-Titanium Single Tracks and Thin Walls. METALS AND MATERIALS INTERNATIONAL, vol. 6, p. 1081-1090, ISSN: 1598-9623

Mazzucato F, Bariani PF (2016). First layer formation issue in Micro Direct Laser Metal Deposition. In: ICOMM2016 Proceedings. 48, Irvine, California, USA, 29/03/2016

Chapter 1

Introduction

In this Chapter, the definition of *Additive Manufacturing* and a general overview on the technologies and systems for Additive Manufacturing are provided. The main capabilities and industrial advantages of these technologies compared to the traditional ones are highlighted, focussing on the recent developments achieved in the realization of innovative metal prototypes and components.

The Direct Laser Metal Deposition (DLMD) technology is introduced and its main technical characteristics and process capabilities are discussed. Moreover, the new frontier of Additive Manufacturing applied at the micro-scale is introduced. Finally, the scope and objectives of the Ph.D. research project are presented.

1.1. Additive Manufacturing

In 2010, the American Society for Testing and Materials (ASTM International) defined *Additive Manufacturing (AM)* as "*a process of joining materials to make objects from 3D model data, usually layer upon layer, as opposed to subtractive manufacturing methodologies*" [1]. This recent and re-known definition clearly distinguishes the AM technologies from the traditional manufacturing techniques where the component is formed through moulds or removing material by cutting tools (e.g. tuning, milling, grinding, casting, etc.) [1].
In the recent years, the interest in AM grew in importance both in commercial and industrial and academic sectors. The over 3500 patents published from 1975 to 2011 demonstrate the considerable attention for these technologies [2]. The possibility of "printing" what we see directly from a three-dimensional CAD model without geometrical or material constrains due to the physical presence of cutting tool, is fascinating both industrial designer and academic researcher. The recent improvements on the final accuracy and mechanical properties of components realized by AM have allowed the production of fully-functional parts for service in a variety of applications, such as: aerospace, automotive, electronics, biomedical, and fashion. The constant technological growth of AM technologies has turned the AM products from simple prototypes (Rapid Prototyping) into end-use parts (Rapid Manufacturing).
Generally, the main AM methods can be summarized in seven families, such as: material extrusion, material jetting, sheet lamination, vat photo-polymerization, binder jetting, direct energy deposition (DED) and powder bed fusion (PBF) [10-11]. The unique capabilities characterizing the AM technologies are [3]:

- *design optimization.* The distinctive characteristic of the AM process is to be capable to realized part adding material layer upon layer. This fact enables the creation of very complex geometrical shape, since there is no need for fixtures or tooling which can cause collision and then bring damage during the realization of complex part [4]. Moreover, the design freedom is enhanced by the possibility to selectively place multi-materials where it is required, allowing the realization of Functionally Graded Material (FGM) without the employment of additional devices or systems. This capability enables the realization of innovative components with an optimized-functional structure and shape and with no additional costs, since no additional tooling, or re-fixturing, or expert operators are required.
- *assembly realization.* AM technologies enable the realization of "single-part assemblies", printing the components of the assembly in place thanks to the employment of structures or support material which have to be removed with post-processing operations. This capability strongly reduces the production time of the overall assembly, since additional joining operations are not needed, and releases possible constrains due to the union of the different parts.
- *impact on the supply chain.* AM strongly affects the supply chain in terms of lead time of production, lead time of transportation, and reduction in stockpile size. The capability to realize parts layer upon layer and the possibility to add different materials during the same process enhance the feasibility to manufacture several products with different shapes and materials at time. This capability has the effect to condense the lead time of production, since in the

same process different products with different properties can be realized. Moreover, the flexibility and versatility of these technologies allow their installation and use in different places and environments, moving closer to the customer. This turns into a decentralization of the production and of the distribution, reducing the lead time of transportation. The employment of digital data (3D CAD model) also turns the physical stockpile into digital stockpile, reducing the space and the costs required to stock end-use or spare parts, but printing them only when it is needed.

- *time and cost efficiency in production run.* AM processes are suitable for low volume of production and are slower compared to cost efficient process for mass production (e.g. Injection Moulding) [5]. Nevertheless, the on-demand and on-location AM production reduces the costs associated with both the inventory and supply chain costs [3]. Moreover, the material waste during AM processes is very low compared to the traditional subtractive technologies where the scrap material can exceed the 90% [6].

Despite the innovative capabilities and great potentialities of AM technologies, their wide diffusion in industrial sector is still limited due to some technological issues and barriers, such as:

- *mass customization vs mass manufacturing.* Currently AM technologies are suitable for low batch of production, where the product presents a strong customization and geometric complexity. Typical sectors where AM finds large employment in realization of end-use products are: aerospace, high-end automotive, bio-medical, and jewelry. For high mass production the AM technologies still have technological limitations in terms of time production and costs. However, there are scenarios wherein the slower cycle time is outweighed by the opportunity to consolidate parts, reduce material waste, and/or there is market demand for customized geometry. Align Technology's Invisalign custom orthodontics, Ownphones custom earphones, and GEs fuel nozzle are emerging examples of using AM to achieve cost-effective large-volume production of products [3].
- *building scalability vs layer resolution [3].* In AM, the deposition of layer with a smaller thickness and consequently with a high resolution is needed to realized part with high final accuracy and surface finishing. Nevertheless, decreasing in the layer thickness, the total build time increases because more layers have to be deposited. On the contrary, thicker layers allow a faster part realization, but a worst final quality of the realized part. In literature, the researchers are focused in two different research activities: improvement on the control of the process parameters to enhance a good dimensional accuracy of the part in shorter time [7,8], and analysis of process chains to improve the part quality through hybrid AM processes [9].
- *raw material.* If AM technologies are capable to treat a wide range of material, both polymers and metals, most of the current materials present in the market are not suitable to be additively manufactured but show to be inadequate, deteriorating the final quality of the part in terms of final dimensional and geometrical accuracy, porosity distribution, surface and structural integrity. Some research activities are going on to design new material batch and solution capable to conform and take advantage of additive process.

- *AM standardization.* One of the weak point in AM is the lack of standards. Given the development and the growing use that these technologies are finding in the industrial sector, it is important to define material, process, calibration, testing and file format standards to ensure part quality, repeatability, and consistency across builds and machines [3]. Nevertheless, the wide typologies of AM technologies and systems makes difficult the development of a unique standard for AM.
- *surface quality.* The final surface quality of AM parts strongly depends on three factors: AM system, process parameters, and raw material. More the deposited layer is small and continuous, more the realized surfaces are smooth. However, this is in contrast with the building time. Moreover, the general surface conditions of the part strongly depend on the printing orientation and employed AM technology. For instance, the aspect of the top surface of the part generally differs from the lateral ones that presents the typical phenomenon called “stepwise effect” caused by the thickness of the deposited layers.
- *structural integrity.* The structural integrity of an AM component strongly depends on the resulting surface conditions and porosity distribution inside the bulk of the part. Uncontrolled porosity formation and distribution affect the static and dynamic mechanical behaviour of the component, causing crack generation and unexpected breakage. Residual stresses involved by the thermal gradients generated during some AM process can also affect the final integrity of the part, warping or damaging the component after the realization.
- *post-processing*. To date, most of the parts realized by AM required post-process operation to improve the final quality of the artefacts in terms of surface finish, dimensional accuracy, and structural integrity (residual stresses). Except for AM system with five or more axes, post-processing operations are needed to remove the built-in support material as well.

In these years, important efforts were done both in academic and industrial fields to improve the final quality of the AM products in terms of dimensional accuracy, surface and structural integrity, and enhanced mechanical properties. In these years, notable achievements were obtained thanks to the design and manufacture of apposite AM materials combined with the development of new systems for the on-line control of the AM process.

The unique advantages and capabilities of these technologies in terms of product design, product concepts, and reduction in energy and material waste push and encourage new research investigations and developments of the AM processes and systems.

1.2. Metal Additive Manufacturing

DED and PBF processes (see Chapter 1.1) are the most employed and reliable AM methods to manufacture 3D metal components [10]. Both processes create components layer upon layer melting metal powder through the employment of a thermal energy source. The usual thermal energy source can be either a laser beam or an electron beam. In the case of laser beam, the two aforementioned AM processes are commonly known as Laser Based Additive Manufacturing (LBAM) and Direct Laser Deposition (DLD) respectively.

An example of AM process for LBAM is the Selective Laser Melting (SLM). This technology additively realizes metal components melting metal particles uniformly distributed on a powder bed selectively. A scheme of the process is represented in the Figure 1.1. At the beginning, a uniform powder bed is previously deposited and then selective melted by a laser beam to create the desire cross section of the part. When the first melted layer is completed, the base plate moves down and a new powder bed is deposited on the previous layer. These operations are repeated until the complete realization of the desired part. During the process, the un-melted powder supports the part during the process, allowing the realization of components with overhanging structures.

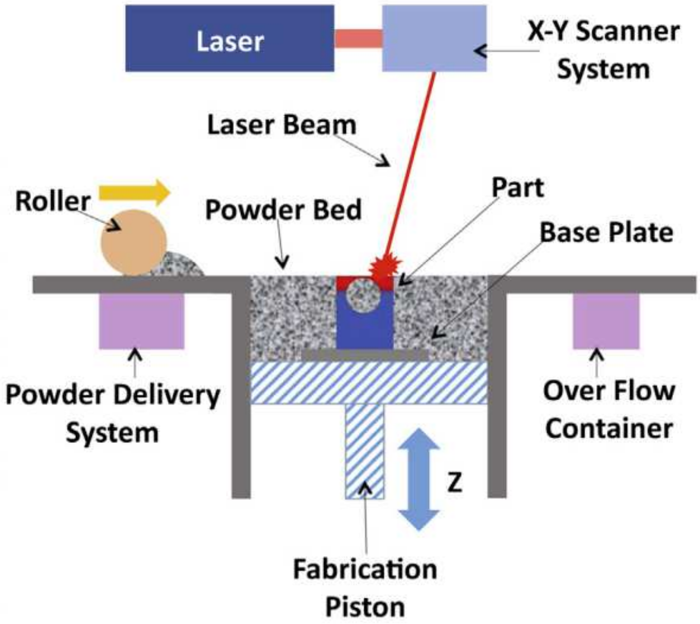

Figure 1.1 Selective Laser Melting technology (SLM) [10].

On the contrary, DLD does not selectively melt a powder bed to created the wanted part, but it directly deposits the powder where it is strictly required, combining the metallic material and the energy supply for a simultaneous deposition and part formation (see Figure 1.2). This turns in less powder consumption in comparison with LBAM because the powder particles do not completely fill all the sintering chamber and do not act as support. In this process, the powder is deposited through one or more nozzles, which can be coaxial with the laser beam or not [11-15].

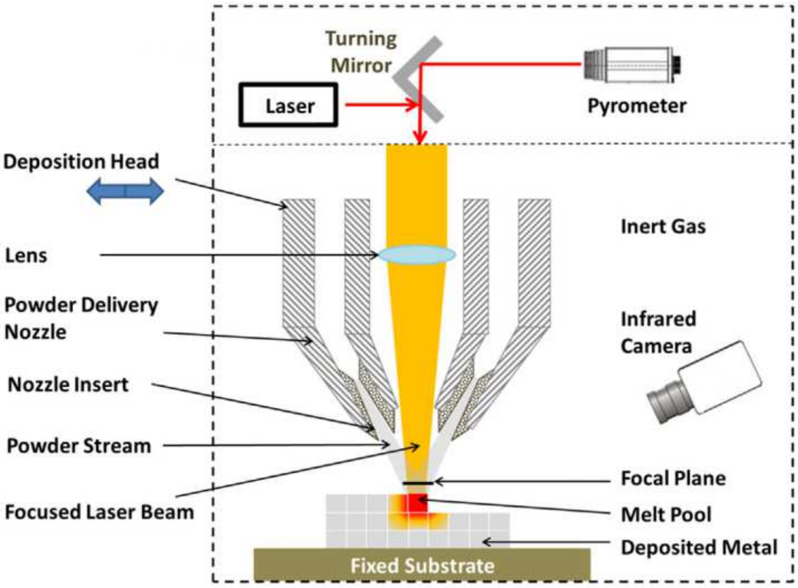

Figure 1.2 Direct Laser Deposition technology (DLD) [10].

The main differences between LBAM and DLD are summarized in the Table 1.1.

LBAM	***DLD***
better final surface finish	coarser final surface finish
un-melted powder removal	no support structure required (for 5-axes system)
better final surface	
spherical-shape powder particles improve the LBAM process	irregular-shape powder particles improve the DLD process
no Functionally Graded Structures (FGS)	Functionally Graded Structures (FGS)
no coating	coating
no repairing	repairing

Table 1.1 Comparison between LBAM and DLD.

1.2.1. Metal Additive Manufacturing at the micro-scale

In the recent years, the interest in the application of metal AM at the micro-scale increased in importance. AM technologies demonstrate to be a valid cost effectiveness alternative to the current methods employed to realized micro artefacts in fields such as biomedical, electronics, microfluidics, and micro optics, thanks to several capabilities which they have (see Chapter 1.1). The possibility to realized artefact strongly customized with the desired functional shape and material, without the employment of cutting tools or lubricants which can damage or contaminate the micro-components, is an unique capability that only AM technologies own.

Direct Laser Metal Deposition (DLMD) is an AM technology that is well suited for the manufacture of micro metal parts. The possibility to reduce the laser spot up to 30 µm combined with powder grain sizes ranging between 5 and 30 µm allows the fabrication of very fine micro-features with a minimum layer thickness of 30 µm [16]. Moreover, the DLMD capability to deposit the metal powder only where is strictly needed in combination with the possibility to deposit different metal alloys simultaneously opens the feasibility to create FMS at the micro-scale with a low powder and energy consumption.

Nevertheless, the down-scaling of this kind of process from macro to micro is not easy to perform due to the change ratio of the process parameters and environmental conditions towards each other (e.g. powder grain size and laser spot size) [16]. Moreover, the downscaling of the direct sintering process is usually followed by an increment of the costs and timing required to manufacture the part. However, these industrial issues can be overshadow by the high accuracy and precision achievable by DLMD and the great potentialities of this technology applied at the micro-scale in terms of geometric complexity and functionality.

Table 1.2 summarizes the main differences between the application of DLMD at the macro and micro-scale.

parameter	***micro-process***	***macro-process***
focusing spot diameter (µm)	30-50	up to 22 mm
powder particle size (µm)	5-30	45-150
resolution/repeatability of x-y stage (µm)	0.05	n.a.
powder mass flow (g/h)	2.5-10	up to 8 kg/h

Table 1.2 Comparison between macro and micro DLD [16].

1.3. Direct Laser Metal Deposition technology

Direct Laser Metal Deposition (DLMD) is a laser based additive manufacturing process for metal powder that belongs to the family of DLD technologies. As explained in the Chapter 1.2, DLMD does not required an uniform powder bed to additively manufacture complex parts, but it concentrates a laser beam with a local deposition of powder particles dragged by an inert gas. Generally, the process takes place into an inert-gas chamber in order to reduce the oxidation of the deposited part and the generation of smokes or powder combustion. The part realization occurs layer upon layer on a metal substrate that can be fixed or relatively move to the laser source.

The process phases required to realize the desired component are common to all the AM technologies. The 3D CAD file of the component is cross-sectioned (slicing operation) by a software for three dimensional model data and a g-code is created. The AM system employs the information contained in the g-code file to build layer upon layer the 3D part, activating the required process parameters and moving the laser beam (or the metal substrate) that reproduces the geometry of the 3D model. The thermal energy hits the surface creating an interaction zone called molten pool. Here the metal powder particles fall inside allowing the creation of a solid bead. When the first deposited layer is completed, the metal substrate moves down and the deposition of a new layer starts. At the end of the process, the realized part has to be removed from the substrate.

The powders used in DLMD have a large variety. Stainless Steel, Titanium alloy, and Nickel alloy are the most used, but the process works well with Aluminium, Copper, Tungsten, and CERMET powders too. The process parameters affecting the DLMD process are numerous and all of them can have a strong impact on the final quality of the part. An example of DLMD process parameters are: laser power, laser spot, laser scan speed, laser defocusing, metal powder, shape of the powder particles, powder particle grain size, thermal properties of the substrate, starting surface conditions of the substrate, deposition strategies, idle time, etc. The factors to take into account are more than 20 and this makes difficult the analysis of the process. Optical or infrared instruments are often employed to monitor the process while it is going on. Several authors attempt to build real-time, closed-loop control to increase the quality, consistency, and repeatability of the process, acting on the control of molten pool size and shape [17-19]. Nevertheless, close-loop control is still difficult to implement and use, due to the complexity of the mutual interactions between the DLM process parameters and, consequently, more efforts have to be done to improve the process control [20].

In the following Subchapters, the main features characterizing the DLMD process will be introduced and discussed.

1.3.1 Mass and energy transfer

In DLMD, the laser sources employed for the deposition process are mainly of two types: Nd:YAG (neodymium-doped yttrium aluminium garnet) laser [21-23], and CO_2-type [24-26].

During the last years, Nd:YAG lasers were favourite to CO_2 since they ensured a higher energy efficiency thanks to their short emission wavelength (1.067 µm instead of 1.067 µm for CO_2). Moreover, thanks to the low energy losses during the process, Nd:YAG lasers could work with limited maximum laser capacities (around 5 kW instead of 18 kW for lasers CO_2-type [27]), reducing the costs of the system and increasing the operating life of the optics. It is noteworthy that a new laser family is currently finding development and application in AM, that is diode lasers. This kind of lasers allows a strong reduction in production time and a significant increase in the energy efficiency of the process (wavelength of circa 808 µm) compared to the actual AM technologies. Nevertheless, to date their employment is tested in SLM technologies, so in this Chapter they will be not taken into account.

Depending on the DLMD application (macro or micro-scale) and on the laser defocusing, the diameter of the laser spot ranges from few tens of microns to some millimetres (see Table 1.2). Nevertheless, the local energy density and heat fluxed involved during the process are very high. For instance, a DLD process operating with a total laser power of 500 W and a beam size of 1 mm provides for an average heat flux excess of 50000 W/cm^2 [10].

Less than 80% of the starting energy power reaches the substrate to form the molten pool [28]. In fact, laser attenuation occurs due to the metal powder absorbing and scattering. Unocic et al. demonstrated that for a fixed laser power, increasing the powder feed rate during the deposition process, the laser attenuation increases [29,30]. Moreover, for lasers with Gaussian profile, near the centre of the laser beam, the energy attenuation seems to be lower, indicating a more absorption of energy for the powder particles close to the beam centre. In addition to laser attenuation, laser-induced plasma can be caused by high laser energies employed during the DLMD process. The onset of plasma deteriorates the efficiency of the process, decreasing the absorption of the laser irradiance [31].

The efficiency in powder supply during a DLMD process can be quantify as a ratio between the powder employed in the part formation and the total powder delivered by the system during the process. This coefficient in powder deposition mainly depend on: nozzle geometry, carrier gas, exit angle, and size distribution of the powder particles. Generally, in DLMD the deposition efficiency is quite low (lower than 30%) [29] and this is a factor that increases the costs of the process. This is because the cross-section diameter of the powder focus usually does not match the diameter of the laser beam [32]. In the common DLMD systems, the laser spot is smaller than the focus of the powder particles and then several particles do not fall inside the molten pool and the deposition efficiency decreases.

1.3.2 Molten pool dynamics and formation

The molten pool is the region where the laser beam reaches the substrate and interacts with the surface. Thanks to the high energy density delivered by the system, the local temperature rapidly increases and the substrate melts, creating a spherically shaped droplet of molten metal (see Figure 1.3). During the part realization, the molten pool moves with the laser beam motion and the powder particles fall into it, creating a solid deposition track.

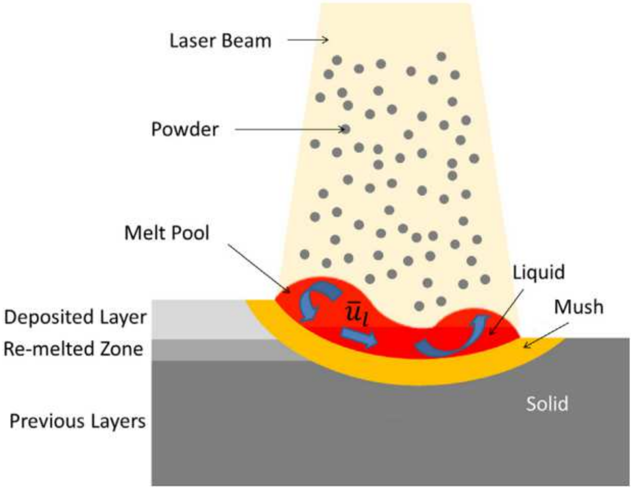

Figure 1.3 Interaction zone between laser beam and metal surface [10].

The local interaction zone between laser beam and metal surface can be divided in three zones (see Figure 1.3):

- molten pool: it is in a liquid state and it is formed by both melted substrate and melted powder particles;
- mush zone: it is also known as Heat Affected Zone (HAZ) and it is located between the molten pool and the solid part of the substrate. It is a two phase mixture zone that behaves as a porous medium [33];
- solid zone: this is the part of substrate not melted by the laser energy irradiation.

The molten pool is thermodynamically unstable and its shape and internal energy strongly depend on the surrounding heat transfer and liquid/solid interactions. The realization of a constant molten pool during the DLMD process is of great importance since it is the initiation of the solid part and determines the final quality of the artefact.

Dimensional accuracy, surface finish, final microstructure, porosity formation and distribution, as well as the presence of residual stresses on the finished part depend on the molten pool behaviour and shape during the DLMD process.

1.3.3 Solidification and microstructure

The solidification of the molten pool in DLMD is a complex phenomenon governed by the net heat transfer and where three main events coexist together: heterogeneous nucleation, mushy-zone heat/mass transfer, and microstructural evolution via heat treatment. Moreover, the complexity of the physical process is increased by the fall of the powder particles into the molten pool.

The temperature dependent microstructure evolution strongly depends on the material. The chemical elements present in the metal alloy can modified the solidification behaviour of the molten pool, determining different microstructures [10]. The microstructural evolution can present columnar, planar or dendritic structures. Nevertheless, the arising of the Marangoni convection during the molten pool formation can modified the solidification heat transfer as demonstrated by Yin et al. [34]. He proves that no significant macro segregation was evident during DLMD-based solidification of SS410 due to Marangoni mixing effect.

Porosity can be present in a 3D part realized by DLMD. Lack of sufficient fusion between successive layers or the presence of un-melted powder particles can cause an extensive porosity formation [35, 36].

The cooling rate is not constant during the DLMD process and it varies along the laser/surface interaction zone. It is higher at the solid/liquid interface and decreases with distance from the centre of the molten pool [37]. Moreover, the molten pool cools very rapidly due to the very high temperature of its bulk in comparison with the surrounding environment. The higher is the cooling rate, the finer is the microstructure [38].

In DLMD, the final microstructure configuration is helpful in understanding the solidification heat flux direction during cooling. For instance, the presence of directional columnar microstructure is indicative of unidirectional heat flux [39, 40].

1.3.4 Effect of DLMD process parameters

The process parameters to be taken into account during a DLMD process are numerous (more than 20) and the interaction between them are very complex and difficult to model and simulate.

Several Authors as Farahmand et al. have analysed the physics of the process, building a theoretical model and simulating the complex interaction between powder particles, laser energy and substrate surface [17]. The results showed controlling the molten pool temperature during the process deposition the quality of the deposited track improves in terms of residual stresses and microstructure evolution. Boddu et al. underline that systematic implementation of process control requires a complete understanding of relation between various parameters and its effect on individual processes and the system as a whole [41]. Nevertheless, further investigation are required to improve the existing DLMD theoretical representation and fully understand the physics involved in the process [18].

To simplify the comprehension of the phenomena occurring in DLMD, the process parameters can be identified such as:

- *dimensional factors*: diameter of the laser spot, laser power, laser scan speed, laser defocusing, powder feed rate, powder grain size, flow rate of the carrier gas, preheating of the substrate, etc.;
- *adimensional factors*: powder deposition efficiency, melting efficiency, Reynolds number, etc.;
- *factor derivatives*: specific energy, energy density, volumetric exposure, exposure time, etc.;
- *geometrical factors*: size of the molten pool, shape factor of the molten pool, dilution ratio, shape of the powder particles, surface conditions of the substrate, etc.;
- *material factors*: material density, tap density of the powder, reflectivity, thermal conductivity, etc.

The complexity of the interactions between them makes difficult to easily identify correct process windows with which make the process more robust. For instance, light differences in raw material characteristics (e.g. shape of the powder particles) can affect the DLMD process, modifying the optimal combination of process parameters [42].

Anyway, the influence of some single process parameters on the final quality of the realized artefact is quite known. For instance, increasing the laser scan speed the cooling rate of the molten pool is higher and the microstructure of the realized component is finer and columnar along the heat flux direction. Moreover increasing the speed of the laser passes the final surface roughness on the top of the artefact improves. Higher laser power allows deeper molten pool and a better adhesion between successive layers, but can induce plasma formation causing a decrease in the efficiency of the laser irradiation. Low values for the laser energy can induce porosity into the bulk of the component due to lack of correct melting and molten pool formation. High powder feed rate increases the molten pool size, but decreases the net laser energy reaching the substrate surface due to the increase in the laser attenuation. Preheating of the metal substrate reduces the thermal gradient at the beginning of the DLMD process, improving the molten pool formation and enhancing a better control on the deposition process.

1.4 Scope and objectives of the Ph.D. project

In this Ph.D. project, the scientific objective is to investigate the application of the DLMD technology at the micro-scale, analysing the influence of the main process parameters on the final quality of the micro-artefact.

The technological issues in downscaling DLMD from macro- to micro-scale will also explored and some consideration and improvements on the micro DLMD system employed during the research project will be provided.

To achieve the aforementioned aims, the following specific objectives are fixed:

- mathematical modelling of the powder deposition process and characterization of the powder cloud coming out from the deposition nozzle;
- investigation of the influence of the process parameters on the continuity and accuracy of the deposited track;
- developing and verification of a new building approach for micro DLMD;
- deposition and characterization of thin micro-features employing laser spot of 30 µm;
- deposition and characterization of 3D dense bulk features realized on a mould insert for micro Injection Moulding.

In terms of novelty, this Ph.D. work has several unique elements such as:

- first case in literature of application of the DLMD technology at the micro-scale and analysis of the technical/industrial issues concerning the downscaling of the technology;
- new building deposition approach for DLMD;
- realization of end-use micro-feature for industrial application (i.e. micro Injection Moulding).

Moreover, this research project represents a significant contribution for the development of the Manudirect ® MSL50 machine designed for micro DLMD applications and for improving the process control on the deposition and realization of micro-components.

Chapter 2

Experimental apparatus and materials

This chapter deals with the experimental apparatus employed during this Ph.D. research project.

The Manudirect ® MSL50 micro DLMD system is here introduced. Its main characteristics such as feeding system, deposition nozzle and machine structure are presented and explained. In addition to the metal powders employed for the experimental test, the equipment involved to analyze and characterize the 3D realized specimens is also introduced and discussed.

2.1. The DLMD system

The AM system employed in this Ph.D. research project is a AM machine based on the DLMD technology and designed for micro-applications. The commercial name of the system is Manudirect ® MSL50 (see Fig. 2.1).

Figure 2.1 Manudirect ® MSL50 micro DLMD system available at Te.Si. lab - University of Padua.

MSL50 is a 3 axes machine for micro laser sintering provided by Manudirect company (Vascon di Carbonera, Treviso – Italy) and available at Te.Si. lab (Department of Industrial Engineering - University of Padua, Rovigo - Italy). The innovative features of the Manudirect Industrial Platform are:

- micro-phased materials (patented technology);
- multiple powder feeders;
- capability to manufacture multimaterial structures (gradient materials);
- virtual engineering material design software;
- CAD slicing software;
- feasibility of a double production scheme (see Chapter 1.1):
    - high resolution - low productivity;
    - high productivity - low resolution.

The system is composed by two parts: an electronic architecture and a hardware structure (see Fig. 2.2).

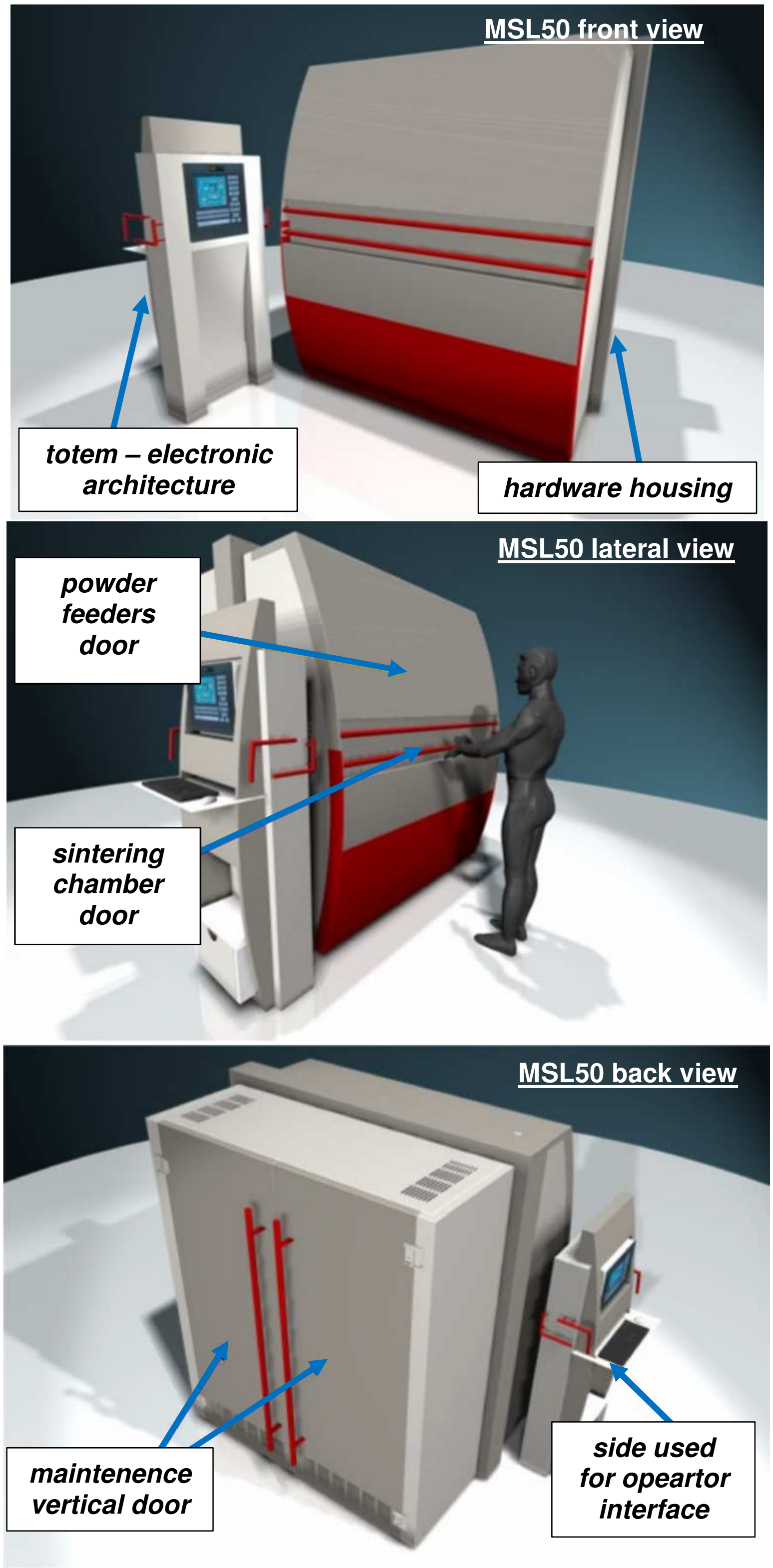

Figure 2.2 Manudirect Industrial Platform views.

The Manudirect electronic architecture consists of two operation interfaces installed on a totem with the possibility to connect PC in stand-alone way, electronic devices and remote controls. An interface is called Centralized Control System (CCS) which has two different working environments: LINUX Operating System, to check the machine operation, and Windows Operating System, to perform CAD programming with the PowerSLICE Delcam SW. The second interface is the Computer Numerical Control unit (CNC - Eckelmann).

Through the CCS interface, it is possible to manage the CAD file, perform slicing operations, translating the geometrical and process information in G-code instructions for the CNC interface, check the system operation and have a preliminary check of the geometrical quality of the realized part.

The main components making the software up are:

- Delcam PowerSLICE software;
- PostPROCESSOR software;
- BigEye software;
- CNC operating system (StdHMI Eckelmann).

The Manudirect hardware structure mainly consists of:

- sintering chamber;
- optical laser head;
- fibre laser device;
- powder feeder system;
- Multifocus system;
- optical sensor (interferometer PRECITEC ® CHRocodile S);
- thermal measurement system (SensorTherm ® pyrometer MQ22);
- cooling system (Eurocold ® chiller)
- oxygen detector equipment (SGM7);
- filtering and cleaning circuit.

The laser device installed in the system is a continuous fibre laser (YLM 100 WC, IPG, wavelength: 1070 nm) with a maximum power of 100 W and a laser spot diameter ranging between 30 and 120 µm (see Fig. 2.3).

Figure 2.3 YLM 100 WC, IPG.

The advantage to have an optical fibre laser is related to its wavelength. Employing laser source having short wavelength allows to reduce the energy dissipation concerning the powder scattering and reflection, obtaining a constant and stable laser beam and limiting the maximum laser power involved during the DLMD process. The machine is equipped with a coaxial powder feeding system employing a conical injection nozzle which allows a multidirectional powder deposition and a small heat affected zone during the DLMD process.

More details are redirected to the Sub-Chapter §4.1.1. and §4.1.2., where the geometry of the coaxial nozzle and the overall powder feeding system will be explained in detail.

The sintering chamber is a not vacuum chamber, but the inert gas Argon is blown in to reduce the level of Oxygen up to a value lower than 100 ppm (see Fig. 2.4). Working with very low values for the Oxygen is extremely important to avoid the combustion or explosion of the powder and to make the DLMD process safe.

In the chamber are placed (see Fig. 2.4):

- the SGM7 detector to continuously detect the level of Oxygen inside the chamber itself;
- the laser head;
- the interferometer and the Multifocus device to get a preliminary evaluation of the final geometry of the sintered artefact.

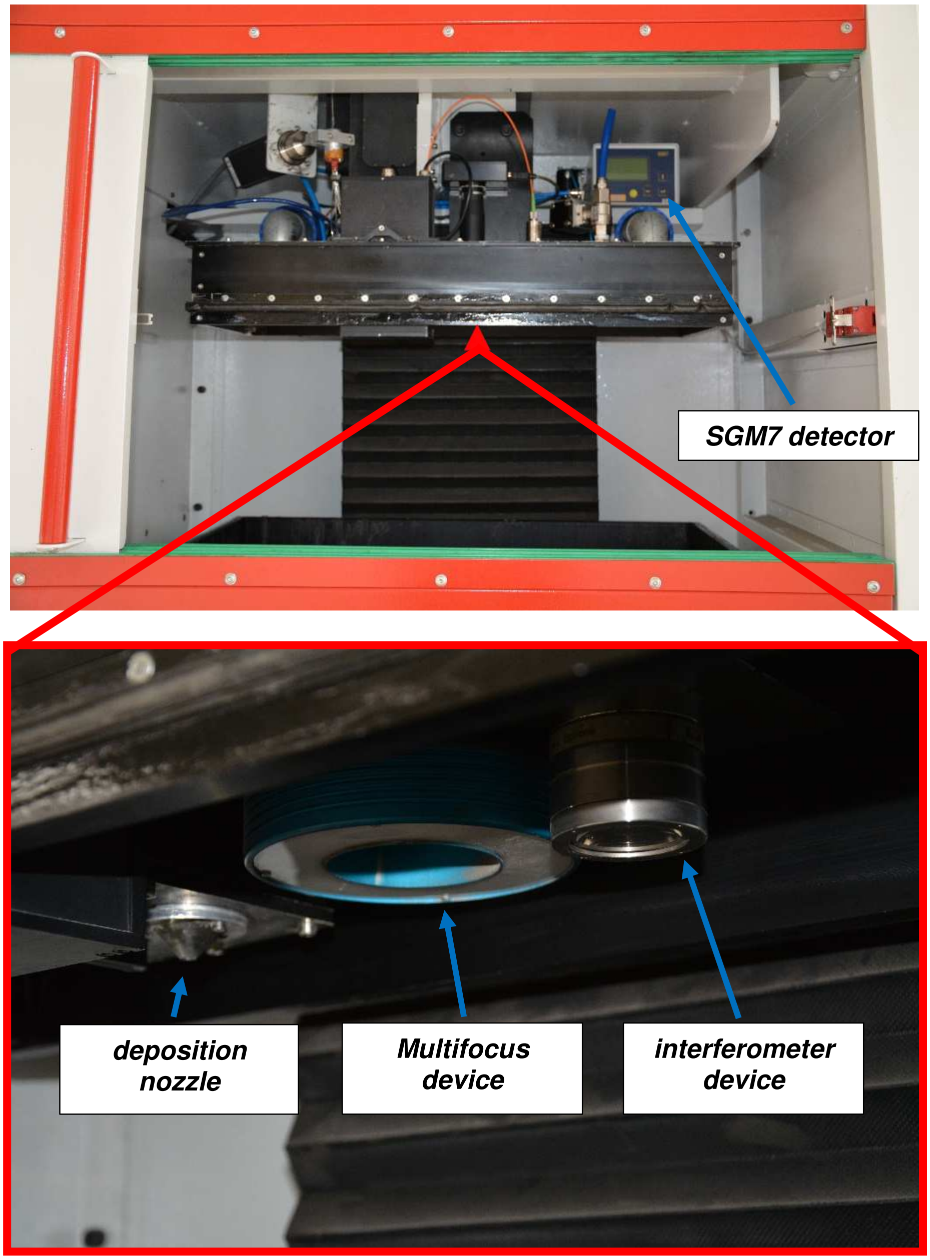

Figure 2.4 Manudirect ® MSL50 sintering chamber.

The technical data are summarized in the Table 2.1.

maximum build size	*50 x 50 x 50 mm (X x Y x Z)*
model-to-Part accuracy	*50 µm*
minimum feature size	*60 µm*
minimum layer thickness	*20 µm*
laser beam power	*2 – 100 W (constant)*
laser beam spot size	*30 – 60 - 120 µm*
laser scanning rate	*10 – 3000 mm/min*
powder size	*20 – 45 µm*
powder feed rate	*0.1 – 800 µm/s*
argon flow	*0.4 – 5.0 l/min*
n. of powder feeders	*1 – 6*
cooling	*Active*
power supply	*220V, 16A, 3,5 kW*
size	*1850 x 1500 x 2200 mm (W x D x H)*
weight	*1700 kg*
accuracy integrated Multifocus measurement system	*10 µm on the 3 axes in a minute*
accuracy integrated confocal measurement system	*3µm on Z-axis*
CAD interface	*PC*
CAD file type	*Standard: STL*
network	*Ethernet 10/100/1000*

Table 2.1 Manudirect ® MSL50 datasheet.

2.1.1. Powder feeding system

The powder feeding systems (called "micro-LS" powder feeding system) installed on the MSL50 machine is a pneumatic feeding system and it was designed to ensure a constant low powder supply on the sintering area during the micro DLMD process. The concept of the system is suitable to create a homogeneous fine solid-gas dispersion of the powder particles (called "particle aerosol") on the carrier gas (see Fig. 2.5).

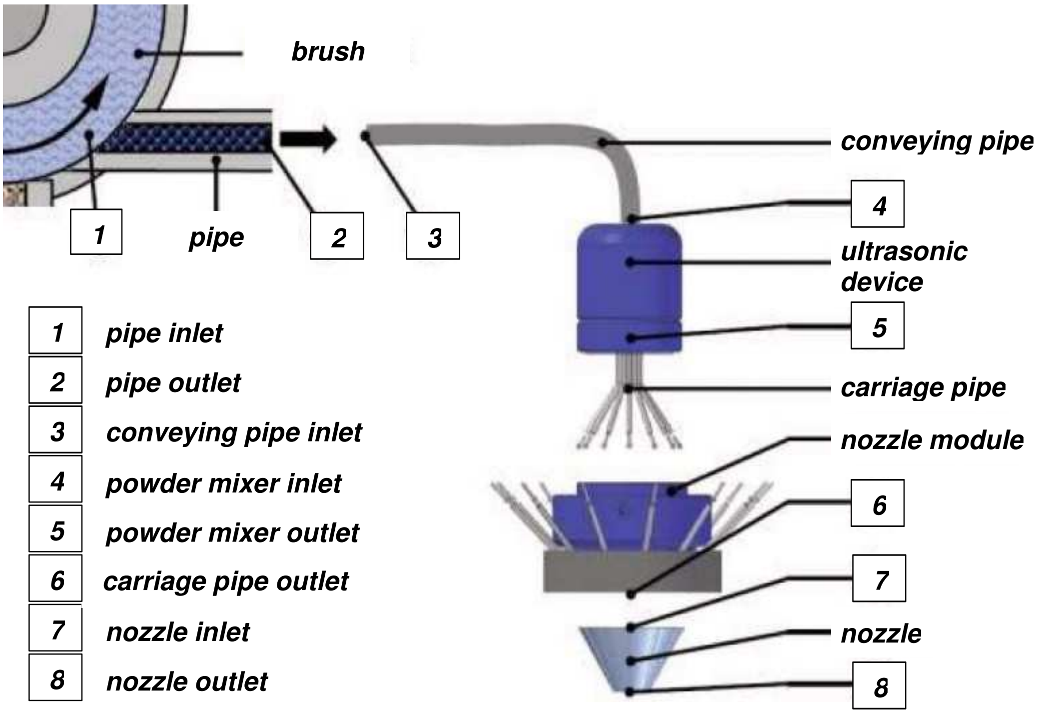

Figure 2.5 Feeding components [see Appendix A].

The powder feeding system is mainly composed by three subsystems:

- powder feeder;
- pipes and ultrasonic device;
- deposition nozzle.

The micro-LS feeder was designed to allow an easy access to the cartridge removal and replacement and it is composed by a powder cartridge, an electric engine and a rotating brush. When the powder supply is activated, the metal powder stored inside the cartridge is pressed against a rotating brush by a metal valve (see Fig. 2.6). The linear translation of the valve is driven by a rotating screw moved up by an electric motor with very high position accuracy (down to 0.1 µm/s). The rotating motion of the brush and the mechanical deformation and relaxation of its bristles enhance the fine powder dispersion and drive the powder particles to the feeder outlet. The brush watertight chamber is connected to a gas supply that drags the metal powders along the connector pipes up to the deposition nozzle. Thanks to the combination of rotating brush and the Argon carrier gas, at the feeder outlet the powder is in a state of fine solid gas dispersion.

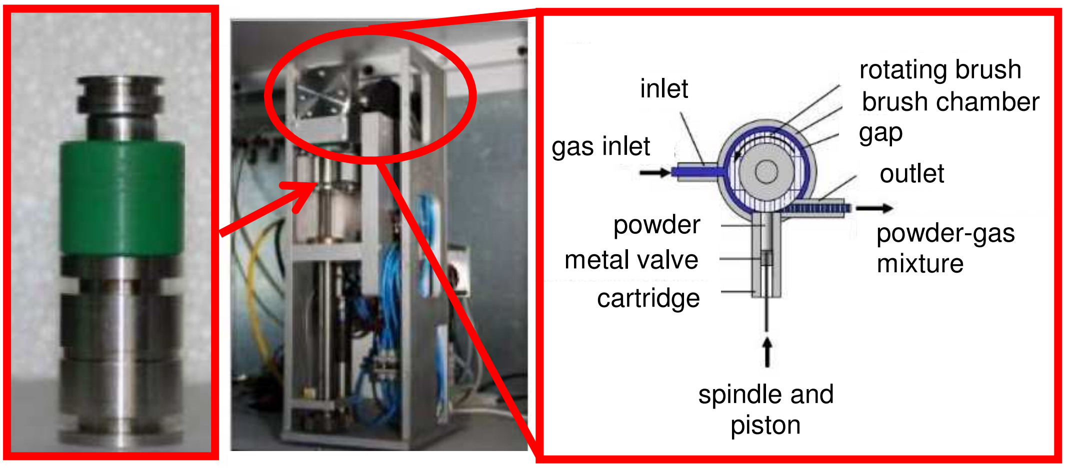

cartridge **Micro-LS feeder**

Figure 2.6 The micro-LS feeder.

The feeder outlet is connected to a pipe which guides the powder gas dispersion to a mixing unit and then to a distributor connected to an ultrasonic vibrating device to lower the risk of powder sedimentation and clogging within the distributor itself (see Fig. 2.5). Eleven activated pipes connect the distributor to the deposition nozzle through which the powder is deposited on the sintering area [see Appendix A].

The MSL50 housing and the structure of the powder feeding system were designed to manage until six different powder feeders. This enables to work with different metal powder compositions and/or powder particles size during the same micro DLMD process. The deposition of different powder blends can happen activating or disabling the feeders filled with different powder blends or employing the mixing unit integrated in the powder feeding system.

Up to now, a direct control on the powder composition and particle size distribution in the mixing unit is missing, so it is preferable to work with pre-mixed powder blend with a known composition and particles size, controlling the powder feeders directly. The advantage to control more than one powder feeder is in the possibility to realize Functionally Graded Structures (FGS) and to deposit layer of different density during the same micro DLMD process.

2.1.2. Deposition nozzle

The nozzle installed in the MSL50 has a special design that ensures a powder deposition coaxial to the laser source employed during the process (see Fig. 2.7). The conical shape of the nozzle gives to the powder-gas mixture coming out from the outlet a nominal inclination that allows the formation of a powder cone (see Fig. 2.8).

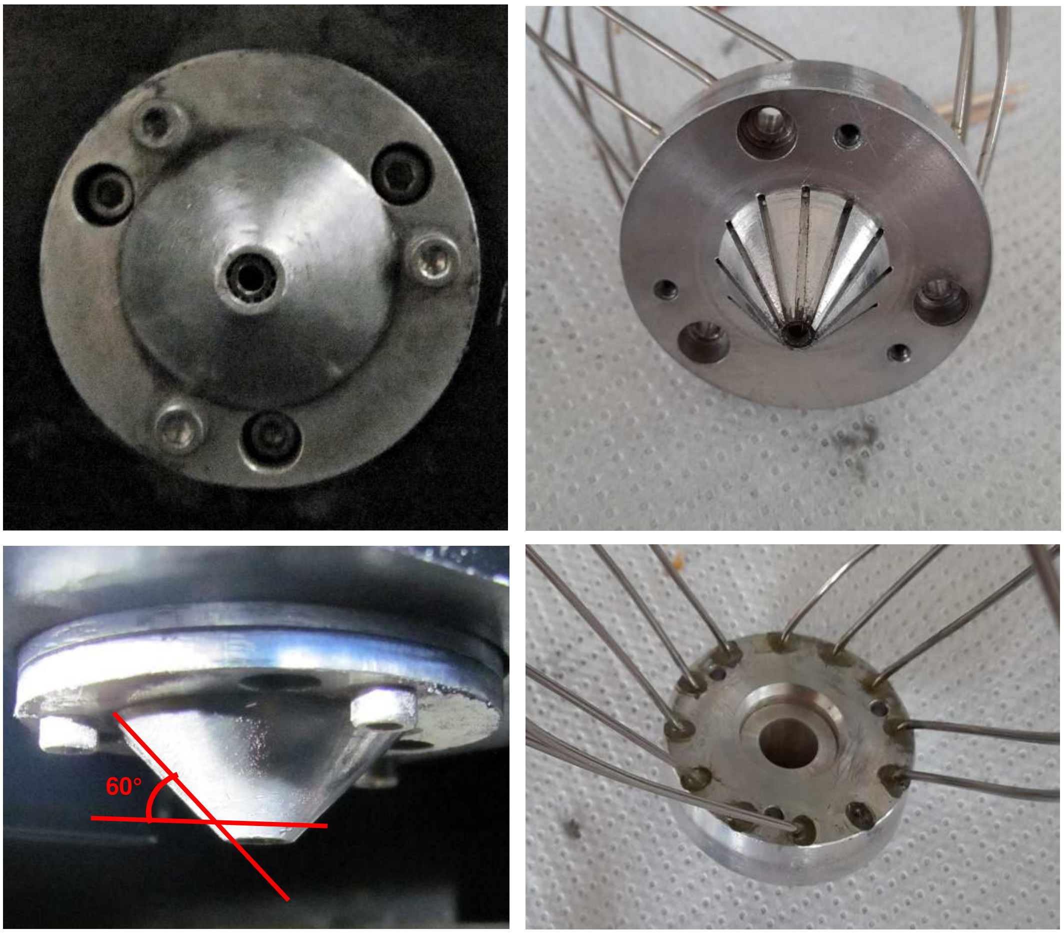

Figure 2.7 Manudirect ® MSL50 deposition nozzle.

Figure 2.8 Powder cone coming out from the deposition nozzle.

The nominal exit angle imposed by the nozzle geometry is equal to 60° (see Fig. 2.7). In truth, the real exit angle of the powder particles depends on the geometry

of the nozzle, the Argon drag force, the shape and size of the powder particles, the quantity of Argon carrier gas and the density of the metal material employed. How the powder distribution and the powder cone geometry vary with these parameters will be discussed in detail in the following Chapter §3.
The powder particles come out from eleven pipes placed along the smallest outlet circumference of the nozzle whereas the laser beam comes out from the centre (see Fig. 2.7). To locally protect the melt pool from oxidation and smoke formation, a shielding gas comes out to the centre of the nozzle in conjunction with the laser beam. This nozzle design allows an omnidirectional powder distribution during the process, avoiding preferential direction on the powder deposition as in case of lateral injection nozzle (see Fig. 2.9).

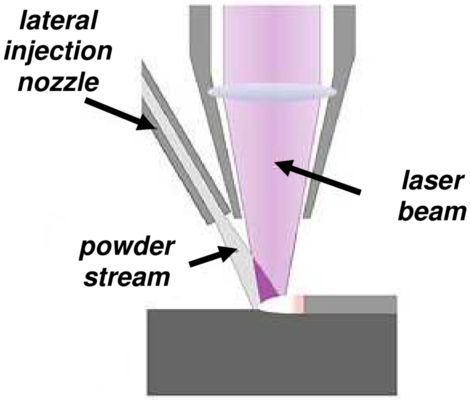

Figure 2.9 DLMD process with lateral injection nozzle.

The nozzle solution installed in the Manudirect ® MSL50 allows thus a symmetric powder distribution with respect to the molten pool and a compact dimensions of the entire powder feeding system.

2.2. Material used in the experiments

The MSL50 system for micro DLMD requires metal powders with a specific grain size and a careful and accurate powder handling. The employment of an appropriate metal powder granulometry with a tight size distribution and a low presence of moisture and oxidation is crucial to get a good powder flow and particles' transportation through the feeding system.
To avoid particles' adhesions and powder clogging inside the feeding pipes, ensuring a stable and homogeneous powder flow along the feeding system, the MBN ® company has experimentally established that the optimum powder particle size should be ranging between 20 and 40 µm (see Appendix A). This is mainly for the following reasons:

- the accuracy of the micro DLMD process;
- the small laser spot size employed during the micro DLMD process;
- the cohesion force between the powder particles.

In DLMD, the third point of the previous bullet list is rather critical. In fact, a micro process is required to be capable to realize very precise features, fine superficial texturing and small parts with a very high accuracy impossible to reach with the usual macro processes. In terms of micro DLMD, these requirements turn in small melt pool and, consequently, in small grain size of the metal powder particles. Nevertheless, to improve the efficiency and the continuity in the layer deposition and formation, a DLMD process needs to employ a laser spot diameter bigger than the powder grain size involved. In other hands, for a micro deposition process employing a laser spot of 30 µm, the powder grain size has not to exceed 25 µm. On the other side, a too much reduction in the powder grain size, the adhesion forces between the metal particles increases (see Fig. 2.10) causing blockage, pipe obtrusions and clogging that could compromise a continuous and uniform feed of the metal powder. MBN ® experimentally demonstrated that for powder particles with a diameter smaller than 20 µm, the adhesion force between particles was too strong and powder agglomerates appeared affecting the efficiency of the powder deposition negatively.

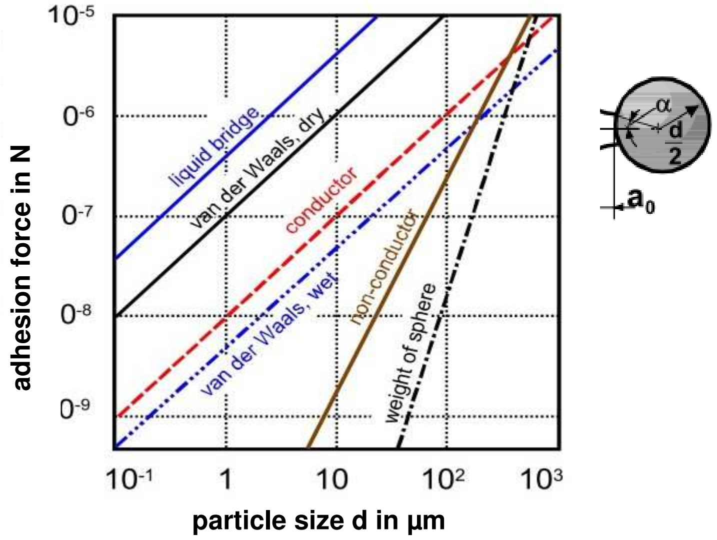

Figure 2.10 Adhesion force diagram (a_0 = 0.4 mm, α = 20° bridge angle, θ = 0° wetting angle, σlg = 72 mJ/m^2 surface tension of water, CH = 19 * 10^{-20} J Hamaker constant, U = 0.5 V contact potential) [43].

In addition to the powder grain size, the percentage of moisture, oxidation and electrostatic force also play an important role on the powder agglomeration (see Fig. 2.10). A good conservation and appropriate handling of the metal powders (for example in inert and controlled environment) is very important to preserve the safety of the worker and a good purity and flowability of the powder.
In this Ph.D. research project the metal powders employed for the analysis of the micro DLMD process were of three batches:

- AISI 316L Stainless steel powder;
- Ti-6Al-4V alloy powder;
- Ni50Ti50 alloy powder.

In the following subchapters the mechanical characteristics, the chemical composition and the particles size of the three blends of metal powders will be discussed in detail.

2.2.1. AISI 316L Stainless Steel

The AISI 316L Stainless Steel metal powder employed during the Ph.D. project has a grain size between 20 µm and 25 µm (see Table 2.2) and it is supplied by MBN ® company.

grain size (µm)	20/25
bulk density (g/$\mathrm{cm^3}$)	3,003
tap density (g/$\mathrm{cm^3}$)	3,658
skeletal density (g/$\mathrm{cm^3}$)	7,7

Table 2.2 AISI 316L Stainless Steel powder properties.

The metal powder is produced by High Energy Ball Milling (HEBM). This process is flexible and allows to synthesize a wide range of materials by driving solid state reactions activated by the mechanical energy delivered during ball impacts.
In particular, this technology allows the production of powders by combination of:

- Crystal size refinement;
- Milling of raw materials in appropriate atmosphere (Argon)
- Mechanical alloying
- Reaction milling

In this case, the AISI 316L Stainless Steel alloy was produced milling AISI 316L raw material blocks in a controlled Argon atmosphere. The powder produced by HEBM was then rounded by a Jet-mill machine in order to smooth the sharp edges and clean the powder particle surface from agglomerations. The final “potato” shape of the powder particles ensures a constant and continuous flow during the DLMD process.
In the Table 2.2 the chemical composition of the metal powder is shown.

C	Cr	Ni	Mn	Si	Mo	P
0.02	18.12	9.58	0.60	0.36	0.29	0.002

Table 2.3 AISI 316L Stainless Steel chemical composition (%).

2.2.2. Ti-6Al-4V alloy

The Ti–6Al–4V metal powder employed during the Ph.D. project has a grain size between 20 µm and 45 µm (see Table 2.3) and it is supplied by TLS Technik ® company.

grain size (µm)	20/45
tap density (g/$\mathrm{cm^3}$)	2.300
skeletal density (g/$\mathrm{cm^3}$)	4.43

Table 2.4 Ti–6Al–4V powder properties.

Contrary to AISI 316L Stainless Steel powder introduced in Chapter §2.2.1, in this case the Ti–6Al–4V metal particles are produced by gas atomization employing an inert gas jet (Argon). In this process, a molten metal alloy is atomized into fine metal droplets which cool down during their fall in the atomizing tower thanks to an Argon jet.

The metal powders obtained by gas atomization have a perfectly spherical shape combined with a high cleanliness level. In particular, the spherical shape allows a very good powder flowability during the process and a continuous powder flow through the MSL50 feeding system.

In the Table 2.4 the chemical composition of the metal powder is shown.

Al	V	C	Fe	O	N	H	Ti
6.53	4.18	0.01	0.14	0.15	0.01	0.002	bal

Table 2.5 Ti-6Al-4V chemical composition (%).

2.2.3. Ni50Ti50 alloy

The Ni50Ti50 metal powder employed during the Ph.D. project was a Nickel-Titanium alloy with a Ni:Ti ratio of 50:50 (at.pct) and a grain size between 30 µm and 40 µm (see Table 2.6).

powder	Nickel	Titanium
particle size [µm]	10-100	200-500
purity [%]	99.99	99.95

Table 2.6 Characteristics of the initial Ni and Ti powders.

The Ni and Ti powder mixtures with a composition of Ni50Ti50 (in terms of atomic percentages) were milled as previously explained in Chapter §2.2.1 by MBN ® company (see Fig. 2.11).

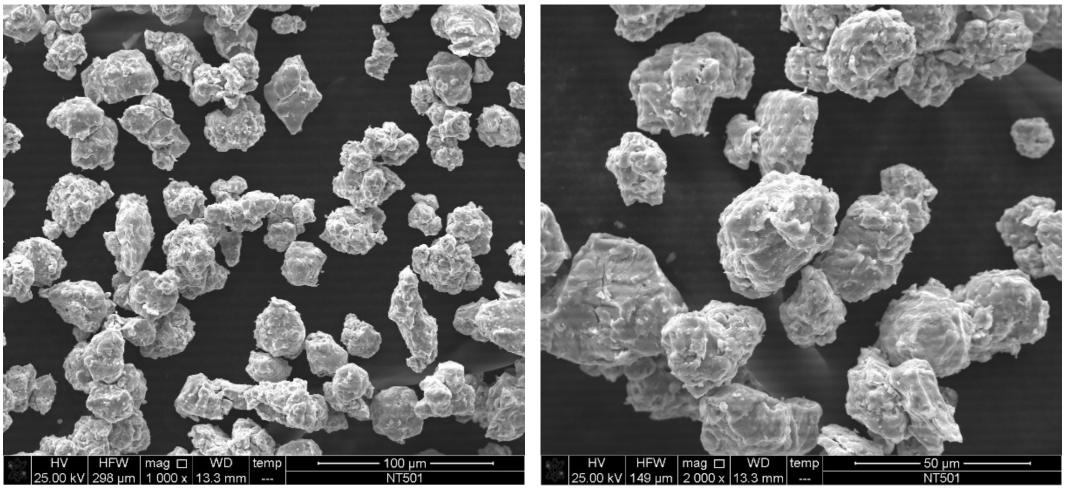

Figure 2.11 Morphology of Ni50Ti50 alloy powder particles after 8h milling time.

X-ray diffraction analysis depicted that, a semi amorphous structure with chemical composition near the austenitic NiTi forms after 8 hours of milling time.

2.3. The equipment characterization

The quality of the experimental artefacts realized in this Ph.D. research project was analysed in terms of dimensional and geometrical accuracy, surface morphology, surface roughness, microstructure and structural integrity in terms of internal porosity distribution.

To analyse how the micro DLMD process parameters affect the final quality of the 3D metal parts, three measurement instruments were employed:

- FEI Quanta 400 ® Scanning Electron Microscope (SEM);
- Sensofar Plus Neox 3D ® Optical Profilometer;
- Nikon Metrology X-Tek MCT225 ® metrological X-ray Computed Tomography system.

In the following Sub-chapters, each instrument will be introduced and discussed in detail.

2.3.1. Scanning Electron Microscope (SEM)

A Scanning Electron Microscope (SEM) is a powerful microscope capable to reach very high magnitude. SEM works employing a focused beam of high-energy electrons to generate a variety of signals at the surface of solid specimens. The signals that derive from electron-sample interactions reveal information about the sample including external morphology (texture), chemical composition, crystalline structure and orientation of materials making up the sample.

It finds many applications in analysis such as:

- generate high-resolution images of shapes of objects
- show spatial variations in chemical compositions
- acquiring elemental maps or spot chemical analyses
- discrimination of phases based on mean atomic number
- compositional maps based on differences in trace element
- identify phases based on qualitative chemical analysis and/or crystalline structure
- Precise measurement of very small features and objects down to 50 nm in size
- examine microfiber and crystallographic orientation in many materials

The SEM instrument employed during this Ph.D. research activity was the FEI Quanta 450 ® located at Te.Si. lab of the University of Padua (see Fig. 2.12).

Figure 2.12 FEI Quanta 450 ® Scanning Electron Microscope (SEM).

This microscope is integrated with a several detectors that increase the performance and the functionalities of the measurements:

- backscattered electrons detector (BSE)
- diffracted backscattered electrons detector (EBSD)
- Energy Dispersive X-ray Spectrometry detector (EDS)
- Heating chamber up to 1500° C for analyses at high temperature

In this work, the SEM instrument was employed mainly to characterized the morphology, microstructure and external surface condition of the realized micro-artefacts.

2.3.2. Optical profilometer

An optical profilometer is a no-contact interferometry measurement instrument employed to detect height variations on surfaces with great precision using the wavelength of light as the ruler. Optical interference profiling is a well-established method of obtaining accurate surface measurements.

The optical profiling uses the wave properties of light to compare the optical path difference between a test surface and a reference surface. Inside an optical interference profiler, a light beam is split, reflecting half the beam from a test material which is passes through the focal plane of a microscope objective and the other half of split beam is reflected from the reference mirror.

This measuring instrument is mainly employed to:

- roughness measurements;
- 2D and 3D profile detection;
- superficial texture detection.

The optical profilometer employed during this Ph.D. research activity was the Sensofar Plus Neox 3D ® located at Te.Si. lab of the University of Padua (see Fig. 2.13).

Figure 2.13 Sensofar Plu Neox 3D ® optical profilometer.

In the experimental analysis, it was mainly employed to accurately detect the final dimension, geometry and surface roughness and texture of the realized metal parts.

2.3.3. Computed Tomography system (CT)

X-ray Computed Tomography (CT) is a no-contact and non-destructive technique for visualizing interior features within solid objects, and for obtaining digital information on their 3D geometries and properties. Tomography imaging consists of directing X-ray at an object from multiple orientations and measuring the decrease in intensity along a series of linear paths. The physical principle is characterized by Beer’s Law, which describes intensity reduction as a function of X-ray energy, path length, and material linear attenuation coefficient. A specialized algorithm is then used to reconstruct the distribution of X-ray attenuation in the volume being imaged.

The elements of X-ray tomography are an X-ray source, a series of detectors that measure X-ray intensity attenuation along multiple beam paths, and a rotational geometry with respect to the object being imaged.

The CT analysis is mainly applied to:

- measure dimensions without sectioning samples (3D size, geometrical shapes, spatial distribution and orientation of crystals, etc.);
- non-destructive volumetric analysis (internal voids, porosity, micro-porosity);
- 3D measurements of fracture extent and internal defects;

- inspection and measurement of morphology and surface roughness;
- verify complex internal structures;
- isolate and inspect included components;
- strip external surfaces from view with ease.

Up to now new CT applications are being continually discovered.
The CT system employed during this Ph.D. research activity was the Nikon Metrology X-Tek MCT225 ® metrological X-ray Computed Tomography system located at Te.Si. lab of the University of Padua (see Fig. 2.14).

Figure 2.14 Nikon Metrology X-Tek MCT225 ® metrological X-ray Computed Tomography system.

In the experimental analysis, it was mainly employed to accurately detect the presence of internal defects in the realized artefacts (such as micro-porosity, voids, etc.) and evaluate the final dimension and geometrical shape of the realized metal parts.

2.3. Conclusions

In this Chapter, the experimental apparatus employed during this research work was explained and discussed.
The Manudirect ® MSL50 system for micro DLMD was introduced and its architecture was explained in details. The employment of a conical nozzle allows coaxial exit between powder cloud and the laser beam during the process. The advantage of this concept solution is double since it ensures a symmetric distribution of powder particles with respect to the molten pool and reduces the entire dimensions of the powder feeding system.

MBN ® company experimentally demonstrated how the metal powder grain size has to be between 20 and 40 µm to ensure a constant and homogeneous powder flow during direct deposition process, avoiding powder agglomerations or powder clogging inside the feeding pipes.

In the end, the measurement instruments employed to characterize the artefacts realized in the experimental tests were introduced and discussed.

Chapter 3

Powder cone and working distance characterizations

In this chapter, the influence of the powder feeding parameters on the distribution of the powder particle mass concentration during the deposition process is investigated and analyzed.

The flow rate of the Argon carrier gas and the powder feed rate coming out from the deposition nozzle are the two process parameters taken into account in this experimental investigation. A Computational Fluid Dynamics (CFD) analysis followed by an experimental validation is implemented to simulate the trajectories and spatial position of the powder particles in steady condition. The numerical results fit well the preliminary experimental results in terms of powder cloud shape, but further analyses have to be carried out to improve and optimize the CFD model in terms of particle density prediction. The Argon flow rate results to be the most important parameter affecting the powder distribution and the particle mass concentration at the nozzle exit.

Finally, an analysis of the influence of the laser defocusing on the final quality of the artefact is carried out, demonstrating a strong influence of this process parameter on the final height of Ni50Ti50 thin walls depending on the working-plane position of the substrate.

3.1. Introduction

In a DLMD process, a deep understanding and control on the metal powder deposition is fundamental to ensure a constant supply of fresh raw material on the sintering interaction zone (commonly known as molten pool or melt pool). A high particle mass concentration in proximity of the molten pool ensures a big number of metal particles participating at the formation of the layer, improving the efficiency in the powder deposition and reducing the material waste and the production time [44, 45]. Moreover, the accurate knowledge of the fluid dynamic behaviour of the powder particle can allow to identify the best position where locating the substrate, improving the quality both in layer formation and in part manufacture [46, 47]. In this context, the deposition nozzle design and the powder feeding parameters play an important role in the overall efficiency of the DLMD process in terms of metal powder waste and final quality of the realized component [48-50]. An enhanced control on the powder deposition derived by a deep understanding of the influence of the powder feeding parameters on the powder mass concentration at the nozzle outlet is the first step to improve the final quality of the part and the performance of the DLMD system.

In this first and preliminary analysis, the influence of the carrier mass flow and powder feed rate on the powder mass concentration during micro DLMD is investigated and the main results in terms of powder cone characterization and zone of maximum powder density are presented.

3.2. Micro DLMD process parameters affecting the powder deposition

In the market the deposition nozzle solutions for DLMD are mainly three and they are represented in the Figure 3.1.

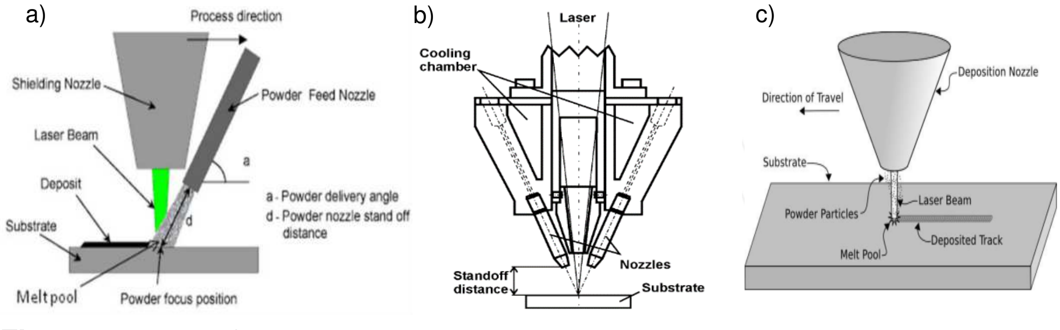

Figure 3.1 a) lateral deposition nozzle solution [51]; b) first coaxial nozzle solution [50]; c) second coaxial nozzle solution [52].

The solution a) is the oldest one and it is mainly employed in macro cladding process. This nozzle configuration is of simply design and of easy integration with the optical system. Nevertheless, the generation of a powder cone not coaxial to the laser beam causes a powder deposition along a preferential direction, generating an instable track formation. Even if this solution is extensively employed in traditional welding and cladding process, it is not suitable for a micro DLMD process where the accuracy in the track formation is fundamental to get an acceptable final quality of the realized component.

On the contrary, the solution b) and c) are the most common in DLMD systems. Both ensure an omnidirectional and symmetrical powder deposition in the respect of the molten pool and a good control on the track formation. Nevertheless, the solution b) usually requires the installation of 2 or 4 external deposition nozzles which increase the size of the deposition head. This is a bulky solution and it is not suitable for a micro system where the sintering chamber is small and the available spaces are tight. On the contrary, the solution c) is a nozzle configuration that ensures an omnidirectional powder distribution combined with a compact design for the deposition head, resulting particularly suitable to be installed in a micro DLMD system.

The concept of the deposition nozzle installed in the Manudirect ® MSL50 is a solution belongs to the family b) and its structure was explained in detail in the previous Chapter §2.1.2. In this case, the main variables affecting the behaviour of powder-gas flow coming out from the nozzle are (see Appendix A):

- power and accuracy of the feeding screw that defines the powder feed rate during the DLMD process (mg/s);
- length, internal roughness, curvature, and cross sectional shape of the feeding pipes;
- geometrical shape of the deposition nozzle;
- carrier gas flow rate and carrier gas properties;
- rotation per minute of the brush responsible of the powder gas fine dispersion;
- powder material properties;
- geometrical shape and size of the powder particles.

Since the deposition nozzle geometry, the accuracy of the feeding screw, the geometrical characteristics of the feeding pipes, and the powder feeder architecture were defined by the powder feeding system installed in the MSL50 machine, the relevant process parameters which are free to vary during the micro DLMD process are:

- the flow rate of the carrier gas that in our specific case is Argon;
- the velocity of the feeding screw that determine the powder feed rate during the process;
- the metal powder.

These three parameters strongly affect both the powder particle dispersion in the carrier gas and the fluid dynamics behaviour of the powder particles during the deposition process.

3.2.1. Analyzed micro DLMD process parameters in the CFD analysis

In this experimental investigation, the process parameters taken into account were the Argon flow rate and the powder feed rate. Concerning the metal powder employed for this analysis, it was an AISI 316L Stainless Steel alloy supplied by MBN company (see Chapter §2.2.1).

The evaluation ranges for Argon and powder flow rate are listed in Table 3.1.

process parameter	level 1	level 2	level 3
Argon flow rate [l/min]	0.7	1.7	2.7
AISI 316L powder mass flow rate [mg/s]	0.574	1.148	1.723

Table 3.1 Analysed process parameters.

The choice concerning the process parameter intervals was done taking into account the typical process window employed in a micro DLMD process (see Table 1.2).

The numerical analysis and the experimental validation were designed according to a full factorial Design of Experiments (DOE) scheme with two factors and three levels each. A total of nine process combinations were implemented.

3.3. CFD simulation of the powder cone

To evaluate the powder cone stream behaviour coming out from the deposition nozzle of the MSL50 system, the *ANSYS ® FLUENT* software was employed. *FLUENT* is a reliable and accurate Computational Fluid Dynamics (CFD) tool extensively used in engineering for fluid flow analysis in a virtual environment. In this particular case, the CFD problem was solved using the Dispersed Turbulence Model (DTM), since this specific physical problem could be simplified as a secondary discrete phase (powder particles) dispersed in a primary continuous one (Argon carrier gas). The application of this model was possible because in a DLMD process the metal powder particles occupy a very low fraction of the total volume represented by the Argon-powder mixture moving inside the feeding pipes, and the collision between metal particles can be neglected [44, 49].

In the following Subchapters, the theoretical equations and the assumptions employed to describe the primary and secondary phase are introduced and discussed

3.3.1. Governing equations of the carrier gas phase

The governing equations for the Argon carrier gas were described in an Eulerian reference frame. The primary continuous phase was modelled on the Navier-Stokes equations, where the averaging time-dependent Reynolds method in combination with the standard k-ε turbulent model was used to modify the governing equations for the laminar flow.

To describe a turbulent flow, the time-averaging governing equations were:

Conservation of mass:

$$\frac{\partial}{\partial x_i}(\rho u_i) = 0$$

Equation 3.1

where ρ was the Argon density (1.623 kg/m^3), u_i the gas velocity and x_i the gas position. Conservation of momentum:

$$\frac{\partial}{\partial x_j}(\rho u_i u_j) = -\frac{\partial p}{\partial x_i} + \frac{\partial \tau_{ij}}{\partial x_j} + \rho g_i$$

Equation 3.2

Where p was the pressure, g was the gravitational acceleration and τ_{ij} was the viscous stress tensor defined by:

$$\tau_{ij} = \left[(\mu + \mu_t)\left(\frac{\partial u_i}{\partial x_j} + \frac{\partial u_j}{\partial x_i}\right)\right] - \frac{2}{3}\mu_t \frac{\partial u_i}{\partial x_i}\delta_{ij}$$

Equation 3.3

where μ was the molecular viscosity (2.125×10^{-5} kg/(m s)) and δ_{ij} was the Kronecker delta (δ_{ij} is equal to 1 for i=j, otherwise δ_{ij} is equal to 0). μ_t was the turbulent viscosity defined by:

$$\mu_t = \rho C_\mu \frac{k^2}{\varepsilon}$$

Equation 3.4

Where C_μ was a constant and usually considered equal to 0.09, k the kinetic energy of turbulence, and ε the dissipation of kinetic energy of turbulence, which was defined in the k-ε turbulence model.

Moreover, two more extra equations were required to solve the mass and momentum conservation equations in a time average manner. The most commonly used model to handle this situation was the standard k-ε model in which the k and ε represented the turbulent kinetic energy and dissipation of kinetic energy respectively. The conservation of kinetic energy of turbulence was given by:

$$\frac{\partial}{\partial x_i}(\rho k u_i) = \frac{\partial}{\partial x_j}\left[\left(\mu + \frac{\mu_t}{\sigma_k}\right)\frac{\partial k}{\partial x_j}\right] + G_k + G_b - \rho\varepsilon$$

Equation 3.5

whereas the conservation of dissipation of kinetic energy of turbulence was defined as:

$$\frac{\partial}{\partial x_i}(\rho \varepsilon u_i) = \frac{\partial}{\partial x_j}\left[\left(\mu + \frac{\mu_t}{\sigma_\varepsilon}\right)\frac{\partial \varepsilon}{\partial x_j}\right] + C_{1\varepsilon}\frac{\varepsilon}{k}(G_k + G_b) - C_{2\varepsilon}\rho\frac{\varepsilon^2}{k}$$

Equation 3.6

$$G_k = \mu_t\left(\frac{\partial u_j}{\partial x_i} + \frac{\partial u_i}{\partial x_j}\right)\frac{\partial u_i}{\partial x_j}$$

Equation 3.7

$$G_b = -g_i \frac{\mu_t}{\rho Pr_t}\frac{\partial \rho}{\partial x_i}$$

Equation 3.8

where $C_{1\varepsilon}$=1.44, $C_{2\varepsilon}$=1.92, k=1.0 and ε=1.3 were empirical constants, Pr_t was the turbulent Prandtl number, G_k was the generation of turbulence kinetic energy due to the mean velocity gradients, and G_b was the generator of turbulence kinetic energy due to buoyancy.

The equations provided above governed the continuous phase constituted by the Argon carrier gas. To complete the theoretical basis of this CFD analysis, the equations governing the secondary phase were discussed in the following Subchapter.

3.3.2. Modeling of powder particles

The behaviour of the discrete phase (powder particles) was computed by integrating the force balance for each particle in the Lagrangian reference frame. Along the x direction, the balance of the forces was given by:

$$\frac{du_p}{dt} = F_D(u - u_p) - g_x\left(\frac{\rho_p - \rho}{\rho_p}\right) + F_x$$

Equation 3.9

where u_p was the particle velocity, u was the fluid phase velocity, ρ was the fluid density, ρ_p was the density of the particles, g_x was the x component of the gravitational acceleration, and F_x was an additional acceleration (force/unit particle mass) term. F_D coefficient was the drag force per powder mass unit and it could be calculated as:

$$F_D = \frac{18\mu}{\rho_p d_p^2}\frac{C_D Re}{24}$$

Equation 3.10

In the equation defining F_D, μ was the molecular viscosity of the fluid, d_p was the particle diameter, Re was the relative Reynolds number, and C_D was the drag coefficient defined as:

$$Re = \frac{\rho d_p |u_p - u|}{\mu}$$

Equation 3.11

$$C_D = a_1 + \frac{a_2}{Re} + \frac{a_3}{Re^2}$$

Equation 3.12

Where a_1, a_2, and a_3 were empirical constants. The second term on the right of Eq. (3.9) consisted of the gravity and buoyancy forces per unit particle mass.

A discrete random walk model was used to consider turbulence fluctuations of the flow. The turbulence was modelled by eddies defined by a Gaussian distributed random velocity fluctuation u', v', w' in the equation Eq. (3.13) and a time scale T_L in Eq. (3.14). ς was a normally distributed random number used for the three directions because of the hypothesis of isotropic turbulence, and C_L was the time scale constant.

$$u' = v' = w' = \varsigma\sqrt{\frac{2k}{3}}$$

Equation 3.13

$$T_L = 2C_L\frac{k}{\varepsilon}$$

Equation 3.14

The particle vortex crossing time (t_{cross}) was defined as:

$$t_{cross} = -\tau\ln\left[1-\left(\frac{L_e}{\tau\left|u-u_p\right|}\right)\right]$$

Equation 3.15

Where τ was the particle relaxation time, L_e was the vortex length scale, and $|u - u_p|$ was the magnitude of the relative velocity. The particle was assumed to interact with the fluid phase vortex over the smaller of the vortex life and crossing times. When this time was reached, a new value of instantaneous velocity was obtained by applying a new value of ς in Eq. (3.13).
The main parameter of this discrete random walk model was the time scale constant C_L. Its recommended value was 0.15 for the k-ε turbulence model by making a link between the eddy lifetime, T_L and the integral time scale, T, defined as:

$$T = \int_0^\infty \frac{u'_p(t)u'_p(t+s)}{\overline{u'^2_p}}ds$$

Equation 3.16

The equations provided above governed the discrete phase constituted by powder particles. Before starting with the CFD simulation and numerical result analysis the boundary conditions and model assumption concerning the deposition process had to be introduced and explained.

3.3.3. Boundary conditions and assumptions

The use of a numerical model involved some boundary conditions and assumptions in order to reduce the number of input parameters and calculation time. These assumptions took into account the research works present in literature concerning the CFD modelling for a coaxial deposition nozzle.
The assumptions taken into account to solve the CFD problem were:

- a constant velocity and a perpendicular flow of the carrier gas to the nozzle inlet;
- a steady-state problem, in this way the powder flux distribution was not time dependent;
- the inlets for the Argon shielding gas and the Argon-powder mixture were considered as a laminar flow (see Appendix A);

- the pressure at the nozzle outlet was equal to the atmospheric pressure;
- the discrete phase model was based on a force balance for each particle and only drag, inertia, and gravity force were considered;
- the collisions between particles were ignored due to the very low concentration of the powder particles in the carrier gas (less than 10%);
- the influence of the particles on the continuous phase was ignored due to the low mass and concentration of the particles;
- laser radiation and the interaction between laser and powder particles were not considered.

3.3.4. Model building and simulation data

The first step in the CFD modelling analysis was to define and implement the simulation domain through a CAD software (see Fig. 3.2 and 3.3).

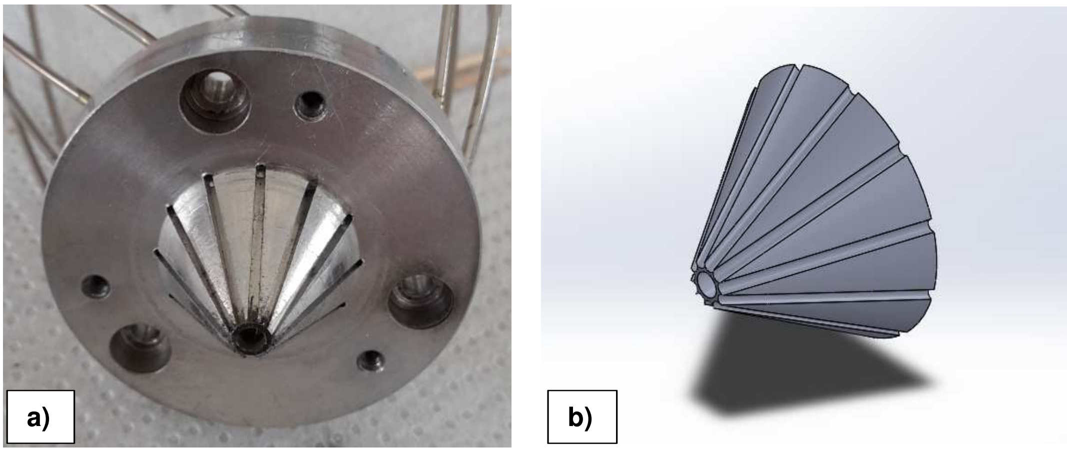

Figure 3.2 a) Manudirect ® MSL50 nozzle; b) 3D model of the deposition nozzle.

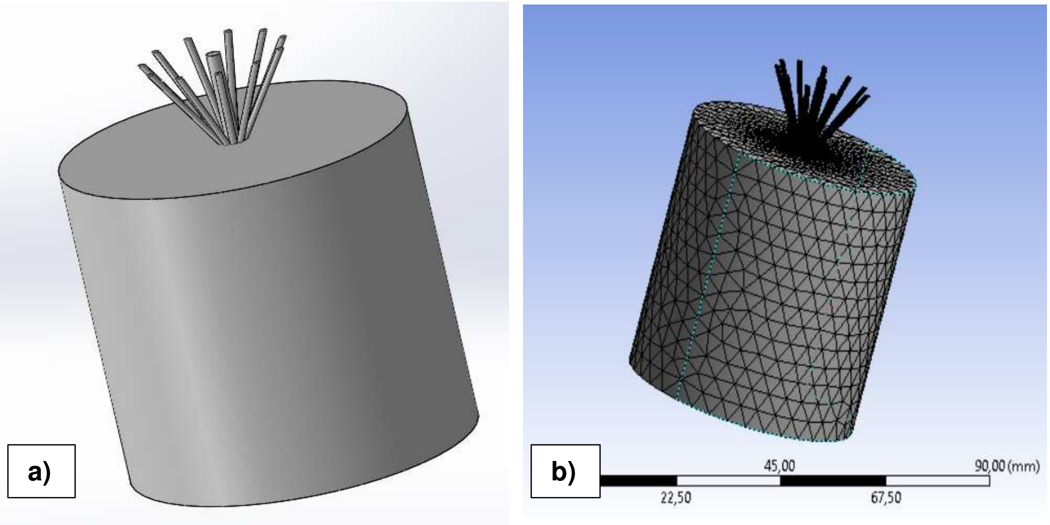

Figure 3.3 a) simulation domain; b) mesh for CFD analysis

The accurate replication of the internal nozzle geometry is of extreme importance to get a reliable fluid dynamics analysis of the Argon-powder mixture. From the 3D representation of the simulation domain a mesh was built (see Table 3.2).

mesh min size	4,236 e-005 m
max face size	4,236 e-003 m
mesh max size	8,471 e-003 m

Table 3.2 Mesh characteristics.

The data employed to estimate Argon-powder mixture behaviour were:

Argon inlet velocity [m/s]	variable
Argon density [kg/m^3]	1.623
AISI 316L powder mass flow	variable
AISI 316L density [g/cm^3]	7.7
powder particle diameter [mm]	0.0225
powder particle inlet velocity [m/s]	variable according to Argon inlet velocity
shielding gas velocity [m/s]	10

Table 3.3 Argon characteristics.

3.3.5. CFD results

The numerical results of the CFD simulation demonstrated a strong influence of the Argon carrier gas and powder feed rate on the particle mass concentration during the deposition process. Figure 3.4 shows how the Argon flow rate affected the powder distribution at the nozzle exit and the overall shape of the powder cone. Increasing the Argon flow rate, the powder cone became wider and moved close to the nozzle outlet. An increment from 0.7 l/m to 2.7 l/min, the powder cloud shifted up from a distance of 2.3 mm to 0.9 mm in average (see Table 3.4).

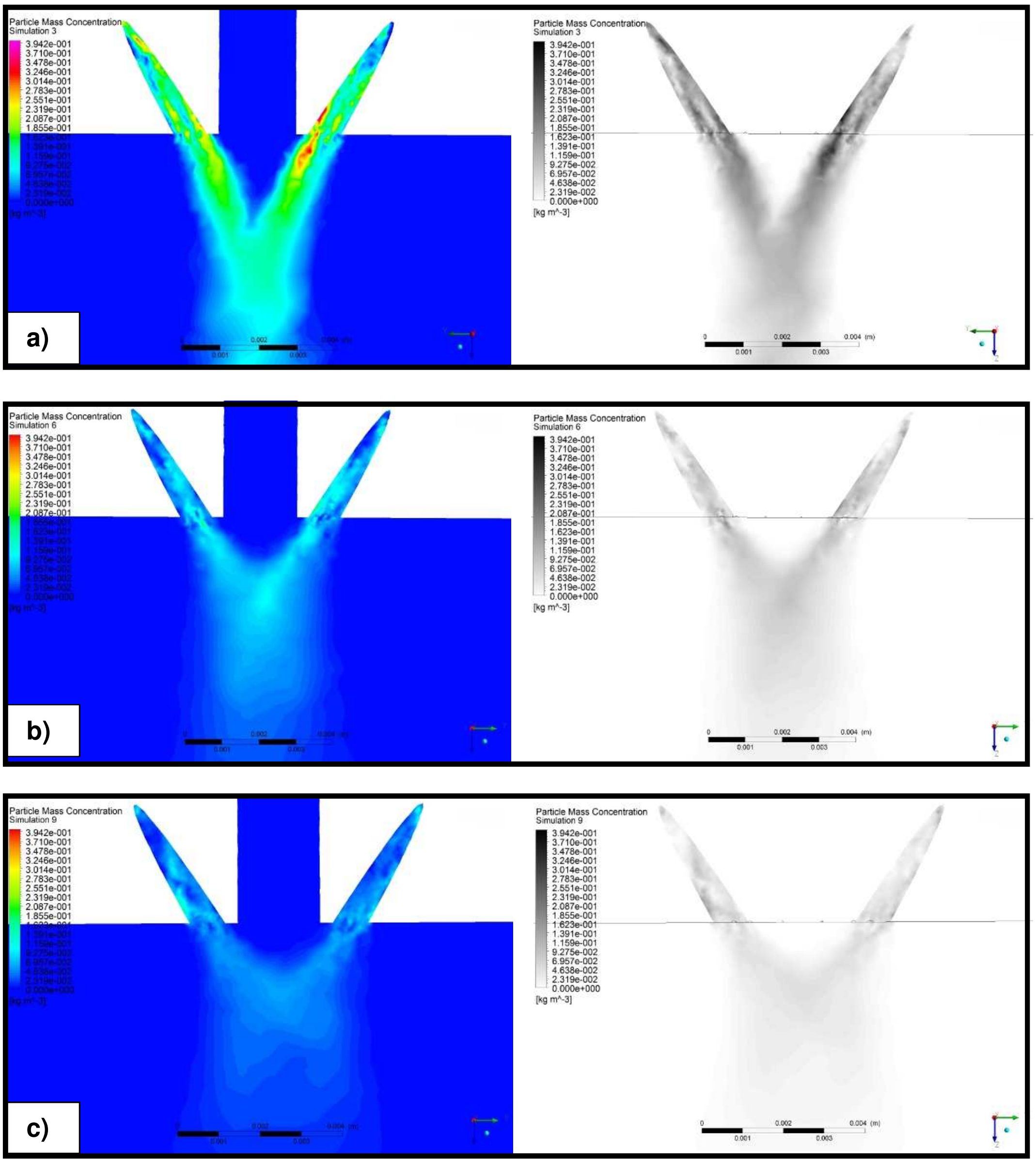

Figure 3.4 Powder cloud coming out from the nozzle outlet: a) Argon flow rate = 0.7 l/min, powder feed rate = 1.723 mg/s; b) Argon flow rate = 1.7 l/min, powder feed rate = 1.723 mg/s; c) Argon flow rate = 2.7 l/min, powder feed rate = 1.723 mg/s.

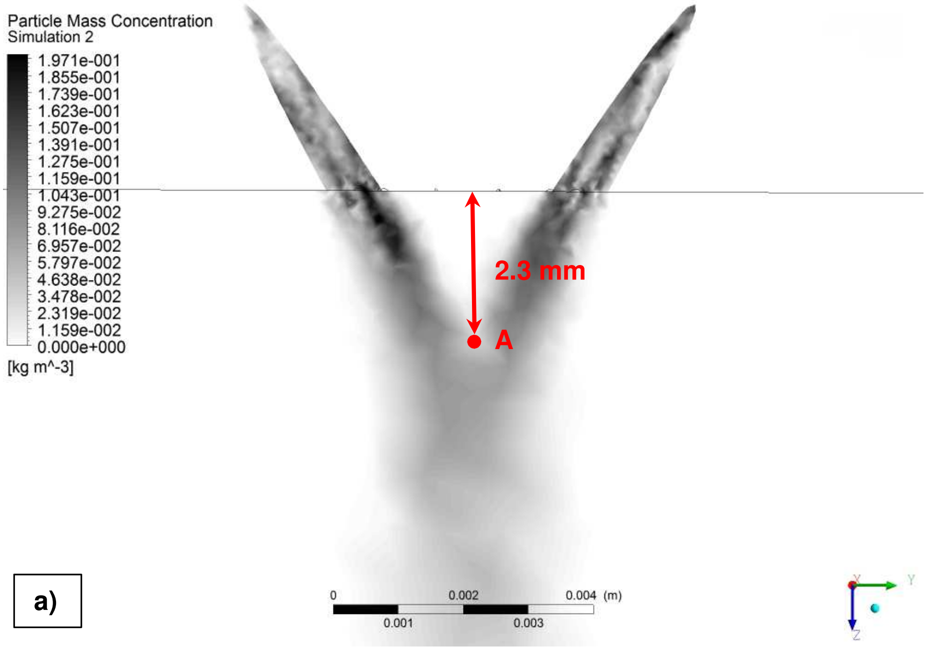

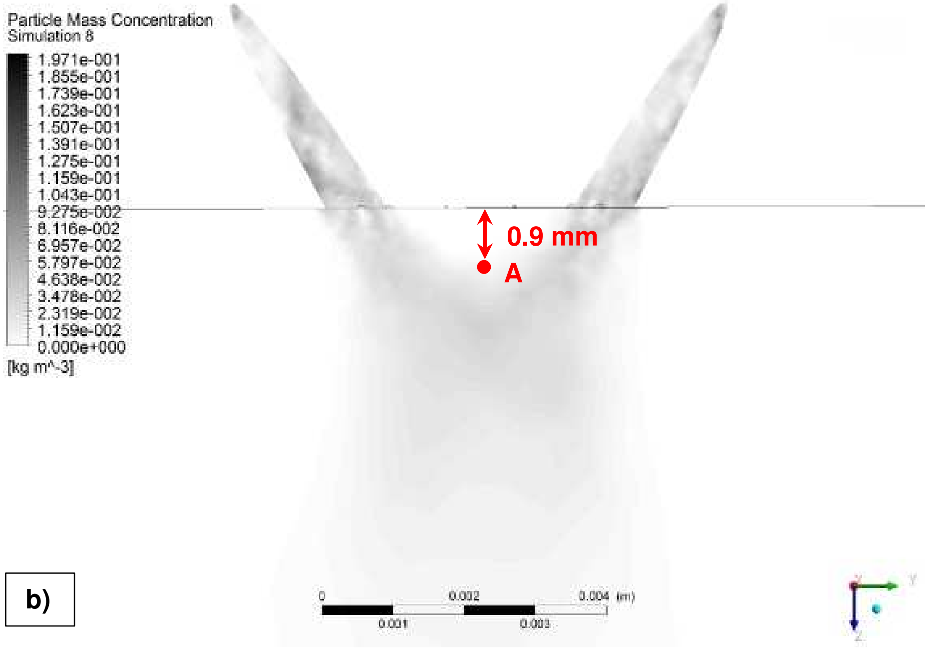

Figure 3.5 a) Argon flow rate = 0.7 l/min, powder feed rate = 1.148 mg/s; b) Argon flow rate = 2.7 l/min, powder feed rate = 1.148 mg/s.

Argon flow rate [l/min]	average distance of A [mm]	average width of the powder cloud [mm]	average elongation along z [mm]
0.7	2.3	1.9	1.9
1.7	1.1	2.1	1.6
2.7	0.9	2.8	1.1

Table 3.4 Influence of the Argon flow rate on the shape of the powder cloud.

As Figures 3.4 and 3.5 show, for low values of the carrier gas, the Argon-powder mixture coming out from the feeding pipes was clearly visible and the point of conjunction between the two fluxes was well defined on the top size of the powder cloud (see Fig. 3.5 a). On the contrary, increasing the flow rate, the two carrier gas streams became less visible and the top size of the powder cloud assumed a flat shape (see Fig. 3.5 b). This turned into a lower particle mass concentration and in a more homogeneous powder distribution along the cross sectional area of the powder cone. As we can see from the Figure 3.6, for an Argon flow rate of 0.7 l/min the particle mass concentration was higher in correspondence to the vertical axis of the powder cone, reaching a maximum values of 0.116 kg/m^3, whereas it decreased at 0.056 kg/m^3 for 2.7 l/min.

Under a process point of view, it meant that for low values of the carrier gas, the powder deposition increased in efficiency since more metal particles converged on the centre of the powder cloud where the molten pool was supposed to be during the micro DLMD process. The Argon flow rate showed also a strong influence on the position and extension of the intermediate zone of maximum powder concentration along the vertical axis of the powder cone (see Table 3.4). An increment of the carrier gas flow rate from 0.7 l/m to 2.7 l/min, shifted the intermediate zone up from a distance of 2.3 mm to 0.9 mm in average closer to the nozzle outlet (see Table 3.4 and Fig. 3.5). Moreover, at higher levels for Argon flow rate, the zone shrank along the z direction and spread along the x axis, reaching a minimum elongation along the vertical axis of 1.1 mm in average when 2.7 l/min were employed (see Table 3.4). Better results were obtained for an Argon flow rate of 0.7 l/min. In this case, the particle mass concentration increased up to 0.116 kg/m^3 for a powder feed rate of 1.723 mg/s and the intermediate zone of the powder cloud extended up to 1.9 mm along the z direction.

The vertical shifting of the powder cloud near the nozzle outlet and the consequent enlargement of the intermediate zone had mainly two main disadvantages for the micro DLMD process:

- a stronger heating of the head of nozzle outlet due to the laser irradiation and consequently a higher risk of powder particle adhesion in correspondence to the nozzle exit causing possible clogging of the feeding pipes;
- a lower number of powder particles falling inside the molten pool and participating to the formation of the deposited layer due to the enlargement of the powder cloud and the consequent reduction of the particle mass concentration.

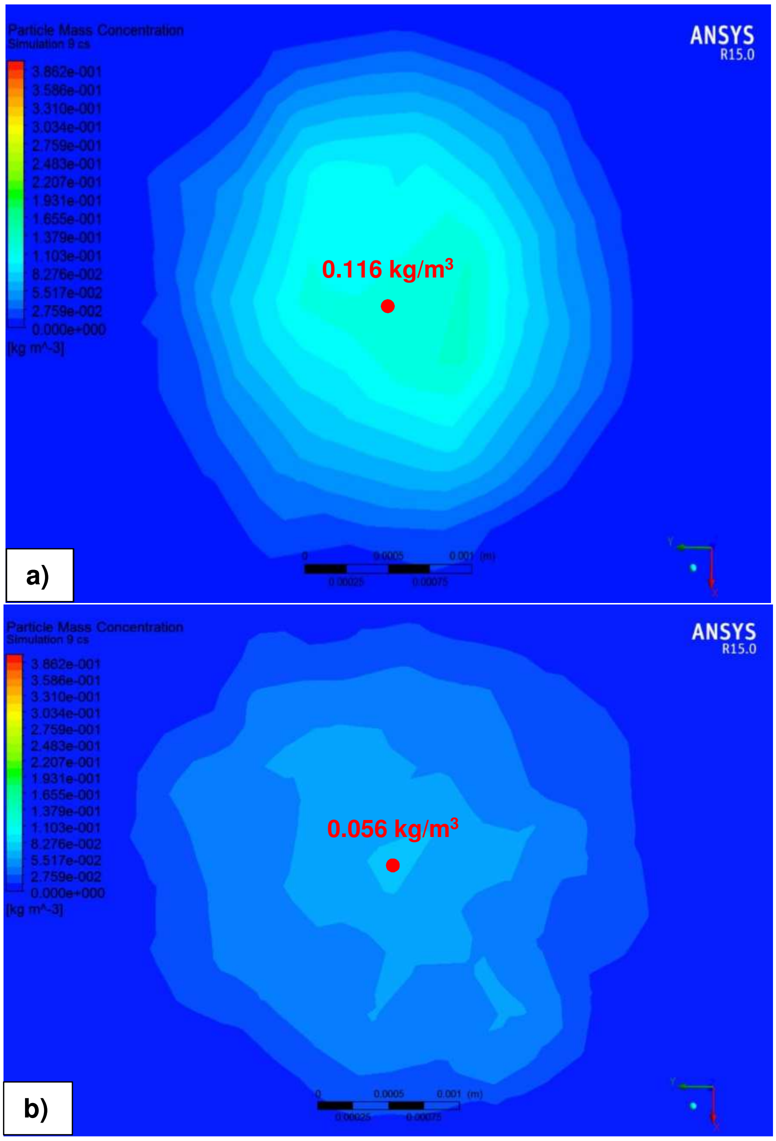

Figure 3.6 Cross section of the intermediate zone: a) Argon flow rate = 0.7 l/min, powder feed rate = 1.723 mg/s; b) Argon flow rate = 2.7 l/min, powder flow rate = 1.723 mg/s.

On the contrary, the employment of low values for the Argon flow rate showed more advantages for the micro DLMD process in terms of higher powder particles concentration and less risk of feeding pipe clogging.

Concerning the powder mass flow rate, for a constant carrier gas an increase from 0.574 to 1.723 mg/s caused an increment in the particles mass concentration as expected. For 0.7 l/min and 1.723 mg/s the zone of maximum powder concentration reached its higher density with 0.116 kg/m^3, determining an increment of +0.077 kg/m^3 compared to the case where 0.574 mg/s were employed. Table 3.5 summarizes the results in terms of particle mass concentration obtained for each combination of process parameters employed in the CFD simulation.

simulation	Argon flow rate [l/min]	powder feed rate [mg/s]	max particle mass concentration at the centre [kg/m^3]
1	0.7	0.574	0.039
2	0.7	1.148	0.08
3	0.7	1.723	0.116
4	1.7	0.574	0.032
5	1.7	1.148	0.063
6	1.7	1.723	0.095
7	2.7	0.574	0.019
8	2.7	1.148	0.037
9	2.7	1.723	0.056

Table 3.5 Particle mass concentration at the centre of the intermediate zone of the powder cloud

As it appears from the Table 3.5, at 2.7 l/min, passing from 0.574 to 1.723 mg/s, the increment of the particle mass concentration is lower compared to the case with 0.7 l/min: +0.077 kg/m^3 against +0.037 kg/m^3 respectively.

3.4. Experimental validation

The CFD validation was a simple experimental procedure designed to detect and evaluate the variation in the powder distribution along the vertical axis of the deposition powder cloud during the micro DLMD process.
Six different positions (working-plane distances) for the substrate were chosen. For each position, single-layer circular ribs were realized, according to the combinations of process parameters defined in the Chapter §3.2.1 (see Fig. 3.7). The six working-plane distances were defined inside an evaluation interval ranging between 2 and 7 mm from the nozzle outlet and assuming a step of 1 mm for each substrate position. The working-plane position was defined as the distance between the nozzle outlet and the surface of the substrate.
The particle mass concentration along the vertical axis of the deposition powder cloud was evaluated characterizing the amount of molten material forming the deposited micro feature. In fact, it was not wrong to presume a deposition track more significant and continuous when the substrate was located in a powder cloud zone with a high particle mass concentration, whereas a discontinuous track with a low presence of molten material along the laser path when the powder particle density on the substrate surface was lower.

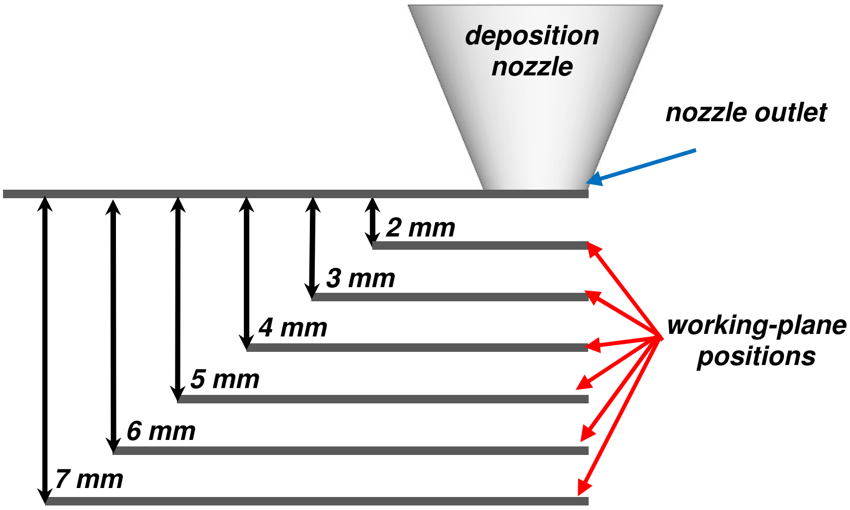

Figure 3.7 Configuration of the working-plane distances.

3.4.1. Material and methods

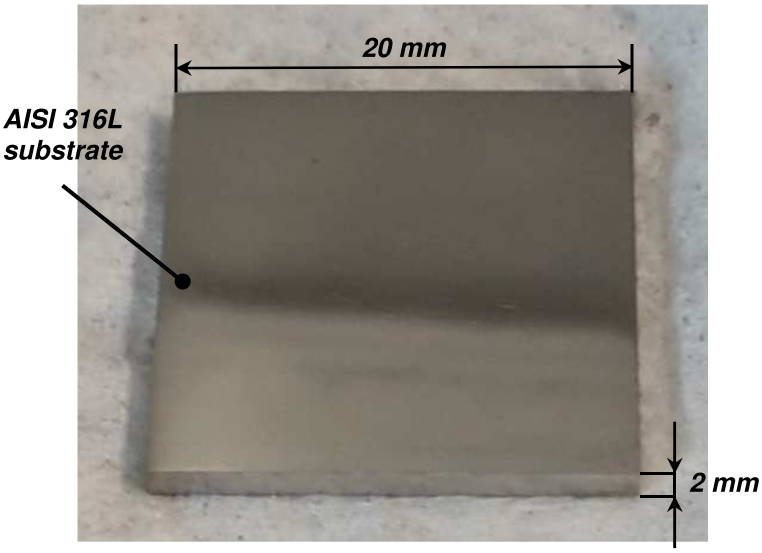

Figure 3.8 AISI 316L substrate.

The metal powder employed for the experimental validation was AISI 316L Stainless Steel alloy with a grain size ranging between 20 and 25 µm. In the chapter §2.2.1 the powder characteristics and composition were explained in detail (see Table 2.2). The micro features were realized on an AISI 316L substrate with a dimension of 20 x 20 mm and a thickness of 2 mm (see Fig. 3.8).

The DLMD process parameters are listed in the Table 3.6 and they were kept constant for all the experimental tests.

laser power	20 W
laser scan speed	150 mm/min
laser defocusing	0 mm
laser spot diameter	30 µm
substrate preheating temperature	0 °C

Table 3.6 Process parameters employed in the experimental validation.

Only the influence of the Argon flow rate and powder feed rate on the powder particle distribution were investigated (see Table 3.1).

3.4.2. Micro features considerations

The micro features as already mentioned in Chapter §3.4 were single-layer circular ribs with a diameter of 2 mm and a width nominally equal to the laser spot. The simple circular geometry was chosen because it allowed a constant velocity of the laser beam motion on the substrate without the generation of sudden acceleration or deceleration which could happen in the presence of sharp profiles (i.e. angles or rapid direction changes). The presence of these sudden accelerations or decelerations during the laser path could respectively cause a lack or an excess in the powder deposition, making more difficult the evaluation of the realized part.

3.4.3. Evaluation and characterization

After deposition, each machined substrate was cleaned in Acetone and deionized water solution using an ultrasonic cleaner to remove the non-sintered powder particles from the substrate surface. The single-layer circular ribs were evaluated through the FEI Quanta 450 ® Scanning Electron Microscope (SEM) suitable at the Te.Si. lab (see Chapter §2.3.1), employing the ETD detector with a 110x of magnitude.

The realized micro features were analysed in terms of track continuity and amount of molten material forming the micro-feature along the laser path.

3.4.4. Experimental results

The designed experimental tests showed a strong influence of the working-plane positions and of the powder feeding parameters on the amount of molten material along the laser path.

At constant Argon flow rate and powder feed rate, increasing the distance of the substrate from the nozzle outlet (from 2 to 7 mm) the continuity of the track formation and the amount of molten material around the deposited track increased. Nevertheless, moving away from the deposition nozzle, the continuity of the deposited track increased up to a maximum and then decreased, whereas the amount of molten powder close to the deposited track increased (see Fig. 3.9).

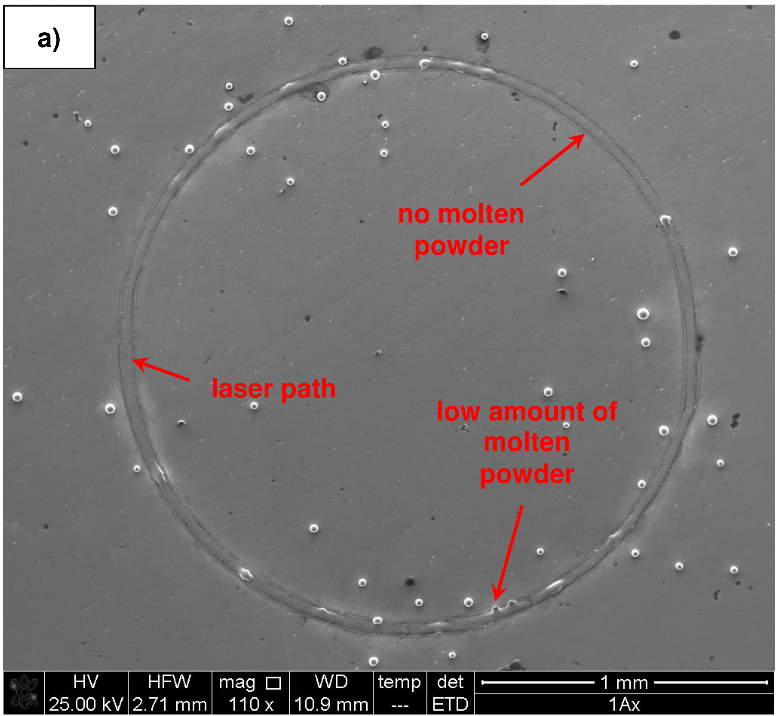
a)
no molten powder
laser path
low amount of molten powder
HV
25.00 kV
HFW
2.71 mm
mag
110 x
WD
10.9 mm
temp
---
det
ETD
1 mm
1Ax

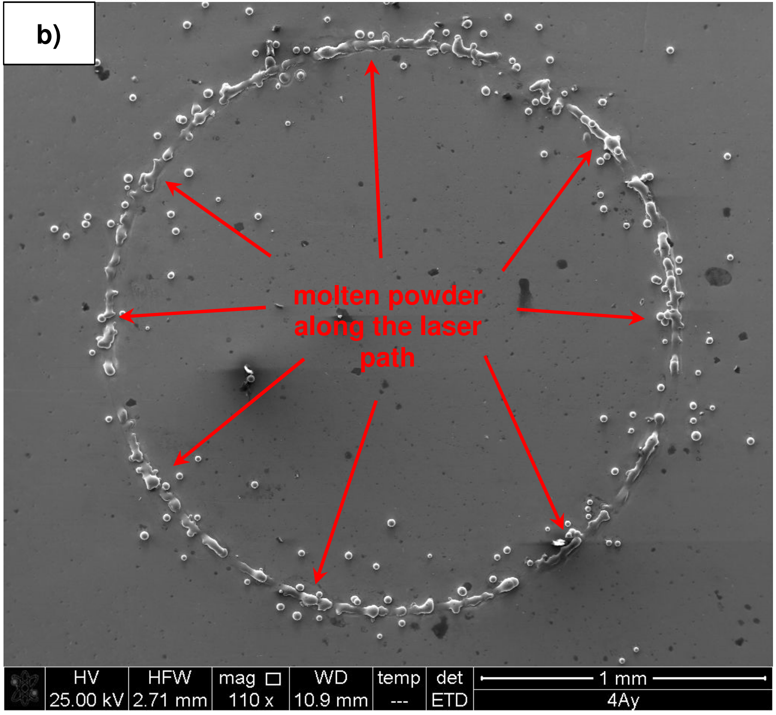
b)
molten powder along the laser path
HV
25.00 kV
HFW
2.71 mm
mag
110 x
WD
10.9 mm
temp
---
det
ETD
1 mm
4Ay

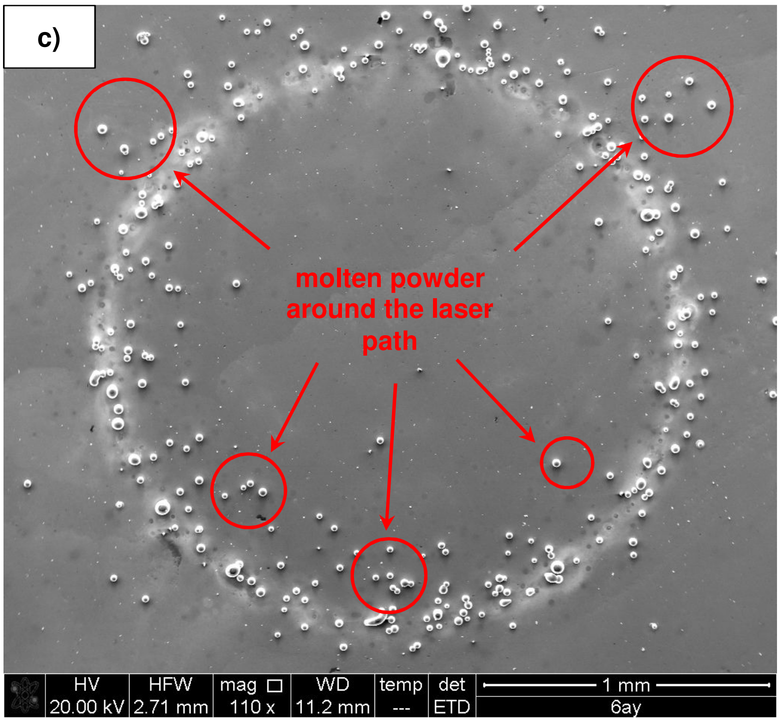

Figure 3.9 Single-layer circular ribs deposited at different working-plane distances (0.7 l/min and 0.574 mg/s): a) 2 mm; b) 5 mm; c) 7 mm.

It was possible to identify three zones with the increase of the distance between substrate and deposition nozzle:

- a zone close to the nozzle outlet with none or low presence of molten material, neither along the laser path nor around it (see Fig. 3.9 a);
- a intermediate zone with a good presence of molten material along the laser path and low number of molten powder particles around it (see Fig. 3.9 b);
- a final zone (higher distances from the nozzle outlet) with a low presence of molten material along the laser path and a large number of molten material particles around it (see Fig. 3.9 c).

The first zone corresponded to a process condition where no powder particles were irradiated by the laser beam or fell inside the molten pool formed by the interaction between laser beam and metal substrate. In this case, the micro DLMD process caused only a remelting of the substrate surface without adding material. From the powder cone point of view, this means that the substrate was located in a position where there was no supply of fresh raw material for the molten pool. Since this phenomenon occurred near the nozzle outlet, it was presumed that here the powder cloud had a convergent shape with no particles falling in correspondence of the centre of the powder cone but only along its external periphery. Moreover, the presence of a central Argon shielding gas flux screened the laser-substrate interaction area, preventing possible particle rebounds into the molten pool (see Fig. 3.10). For an Argon flow rate of 0.7 l/min and a powder feed rate of 0.574 mg/s, this first zone was located between 2 and 3 mm from the nozzle outlet.

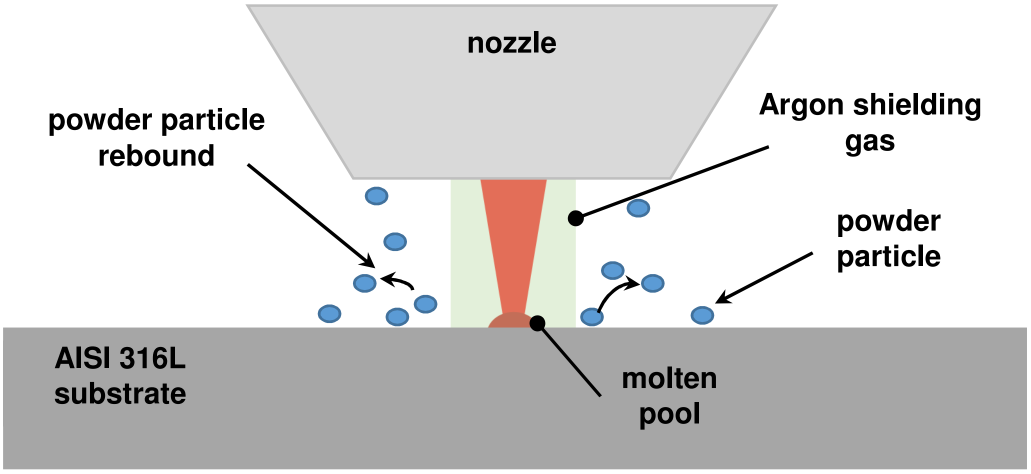

Figure 3.10 The effect of the Argon shielding gas for working-plane distances close to the nozzle outlet.

On the contrary, moving away from the nozzle outlet and increasing the working-plane distance, the process condition improved and a formation of a significant deposited layer was possible. In this intermediate zone of the powder cloud, a larger number of powder particles fell inside the molten pool, allowing the deposition of a solid track along the laser path. Moreover, the limited presence of molten metal particles close to the deposited track presumed that most of the metal powder coming out from the deposition nozzle was concentrated in correspondence to the centre of the powder cone where the molten pool was supposed to be, determining a higher deposition efficiency. This behaviour showed to be constant along all the intermediate zone extension (roughly between 4 to 6 mm from the nozzle outlet for an Argon flow rate of 0.7 l/min and 0.574 mg/s).
Nevertheless, with a further increase in the working plane distance, the process condition changed and most of the molten powder particles fell around the laser path and not inside it, causing a sintered track strongly discontinuous. This meant that the powder was not mainly concentrated in the middle of the powder cloud as happened for the intermediate zone, but the distribution of the metal particles was more homogeneous along the cross sectional area of the powder cloud. This homogeneous particle distribution reduced the powder deposition efficiency, decreasing the number of powder particles falling inside the molten pool and causing a confused and scattered powder deposition along the laser path (see Fig. 3.9 c). This zone was called “divergent zone” due to the changing in the powder density along the powder cloud.
The overall shape of the powder cloud coming out from the nozzle during the deposition process could be represented as a convergent/divergent cone (see Fig. 3.11).

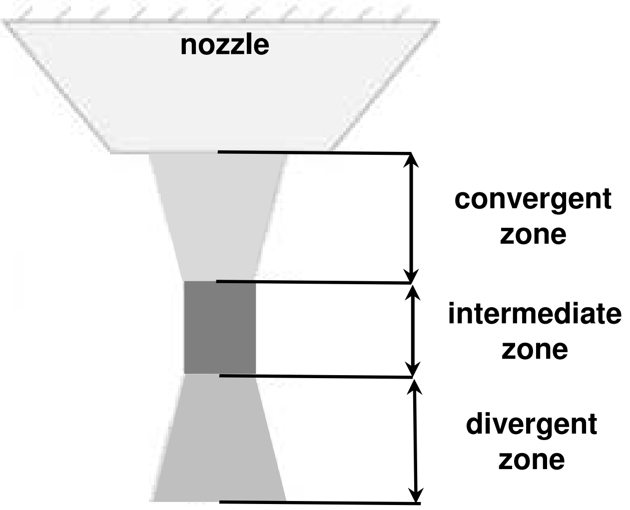

Figure 3.11 Schematic representation of the deposition powder cloud.

At constant Argon flow rate and at constant working-plane position, a variation in the powder mass flow rate from 0.574 to 1.723 mg/s brought in a deposited layer more significant and continuous. Nevertheless, it also determined an increase in the number of molten particles which fell around the deposited layer. This phenomenon was more evident when the substrate was placed in correspondence to the divergent zone of the powder cloud. From the analysis of the deposited tracks, a variation in the powder mass flow rate did not affect the powder distribution along the vertical axis of the powder cloud but only the powder density. On the contrary, the experimental results showed a strong influence of the Argon flow rate on the formation and extension of the three zones characterizing the deposition powder cone. Increasing the Argon flow rate from 0.7 to 2.7 l/min, the continuity of the deposited layer improved for working-plane distances closer to the nozzle outlet compare to those obtained for low value of the carrier gas. For 2.7 l/min and 1.723 mg/s the formation of a significant deposited track started with a substrate distance of 3 mm from the deposition nozzle against 4 mm when the Argon flow rate was decreased at 0.7 l/min.

Nevertheless, for high values of the carrier gas flow rate, the continuity in the track deposition remained low in every working-plane position (see Fig. 3.12).

This meant that for high values of the carrier gas, the mass concentration along the powder cloud decreased, deteriorating the deposition efficiency of the process. Moreover, Figure 3.12 shows some molten powder particles at circa 1 mm far from the deposited track for working-plane distances of 6 and 7 mm, indicating a general enlargement of the width of the powder cloud during the deposition process. This results were in strong agreement with the numerical outputs of the CFD analysis carried in the Chapter §3.3.5.

Decreasing the Argon flow rate up to 0.7 l/min, the intermediate zone of the powder cone increased its distance from the nozzle outlet and the deposition continuity improved. In Figure 3.9 b, for 0.7 l/min and 0.574 mg/s the deposited layer is more significant even if the powder mass flow is three times lower than in Figure 3.12. This was because for low levels for the carrier gas flow rate, the particle mass concentration was higher in correspondence to the centre of the powder cloud, allowing a bigger number of powder particles to fall inside the molten pool.

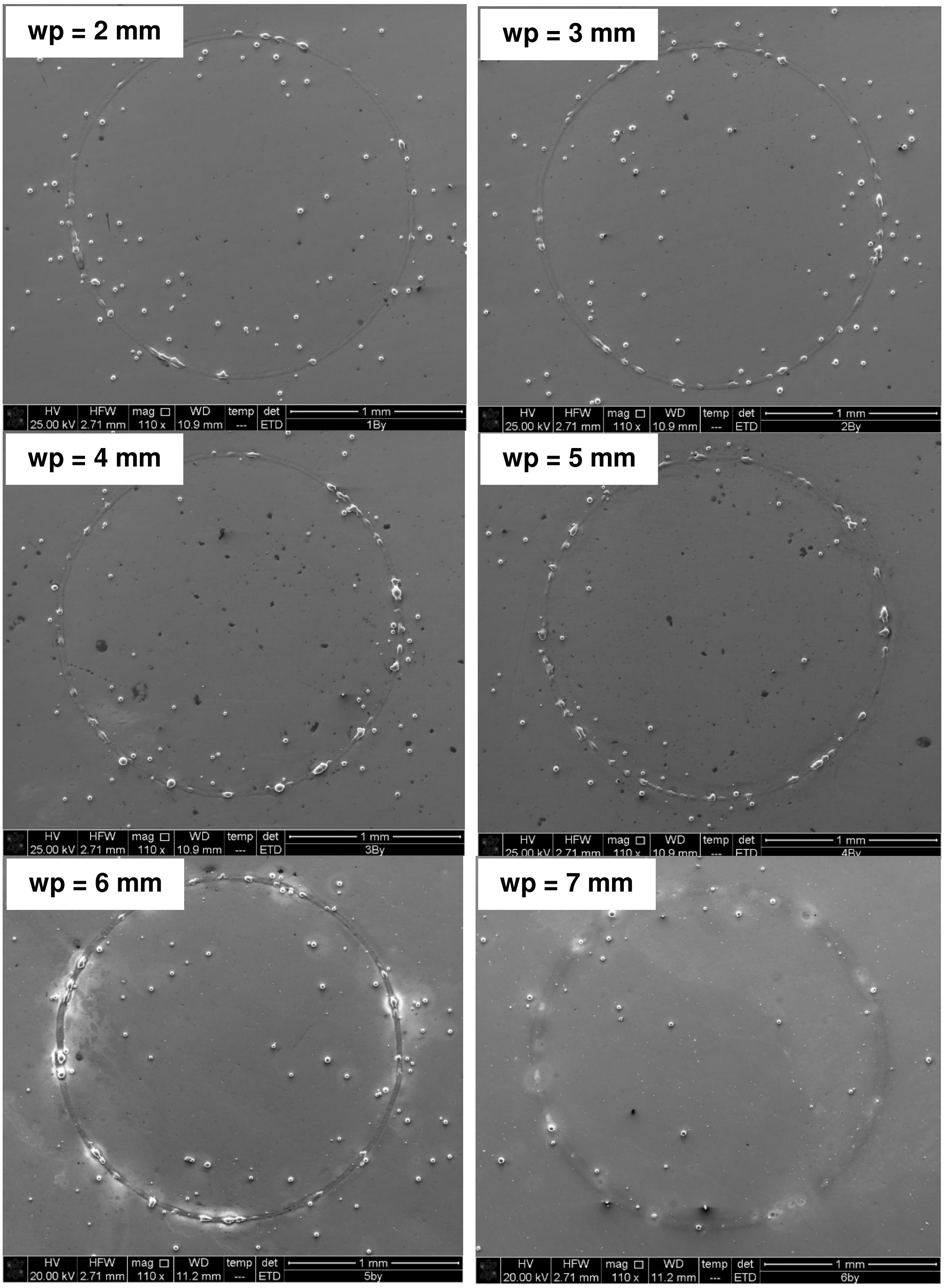

Figure 3.12 Working-plane distances (wp) for Argon flow rate = 2.7 l/min and powder feed rate = 1.723 mg/s.

The best results in terms of track continuity and presence of molten material along the laser path were obtained for an Argon flow rate of 0.7 l/min and a powder flow rate of 1.723 g/s.

Argon flow rate [l/min]	CFD simulation result	experimental investigation result
0.7	from 2.3 to 4.2 mm	from 5 to 6 mm
1.7	from 1.1 to 2.7 mm	from 4 to 5 mm
2.7	from 0.9 to 2 mm	from 4 to 5 mm

Table 3.7 Distance of the intermediate zone of the powder cloud from the nozzle outlet.

3.5. Conclusions

The results obtained from the experimental validation showed to be in agreement with the numerical outputs of the CFD analysis in terms of influence of the analysed process parameters on the overall behaviour of the deposition powder cloud. Nevertheless, the theoretical model was inaccurate in determining the correct position of the intermediate zone along the extension of the powder cloud. The deposition behaviour of the metal particles and the powder cloud geometry were well represented by the theoretical equations and assumptions assumed in Chapter §3.3. Table 3.7 shows a comparison between the numerical results and the experimental one.

The deposition powder cloud had a convergent/divergent conical shape characterized by three defined zones. The substrate had to be located inside the intermediate zone to ensure a high particle mass concentration falling inside the molten pool and a continuous deposited layer formation. Moreover, the Argon flow rate was the most significant process parameters affecting the distribution of the powder coming out from the deposition nozzle. High levels for the carrier gas determined a general enlargement of the width of the powder cloud and a translation of the intermediate zone close to the nozzle outlet. This turned in a lower deposition efficiency due to the decrease in the particle mass concentration reaching the substrate. For 0.7 l/min the intermediate zone was located at 5 mm in average from the nozzle. In this case, the particle mass concentration was higher and the deposited layer more continuous, indicating a bigger number of metal particles falling inside the molten pool.

The position of the intermediate zone detected from the experimental tests differed of 2.6 mm in average from the numerical results provided by the CFD analysis.

3.6. Laser defocusing considerations

3.6.1. Introduction

In micro DLMD, a full understanding of the behaviour and distribution of the metal powder particles coming out from the deposition nozzle is of great importance to correctly detect the appropriate working-plane distance and ensure a constant supply of fresh raw material falling into the molten pool. Another significant process parameter to analyse before starting with future experimental investigations is the laser defocusing. The laser defocusing is defined as the gap existing between the working-plane of the substrate and the focus plane of the laser. It plays a fundamental role in micro DLMD since it affects the molten pool size and the preheating of the powder particles coming out from the nozzle outlet.

Several authors investigated the effect of this process parameter in literature. Zhu et al. [53] found a strong influence of the laser defocusing distance on the final height and surface roughness of the realized part, obtaining high surface quality with the powder focussed below the substrate and laser focussed above. Gharbi et al. [54] demonstrate that larger molten pools induced by a positive laser focussed improve the final surface roughness and increase the powder particles preheating that results in a beneficial factor for the surface finish. Moreover, wrong values for the laser defocusing can cause a growth not uniform of the deposited layer, decreasing the final quality of the realized part [46, 55].

To the best of Author’s knowledge, no investigation is available for a DLMD process applied to the micro-scale. In this research work the influence of the laser defocusing on the deposited track formation and on the uniformity of growth of the realized micro-feature was analysed.

3.6.2. Material and method

This experimental investigation was made in collaboration with Saeed Khademzadeh, a Ph.D. student from the Mining and Metallurgy Engineering Department, Amirkabir University of Technology (Tehran Polytechnic). Being a partnership research work, for this experimental campaign the employed powder was a Nickel-Titanium alloy with a Ni:Ti ratio of 50:50 (see Chapter §2.2.3).

3.6.2.1. Experimental procedure

In this experimental investigation, some preliminary DLMD tests were carried out to define the process parameters to employ during the experimental plan. The laser power, the laser scan speed, and the working-plane distance of the substrate resulting from these preliminary experiments were kept constant during all the experimental investigation (see Table 3.8).

laser power	30 W
laser scan speed	50 mm/min
laser spot	30 µm
powder feed rate	1.26 mg/s
nominal height of the thin wall	300 µm
nominal layer thickness	10 µm
intermediate zone location	from 3.8 to 5 mm

Table 3.8 Micro DLMD process parameters.

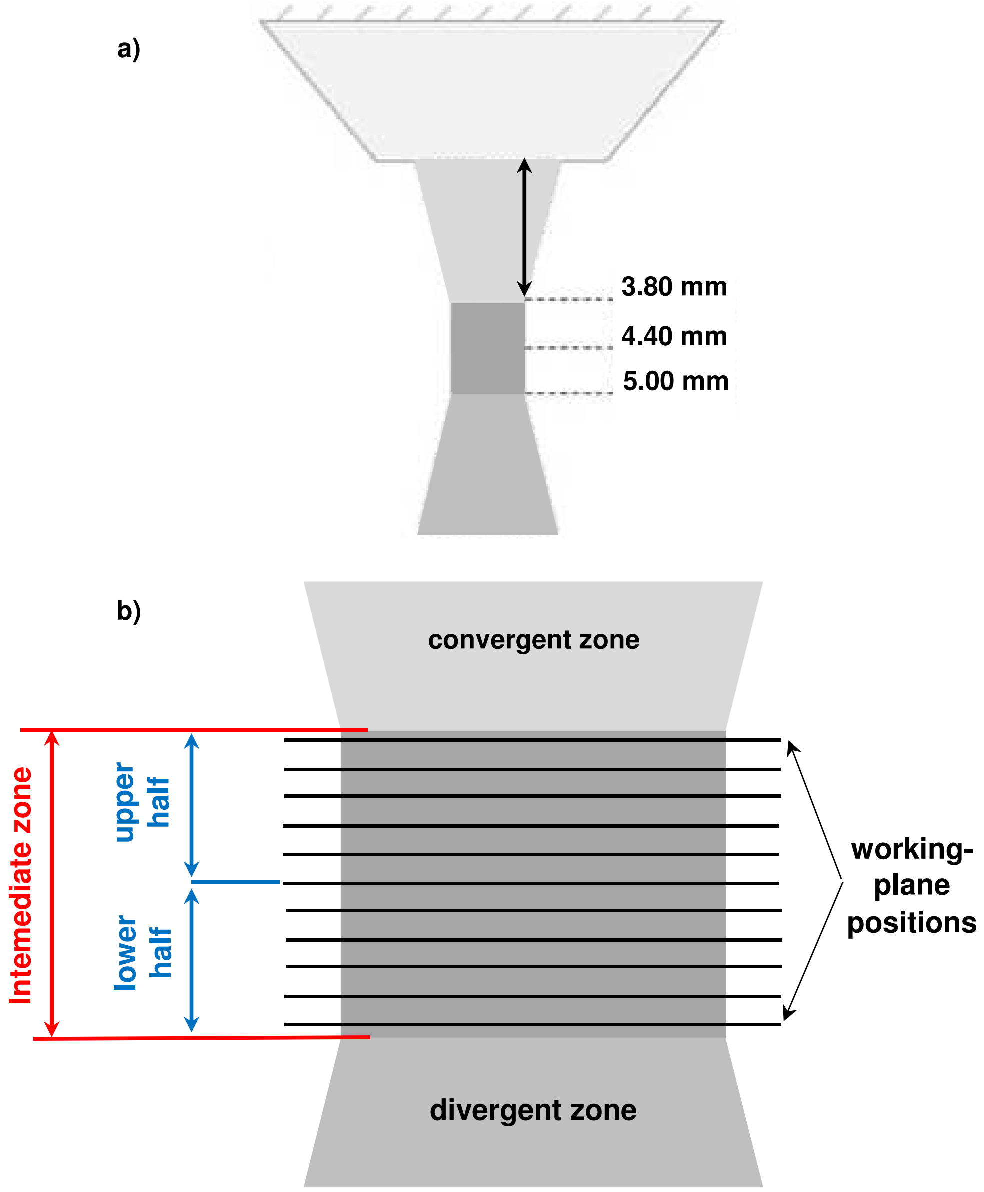

Figure 3.13 a) definition of the intermediate zone of the powder cloud; b) working-plane position employed during the experimental plan.

The experimental procedure was divided in two parts:

- the realization of single-layer deposited track to analyse the influence of the laser defocusing on the track deposition and formation in relation with different relative positions of the substrate inside the intermediate zone of the powder cloud;
- the realization of thin walls to analyse the influence of the laser defocusing on the uniformity of growth and final roughness at the top side of the manufactured micro-feature (see Table 3.7).

Concerning the single-layer track deposition, 11 different working-plane positions and 11 configurations for the laser defocusing were chosen for a total of 121 deposited tracks. All the 11 positions of the substrate were included in the intermediate zone of the powder cloud (see Fig. 3.13 b).
In this experimental tests the laser defocusing was defined as:

a) negative laser defocusing: $(d_{WP} - d_{LF}) < 0$. The laser was focused below the working-plane;
b) positive laser defocusing: $(d_{WP} - d_{LF}) > 0$. The laser was focused above the working-plane;
c) no laser defocusing: $(d_{WP} - d_{LF}) = 0$. The laser was focused on the working-plane.

Where d_{WP} was the distance between the working-plane and the nozzle outlet, whereas d_{LF} was the distance between the focus plane of the laser and the nozzle outlet.
The chosen values for the laser defocusing are summarized in Table 3.9.

positive laser defocusing [mm]	+0.5, +0.4, +0.3, +0.2, +0.1
no laser defocusing [mm]	0
negative laser defocusing [mm]	-0.5, -0.4, -0.3, -0.2, -0.1

Table 3.9 Laser defocusing values for single-layer track deposition

Concerning the thin walls, they were produced with the process parameters listed in the Table 3.8, employing three values for the laser defocusing (-0.2, 0, +0.2), and three repetitions for each combination of factors, for a total of 9 micro features. All the micro-artefacts were realized on an AISI 316L square substrate of a size of 20 x 20 mm and 2 mm in thickness. All samples were cleaned in Acetone and deionized water solution using an ultrasonic cleaner to remove the un-melted powder particles on the substrate surface.
The surface morphology of the single-layer deposited tracks was characterized using the Scanning Electron Microscope (SEM, see Chapter §2.3.1), whereas the uniformity of growth and the final surface roughness at the top of the thin walls were analysed through the Sensofar Optical Profilometer (see Chapter §2.3.2).

3.6.3. Results and discussion

3.6.3.1. Single-layer tracks

In the single-layer track analysis, the experimental results showed a strong influence of the chosen micro DLMD process parameters on the final integrity of the deposited layer.
A positive laser defocusing improved the deposition continuity of the sintered track. Figure 3.14 shows 8 single-layer tracks realized on a working-plane position located at 4.2 mm from the nozzle outlet. In this case, the laser defocusing increased from the left side of the substrate to the right side. Tacks 8, 9, 10, and 11 showed a more presence of molten powder particles along the laser path and

a deposited bead more continuous with the increase of the laser defocusing (from +0.2 to +0.5 mm).

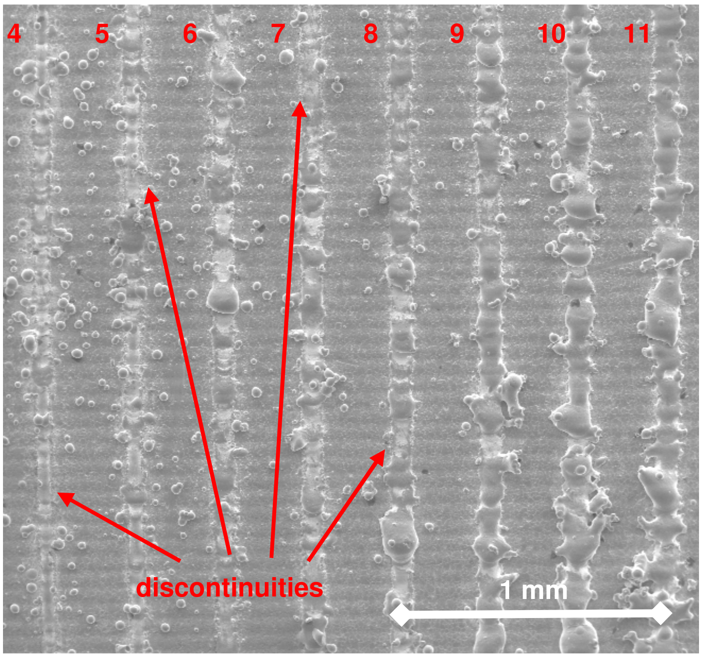

Figure 3.14 Deposited single layer tracks at different laser defocusing: 4 = -0.2 mm, 5 = -0.1 mm, 6 = 0 mm, 7 = +0.1 mm, 8 = +0.2 mm, 9 = +0.3 mm, 10 = +0.4 mm, 11 = +0.5 mm (working-plane position = 4.2 mm).

Nevertheless, the quality of the deposited layer was affected by the working-plane position too. Remaining inside the intermediate zone of the powder cloud defined during the previous preliminary DLMD tests (see Chapter §3.4.4), the process deposition efficiency increased moving the substrate in the lower half of the intermediate zone (see Fig. 3.13). Locating the substrate between 3.8 and 4.4 mm, the presence of molten material along the laser path was high, but the structure of the deposited track was strongly discontinuous independently from the laser defocusing employed. On the contrary, moving the substrate down along the intermediate zone (between 4.4 and 5 mm), the quality of the sintered track improved in terms of deposition continuity and structural integrity (see Fig. 3.15).

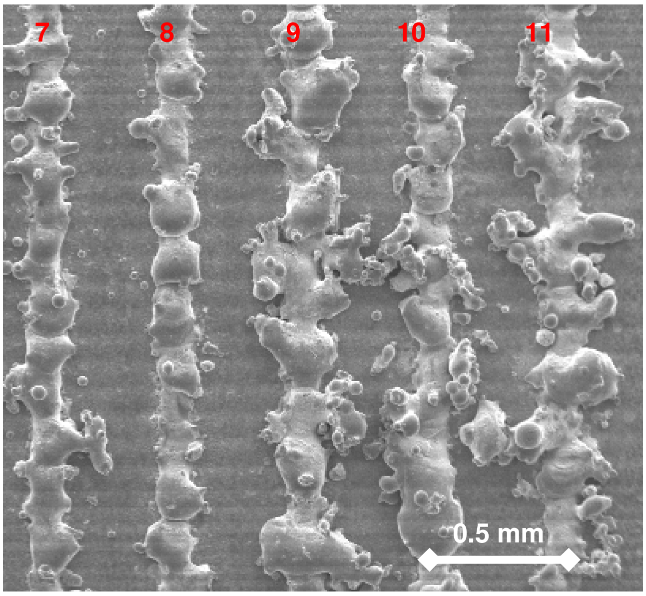

Figure 3.15 Deposited single layer tracks at different laser defocusing: 7 = +0.1 mm, 8 = +0.2 mm, 9 = +0.3 mm, 10 = +0.4 mm, 11 = +0.5 mm (working-plane position = 4.9 mm).

The better single-layer deposited tracks in terms of final continuity and integrity were realized for a working plane placed at 4.8 mm from the nozzle outlet and a laser defocusing between +0.2 and +0.5 mm.

3.6.3.2. Thin walls

As a result of the single-layer deposited tracks analysis, the thin walls were realized setting the substrate at a distance of 4.8 mm from the nozzle outlet and with a laser defocusing varying between -0.2 and +0.2 mm.

The experimental results showed a strong influence of the laser defocusing on the uniformity of growth and final surface roughness on the top of the micro walls realized. For value of -0.2 mm for the laser defocusing, the final height was strongly deteriorated and irregular. On the contrary, positive laser defocusing (+0.2 mm) improved the uniformity of growth of the micro thin walls, reducing the unevenness of the surface (see Fig. 3.16). This could be explained by the higher preheating that the metal powder were subjected in the case of a laser focused at +0.2 mm. Moreover, the employment of a defocusing enlarged the laser spot on the substrate surface, increasing the powder quantity falling inside the molten pool.

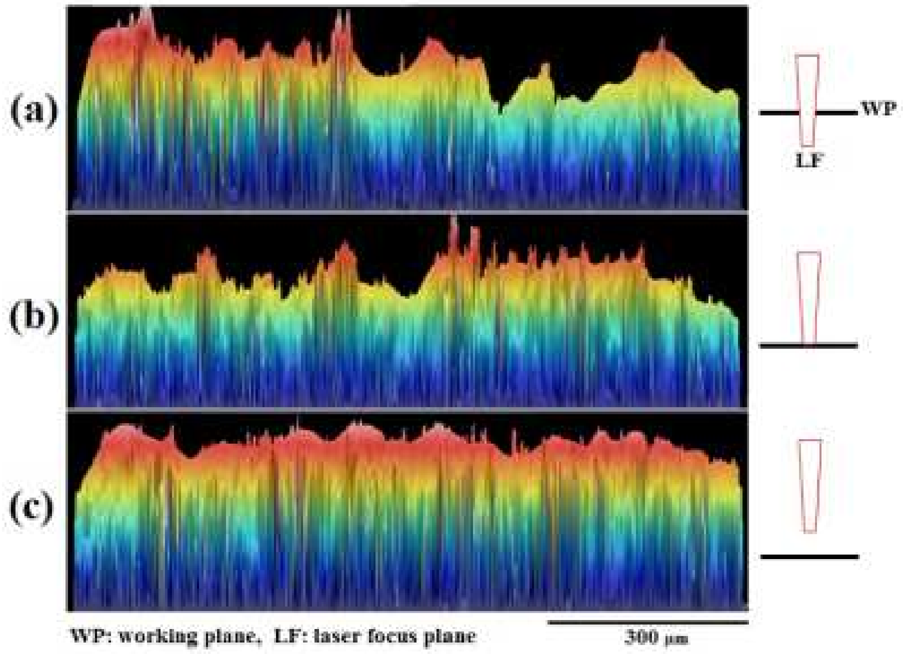

Figure 3.16 Optical profiles of thin walls produced by micro DLMD: a) laser defocusing = -0.2 mm; b) laser defocusing = 0 mm; c) laser defocusing = +0.2 mm.

Concerning the final roughness on the top of the realized micro feature, the average measurements are summarized in Table 3.10. The higher is the laser defocusing, the lower is the final surface roughness in terms of R_a. Moving the laser focus from -0.2 to +0.2 mm above the substrate surface, the surface roughness decrease from 28.9 µm to 16.8 µm, improving the final quality of the micro thin wall.

	laser defocusing [mm]	**R_a [µm]**
wall a	-0.2	28.9
wall b	0	22.8
wall c	+0.2	16.8

Table 3.10 Surface roughness on the top of the thin walls.

3.6.4. Conclusions

The experimental investigation showed that the position of the substrate inside the intermediate zone of the powder cloud and the employed laser defocusing strongly affected the deposition of continuous single-layer tracks and the realization of thin walls with uniform height.

The main achievements came out from the experimental tests are summarized as follows:

- the continuity of the deposited track improved when the substrate was located in the lower half of the intermediate zone of the deposition powder cloud;
- an increase of the laser defocusing improved the quality of the deposited layer and the continuity of the metallic bead. The best results were obtained for laser defocusing ranging between +0.2 and +0.5 mm;
- the uniformity of growth get better when a laser defocusing of +0.2 mm was employed, reducing the unevenness of the surface at the top of the thin wall;
- the final roughness on the top of the thin walls decreased from 28.9 µm to 16.8 µm when positive laser defocusing were employed.

3.7. Conclusions

In this Chapter, a characterization of the deposition powder cloud coming out from the nozzle outlet of the Manudirect ® MSL50 system was provided and the influence of the substrate working-plane position and of the laser defocusing on the track and thin walls manufacture was analysed.

The overall experimental plan showed that the laser defocusing combined to the correct location of the working plane inside the deposition powder cone was fundamental to get a continuous track formation and micro-artefact with high dimensional accuracy.

The main achieved outputs were summarized as follows:

- the CFD model fit well the obtained experimental results;
- the powder cloud coming out from the deposition nozzle could be represented as a powder cone characterized by three main zones: a convergent zone, an intermediate zone, and a divergent zone;
- the intermediate zone was the most suitable for the location of the substrate since it ensured a higher particle mass concentration during the process;
- the Argon flow rate strongly affected the overall shape of the powder cone, shifting the intermediate zone close to the nozzle outlet for high values of the carrier gas (2.7 l/min);
- increasing the Argon flow rate, the powder cloud spread decreasing the powder density on the substrate surface locally;
- low values for the carrier gas (0.7 l/min) ensured a high particle mass concentration in correspondence to the molten pool, promoting a continuous layer formation;
- for 0.7 l/min, the location of the intermediate zone was experimentally between 5 and 6 mm from the nozzle outlet against the theoretical results of 2.3 and 4.2 mm obtained by the CFD analysis;
- the continuity of the deposited track improves if the substrate was located in the lower half of the intermediate zone of the deposition powder cloud (working-plane position between 4.4 and 5 mm for the Ni50Ti50 deposition);
- a positive laser defocusing improved the uniformity of growth of Ni50Ti50 thin walls, reducing the unevenness of the surface and decreasing the final surface roughness from 28.9 µm to 16.8 µm.

Chapter 4

AM building philosophy

This chapter deals with the technological issue in getting continuous track depositions when the micro DLMD process is performed with only one pass per layer.

Two different approaches are here introduced and compare: the One Pass per Layer approach (OPL) and the Multi Passes per Layer approach (MPL). The experimental results obtained by these two different “AM building approaches” are discussed and analyzed.

The MPL approach ensures a sintered track deposition more stable and continuous in comparison to OPL, resulting to be more suitable for a DLMD process applied at the micro-scale.

4.1. Introduction

In DLMD, the successful realization of a 3D metal part strongly depends on the integrity, accuracy and shape of the deposited layer. In particular, the final dimension accuracy, microstructure, mechanical properties, and internal porosity distribution of the realized artefact depend on the characteristics of the deposited metal tracks [10, 54, 56, 57].
To get a good and efficient deposition process, a constant interaction between the molten pool and the powder particles coming out from the feeding system and falling inside the pool must to be ensured [58-60]. This happens in macro DLMD, where the laser spot size and the corresponding melt pool are typically large enough to continuously capture a big number of powder particles during the process and create a thick and stable deposited track with only one pass per layer [61]. This process condition is simply illustrated in the Figure 4.1. Here, the laser spot diameter is comparable to the powder spot size (unless ten times bigger than the powder grain size), allowing to capture a large number of metal particles coming from the injection nozzle.

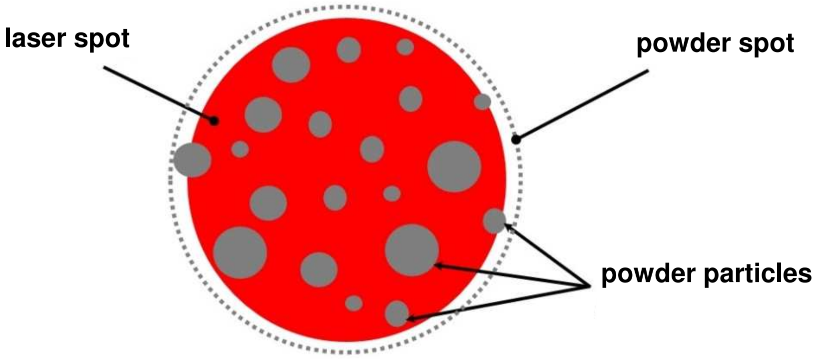

Figure 4.1 Process interaction zone between molten pool and powder particles in macro DLMD.

On the contrary, getting a continuous and stable track deposition is more critical in micro DLMD because a constant interaction between molten pool and powder particles is difficult to achieve and rarely happens. This is due to the concurrence of two factors characterizing the micro DLMD process:

- the small size of the laser spot;
- the low efficiency in the powder deposition provided by the common nozzle solutions.

Indeed contrary to what happens in macro DLMD, in this case the laser spot employed during the process is fine and very close to the powder particles dimension. Consequently, the corresponding molten pool is small and it is capable to capture only a little number of powder particles at time. Moreover, the common powder feeding systems used in macro DLMD and applied at the micro-scale do not ensure the correct supply of powder particles to the molten pool, decreasing the efficiency in the powder deposition drastically. Indeed, the corresponding powder spot generated by the deposition nozzle is usually ten times bigger than the employed laser spot size, causing a fall in the powder concentration in correspondence to the molten pool (see Fig. 4.2).

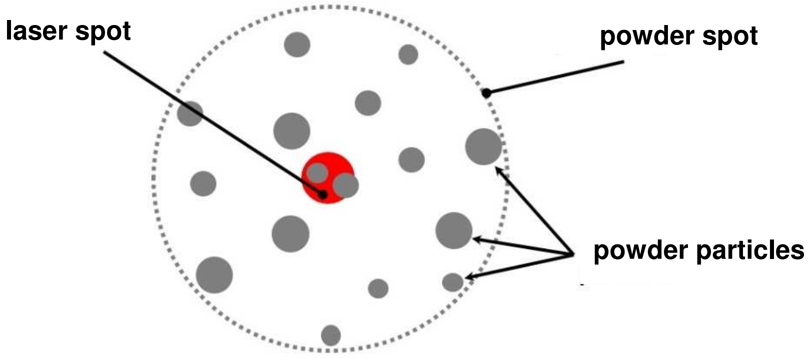

Figure 4.2 Process interaction zone between molten pool and powder particles in micro DLMD.

The incapacity to supply the molten pool with a high and constant number of powder particles combined with the employment of a laser spot very close to the powder particles size does not allow a constant and stable interaction between the molten pool and the powder particles (see Fig. 4.3), creating a discontinuous track deposition.

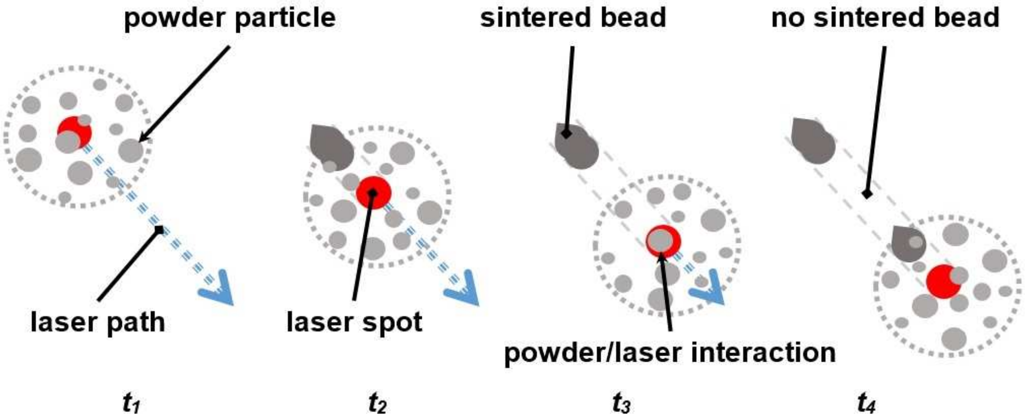

Figure 4.3 Discontinuous interaction between molten pool and powder particles in micro DLMD.

In other hands, in micro DLMD is not possible to get a significant and continuous layer formation with only one pass, but more passes per layer are required in order to increase the continuity and the quality of the sintered track.

Nevertheless, an increase in the number of passes causes an increment in the production time, powder waste, and heating cycling. Moreover, the high thermal gradients produced by repetitive reheating cycling can introduce high residual stresses that can break or warp the metal part during the AM process.

For this reason, in micro DLMD the correct combination of process parameters in addition to the correct choice for the number of passes per layer is critical but fundamental to ensure a continuous layer formation and a successful micro-part realization.

4.2. One Pass per Layer (OPL)

With the term “One Pass per Layer (OPL)” is indicated the common approach generally employed in DLMD to additively manufacture 3D parts. This “AM building philosophy” is mainly based on the constant interaction between molten pool and powder particles during the deposition process and it consists in building a continuous and significant deposited track with just one pass of the laser (see Fig. 4.4).

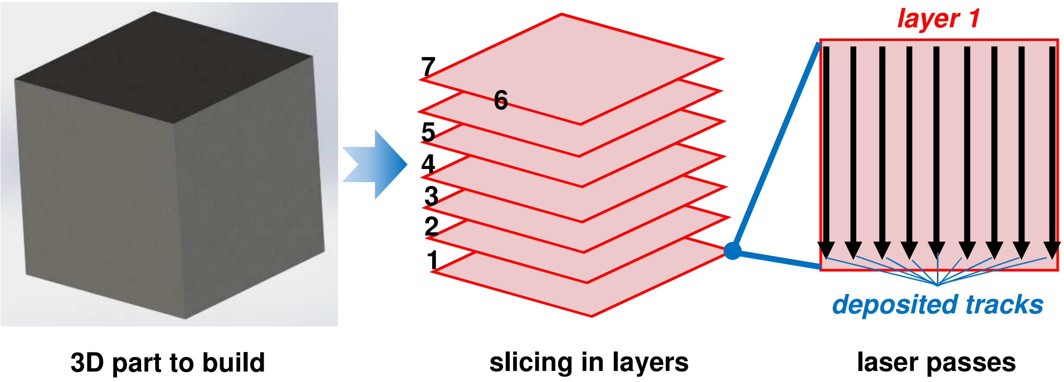

Figure 4.4 Generic operational scheme of DLMD.

The OPL correctly works in macro DLMD (see Fig. 4.5) where the laser spot is much bigger than the powder particles falling in the interaction zone and the size of the molten pool is comparable to those of the powder spot (see §4.1).

In a macro deposition process, the laser spot generally ranges between 0.5 and 22 mm, whereas the common powder grain size employed is between 45 and 150 µm. This means that for a constant powder mass flow a very large number of powder particles can fall continuously into the molten pool realizing a thick and significant sintered bead.

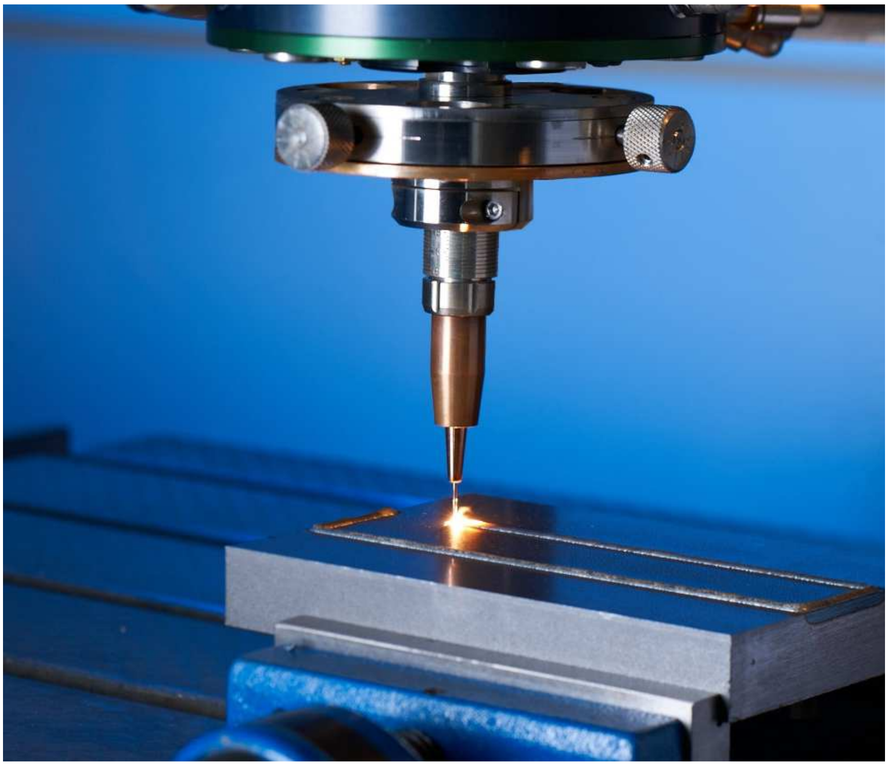

Figure 4.5 Example of macro DLMD.

4.3. Critical issue in micro DLMD: the deposited layer formation

In micro DLMD, the process condition of a constant interaction between molten pool and powder particles is not always satisfied. This is because of two factors:

- the very fine laser spot;
- the low efficiency in the powder deposition.

As explained in Chapter §4.1, in micro DLMD the laser spot employed during the process is very fine (usually smaller than 50 µm) and creates a molten pool too small to allow a conspicuous number of powder particles to fall in. This fact does not permit a sufficient amount of fresh material to participate at the bead formation. In addition to the restricted laser spot size, the low efficiency in powder deposition of the conventional feeding nozzles decreases the powder particle mass concentration in correspondence to the molten pool, preventing a constant fall of metal particles into the pool. The concurrence of these two factors causes the formation of a discontinuous deposited track if only one pass per layer is employed during the process.

Figure 4.6 shows how the first deposited layer appears when the OPL building strategy is performed in micro DLMD. In this case, Ti-6Al-4V powder with a grain size between 40 and 45 µm was deposited on a AISI 316L substrate employing a laser spot of 60 µm and a powder mass flow of 4 g/h. As it is shown in the Figure, the resulting deposited layer was a sort of a discontinuous assemble of melted masses along the path traced by the laser. The continuity of the deposited layer did not improve if the powder mass flow was increased up to 7 g/h (see Fig. 4.7).

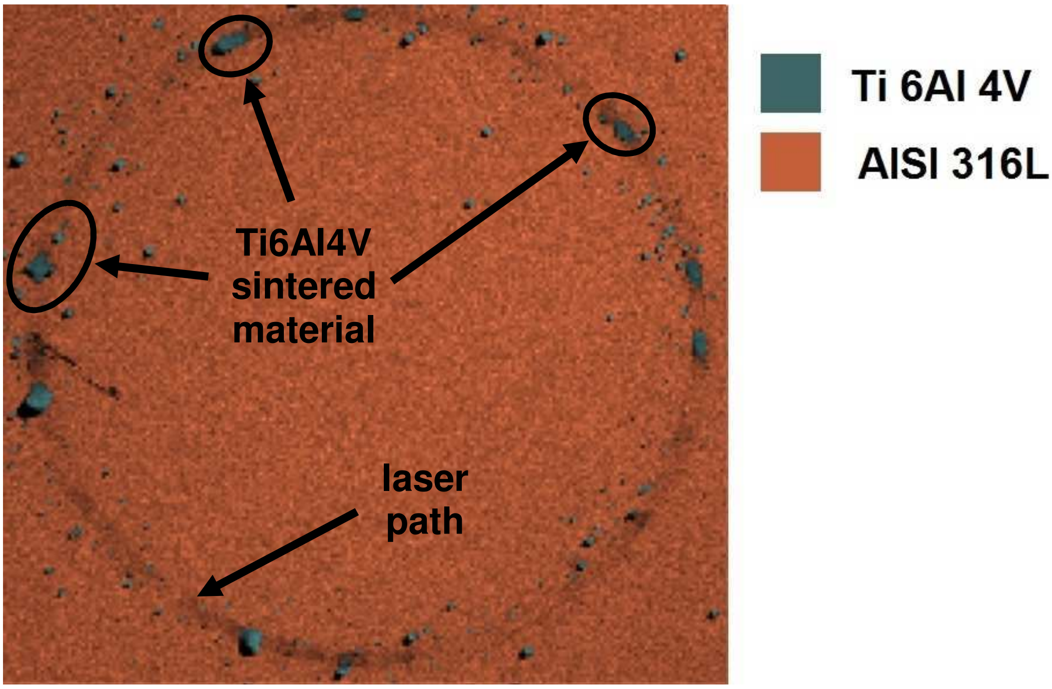

Figure 4.6 Deposition of Ti-6Al-4V powder on AISI 316L substrate: OPL building approach with a powder mass flow of 4 g/h.

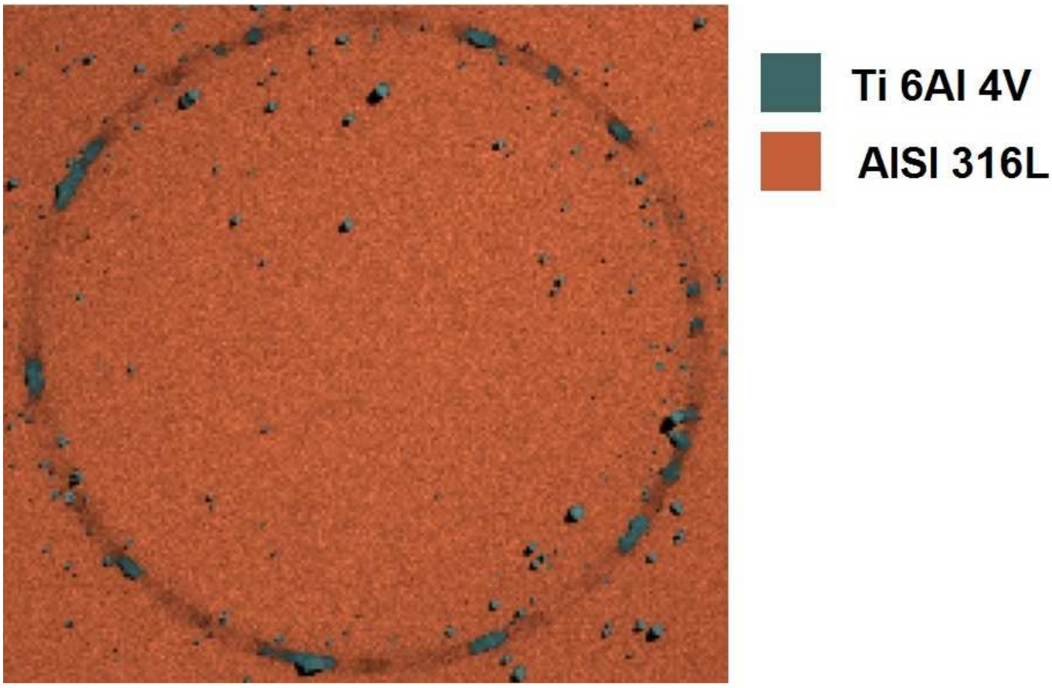

Figure 4.7 Deposition of Ti-6Al-4V powder on AISI 316L substrate: OPL building approach with a powder mass flow of 7 g/h.

Figure 4.6 and 4.7 underline how the low efficiency in powder deposition strongly affects the process, providing a not constant interaction between molten pool and powder particles during the micro DLMD process. This process issue forced to increase the number of passes per layer to improve the layer continuity and the final quality of the sintered track.

4.4. Multi Passes per Layer (MPL)

With the term “Multi Passes per Layer (MPL)” is indicated the new approach assumed in this research work to additively manufacture 3D micro-parts for DLMD. This “AM building philosophy” wants to overcome the critical issue in the deposited layer formation presented in the Chapter §4.3.

The MPL approach mainly consisted in increasing the number of passes per layer keeping constant the laser power, the laser scan speed, the powder mass flow rate and the distance between the nozzle and the sintering plane for each deposited track. The Author of this Ph.D. project designed this process solution since the known commercial feeding systems did not ensure a powder spot size smaller than 300 µm and the development of a new deposition nozzle required a significant redesign of the MSL50 machine with a conspicuous elongation of the time required to complete the Ph.D. project. An increment of the number of passes per layer directly caused an increase in the number of powder particles falling inside the molten pool randomly, filling the discontinuities caused by the lack of interaction between molten pool and powder particles (see Fig. 4.6 and 4.7). Nevertheless, an increase in the number of passes per layer involved an increase in the production time, powder waste and heating cycling.

It was hence fundamental to analyse how the process parameters and the number of passes per layer affected the micro DLMD to improve the efficiency of the process and the final quality of the realized part.

4.5. Conclusions

In this chapter, two different approaches were introduced and discussed. The more common “AM building philosophy” employed in macro DLMD is the OPL, where only one pass per layer is sufficient to ensure the deposition of a constant and significant sintered bead since the laser spot size is big enough to guarantee a large number of powder particles falling inside the molten pool.

On the contrary, OPL does not work well in micro DLMD, where the laser spot size is very small (generally between 30 and 50 µm) and its dimensions are comparable to the powder grain size employed during the process. Moreover, the low efficiency in the powder deposition of the common powder feeding systems do not ensure a constant interaction between molten pool and powder particles during the deposition process, resulting in a deposited sintered bead discontinuous and not well defined. For this reason, in micro DLMD it is necessary to change the building approach assuming one more suitable for the process and ensuring the formation of a constant and stable layer.

MPL is a new approach that allows the formation of a constant sintered bead increasing the number of passes per layer and keeping constant the laser power, the laser scan speed and the powder mass flow during the track deposition.

MPL works well in micro DLMD, but the number of passes have to be carefully chosen to avoid the formation of undesired residual stress which can warp or break the realized 3D part.

Chapter 5

The first deposited layer in micro DLMD

This chapter takes into account the considerations and conclusions made in the Chapter §4 and deals with the process issue related to the deposition and formation of a continuous and stable deposited track in micro DLMD.

MPL approach is assumed in this experimental investigation and the influence of specific energy (I), laser power (P), and number of passes (n°p) on the final quality of the deposited layer is analysed.

The final shape and the overall integrity of the starting deposited tracks are analysed in terms of track continuity, integrity, accuracy, HAZ penetration depth and variation in the cross section geometry. The experimental results show a strong influence of the three analysed process parameters on the continuity of the deposited track. Moreover, the starting surface condition of the substrate strongly affects the final cross-sectional shape of the solid metal bead and the penetration depth of the HAZ.

A preliminary process window is also provided.

5.1. Introduction

One of the most critical issue in DLMD with coaxial powder feeding is the first deposited layer formation. The shape, the uniformity, and the continuity of the starting layer significantly affect the final quality of the artefact and the overall efficiency of the DLMD process in terms of powder waste and production time.

In the recent years, several authors have analyzed how the DLMD process parameters affect the first layer formation and the overall quality of the final components [53, 54, 62-66]. Ocylok et al. [67] have demonstrated the positive correlation between laser power and molten pool size, proving the largest influence of the provided thermal energy in comparison to the other process parameters on the metal bead formation. Anime et al. [61] have analysed the effect of the laser power, traverse speed, and powder feed rate on the temperature field evolution and distribution during a DLMD process, underlining the influence of the thermal gradients and reheating cycles on the final properties of the metal artefact. Lu et al. [68] have shown how the powder feeding rate, the specific energy, and the scanning speed are the most important factors affecting the temperature of the molten pool and consequently the forming quality and microstructure of the deposited layer for a macro DLMD process employing large laser spot.

The critical issue in the first deposition layer formation is an important topic in Selective Laser Melting (SLM) too. Yadroitsev et al. [69] have demonstrated that the formation of a continuous track is limited to a “stability zone” depending on the scanning speed and laser power. Gu et al. [70] have also demonstrated as a wrong combination of the process parameters can introduce instability in the molten pool causing discontinuous sintered tracks.

Understanding how DLMD process parameters affect the molten pool and the solid bead formation is fundamental to get metal part with high geometrical accuracy and mechanical properties [71]. The issue growths in importance when DLMD is applied at the micro-scale [16]. Here, the small molten pool size prevents a large number of powder particles to participate at the layer formation continuously. Therefore, a deep control on the molten pool and layer formation is extremely important to get micro-artefacts with high accuracy and high performance [72, 73]. To the best of the Author’s knowledge, no investigation is available in literature for the first deposited layer formation in micro DLMD. In this study, the influence of laser power (*P*), specific energy (*I*), and number of passes per layer (*n°p*) on the continuity, integrity, and cross section variation of the single sintered layer is analyzed providing a preliminary process window.

5.2. Material & methods

5.2.1. Experimental procedure

The micro DLMD system employed for this experimental investigation was the Manudirect ® MSL50 machine introduced in the Chapter §2.1. The metal powder was a Ti-6Al-4V alloy of a grain size between 20 and 45 µm and a tap density of 2.3 g/cm^3 (see Chapter §2.2.2).

The Titanium alloy powder was deposited on a square AISI 316L Stainless Steel substrate with a size of 20 x 20 mm and a thickness of 2 mm. Sahasrabudhe et al. [74] demonstrated that the direct deposition of Ti-6Al-4V on a Stainless Steel substrate was possible for a limited number of layers. Indeed, increasing the number of layers a brittle intermetallic phase occurred on the interface between the two different materials and the realized part broke in correspondence of the base. Nevertheless, in this case, the experimental analysis was focused on the formation of micro-features through the deposition of only one layer, ensuring the integrity of the final part in terms of bonding between deposited Ti-6Al-4V and AISI 316L substrate.

The experimental process parameters employed for this experimental investigation were the specific energy (I), laser power (P), and the number of passes per layer (n°p). The experimental plan was designed taking into account three levels for I, seven for P, two for n°p and three repetitions for each combination of factors (see Table 5.1). An overall of 126 single layer circles were realized to complete the experimental tests.

Process parameter	**Min value**	**Max value**	**Step**	**Total levels**
specific energy (J/mm^2)	24	72	24	3
laser power (W)	18	30	2	7
number of passes for layer	5	10	5	2

Table 5.1 Experimental plan.

In DLMD, the specific energy is defined as:

$$I = \frac{P}{Fd}$$

Equation 5.1

where F is the laser scan speed (mm/s) and d is the laser spot diameter (mm). Since I and P were two factors of the designed experimental plan, F was adapted for each combination of process parameters according to Eq. (5.1). In this study, the energy density defined as E_d = P / d (Equation 2) was not explicitly expressed since it is well represented by the laser power behaviour when the laser spot diameter is kept constant.

A constant powder feed rate of 3.2 mg/s and a constant preheating substrate temperature of 200° C were employed during the experimental plan. The laser (a continuous fibre laser YLM 100 WC, IPG, wavelength: 1030 nm) with a constant spot diameter of 60 µm was focused at 4.19 mm from the nozzle outlet, whereas the substrate was located at 4.39 mm (see Fig. 5.1).

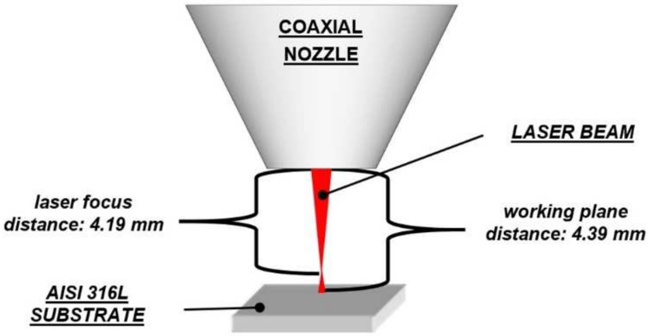

Figure 5.1 Working plane distance employed in the experimental test.

For each substrate, thirty single-layer circles were realized following the order showed in the Figure 5.2.

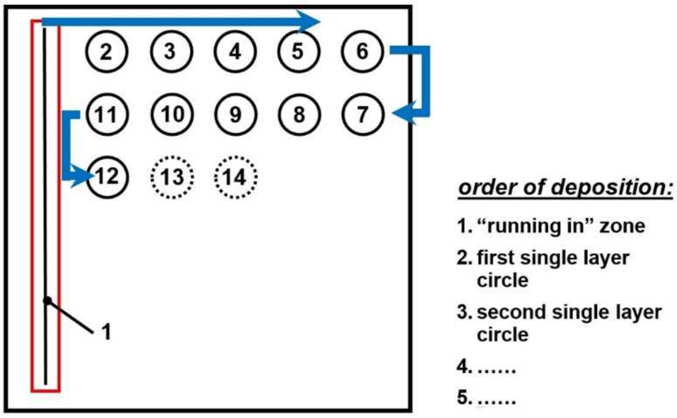

Figure 5.2 "Running in" zone and deposition order of the single-layer circles.

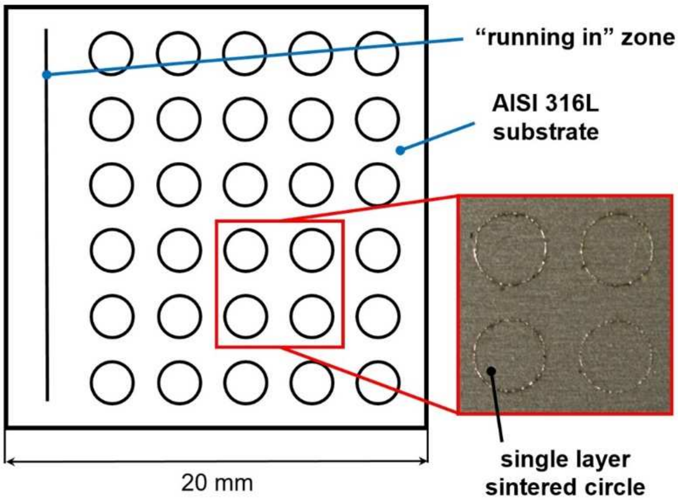

Figure 5.3 Configuration of the artefact deposition.

As showed in Figure 5.2 and 5.3, before starting with the single layer circles manufacture, a “running in” zone was scheduled for each substrate. This zone was required to locally increase the temperature field of the substrate surface before starting with the deposition of the first single layer circle. If a “running in” zone was not designed, the deposition of the first circle would occur with a local starting surface temperature too low in comparison with the other starting temperatures of the following circles. The deposition of a “running in” zone was supposed to ensure more uniform thermal conditions at the beginning of each single layer circles realization.
All the samples were cleaned after the deposition in Acetone and deionized water solution using an ultrasonic cleaner.

5.2.2. Micro-feature considerations

The realized single-layer micro-features were single-layer circular ribs with a diameter of 2 mm and a track nominal width equal to the laser spot. The circular geometry was chosen to allow a constant interaction between the laser beam and the metal substrate surface keeping a constant speed and avoiding local and sudden decelerations or accelerations which might occur in presence of sharp feature (e.g. 90 degree angles in square ribs). The presence of these rapid changings in the laser beam motion usually affect the temperature distribution field on the substrate surface locally, causing heat accumulations and altering the molten pool size. The local change in the molten pool size during the DLMD process may cause an excess in the deposited bead height (during the laser decelerations) or in a lack of deposition (during the laser accelerations), deteriorating the continuity and integrity of the deposited track and making more difficult their evaluation.

5.2.2. Micro-feature characterization

The final quality of the single-layer circles was evaluated in terms of layer continuity, integrity, width variation, and presence of undesired powder accumulations deteriorating the Ti-6Al-4V micro-feature integrity. The measure instrument employed to characterized the micro-part was a FEI Quanta 450 ® Scanning Electron Microscope (SEM) through the ETD and BSED detectors (see Chapter §2.3.1).
Concerning the single-layer Ti-6Al-4V showing a continuous and significant metal bead formation, a preliminary evaluation of the final layer height was provided employing a Sensofar Neox 3D ® Optical profilometer equipped with 20x lens (see Chapter §2.3.2). Eight measurements for each deposited circles were carried out to characterize the mean value of the layer height (see Figure 5.4).

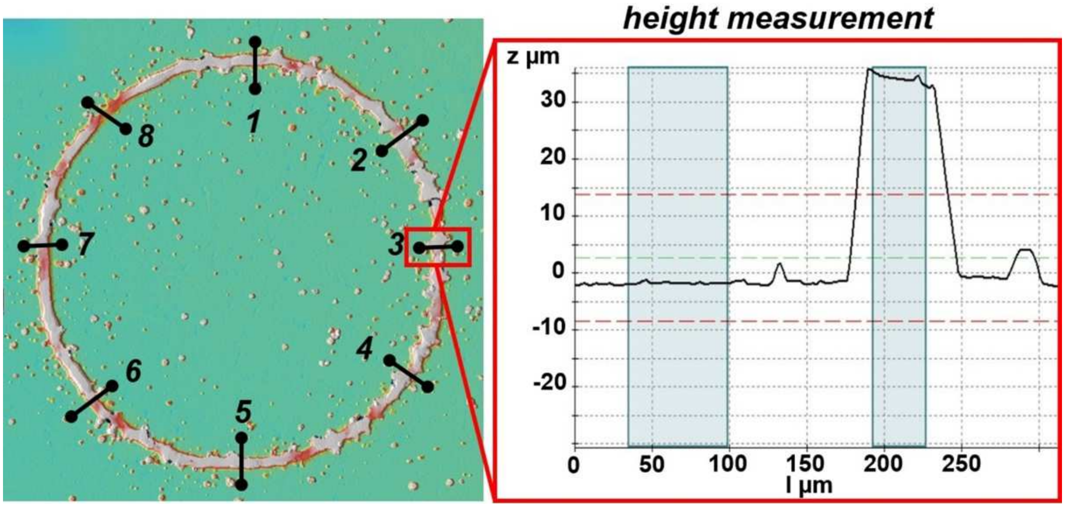

Figure 5.4 Measurements of the micro circle height.

In order to evaluate the layer cross section, the single-layer circles were cross sectioned along their diameter, embedded in a graphitic resin, polished and analysed by SEM imaging.

5.3. Results and discussion

The designed experimental plan showed a strong influence of I, P, and n°p on the final accuracy, integrity and cross section shape variation of the deposited layer. The overall quality of the single-layer circular ribs and the cross section variation of the deposited track were analysed separately and the results are discussed in the following subchapters.

5.3.1. Single layer quality

The integrity of the single-layer micro-features was evaluated analysing the continuity, the width, and the presence of undesired powder accumulations deteriorating the accuracy of the deposited tracks. A preliminary layer height evaluation of the successful single-layer circles was also provided.

All the three process parameters taken into account during the experimental plan showed a strong influence on the final quality of the deposited layer.

Concerning the track accuracy, the continuity of the metallic bead increased with the laser power. At constant I and n°p, for laser power lower than 24 W the deposited tracks resulted strongly discontinuous with the formation of numerous coarse metal masses along the laser path (see Fig. 5.5).

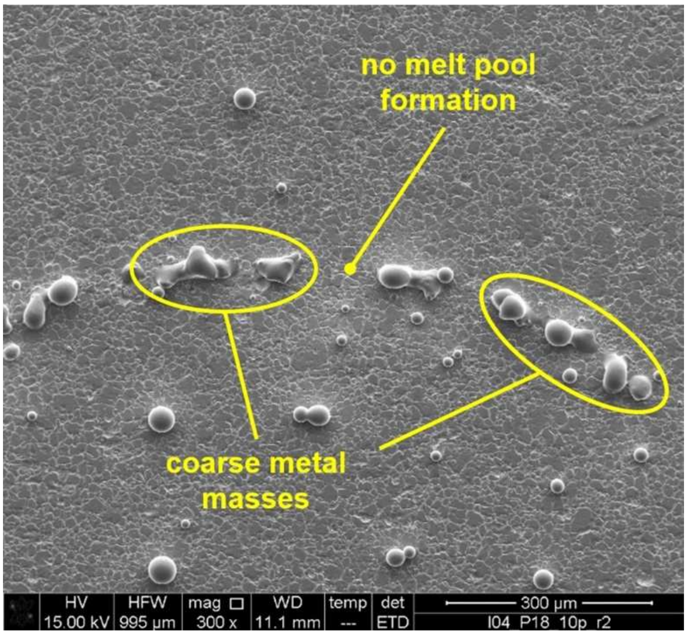

Figure 5.5 Discontinuous track (I = 72 J/mm^2, P = 18 W, n°p = 5).

This phenomenon happened was attributed to the moderate laser energy reaching the substrate surface and mainly dissipated by the metal powder particle attenuation, scattering, and absorption. For laser power lower than 24 W, the energy supplied by the laser beam was not sufficient to cover the energy loss and property melt the surface allowing the formation of an appropriate molten pool (see Fig. 7). Figure 5.5 shows that for P equal to 18 W and I of 72 J/mm^2 no remelting was possible along the laser path.
The track continuity improved increasing the laser power. For P higher than 24 W, the deposited layer became continuous and more significant.

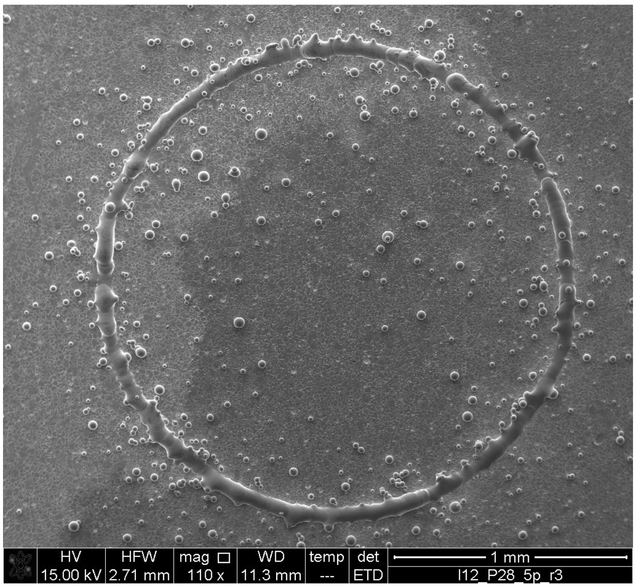

Figure 5.6 Single-layer circular rib realized with I = 72 J/mm^2, P = 28 W, n°p = 5.

Figure 5.6 shows how for P = 28 W the metallic bead was consistent without discontinuities or presence of coarse metal masses along the laser path.
The layer continuity improved with the specific energy too. Increasing I from 24 to 72 J/mm^2, the process window became wider and the sintered bead became more significant (see Fig. 5.7).

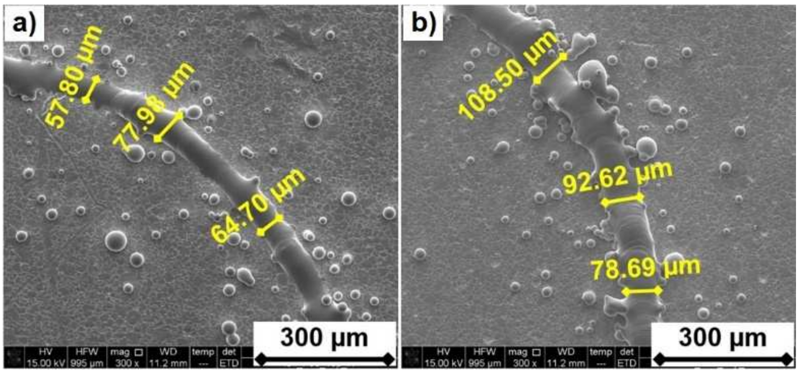

Figure 5.7 a) I = 24 J/mm^2, P = 30 W, n°p = 10; b) I = 72 J/mm^2, P = 30 W, n°p = 10.

This happened because at constant P and d, an increment in the specific energy produced a reduction in the laser scan speed (see Eq. 1), enlarging the exposure time of the laser on the surface. Therefore, for a constant energy density (see Eq. 2), a bigger number of powder particles fell inside the melt pool when the specific energy was at higher levels, improving the continuity and the uniformity of the deposition also for a number of passes per layer equal to 5. Figure 5.8 shows a continuous sintered track for P = 26 W and n°p = 5 when I is equal to 48 J/mm^2.

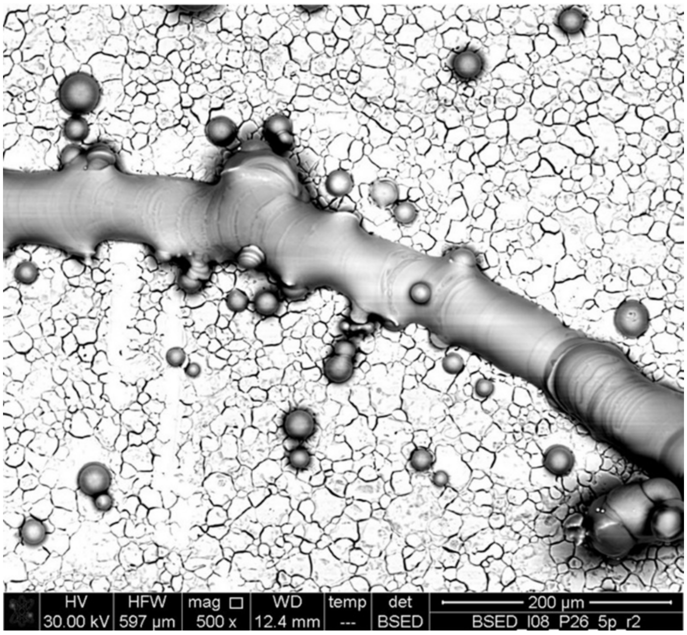

Figure 5.8 I = 48 J/mm^2, P = 26 W, n°p = 5 (BSED image).

On the contrary, for low specific energy (i.e. high laser scan speed) continuous depositions were possible only increasing the number of passes per layer (see Fig. 5.9).

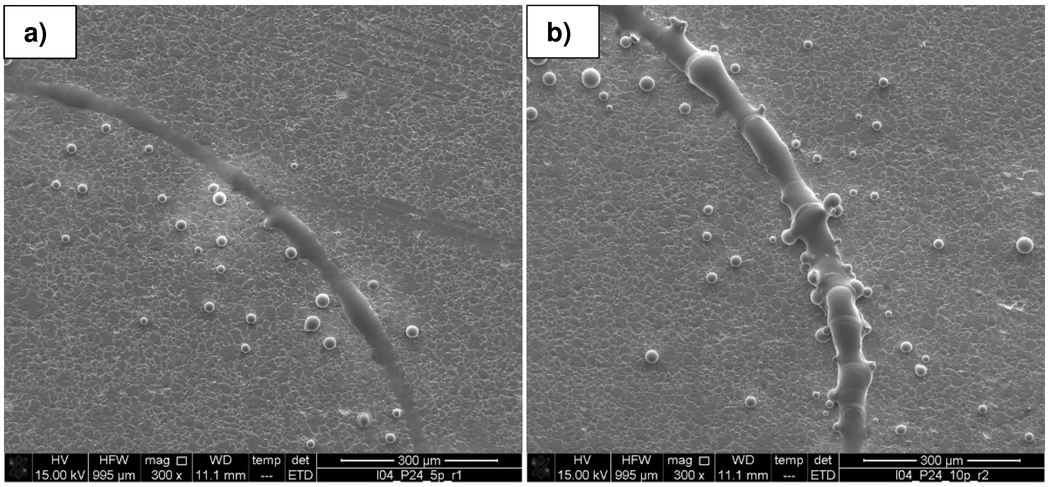

Figure 5.9 a) I = 24 J/mm^2, P = 24 W, n°p = 5; b) I = 24 J/mm^2, P = 24 W, n°p = 10.

Increasing the number of passes the track continuity improved. At constant I and P, 10 laser passes involved sintered beads more relevant. This behaviour is directly related to the increase of the powder particles provided to the molten pool during the process. In fact, at higher levels of n°p, the low efficiency in the powder deposition of the feeding system discussed in the Chapter §4 was partially overcome and more particles were injected into the molten pool thanks to the repeated laser passes per layer (see Fig. 5.10).

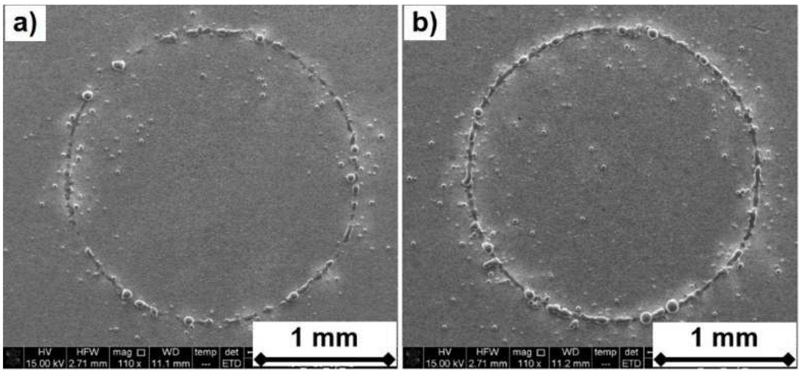

Figure 5.10 a) I = 24 J/mm^2, P = 20 W, n°p = 5; b) I = 24 J/mm^2, P = 20 W, n°p = 10.

Nevertheless, if a high number of passes per layer is followed by a high level for I and medium low levels for P, the accuracy of the single-layer circular ribs strongly deteriorated. For a P ranging between 20 and 24 W, I of 72 J/mm^2, and n°p of 10, the process was not capable to melt the substrate surface and the amount of powder particles provided by the deposition nozzle correctly. In this case, the excess of powder particles that did not fall inside the molten pool, remained close to the track edges and adhered to the semi-solid metal bead, building up a large amount of powder accumulations compromising the integrity of the sintered track. The formation of these powder piles could be so pronounced to exceed the layer height and adversely affect the geometry of the deposited layer. Moreover, in some cases, the large presence of partially-melted powder particles could be so destructive to deviate the metallic bead from the regular path imposed by the laser beam and compromise the structural integrity of the micro-feature (see Fig. 5.11).

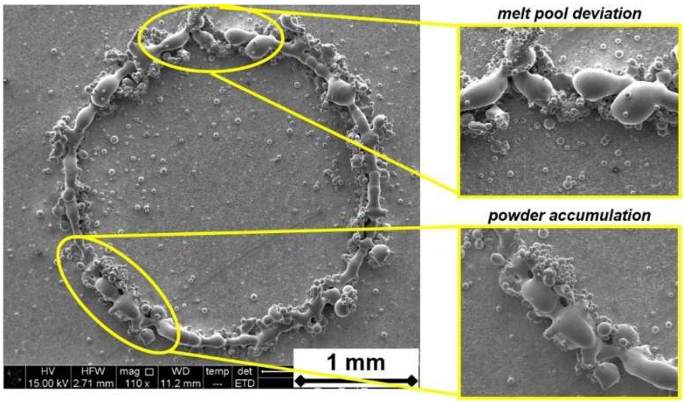

Figure 5.11 Accuracy degradation of the single-layer circular rib (I = 72 J/mm^2, P = 22 W, n°p = 10).

Figures 5.12 and 5.13 provide a qualitative evaluation of the realized single-layer circles. The colored dots represent an average evaluation of the three repetitions for each combination of process parameters. The meaning of each colored dot illustrated into the two Figures is here summarized:

- a red dot indicated a sintered track strongly discontinuous with a very low or completely absent remelting of the substrate along the laser path;
- an orange dot indicated a sintered track with a well defined edges and geometry without powder accumulations along the edges but with some discontinuities along the metallic bead;
- a green dot indicated a powder accumulation free track with a continuous and well defined bead;
- a blue dot indicated a deposited track with a strong presence of partially molten powder accumulations along the track edges.

As shown in Figure 5.12, continuous and powder agglomeration free tracks were obtained for P between 24 and 30 W when high values for I and low values for n°p were employed. For specific energy of 24 J/mm^2 and 5 passes for layer, the single-layer circular ribs strongly resulted discontinuous for all the levels of laser power taken into account during the experimental analysis. In this case, the energy provided during the process was not sufficient to cover the energy dissipations and properly melt the surface ensuring a correct melt pool formation. On the contrary, for 10 passes for layer (see Fig. 5.13), the process window was larger and well defined tracks were generally obtained for specific energy between 24 and 72 J/mm^2 and P higher than 24 W. For laser powers lower than 24 W, the single-layer sintered circles resulted generally discontinuous even if the number of passes for layer were increased up to 10. Moreover, the zone where a strong track deterioration occurred was well defined for I = 72 J/mm^2, P = 20-24 W, and n°p = 10.

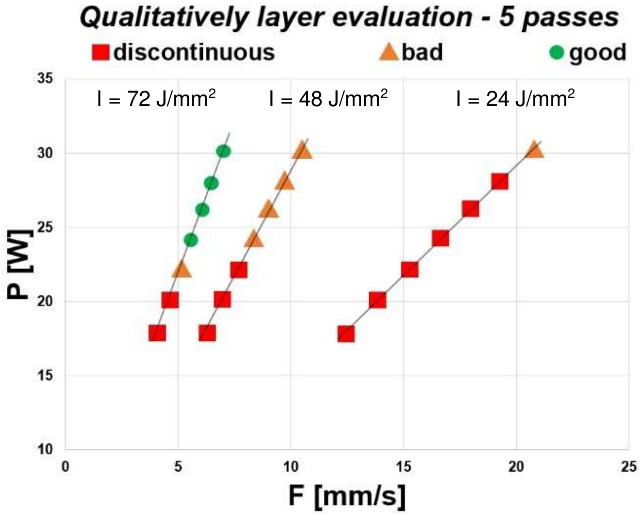

Figure 5.12 Single-layer process map at 5 passes.

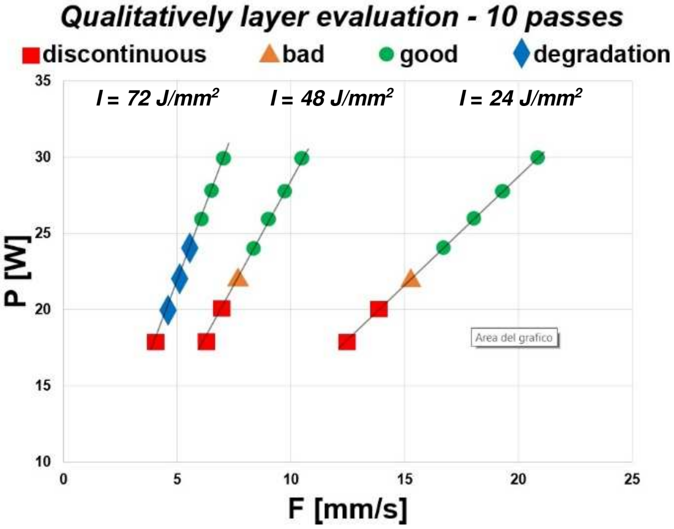

Figure 5.13 Single-layer process map at 10 passes.

Table 5.2 summarizes the experimental results for the single-layer circular ribs defined in the Figure 5.12 and 5.13 and underlines the strong influence of the three process parameters on the track integrity and width (see Fig. 5.14).

I $[J/mm^2]$	*P [W]*	*F [mm/s]*	*qualitatively layer evaluation at n°p = 5*	*qualitatively layer evaluation at n°p = 10*	*$width_{AVG}$ at n°p = 5 [µm]*	*$width_{AVG}$ at n°p = 10 [µm]*	*$height_{AVG}$ at n°p = 5 [µm]*	*$height_{AVG}$ at n°p = 10 [µm]*
24	18	12.5	discont.	discont.	nd	nd	nd	nd
24	20	13.89	discont.	discont.	nd	nd	nd	nd
24	22	15.28	discont.	discont.	nd	nd	nd	nd
24	24	16.67	discont.	good	nd	55	nd	20
24	26	18.06	discont.	good	nd	54	nd	21
24	28	19.44	discont.	good	nd	59	nd	18
24	30	20.83	bad	good	nd	64	nd	22
48	18	6.25	discont.	discont.	nd	nd	nd	nd
48	20	6.944	discont.	discont.	nd	nd	nd	nd
48	22	7.639	discont.	bad	nd	nd	nd	nd
48	24	8.333	bad	good	nd	64	nd	23
48	26	9.028	bad	good	nd	69	nd	30
48	28	9.722	bad	good	nd	80	nd	39
48	30	10.42	bad	good	nd	79	nd	31
72	18	4.17	discont.	discont.	nd	nd	nd	nd
72	20	4.63	discont.	deteriorate	nd	211	nd	nd
72	22	5.09	bad	deteriorate	nd	179	nd	nd
72	24	5.56	good	deteriorate	62	136	26	nd
72	26	6.02	good	good	70	69	24	63
72	28	6.48	good	good	77	77	25	53
72	30	6.94	good	good	77	95	32	42

Table 5.2 Results of the experimental investigation (discont = discontinuous; nd = not defined).

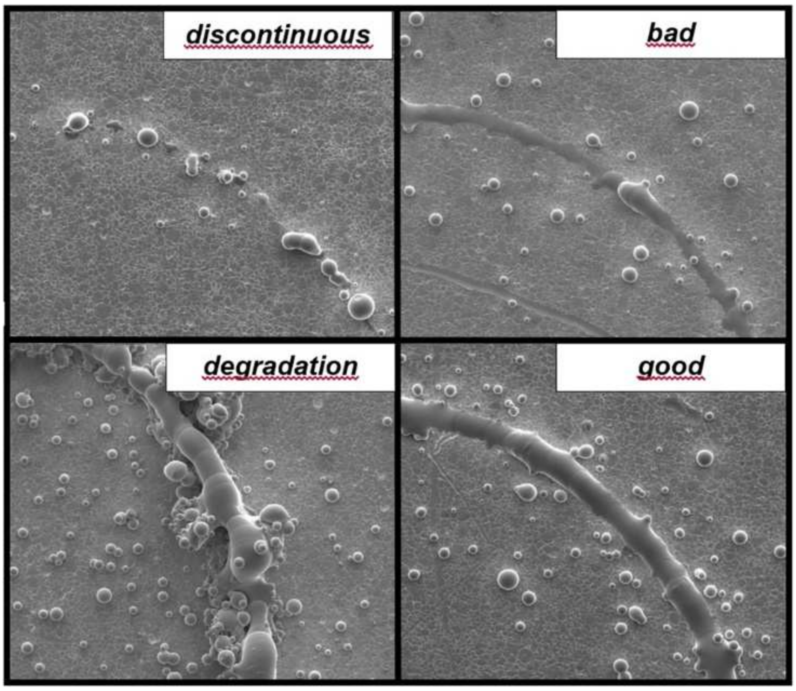

Figure 5.14 Qualitative evaluation of the single-layer circular ribs.

For discontinuous deposited tracks it was not possible to measure and characterize the width due to their strong bead discontinuities and deteriorated structural integrity. Therefore, only the width of the deposited layer with a significant and continuous metallic bead was possible to detect and report in Table 5.2.

The results showed a width variation from a minimum of 54 µm to a maximum of 211 µm in average, depending on the process parameter combination employed during the process. In particular, for the powder accumulation free tracks (represented by the green dots in Figure 5.12 and 5.13), the metallic bead was well defined and the corresponding width ranged between 54 µm to a maximum of 95 µm in average. An increase of I, P, and n°p caused an increment in the track width. At constant P of 30 W and n°p of 10, increasing I from 24 to 72 J/mm^2 the width passes from 64 to 95 µm in average. The same happened with P. At constant I = 48 J/mm^2 and n°p = 10, an increase in P from 24 to 30 W causes an increment of the track width from 64 to 79 µm.

The width exceeded the 95 µm when the combinations of process parameters belonged to the deteriorating zone represented by the blue dots (I = 72 J/mm^2, P = 20-24, n°p = 10). In this case, the track enlarged up to 175 µm in average due to the strong presence of partially melted powder particles along the edges of the metallic bead.

In addition, the specific energy and the number of passes per layer demonstrated a strong influence on the final height variation of the realized micro features. The final height of the single-layer circles was ranging between 20 and 63 µm in average (see Table 5.2). Moreover, at constant P, increasing I and n°p the layer height increased. On the contrary, the laser power did not show a great influence on the increasing of the sintered bead.

5.3.2. Cross section of the deposited track

The track cross section analysis was carried out to understand how the shape of the molten pool and the heat affected zone (HAZ) depended on the process parameters variation, initial surface conditions, and presence of partially melted powder particles adhered along the edges of the sintered track. This investigation was of extremely importance since the geometry of the first deposited layer affected the successive deposition of the next layers required to build a 3D micro part.
The analysis of the cross sectioned circular ribs showed a strong influence of the initial surface conditions and of the powder particle adhesion along the track edges on the final shape of the sintered bead.

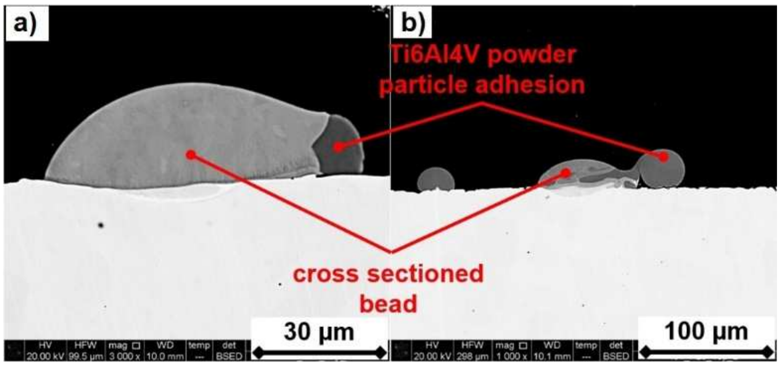

Figure 5.15 Cross-section of the deposited track: a) I = 24 J/mm^2, P = 28 W, n°p = 10; b) I = 24 J/mm^2, P = 28 W, n°p = 10.

As illustrated in Figure 5.15, the powder particles which did not directly participate to the bead formation, stuck along the track edges affecting the cooling rate of the molten pool and causing a deformation on the final cross section shape of the metallic bead. This deformation locally modified the height and the width of the sintered track, affecting the uniformity of the deposited layer (see Fig. 5.16).

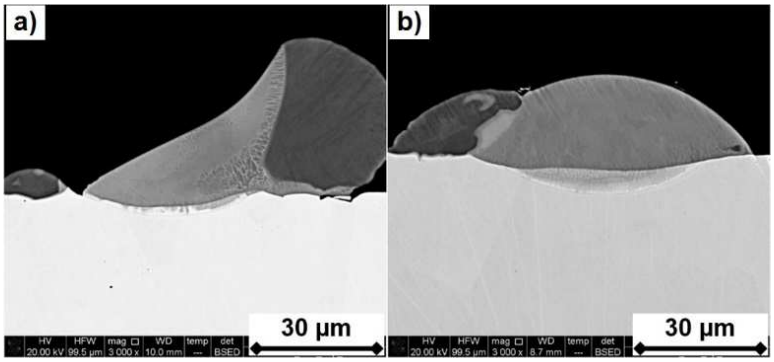

Figure 5.16 Influence of the un-melted powder particles on the final cross sectional shape of the deposited tracks: a) I = 24 J/mm^2, P = 24 W, n°p = 10; b) I = 48 J/mm^2, P = 30 W, n°p = 5.

The presence of powder particles along the track edges were a consequence of the low nozzle deposition efficiency (see Chapter §3) and of the powder particle size that was very close to the laser spot diameter (powder grain size between 20 and 45 µm with a laser spot of 60 µm). The combination of these two effects did not ensure a high presence of powder particles falling into the molten pool, but part of them fell close to it deteriorating the continuity and uniformity of the sintered track.

Another factor that affected the cross section shape of the sintered bead strongly was the starting surface conditions. Coarse surface roughness and the presence of local grooves or peaks that could locally modify the geometry and planarity of the surface, could impact the formation of a correct molten pool. For constant process parameters, Figure 5.17 shows how HAZ was strongly altered by the initial surface conditions. The presence of superficial grooves or peaks locally modified the incidence angle of the laser, affecting the geometry of the HAZ and consequently the final shape of the sintered bead cross section. Figure 5.17 shows how the depth and the penetration depth of HAZ drastically changed depending on the starting superficial conditions of the AISI 316L substrate.

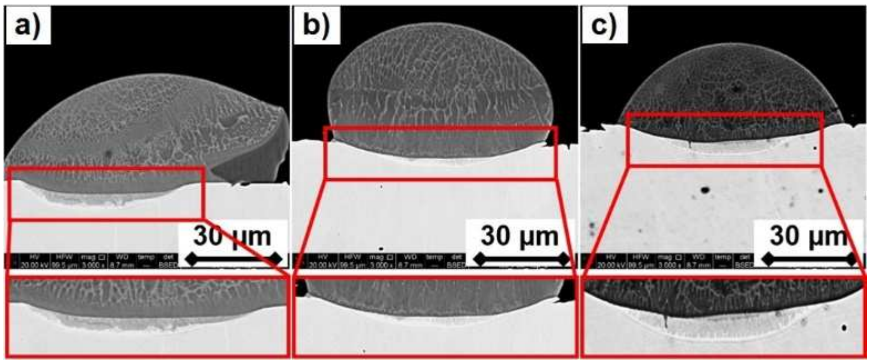

Figure 5.17 Different HAZ for the same process parameters: I = 48 J/mm^2, P = 30 W, n°p = 10.

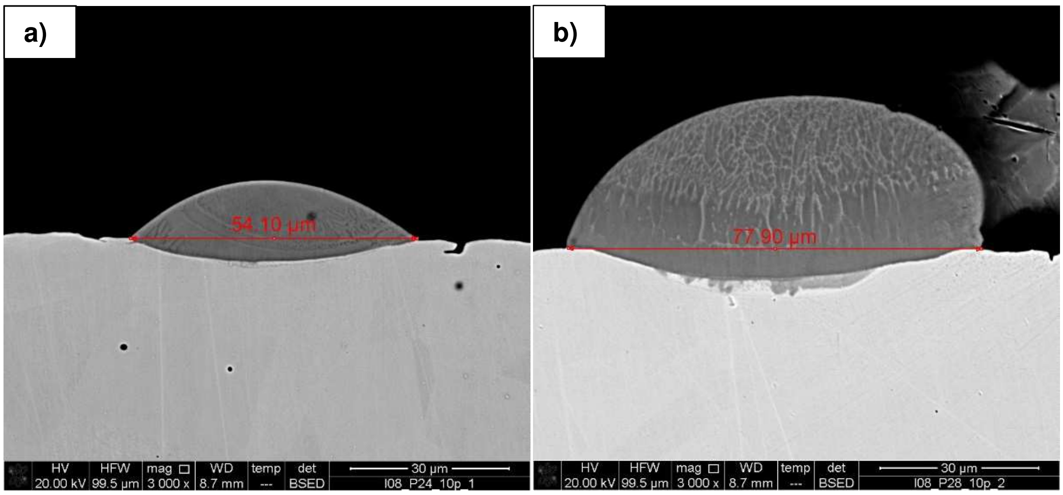

Figure 5.18 a) I = 48 J/mm^2, P = 24 W, n°p = 10; b) I = 48 J/mm^2, P = 28 W, n°p = 10.

The cross section analysis also confirmed the results explained in the previous Chapter §5.3.1. Figure 5.18 shows that with an increase of P from 24 W to 28 W, the bead width increased from 54 µm to 78 µm in average. The same effect was showed increasing I and n°p.
In particular, Figure 5.19 shows what happened at the cross section of the deposited track when the process parameters met the zone of strong deterioration of the process window. In this case, the shape of the molten pool was strongly affected by the partially melted powder particles adhering to the metallic bead edges. The geometry of the cross section was strongly irregular and jagged along the edges, deteriorating the stability and accuracy of the deposited layer and preventing a correct control on the deposition process and on the micro-feature realization.

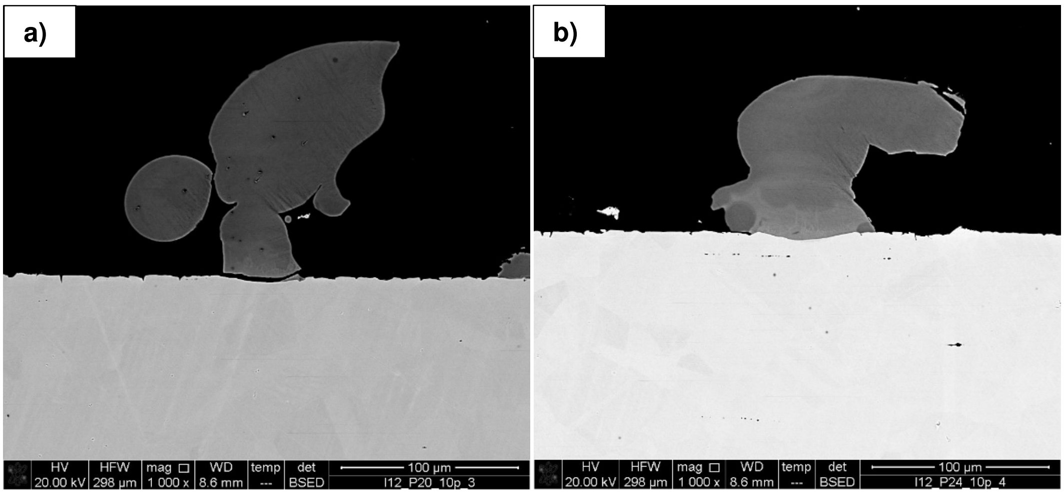

Figure 5.19 a) I = 72 J/mm^2, P = 20 W, n°p = 10; b) I = 72 J/mm^2, P = 24 W, n°p = 10.

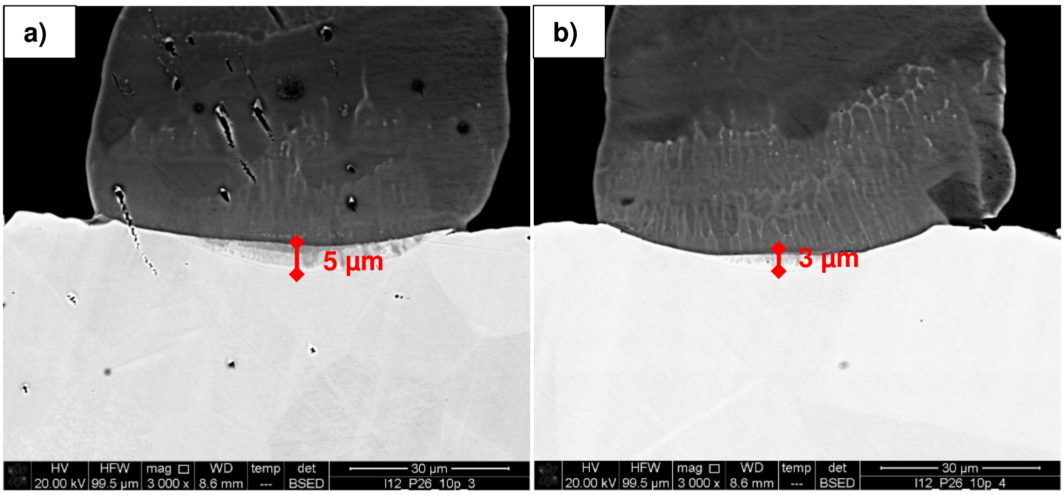

Figure 5.20 Different HAZ penetration for I = 72 J/mm^2, P = 28 W, n°p = 10.

Moreover, I, P, and n°p showed an important influence on the HAZ formation and extension. For high level of P, the penetration depth was deeper reaching a maximum penetration depth ranging between 5 and 6 µm in average. For deeper HAZ zone, the dilution area between Ti-6Al-4V and AISI 316L Stainless Steel was higher. Nevertheless, the shape, onset, and extension of the HAZ strongly depended on the starting surface conditions of the substrate.

Figure 5.20 shows that for constant process conditions (I = 72 J/mm^2, P = 28 W, n°p = 10), the HAZ extension varied from 5 µm to 3 µm due to the different status of the surface.

5.4. Conclusions

In this study, the influence of specific energy, laser power, and number of passes per layer on the formation of the first deposited layer in micro DLMD process was analyzed. The final quality of the single-layer circles was evaluated in terms of accuracy, integrity of the deposited track, and cross section variation of the metallic bead. The main results obtained can be summarized as follows:

- I, P, and n°p strongly affected the first deposited layer continuity and integrity;
- for P lower than 24 W, the energy provided by the laser beam was not sufficient to cover the energy dispersions and property create a melt pool;
- at constant I and n°p, an increase in P determined sintered track more continuous and wider;
- increasing I and n°p the process window became wider;
- for I = 72 J/mm^2, n°p = 10, and P ranging between 20 and 24 W an instability zone was met and the single layer circles accuracy and integrity strongly deteriorated with an excess in powder accumulations along the track edges;
- continuous and significant deposited layer showed an average width between 54 and 95 µm and an average height between 20 and 63 µm;
- bead cross section variation strongly depended on the initial surface conditions and on the efficiency in the powder deposition;
- grooves and peaks could modify the HAZ affecting the bead formation
- presence of partially melted powder particles stuck along the sintered track edges locally modified the shape of the bead affecting the uniformity in height and width of the deposited layer.

Chapter 6

Comparison between OPL and MPL building approach in micro DLMD

This Chapter deals with the comparison between the two different building approaches defined in the Chapter §4.

The influence of the DLMD process parameters in combination with the two building approaches is investigated on the realization of micro thin square ribs. The influence of laser power, laser scan speed, and powder mass flow rate on the final dimensional accuracy of the micro-features is analysed. Moreover, the *Balling phenomenon* is investigated and its onset is correlated to inappropriate settings of the process parameters.

Very good results in terms of final accuracy of the micro-features are obtained with the MPL building approach employing low values for the laser power.

6.1. Introduction

As for every AM technology, one of the main issues still open in DLMD process regards the final accuracy and quality achievable for the manufactured components. The high tolerances and the poor surface roughness characterizing the metal DLMD parts confine the full success of this technology and its wide employment in the industrial sector. A deep comprehension of the influence of the process parameters on the overall final quality of the artefact is fundamental to get components with a good surface and structural integrity.

Several Authors investigated the complex relationship which exists between DLMD process parameters and final properties of the artefact. According to Ma et al. [75], high dimensional accuracy and surface finishing are possible when a small diameter of the laser spot and a small thickness of the single deposited track are employed. Zhu et al. [53] demonstrated that a uniform growth of the sintered thin walls is obtained when the laser focus is located above the substrate.

In the scientific literature, the effect of the main process parameters on the dimensional and geometrical accuracy of the final part is deeply dealt for application of the DLMD to regular-scale part fabrication [54, 76, 77]. To the best of Author’s knowledge, no investigation is available in literature for applications of DLMD to the micro-scale, where a very fine laser spot and a low powder feed rate are utilised.

In this experimental investigation, the relationship between laser power, laser scan speed, powder mass flow rate, and building deposition approach is investigated when DLMD is applied at the micro-scale. The final quality of AISI 316L Stainless Steel micro square ribs is evaluated in terms of dimensional and geometrical accuracy of the deposited tracks. Moreover, the *Balling phenomenon* [70, 72, 78] is analysed and its onset is correlated to inappropriate settings of the process parameters.

6.1.1. *Balling phenomenon*

Balling (called also *spheroidization*) is an undesirable phenomenon that may occur in Direct Laser Deposition processes. It consists in the formation of isolated or grouped spherical droplets which deteriorate the quality of the realized part in terms of dimensional accuracy and structural integrity. The size of these solid droplets can vary from few tens to hundreds microns, exceeding the dimension of the laser spot and spreading out the deposited metal track (see Fig. 6.1).

This phenomenon was deeply analysed in Selective Laser Melting (SLM). Here, *Balling* occurs when the melted material is unable to fully wet the substrate because of surface tension and results from a combination of laser deposition parameters which is inappropriate to the particular powder material properties [70, 72]. *Balling* can seriously limit the quality of the produced part due to the decrease of density, uncontrolled porosity, instability of track dimension, poor inter-track bonding, high surface roughness and reduced dimensional accuracy [79, 80]. The *Balling phenomenon* was investigated by several Authors with reference to in SLM process. Tolochko et al. [72] proved that this phenomenon strongly depended on irregular laser heating conditions and it could be avoided by limiting the laser power. Gu et al. [70] identified two kinds of *Balling* in the SLS of pre-alloyed 316L SS powder: the first one was caused by a restricted liquid formation due to a low laser power, and the second one by laser-induced melted splashes due to a high scan speed. Gu and Shen also analysed the *Balling phenomenon* in SLS of Cu-based metal powders [78]. In this case, three kinds of *Balling* mechanism were observed: (i) *"first line scan balling"* which was induced by the high thermal gradient between the cold powder bed and the melt; (ii) *"shrinkage-induced balling"* that was due to a high scan speed, and (iii) a *"self-balling"* which was caused by the combination of a high laser power and a low scan speed (see Fig. 6.2).

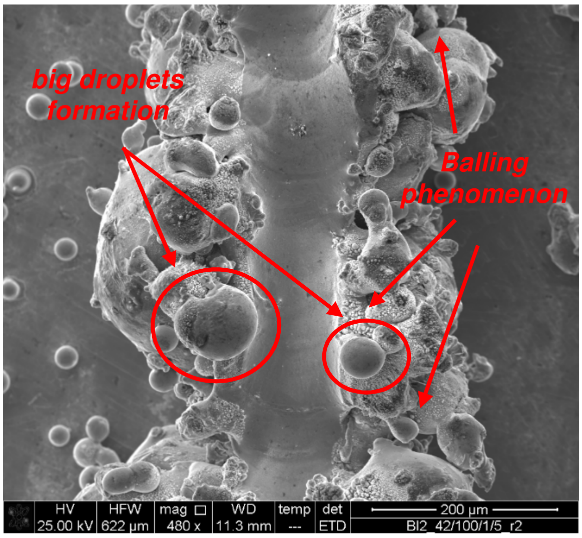

Figure 6.1 Example of *Balling phenomenon* in micro DLMD process.

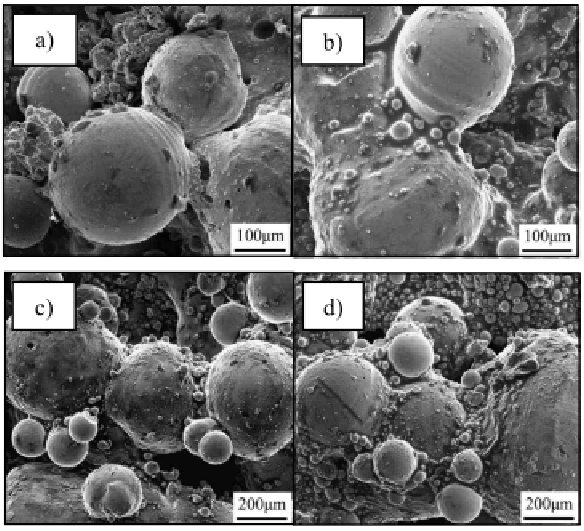

Figure 6.2 Different mechanisms in balling formation in SLS: a) first line scan balling, no preheating temperature; b) first line scan balling, 100°C preheating temperature; c) shrinkage-induced balling; d) self-balling [78].

To the best of Author's knowledge, no investigation on this phenomenon is available in literature for the DLMD process. Because of the powder flux coaxial to the laser beam, in DLMD the process control is more complex than in SLS where the powder is deposited layer by layer.

6.2. Realization of AISI 316L micro features employing the OPL building approach

In this Section, the OPL building approach (One Pass per Layer) is assumed and the influence of the chosen DLMD process parameters on the dimensional and geometrical accuracy of the metal micro-artefact is analysed.

6.2.1. Material & methods

6.2.1.1. Experimental procedure

The micro DLMD system employed during the experimental plan was the Manudirect ® MSL50 (see Chapter §2.1). The metal powder was AISI 316L Stainless Steel alloy with a grain size ranging between 20 and 25 µm (see Chapter §2.2.1) and the process parameters analysed during the experimental tests were the laser power (P), the laser scan speed (F), and the powder mass flow rate (f) (see Table 6.1).

process parameter	min value	max value
laser power [W]	18	42
laser scan speed [mm/min]	100	500
powder mass flow [mg/s]	0.29	0.57

Table 6.1 Process parameters employed in the experimental plan.

The plan of experiments was designed according to the DOE Full Factorial scheme. Two levels for each parameter and three repetitions for each process combination were taken into account, for a total of 24 metal micro-artefacts. During all the experiments no feedback control on the current height of the deposited layer was activated.

The laser spot diameter was 30 µm focused at 4.69 mm from the nozzle outlet, whereas the working-plane distance of the substrate was set at 4.89 mm. Focusing the laser beam above the metal surface, a positive laser defocusing of +0.2 mm was employed during the experimental tests. Moreover, the vertical displacement of the metal substrate was set at 5 µm after each deposited layer.

At the end of the deposition process, the samples were cleaned in Acetone and deionized water solution using an ultrasonic cleaner to remove the non-sintered powder particles from the substrate.

6.2.1.2. Micro-features considerations

The micro-artefacts were 2mm x 2mm squares with a nominal height of 330 µm and a nominal width equal to the spot of the laser reaching the top of the substrate (see Fig. 6.3). Shape and size of the artefacts were chosen for the reasons that follow:

- the laser was always on working continuously and not discontinuously as for parallel and separate thin walls [75, 53, 81-83];
- with a length of 2 mm of the square rib sides, the thickness variation of the sintered track caused by both the variation of process parameters and the *Balling phenomenon* were easily evaluated;
- in a square rib, the height measurement was more accurate and easy than a in circular one;
- a wall height of 330 µm allowed an accurate and easy evaluation of the height variation and at the same time the consumption of metal powder was limited.

The substrate utilized in the experiments was a 20x20 mm and 2 mm thick AISI 316L Stainless Steel square plate (see Fig. 6.3).

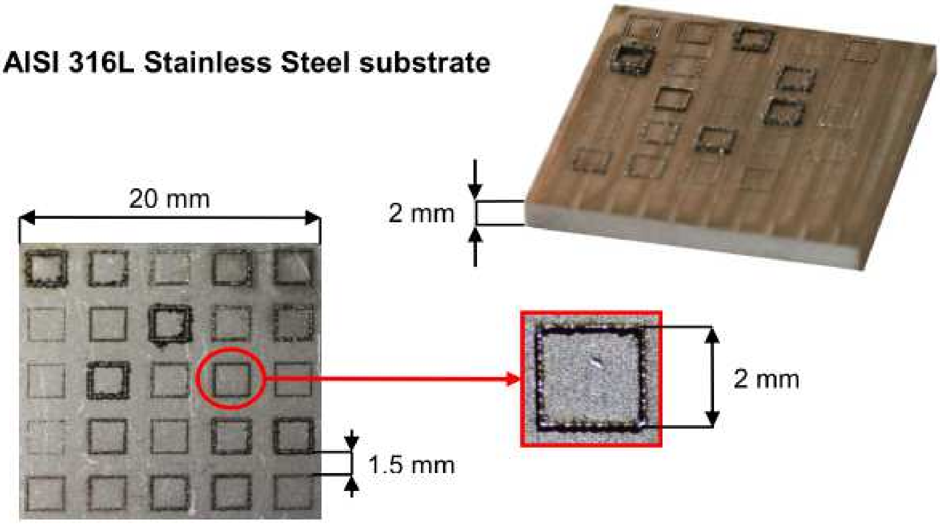

Figure 6.3 Substrate and sintered artefact configuration.

6.2.1.3. Evaluation and characterization

The geometrical accuracy of the micro-artefacts were analysed with both Sensofar Neox 3D ® Optical Profilometer equipped with 20x lens and FEI Quanta 450 ® Scanning Electron Microscope (SEM) introduced in the Chapter §2. At the optical profilometer, three measurements for each side were made to evaluate the mean height of the walls (see Fig. 6.4 a) and the standard deviation of these measurements was utilized to define the growth uniformity of the side walls.
SEM was employed to detect and analyse the *Balling phenomenon*, measuring the relative increase in the track width due to the presence of spherical droplets adhered to the edges of the micro-features. An analysis of the width variation in relation to the process parameters employed during the experimental plan is also provided. Twenty measurements for each sintered square (five for each side) were carried out to evaluate the mean value of the track width (see Fig. 6.4 b).

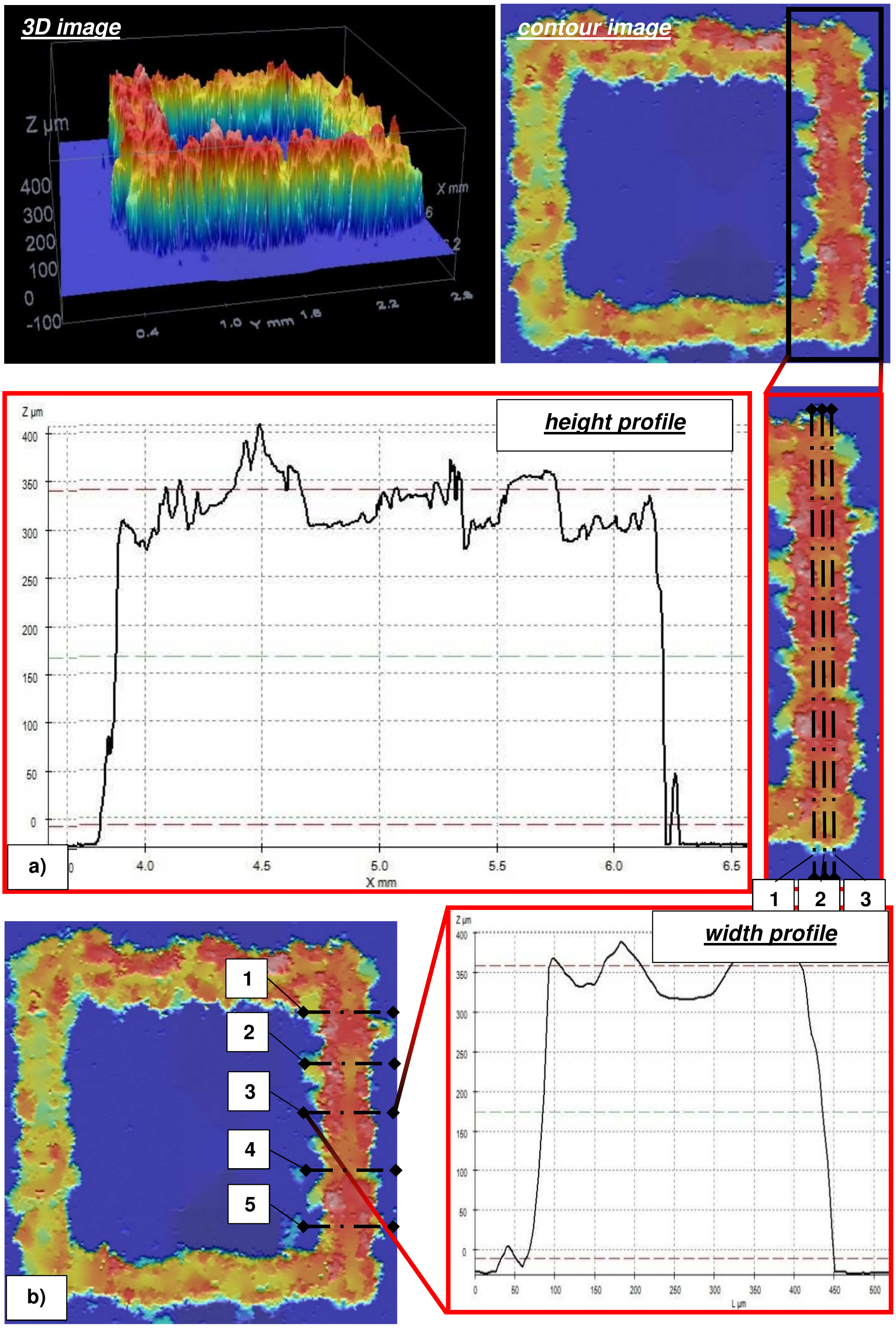

Figure 6.4 a) height profile detection; b) width profile detection (P=42 W; F=100 mm/min; f=0.29 mg/s).

6.2.2. Results and Discussion

Laser power, laser scan speed, and powder feed rate showed a strong influence on the final quality of the realized micro-parts when the OPL building approach was employed. The dimensional and geometrical accuracy of the micro-features was evaluated detecting the difference between the nominal and final height reached by the micro-squares and the track width variation in relation with the onset and extension of the *Balling phenomenon*.

In the following Subchapters, the experimental results are introduced and the influence of the evaluated process parameters on the final accuracy of the micro-DLMD process is discussed in detail.

6.2.2.1. Evaluation of the final height

For the analysis concerning the height variation, the data confidence interval was stated at the 95% confidence level. The actual height was compared with the nominal height of 330 µm and the results are summarised in the Pareto chart of Figure 6.5.

All the three process parameters investigated in the experimental plan were significant. Nevertheless, the Pareto chart indicates that the influence of the laser scan speed on the final height of the micro-features was predominant, with an effect almost double compared to that of the laser power and powder feed rate (see Fig. 6.5).

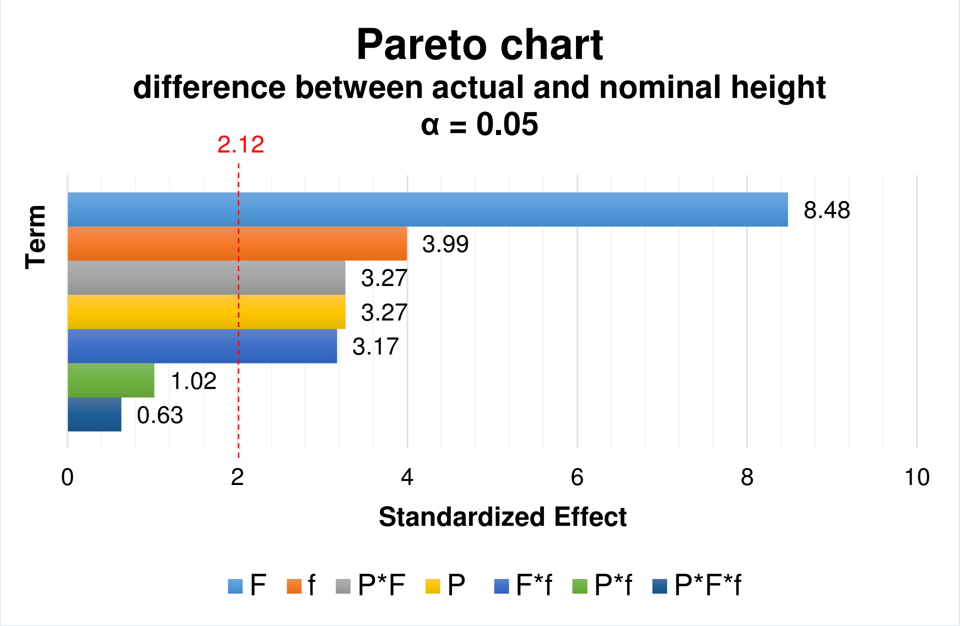

Figure 6.5 Pareto chart.

For the highest level of the laser scan speed employed in the experimental tests (500 mm/min), a very low growth of the micro-square ribs was possible. In this process conditions, the micro-features reached a final height of 15.42 µm in average against the nominal 330 µm imposed during the experimentation (see Fig.

6.6). Moreover, high laser scan speed combined with low powder feeding regime did not allow the formation of a solid and continuous metal bead (see Fig. 6.7).

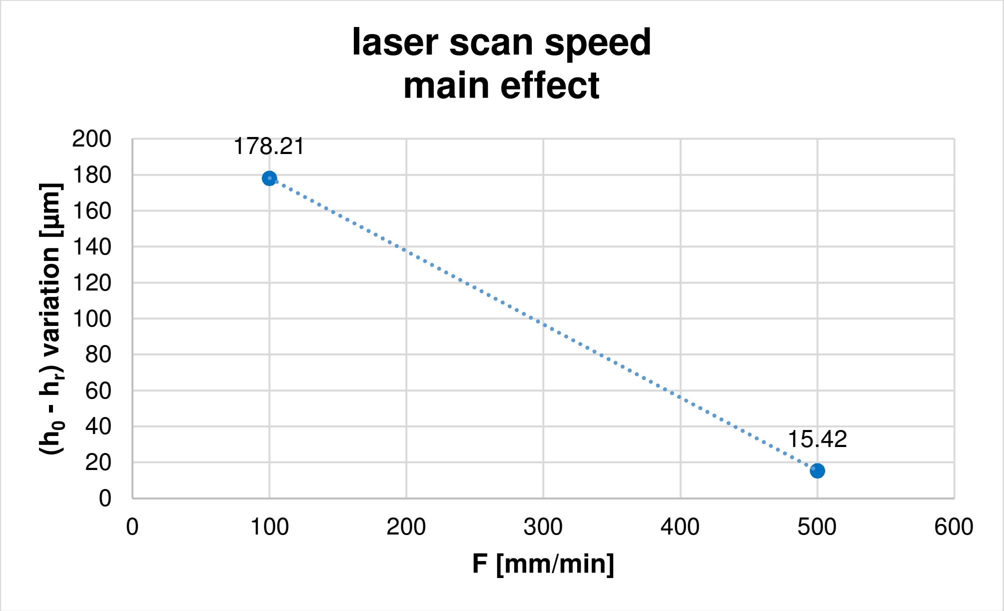

Figure 6.6 Influence of the laser scan speed on the final height of the micro-artefact (h_0 = nominal height, h_r = final reached height of the micro-square).

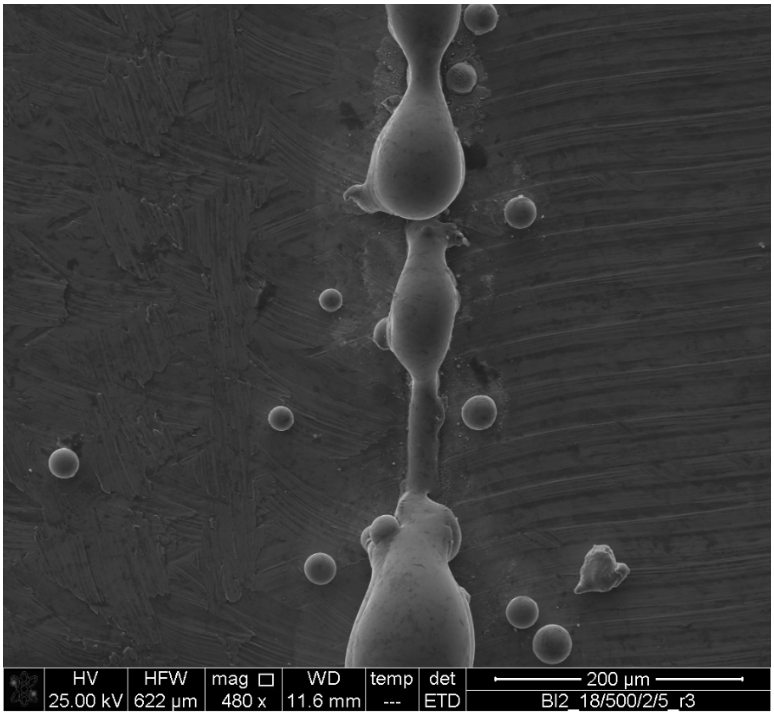

Figure 6.7 Instability in the layer formation at F = 500 mm/min.

This was mainly due to the very short exposure time of the laser beam on the metal surface of the substrate. Indeed, increasing F the exposure time reduced and only a very small portion of the substrate could be melted, limiting the number of powder particles falling into the molten pool and generating a metal deposited track strongly discontinuous. In addition to the high laser scan speed, the low powder deposition efficiency characterizing the micro DLMD process made the formation of a stable metal bead worse. On the contrary, decreasing the laser scan speed up to 100 mm/min and consequently increasing the exposure time of the laser, the final height of the artefact grew up to 178.21 µm in average (see Fig. 6.6). This was because at lower exposure time, the molten pool is larger and more particles get involved in the micro-part realization.

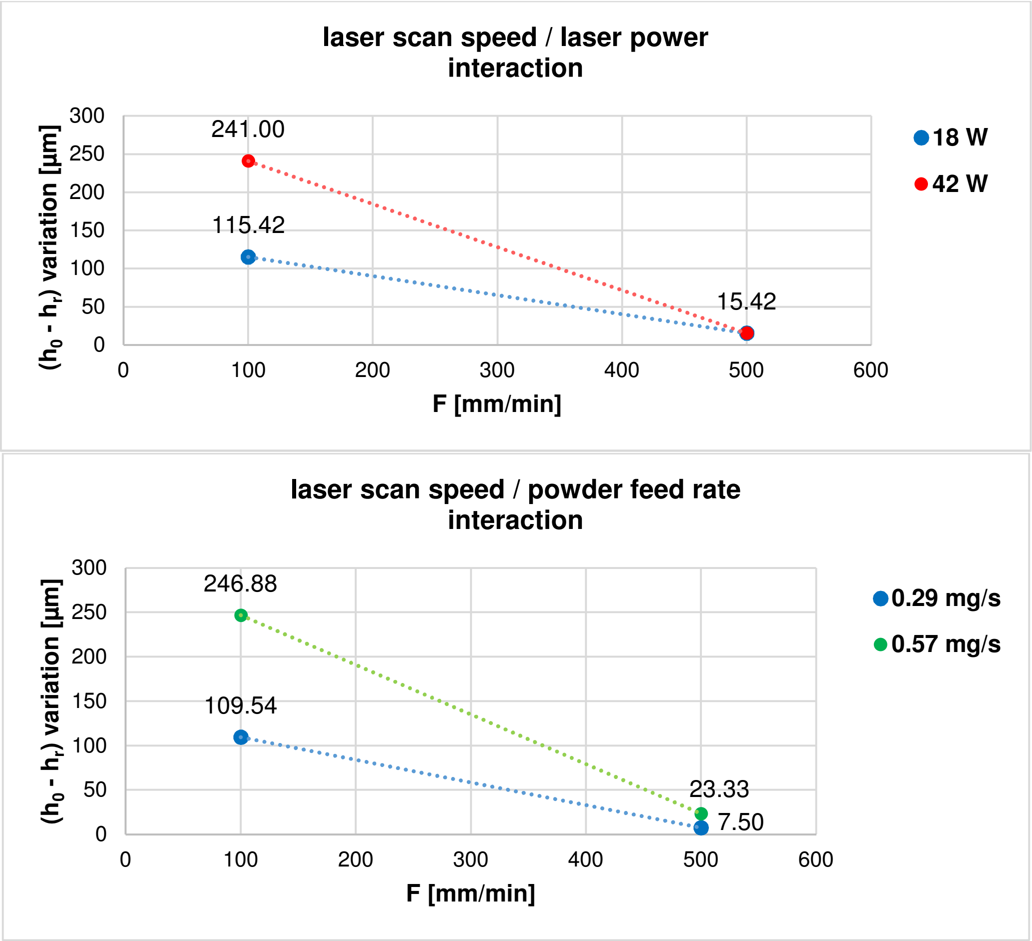

Figure 6.8 a) interaction effect between laser scan speed and laser power; b) interaction effect between laser scan speed and powder feed rate.

The great influence of the laser scan speed was confirmed when the effects of the interactions between the process parameters were analysed. Figure 6.8 a) shows that at the highest laser scan speed the final height of the walls remained very low independently of the levels of the laser power and the powder feed rate. On the contrary, for F = 100 mm/min the influence of the laser power and powder mass

flow on the growth of the micro-artefact was more important and taller height could be reached when P and f were set at their maximum levels.
Table 6.2 summarizes the experimental results in terms of final heights reached by the realized micro-artefact.

process parameters			average height [µm]	Standard Deviation [µm]
P [W]	***F [mm/min]***	***f [mg/s]***		
18	100	0.29	62.5	6.87
18	100	0.57	168.33	6.80
18	500	0.29	11.25	0.83
18	500	0.57	19.58	2.10
42	100	0.29	157.83	9.38
42	100	0.57	325.42	20.70
42	500	0.29	3.75	1.60
42	500	0.57	27.08	2.10

Table 6.2 Final height measurements and corresponding Standard Deviations.

For F = 100 mm/min, an increase in P and f determined an increase in the final height.
For high values of the laser power (42 W), the final height increased up to 128.52 µm in average. This was due to the high energy irradiated by the laser. In fact, the higher is the energy reaching the substrate, the more surface is melted producing a larger molten pool and allowing a bigger number of powder particles to fall inside it. The tallest final heights of the manufactured thin squares were obtained for a laser scan speed of 100 mm/min, a laser power of 42 W, and a powder feed rate of 0.57 mg/s.
P, F, and f showed a relevant influence on the geometrical and dimensional accuracy of the realized micro-artefact in terms of uniformity of growth as well. To analyse this output, the standard deviations resulting from the height measurements were evaluated and compared each other.
Pareto chart of Figure 6.9 summarises the results in terms of significance in the influence of the process parameters taken into account in the experimental plan. It is noteworthy that the combinations of process parameters not resulting in a continuous track deposition and a significant growth of the micro-artefact were excluded from this specific analysis because it was not possible to detect the influence of the experimental factors correctly. Table 6.3 shows the combinations of factors excluded from this analysis.

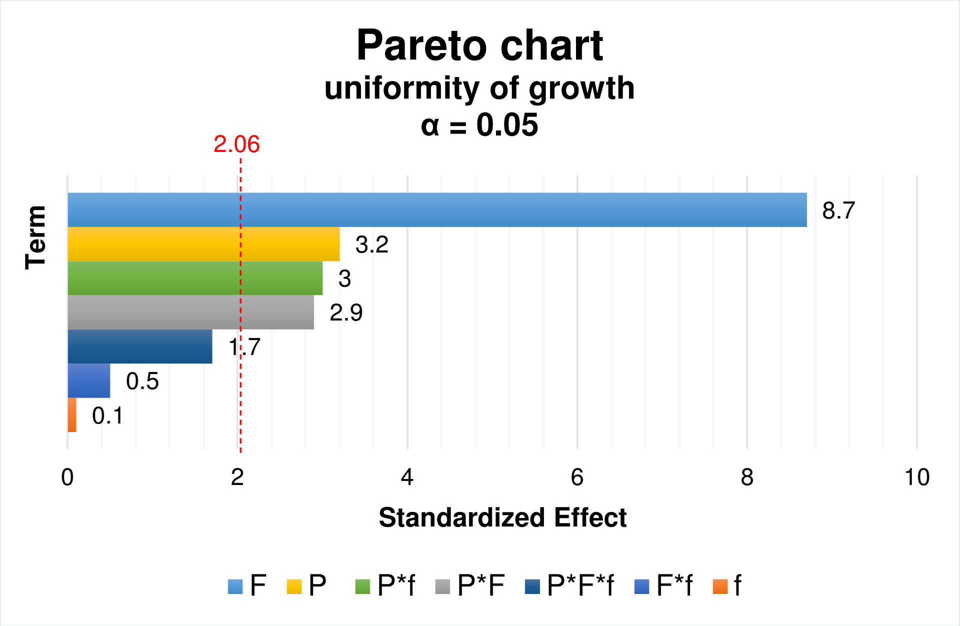

Figure 6.9 Pareto chart for growth uniformity.

process parameters		
P [W]	***F [mm/min]***	***f [mg/s]***
18	500	0.29
42	500	0.29

Table 6.3 Combinations of process parameters excluded from the width variation analysis.

The laser scan speed, the laser power, the interaction between laser power and powder feed rate and the interaction between P and F significantly affected the uniformity of growth.

The best micro-artefacts showing the lower unevenness on the top surface were achieved for medium-high values of the laser scan speed and low level of the laser power. For F of 500 mm/min and P of 18 W, the standard deviation was less than 5 µm in average. Nevertheless, a high value for the laser scan speed (500 mm/min) combined with low values for the laser power (18 W) was not sufficient to ensure acceptable growth of the realized artefact due to the very low exposure time provided during the track formation (see Fig. 6.10). Better results in terms of uniformity of growth and relevant final heights of the micro-features were achieved when the laser power and the laser scan speed were set at 18 W and 100 mm/min respectively. In this case, the average value of the standard deviation was around 15 µm in average.

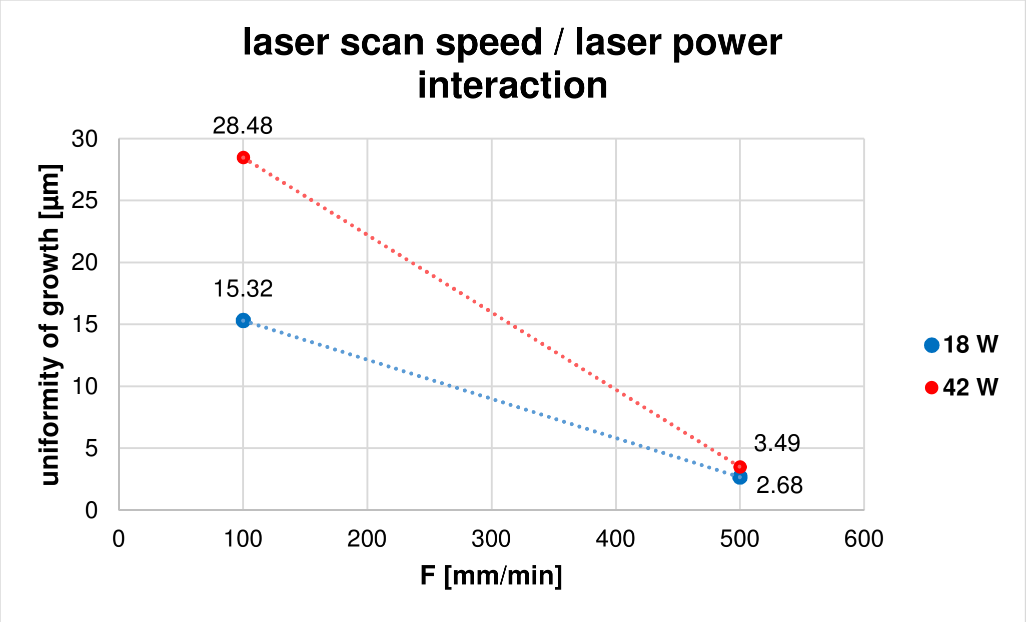

Figure 6.10 Interaction effect between laser scan speed and laser power on the uniformity of growth.

It was important to remark that employing the OPL approach, all the analysed combinations of process parameters did not reach the final height required in this experimental analysis, but the growth of the artefacts resulted to be insufficient (see Fig. 6.11). This experimental findings underlined the ineffectiveness of the OPL building approach when the DLMD was applied at the micro-scale.

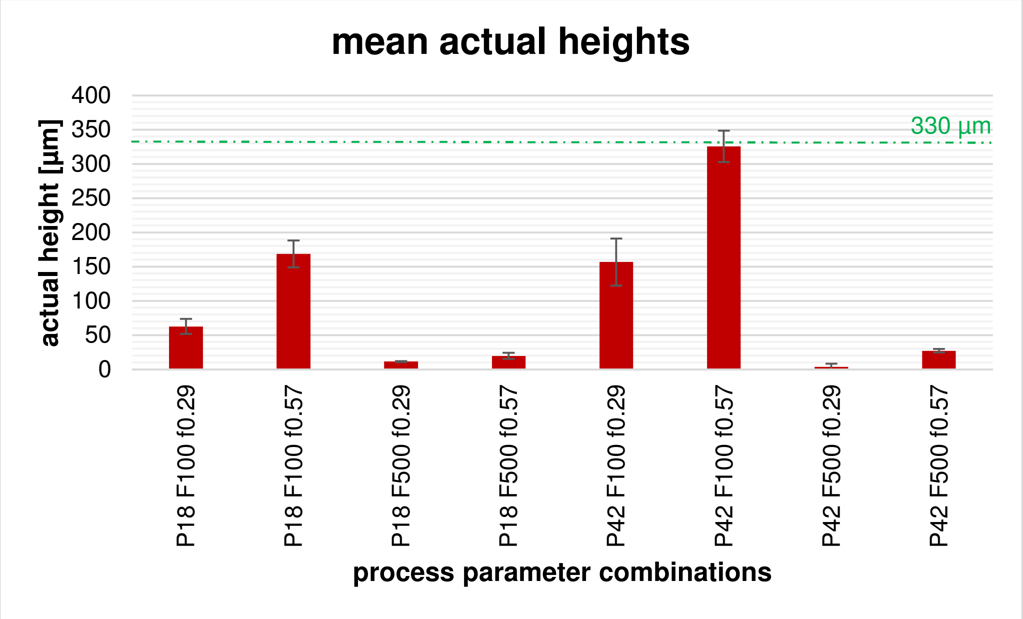

Figure 6.11 Comparison between the nominal height set during the experimental plan and the actual height of the realized micro-artefacts.

6.2.2.2. Track width variation and *Balling phenomenon*

The Pareto chart of Figure 6.12 summarizes the results in terms of significance of the influence of the single parameters and their combinations on the *Balling phenomenon* onset and track width variation. According to the chart, all the three process parameters together with the interaction between laser power and laser scan speed showed to be significant. For high levels for the laser power energy (42 W), the deposited track width increased up to 258.37 μm in average (see Fig. 6.13), causing a strong deterioration of the micro-feature due to the *Balling* formation. High laser energies caused the formation of large drops along the edges of the square side (see Fig. 6.14), causing an irregular widening of the deposited track.

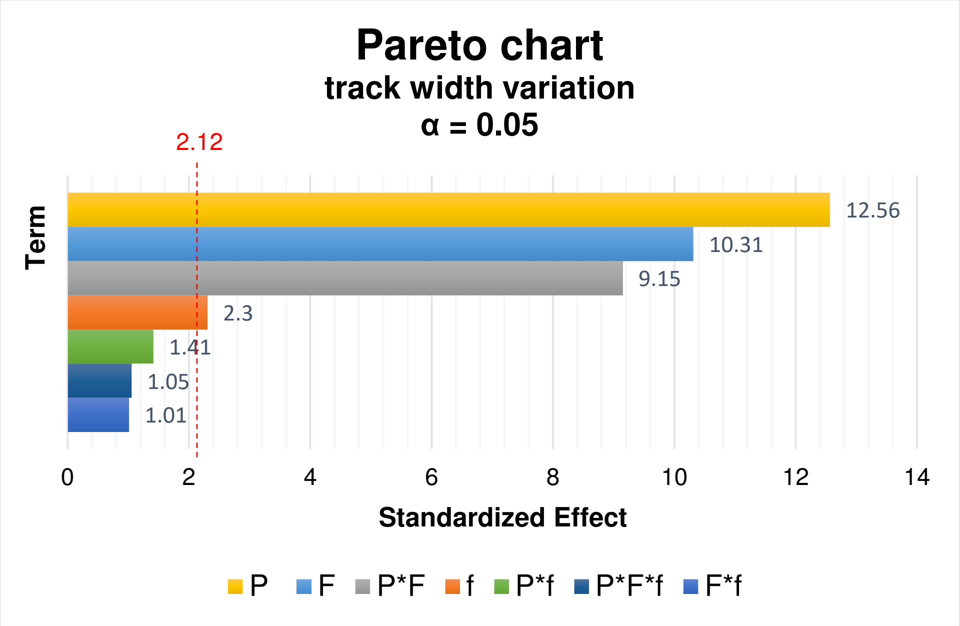

Figure 6.12 Pareto chart for track width variation.

Moreover, together with the *Balling phenomenon*, the splashing of the molten pool outside the laser path occurred causing the formation of very large drops (with diameter between 100 and 200 μm) and the bonding of partially melted powder particles on the surface of the artefact walls (see Fig. 6.15 a and b).

The splashing phenomenon in DLMD occurred when high laser power push the molten pool outside the laser track, causing the solidification of the melted material along the edge of the sintered track with a significant deterioration of the surface quality.

The worst results were obtained for P = 42 W, F = 100 mm/min, and f = 0.57 mg/s. With this combination of process parameters, the track width reached the 473.91 μm in average and the geometrical shape of the part emerged strongly deteriorated. Very fine track width and well defined solid bead were obtained for low levels of the laser power (18 W). In this case, the track width decreased up to 54 μm in average and no *Balling* was present.

Concerning the effect of the laser scan speed, no *balling* phenomenon was observed at the highest values (500 mm/min). Nevertheless, at high laser scan speed the deposited track was not continuous and the structural integrity of the realized micro-part was strongly compromised (see Fig. 6.7).

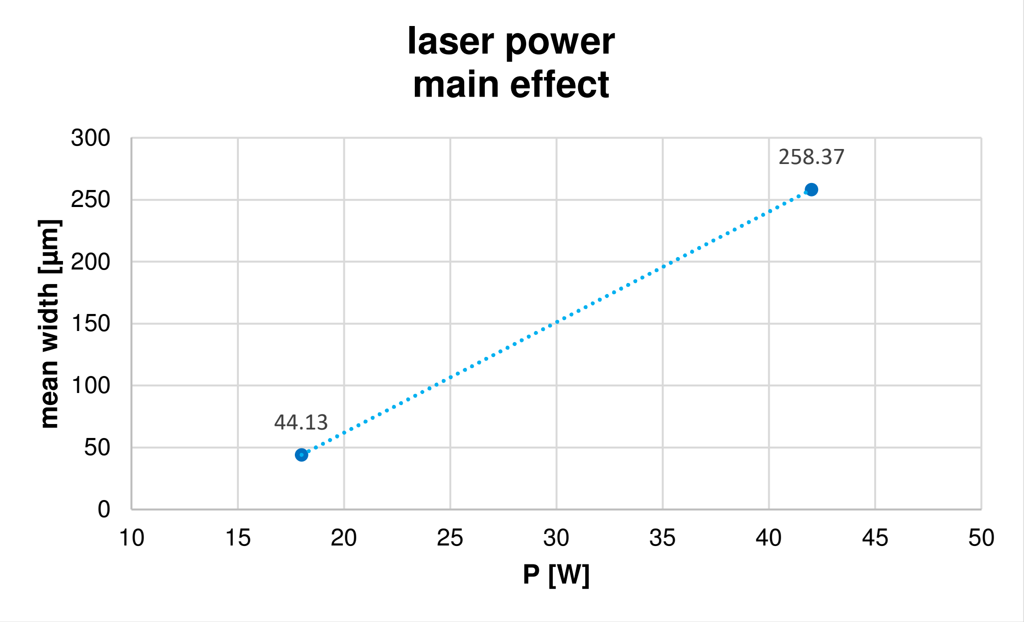

Figure 6.13 Laser power main effect on the track width variation.

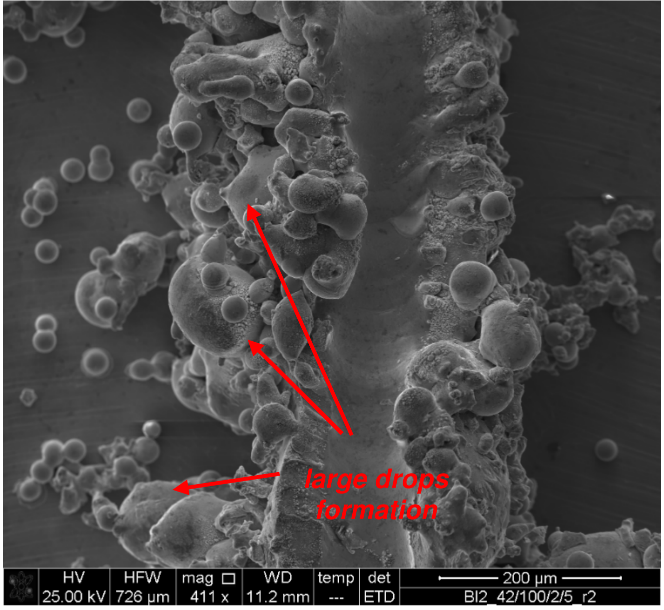

Figure 6.14 Large drop formation at P = 42 W.

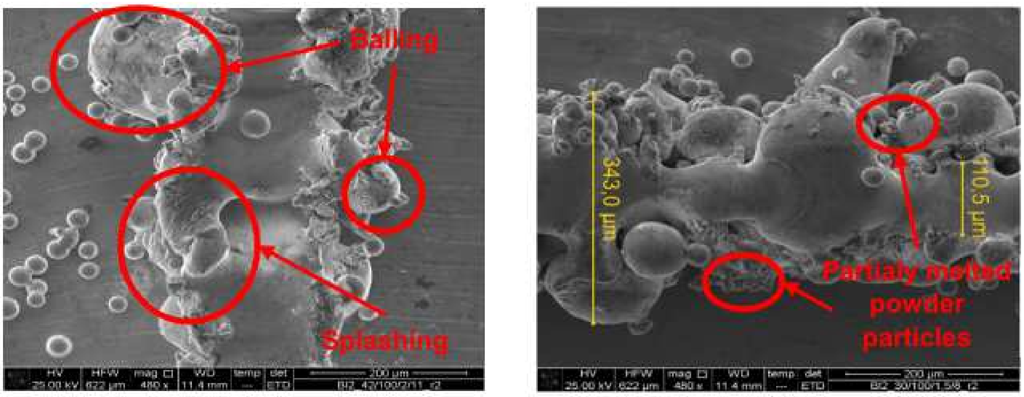

a) b)

Figure 6.15 a) splashing and *Balling phenomenon* [P=42 W; F=100 mm/min] (b) partially melted powder particles [P=30 W; F=100 mm/min].

Table 6.4 summarizes the results concerning the width variation analysis.

process parameters			**average width [µm]**
P [W]	***F [mm/min]***	***f [mg/s]***	
18	100	0.29	46.48
18	100	0.57	61.52
18	500	0.57	42.34
42	100	0.29	374.79
42	100	0.57	473.91
42	500	0.57	106.78

Table 6.4 Final width measurements and corresponding Standard Deviations.

Decreasing the laser scan speed up to 100 mm/min in combination with 18 W in the laser power, continuous and well defined solid bead with no *Balling* presence were observed (see Fig. 6.16). In this case, no splashing and no track instability appeared and good micro-square ribs were obtained with a track with of 54 µm in average.

The best result in terms of deposited track accuracy was achieved combining for P = 18 W, F = 100 mm/min, and f = 0.57 mg/s.

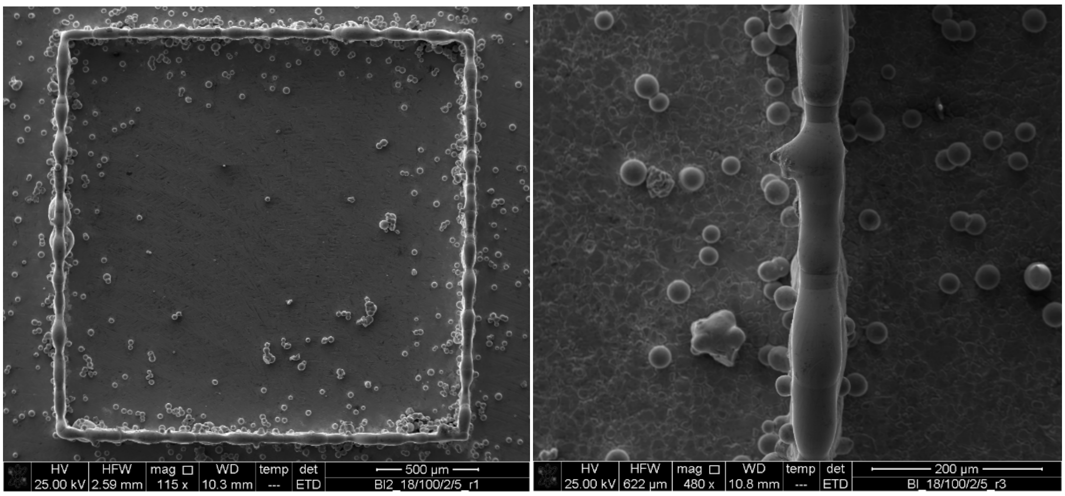

Figure 6.16 P = 18 W, F = 100 mm/min, f = 0.57 mg/s.

6.2.3. Conclusions

The dimensional accuracy of AISI 316l square micro-features was investigated applying the DLMD process at the micro-scale. OPL building approach was assumed and the influence of laser power, laser scan speed and powder feed rate on the final dimensional and geometrical quality of the artefacts was analysed.
The main achievements can be summarized as follows:

- all the three process parameters evaluated in the experiment plan proved to affect the dimensional accuracy of the micro-artefacts significantly;
- laser power and laser scan speed are the two most important parameters affecting the quality of the micro-part in terms of actual final height, width variation, and *Balling phenomenon* onset and extension;
- in all the experiments, the actual value of the thin square height did not reach the nominal value of 330 µm, demonstrating the inefficiency of the OPL building approach for the DLMD process applied at the micro-scale;
- high values for the laser power (42 W) increased the final height of the micro-artefacts, but facilitated the onset of the *Balling phenomenon* in combination with splashing (Figure 15a and 15b) with a consequent decrease of the artefact quality;
- high values for the laser scan speed (500 mm/min) delimited the *Balling phenomenon* and ensured a more uniform growth of the square sides, but introduced strong discontinuities in the track deposition;
- good results in term of absence of *Balling phenomenon* and uniformity of the growth were achieved when a laser power of 18 W was combined with a laser scan speed of 100 mm/min;
- the best dimensional accuracy was obtained combining a low laser power (18 W) with a high powder feed rate (0.57 mg/s) and a low laser scan speed (100 mm/min)

6.3. Realization of AISI 316L micro features employing the MPL building approach

In this Section, the MPL building approach (Multi Passes per Layer) is assumed and the influence of the chosen DLMD process parameters on the dimensional and geometrical accuracy of the metal micro-artefact is analysed.

6.3.1. Material & methods

6.3.1.1. Experimental procedure

One of the aim of this experimental investigation was to analyse the influence of the two different building approaches on the final accuracy of the realized micro-artefacts. To accomplish this purpose, the DLMD system, metal powder, process parameters, and the experimental plan design for this analysis were the same used in the Chapter §6.2.1 previously. To perform the MPL building approach, 5 passes per layer were employed.

6.3.1.2. Micro-features considerations

The realized micro-feature were the micro-square ribs introduced in the previous Chapter §6.2.1.2.

6.3.1.3. Evaluation and characterization

The scientific instruments and methodology employed to analyse and characterize the realized micro-features were the same introduced in the Chapter §6.2.1.3.

6.3.2. Results and Discussion

The experimental results obtained from the analysis of the influence of the chosen process parameters combined with the MPL building approach on the final quality of the realized micro-squares are here analysed and discussed.
As done in the Chapter §6.2.1, the final quality of the micro-features was evaluated in terms of final height and track width variation in relation with the onset and extension of the *Balling phenomenon.* In the following Sub-chapters, the experimental findings are introduced and discussed.

6.3.2.1. Evaluation of the final height

The final height of the realized micro-square ribs was compared to the nominal height of 330 µm defined in the experimental design. The data confidence interval was stated at the 95% confidence level. The Pareto chart shows the influence of the analysed process parameters on the growth of the realized micro-artefact (see Figure 6.17).

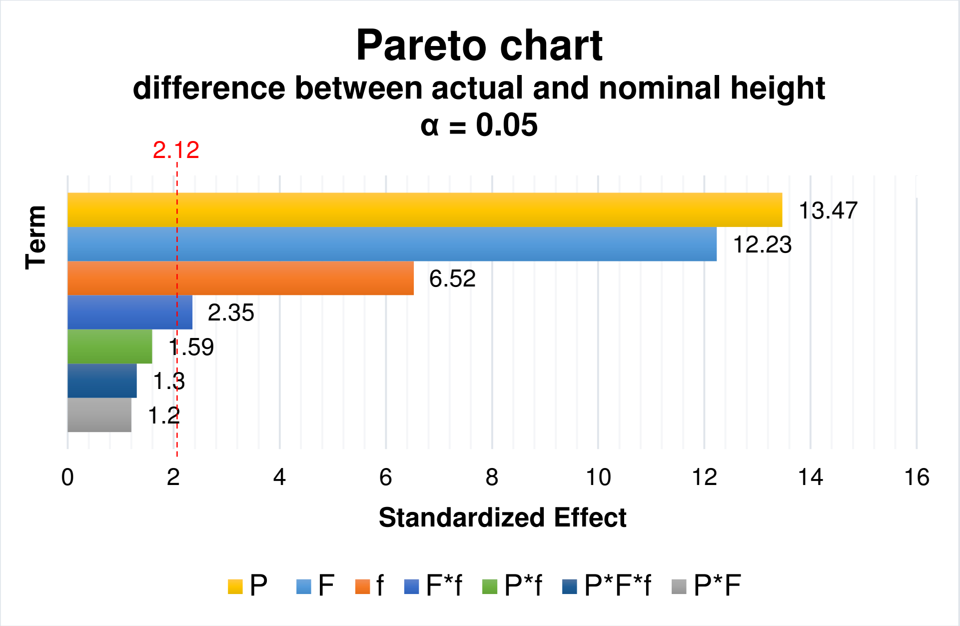

Figure 6.17 Pareto chart for final height variation (MPL building approach).

For the MPL building approach, the most important process parameters affecting the growth of the manufactured part was the laser power and the laser scan speed. Increasing P, the final height of the micro-square increased, moving closer and sometimes exceeding the nominal height of 330 µm defined in the experimental procedure.
Keeping F and f constant, an increment of P form 18 to 42 W caused an increase of the final height from 210.62 µm to 592.47 µm in average.

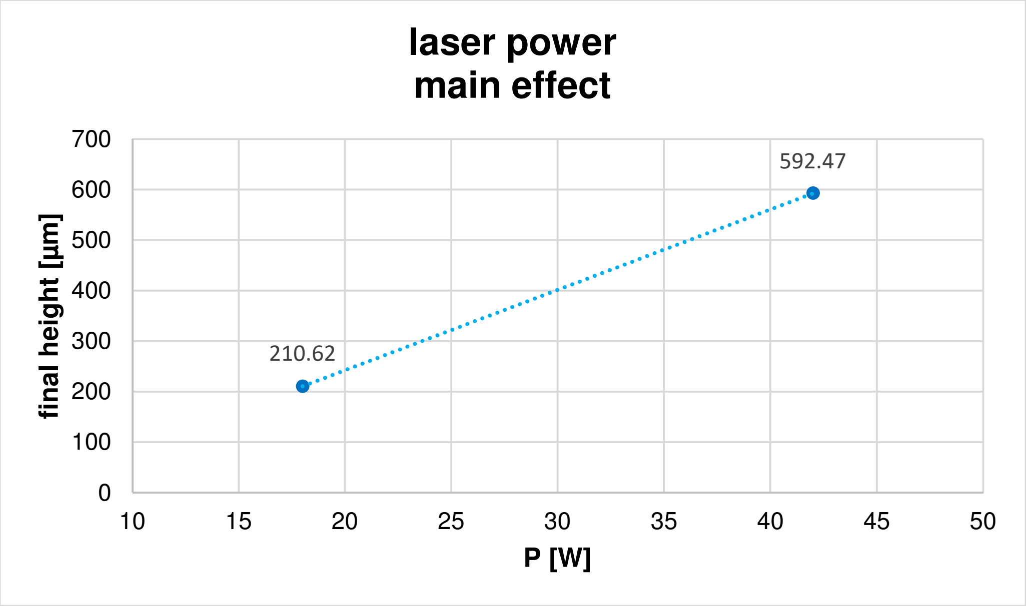

Figure 6.18 Laser power main effect on the final height variation.

The reason of this significant increment in the final height was the consequence of two coupled effect: the enlargement of the molten pool and the bigger number of powder particles participating to the track formation due to the multiple passes per layer. In fact, if an increase in P determined an increase in the laser energy irradiation on the substrate surface and, consequently, a larger molten pool, an increment of the passes per layer from 1 to 5 determined a powder supply on the local laser-surface interaction area five times bigger than in OPL approach. This meant that under these process conditions a bigger amount of powder particles went to form the deposited solid bead, causing a final height much taller than the nominal one of 330 μm.

The growth of the micro-squares was lower when the laser power decreased up to 18 W. Nevertheless, the minimum value of 210.62 μm in average obtained for the MPL building approach was more than three times higher than the average final height obtained with the same process conditions but employing the OPL approach.

Table 6.5 summarizes the results concerning the final height reached by every combination of process parameters employed in the experimental plan.

process parameters			**average height [μm]**	**Standard Deviation [μm]**
P [W]	***F [mm/min]***	***f [mg/s]***		
18	100	0.29	245.34	25.58
18	100	0.57	488.58	38.09
18	500	0.29	36.02	10.33
18	500	0.57	72.53	12.87
42	100	0.29	653.15	42.60
42	100	0.57	912.58	110.74
42	500	0.29	301.97	71.56
42	500	0.57	502.18	73.87

Table 6.5 Final heights reached in the experimental plan.

The higher micro-square was 912.58 μm tall in average and it was obtained for a P = 42 W, F = 100 mm/min, and f = 0.57 mg/s.

The second DLMD process parameter strongly affecting the final height of the artefacts was the laser scan speed. Decreasing F up to 100 mm/min, the micro-square grew up to 575 μm in average. This was mainly due to the increase in the laser exposure time when F was at the lower level. As for OPL, even for MPL an increase in the exposure time allowed a larger number of particles to fall inside the molten pool during the deposition process. Increasing F up to 500 mm/min, the final height of the micro-artefact did not exceed the 228 μm in average. Nevertheless, thanks to the employment of the MPL approach, the continuity of the deposited track was consistent also for the highest levels of the laser scan speed (see Figure 6.19), due to the employment of more passes per layer during the deposition of the artefact.

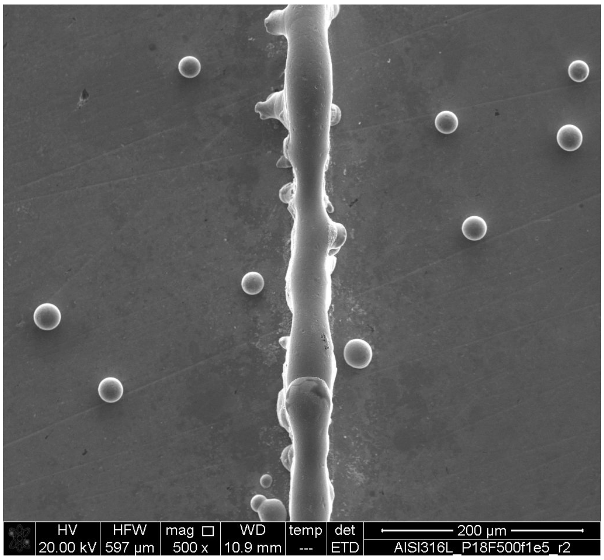

Figure 6.19 P = 18 W, F = 500 mm/min, f = 0.29 mg/s.

Pareto chart shows an effect of the powder feed rate lower twice compared to that of P and F (see Fig. 6.17). Nevertheless, increasing f from 0.29 to 0.57 mg/s, the final height increased from 309 to 494 µm in average.

The experimental investigation showed a not significant influence of the analysed process parameters on the uniformity of growth of the micro-square sides. This was due to the strong influence of the MPL building approach on the continuity and uniformity of growth of the deposited track. Indeed, increasing the number of passes per layer, the main effects of the chosen process parameters on the continuity and uniformity of growth of the deposited solid bead became less significant.

In other words, if the P, F, and f were important in the molten pool formation and size, they did not affect the continuity of the deposition and the uniformity of growth because it was ensured by the MPL building approach assumption.

6.3.2.2. Track width variation and *Balling phenomenon*

The Figure 6.20 shows the great influence of laser power, laser scan speed, and their interaction on the track width variation of the realized thin micro-squares.

At higher laser power (42 W) the track width increased up to 810 µm in average. Moreover, for P = 42 W, F = 100 mm/min, and f = 0.57 mg/s, the track width exceeded the millimetre, reaching 1.135 mm in average. This was mainly because the high laser energy reaching the substrate surface that combined with a low laser exposure time due to the low laser scan speed caused a large *Balling* formation and extension along the track edges. Figure 6.21 shows how the presence of solid drops and partially-melted powder accumulations strongly deteriorated the dimensional and geometrical accuracy of the deposited micro-features. The irregularities at the track edges could extend up to 500 µm in size.

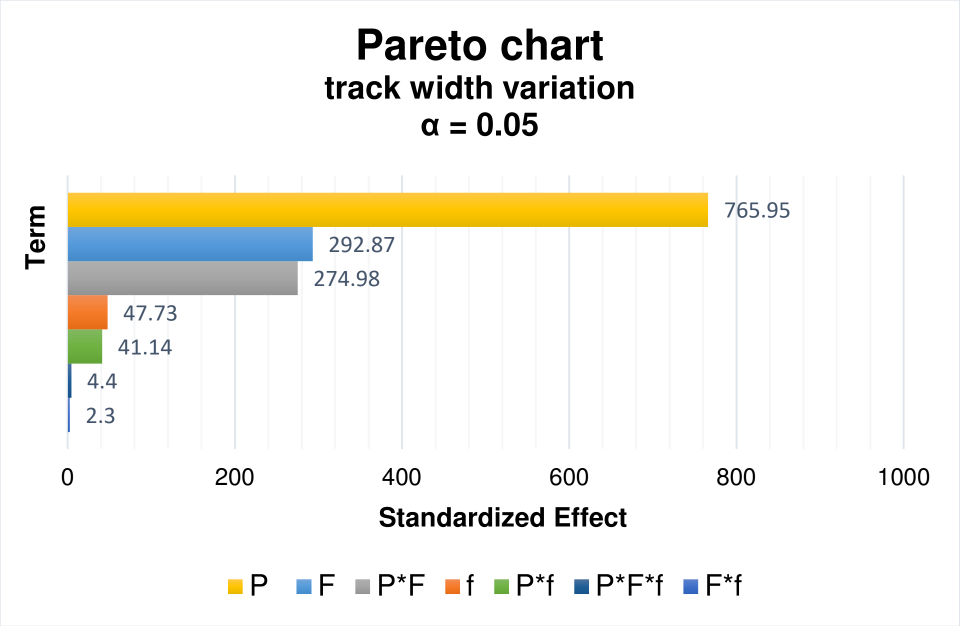

Figure 6.20 Pareto chart for width variation (MPL building approach).

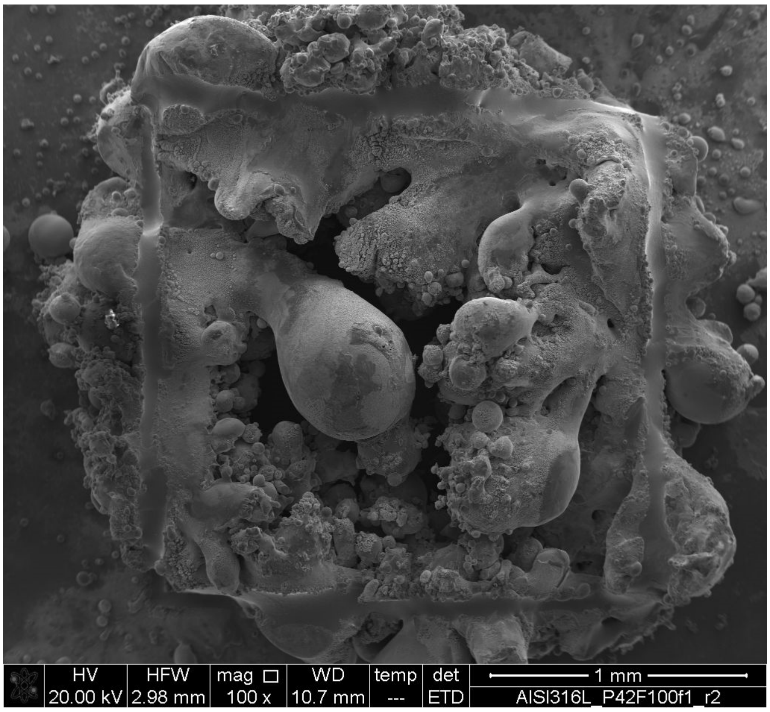

Figure 6.21 Strong *Balling* formation (P = 42 W, F = 100 mm/min, f = 0.29 mg/s).

The onset of the *Balling phenomenon* was aggravated by the increased number of passes per layer as well. Indeed, an increment in the number of passes caused a sudden increase in the local temperature and in the thermal gradient between molten pool and the surrounding, increasing the adhesion of the un-melted powder particles along the track edges.

Decreasing P up to 18 W, the deposited solid bead became more accurate and defined. No *Balling* was detected at the lowest energy values and the track width decreased up to 44 µm in average.
Table 6.6 summarizes the results concerning the width variation for every combination of process parameters employed in the experimental plan.

process parameters			**average width [µm]**
P [W]	***F [mm/min]***	***f [mg/s]***	
18	100	0.29	48.31
18	100	0.57	57
18	500	0.29	32.52
18	500	0.57	37.01
42	100	0.29	1052.50
42	100	0.57	1134.67
42	500	0.29	477.95
42	500	0.57	573.53

Table 6.6 Final width reached in the experimental plan.

The best results were obtained for P = 18 W and F = 100 mm/min with a track width ranging between 48 and 57 µm in average, depending on the powder feed rate employed (0.29 and 0.57 respectively) (see Fig. 6.22).

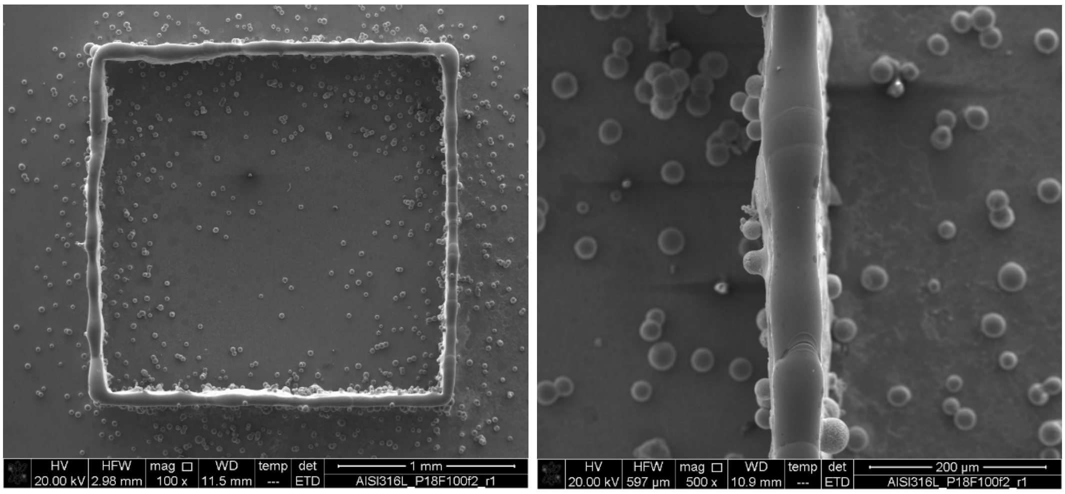

Figure 6.22 P = 18 W, F = 100 mm/min, f = 0.57 mg/s.

Concerning the laser scan speed, it showed to have a great influence on the *Balling* extension if high values of P were employed (42 W). Increasing F from 100 to 500 mm/min and keeping P at 42 W, the track width decreased from 1094 to 526 µm in average. Nevertheless, the micro-feature still resulted deteriorated due to the high energy involved. At 18 W, an increase in F determined a decrease of the track width up to 35 µm in average. Nevertheless, the resulted solid bead did not appear stable and accurate. The results improved with the decrease of F.

6.3.3. Conclusions

The dimensional accuracy of square micro-features in micro DLMD process of AISI 316L Stainless Steel was investigated, analysing the influence of P, F, and f in combination with the MPL building approach.
The main achievements are summarized as follows:

- the laser power and the laser scan speed were the two most important process parameters affecting the final quality of the micro-artefact when the MPL abuilding approach is employed;
- almost all the micro-features realized reached or exceeded the nominal final height designed by the experimental plan;
- increasing P from 18 to 42 W, the final height of the micro-square ribs increased up to 592.47 µm in average, reaching the 912.58 µm in average for P = 18 W, F = 100mm/min, and f = 0.57 mg/s;
- high laser energies were the main reason of the *Balling* onset and extension;
- for P = 42, the deposited track had large width (up to 809.66 µm in average) and the formation of solid metal drops with a diameter of 500 µm in average which deteriorated the dimensional and geometrical accuracy of the micro-square;
- for low laser power (18 W), no *Balling* was detected and the deposited solid bead was accurate with track width of 44 µm in average;
- high laser scan speed (500 mm/min) limited the *Balling phenomenon* decreasing the track width from 1094 to 526 µm in average;
- F = 100 mm/min combined to P = 18 W allowed a good growth of the deposited sides of the micro-squares with an accurate bead formation;
- P, F, and f were not significant in the uniformity of growth of the realized micro-square ribs due to the increased number of passes per layer which ensured a good continuity and height uniformity of the deposited track;
- the best results in terms of actual final height, geometrical and dimensional accuracy of the deposited micro-parts were obtained for P = 18 W, F = 100 mm/min, and f ranging between 0.27 and 0.59 mg/s.

6.4. Comparison between OPL and MPL

The designed experimental plan showed a strong influence of the two different building approaches on the final quality of the realized micro-part.

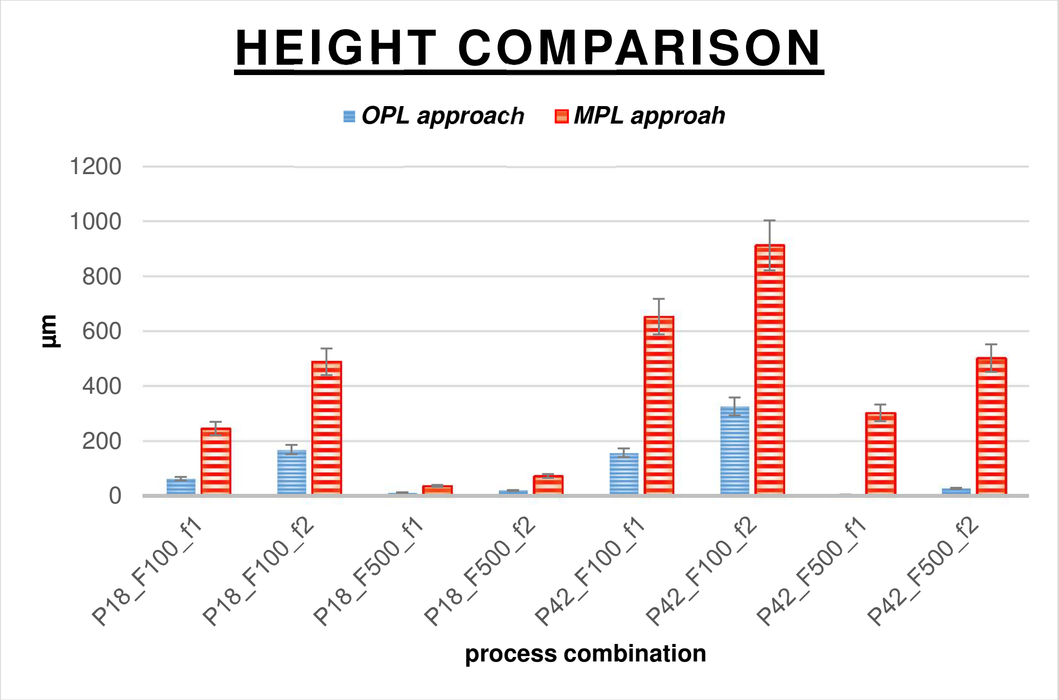

Figure 6.23 Final height comparison between OPL and MPL building approach.

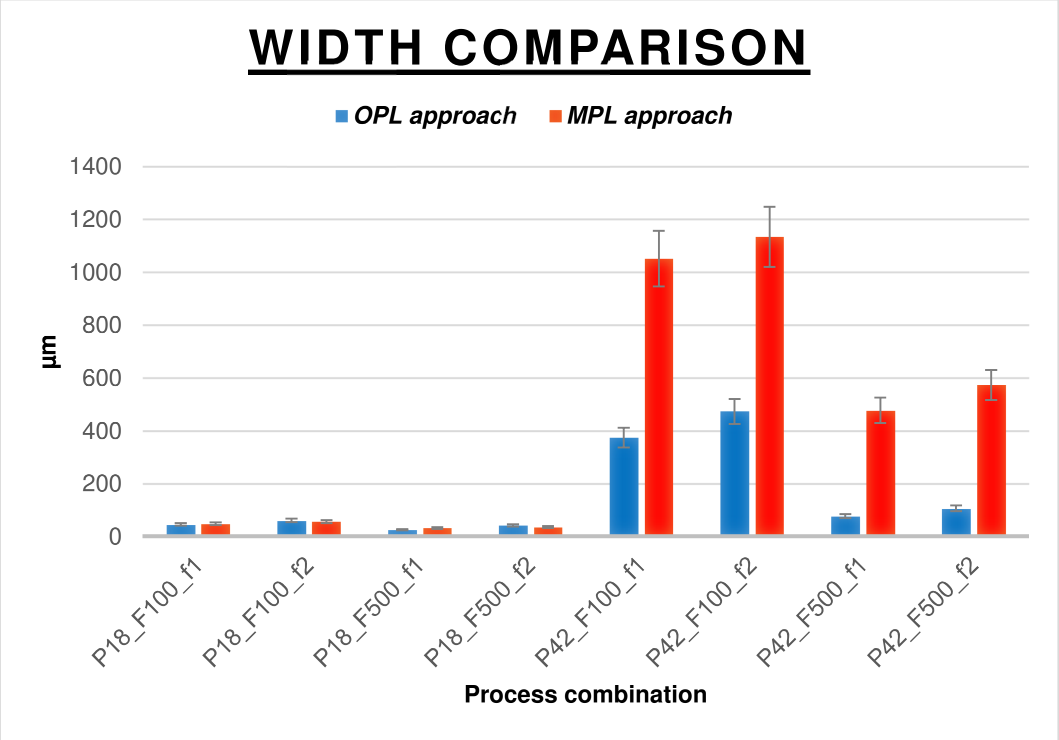

Figure 6.24 Final width comparison between OPL and MPL building approach.

The main outputs and differences between OPL and MPL approaches are summarized as follows:

- for the OPL approach, the design final height of 330 µm was not respected for almost all the process parameter combinations employed in the experimental design;
- at constant P, F, and f, the micro-square ribs realized by MPL approach resulted to be higher than those realized by OPL approach;
- at high laser scan speed (500 mm/min), the discontinuities in the track deposition were reduced if MPL was employed;
- at high laser power (42 W) the *Balling phenomenon* and the degradation of the realized micro-squares made worse in MPL than OPL for the increase of the number of passes per layer;
- for P = 18 W, for both the building approaches, the formation of accurate solid beads was possible, getting width close to 50 µm in average;
- for OPL approach, the uniformity of growth strongly depended on the laser power and the laser scan speed employed during the micro DLMD process. On the contrary, in MPL building approach, the analysed process parameters were not significant;
- in micro DLMD, the assumption of the MPL building approach showed to be more efficient than OPL in the realization of accurate AISI 316L Stainless Steel micro-features.

6.5. Conclusions

In this experimental investigation, the influence of laser power, laser scan speed, powder feed rate, and DLMD building approach on the final quality of AISI 316L Stainless Steel micro-artefacts was analysed.

The results underlined the important role of P and F in the final quality of the realized micro-features.

Moreover, the MPL demonstrated to be an AM building approach more efficient than OPL in terms of deposited track formation and control of the deposition process.

The main achievements are summarized as follows:

- laser power was the most important micro DLMD process parameters affecting the *Balling* onset and extension;
- high laser energies (42 W) allowed a significant growth of the sintered micro-artefact, but strongly deteriorated the track accuracy due to the formation of large drops (up to 500 µm) which get worse the dimensional and geometrical accuracy of the micro-artefacts;
- high laser scan speed (500 mm/min) limited the extension of *Balling*, but did not facilitate the deposition of continuous and high solid beads;
- powder feed rate had not influence on the final quality of the micro-artefact in terms of geometrical accuracy, but it affects the final height reached by the micro-part;
- low laser energies (18 W) and low laser scan speed (100 mm/min) allowed the formation of a constant deposited track with an average width of 50 µm;

- MPL building approach was more efficient than OPL for DLMD process applied at the micro-scale;
- at constant P, F, and f, the actual final height reached by the micro-squares were higher if MPL is assumed instead of OPL;
- in MPL the influence of the process parameters on the uniformity of growth was not significant, but it was affected by the number of passes per layer;
- for wrong combinations of process parameters (P = 42 W and F = 100 mm/min) the deterioration in the track accuracy was higher when the MPL building approach was employed;
- very accurate micro-square ribs were obtained for P = 18 W, F = 100 mm/min, f between 0.29 and 0.57 mg/s when MPL building approach was employed.

Chapter 7

The influence of DLMD deposition strategies

This chapter deals with the manufacture of bulk micro-components (i.e. micro cylindrical PIN) to analyse the influence of the DLMD building strategies on the final quality of the part. The influence of the inter-track idle time and substrate preheating temperature on the dimensional accuracy, internal porosity, and final surface roughness along the vertical sides of the artefact is investigated.

The experimental results demonstrate that the realization of full dense structures with very fine lateral surface roughness and a reduced “stepwise” effect is feasible when high values for the preheating temperature are employed and the idle time is correctly combined with the specific energy and laser power. Nevertheless, further process analysis are required to realized micro-artefacts with an internal structure more homogeneous.

This experimental investigation suggests also an empirical procedure for the realization of bulk micro-component through micro DLMD.

7.1. Introduction

In DLMD, the number of process parameters affecting the dimensional accuracy, final surface integrity, mechanical properties, and microstructure of the realized part is very high [10] and the influence of their interactions on the efficiency of the process and on the final quality of the artefact is not well know yet [10, 84].
Deposition strategies and preheating temperature of the substrate are two of the main process parameters affecting thermal gradients and heat fluxes evolution during the DLMD process. Wang et al. [85] demonstrated the strong influence of the deposition strategy on the mechanical characteristics of the realized part, improving the quality of the artefact in terms of microstructure, hardness, and tensile strength when a parallel deposition strategy was employed. Moreover, a preheated substrate facilitates the generation of a stable molten pool and smaller cooling rates, promoting the formation of a uniform dendritic structure and limiting the generation of residual stresses for normal-size parts [86]. Yadollahi et al. [87] analysed the effect of the idle time during the DLMD process applied at the macro-scale, detecting higher yield and tensile strength for AISI 316L Stainless Steel artefacts realized with longer inter-layer time intervals. On the contrary, in AISI 420 Stainless Steel artefacts the martensite phase during the part build-up could be reduced employing short idle time between consecutive depositions [88].
The influence of deposition strategies and preheating substrate temperatures is more critical when DLMD is applied at the micro-scale due to the high dimensional accuracy and structural integrity required. To the best of Author’s knowledge, no investigation is available in literature concerning the influence of deposition strategies and preheating substrate temperature on the final quality of part realized by DLMD applied at the micro-scale.
In this experimental investigation, cylindrical micro-PIN are realized through micro DLMD process, employing the MPL building approach introduced in the previous Chapters §4 and §6 and analysing the influence of inter-track idle time and preheating temperature on the internal porosity formation and final surface roughness along the vertical sides of the micro-artefacts.

7.2. Procedure to build 3D micro-components

In this research work, an empirical procedure for the manufacture of bulk micro-parts is provided. The suggested experimental method recognizes specific process steps acting to defined suitable process conditions for the additive realization of micro-parts and structures through DLMD.
The suggested procedure consists of the following process steps:

- *first step:* characterization of the powder particles distribution at the exit of the injection nozzle and definition of the optimal working-plane position for the metal substrate into the deposition powder cloud;
- *second step:* recognition of the best combination of process parameters in terms of laser power and specific energy allowing a continuous and significant deposition of single-layer micro-features and consequent characterization of the track geometry in terms of average height and width;
- *third step:* additive manufacture of bulk micro-parts (i.e. bulk micro-PIN), analysing the influence of different inter-track idle times and preheating substrate temperatures on the final quality of the artefacts.

Each step of the empirical procedure will be introduced and explained in the following Sub-chapters. The experimental results and considerations concerning each process phase will be also discussed.

7.3. Deposition powder cloud

The first process step dealt with the characterization of the powder particle mass flow coming out from the deposition nozzle. The importance of this analysis was discussed and introduced in the previous Chapter §3 in which the shape of the deposition powder cloud was simplified as a sum of three different zones (i.e convergent zone + constant width zone + divergent zone). In this first section, the objective was to characterize the powder particle mass concentration and distribution employing the process parameters listed in Table 7.1 and identify the zone of the powder cloud ensuring the highest density of metal particles falling into the molten pool during the DLMD process. In correspondence to this zone, the substrate had to be placed, ensuring the maximum supply of fresh raw powder falling into the molten pool and the highest deposition efficiency as possible.
The analysis of the fluid-dynamic behaviour of the powder and the successive identification of the powder cloud zone with the highest particle mass concentration was carried out both numerically (through *FLUENT*® software) and experimentally. Moreover, a new validation method is provided as alternative to the previous one explained in the Chapter §3.4.

7.3.1. CFD analysis

Table 7.1 summarizes the process parameters employed in this analyses. Argon flow rate and powder feed rate were kept constant since the aim of this investigation was to detect the best location for the substrate during the deposition process, neglecting the influence of these two process parameters on the fluid-dynamic behaviour of the powder particles since it was previously dealt in the Chapter §3.

process parameter	**value**
Argon flow rate [l/min]	0.7
AISI 316L powder feed rate [mg/s]	1.723
powder particle inlet velocity [m/s]	according to the employed value for the Argon flow rate

Table 7.1 Process parameters.

The mixture of powder and gas coming out from the nozzle outlet was analysed as a discrete phase (i.e. powder particles) dispersed in a continuous phase (i.e. Argon). The governing equations and assumptions describing the CFD problem were the same introduced in the previous Chapter §3.3 and they will not here reported (see Chapter §3.3 for more details).

7.3.1.1. CFD results

Figure 7.1, 7.2 and Table 7.2 summarize the results of the CFD analysis carried out through *FLUENT*® software.

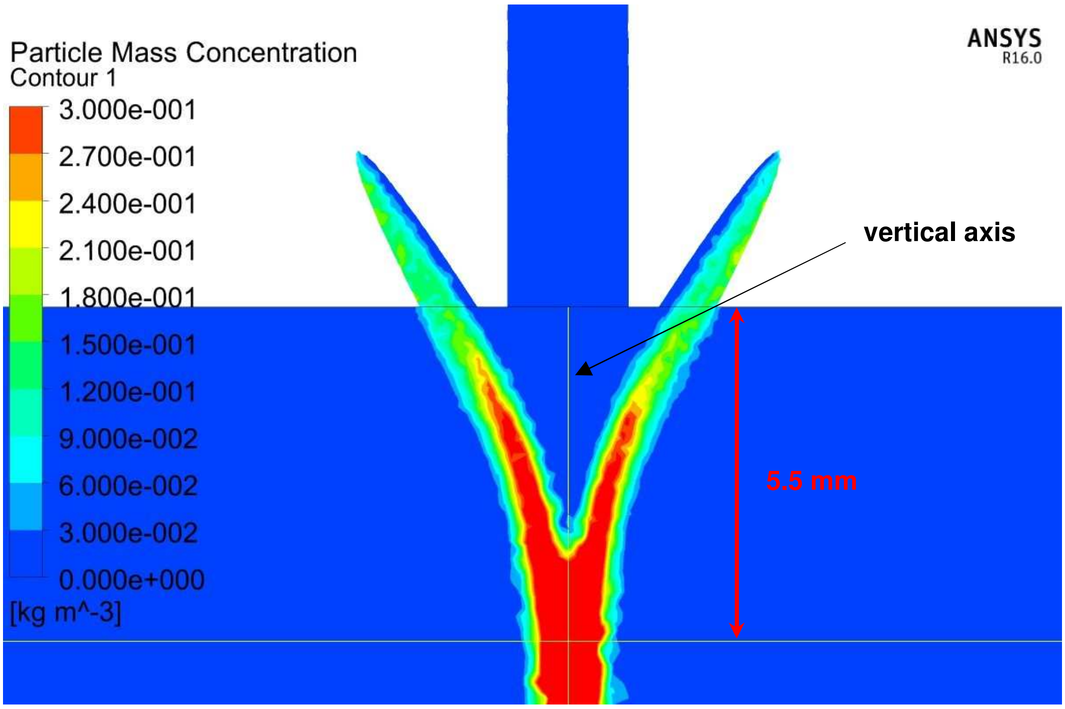

Figure 7.1 CFD image of the particle mass concentration along the vertical extension of the powder cloud.

distance from the nozzle outlet [mm]	particle mass concentration [Kg/m^3]
0	0
1.1	0
2.2	0
3.3	0.004
4.4	0.370
5.5	0.824
6.6	0.737
7.7	0.604
8.8	0.447
9.9	0.290

Table 7.2 CFD particle mass concentration data.

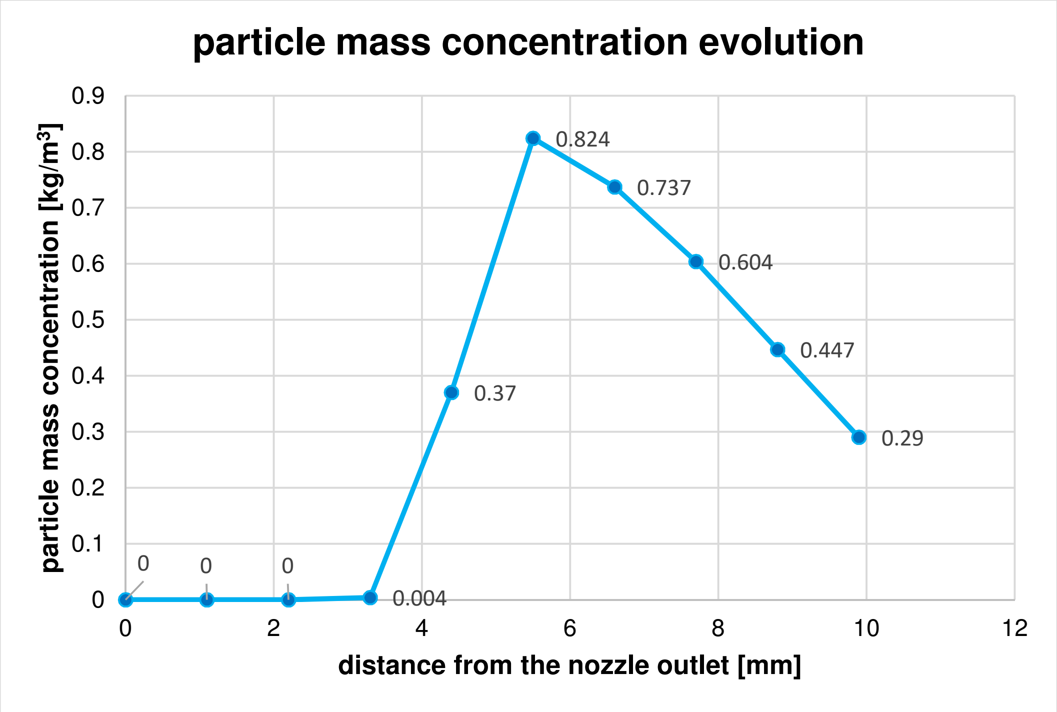

Figure 7.2 Evolution of the particle mass concentration along the vertical axis of the powder cloud.

Figure 7.1 and 7.2 showed the shape of the powder cloud and the distribution of the metal particles which resulted to be in agreement with the findings obtained in the Chapter §3. The three zones characterizing the deposition cloud were well defined. Table 7.2 and Figure 7.2 underline a rapid increase of the particle mass concentration for a distance higher than 3 mm, indicating the zone where the different fluxes of the powder cloud met each other to form the area with the highest powder concentration. High values for the powder density appeared for distances ranging between 5 and 7 mm from the nozzle outlet. After this zone of maximum powder concentration, the particle mass concentration decreased with the increased of the distance.
The maximum value of particle mass concentration was obtained for a theoretical distance of 5.5 mm from the deposition nozzle.

7.3.2. Validation method

For the CFD model validation, a new experimental method was introduced and employed. Contrary to the previous one discussed in the Chapter §3.4, in this case the experimental procedure of validation derived from the work of Tabernero et al. [89], where containers with different sizes were employed to collect the powder particles coming out from the nozzle outlet. The experimental methodology consisted into weighing the containers before and after the filling, relating the particle mass concentration along the powder cloud extension with the weight of the powder particles fell into the containers. Placing the containers at different distances from the nozzle outlet the entire vertical powder distribution could be characterized and the zone with the highest powder particle concentration detected (see Fig. 7.3).

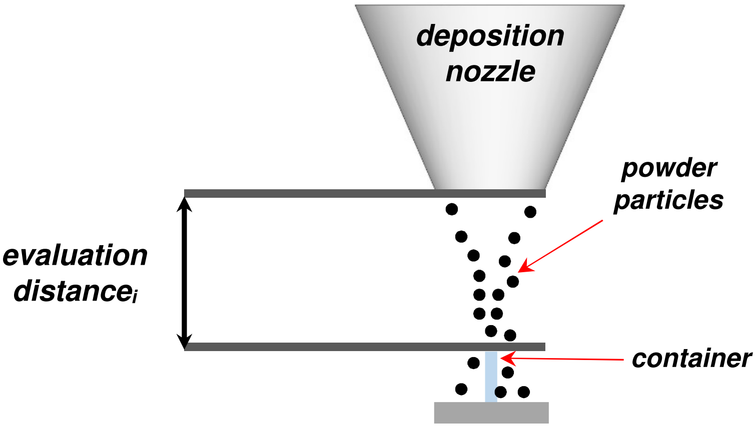

Figure 7.3 Example of container placement to characterize the particle mass concentration of the powder cloud.

During the experimental validation, no thermal sources were involved so it was possible to 3D print the containers through plastic resin material by PolyJet technology (see Fig. 7.4). In order to confirm the coherence of results and to accurately detect the variation in the particle mass concentration, containers with two different diameters were used. Their sizes were 10 mm tall with diameters of 1.5 and 3 mm respectively. This geometric dimension was specifically chosen to avoid the complete filling of the containers during the test time of 60 seconds (Fig. 7.5), preventing the powder transhipping before the end of each single filling.

Figure 7.4 Objet30 Prime, PolyJet ® Technology.

The containers were placed at different evaluation distances ranging between 2 and 8 mm from the nozzle outlet with steps of 1 mm. Three additional positions

(4.5, 5.5, and 6.5 mm) were added during the experimental validation in order to better characterized the distribution of the metal particles inside the powder cloud. To detect the amount of powder entrapped during the validation tests correctly, the weight of the containers was measured three times before and after the deposition process, repeating the test three times for each evaluation distance.

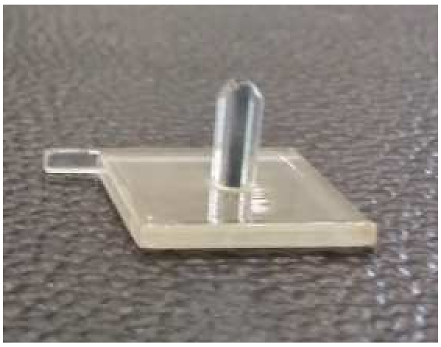

Figure 7.5 3D printed container with a diameter of 1.5 mm and a height of 10 mm.

7.3.2.1. Results

Table 7.3 and Figure 7.6 show the results of the experimental validation and depict the variation in the powder mass (mg) captured by the two containers for different evaluation distances taken into account during the test. The blue and red curves represented the amount of powder collected by the containers with a diameter of 3 and 1.5 mm respectively. Their general trend was in good agreement with that obtained by the numerical analysis (see Fig. 7.2). Nevertheless, the two curves showed a profile behaviour slightly different each other.

Concerning the blue curve, a sudden increase in the weight of the powder mass collected by the largest containers was evident when the evaluation distance went from 2 to 4 mm. At 2 mm from the nozzle outlet, the captured powder showed an average weight of 35.58 mg that increased up to 64.11 mg for a distance of 4mm. This specific trend clearly identified the point where the different fluxes characterizing the powder cloud collided each other, forming an area with a higher powder mass concentration. Incrementing the gap between the largest container and the nozzle, a zone of semi-constant weight resulted for all the distances ranging between 4 and 8 mm, obtaining a measured powder weight higher than 60 mg (see Table 7.3). In this case, the divergent zone of the powder cloud analysed in the previous Chapter §3.4 was not clearly visible due to the large diameter of the employed container. In fact, the big inlet section of 3 mm was not capable to appreciate the variation in particle mass concentration showed in the previous validation method introduced in the Chapter §3.4, but a big portion of metal particles were collected even with a decrease in the particle mass concentration.

The trend of the curve lightly changed when the results concerning the container with the smaller diameter were analysed. In this case, the profile behaviour of the red curve was slightly different compared to the blue one, showing a clear descending trend for evaluation distances ranging between 6.5 and 8 mm. The experimental results underlined a higher sensitivity of the smaller container compared to the big one in the variation of the particle mass concentration. For lower gaps between nozzle outlet and the inlet of the container, the weight of the captured powder rapidly increased from 5.89 mg to 48.33 mg for an increment of the evaluation distances from 2 to 4.5 mm. Moreover, the zone with the higher amount of captured powder particles was well visible in the Figure 7.6 and confined for a nozzle-container distance ranging between 4.5 and 6.5 mm (see Table 7.3). For higher evaluation distances (between 6.5 and 8 mm) the measured weight decreased (from 42.44 to 27.44 mg), indicating a lower number of metal powder collected by the container located below the nozzle outlet. The behaviour profile of the red curve showed to be more in agreement with the previous analysis and conclusion discussed in the Chapter §3. In this case, the three zones characterizing the powder cloud (i.e. convergent zone, constant zone, and divergent zone) were well visible and defined by an evident weight variation.

On the base of these experimental results, it was evaluated as optimal working-plane position a distance of 5.5 mm from the nozzle, placing the substrate in the centre of the maximum particle mass concentration zone of the powder cloud identified in the validation method.

distance from the nozzle outlet [mm]	**weight of the collected powder mass [mg]**	
	container φ = 3 mm	**container φ = 1.5 mm**
2	35.58	5.89
3	55.89	22.22
4	64.11	29.67
4.5	61.22	48.33
5	64.22	45.22
5.5	65.89	48.11
6	67.78	39.67
6.5	68	42.44
7	67	34.33
8	63.56	27.44

Table 7.3 Powder mass collected by the two containers at different distances from the nozzle outlet.

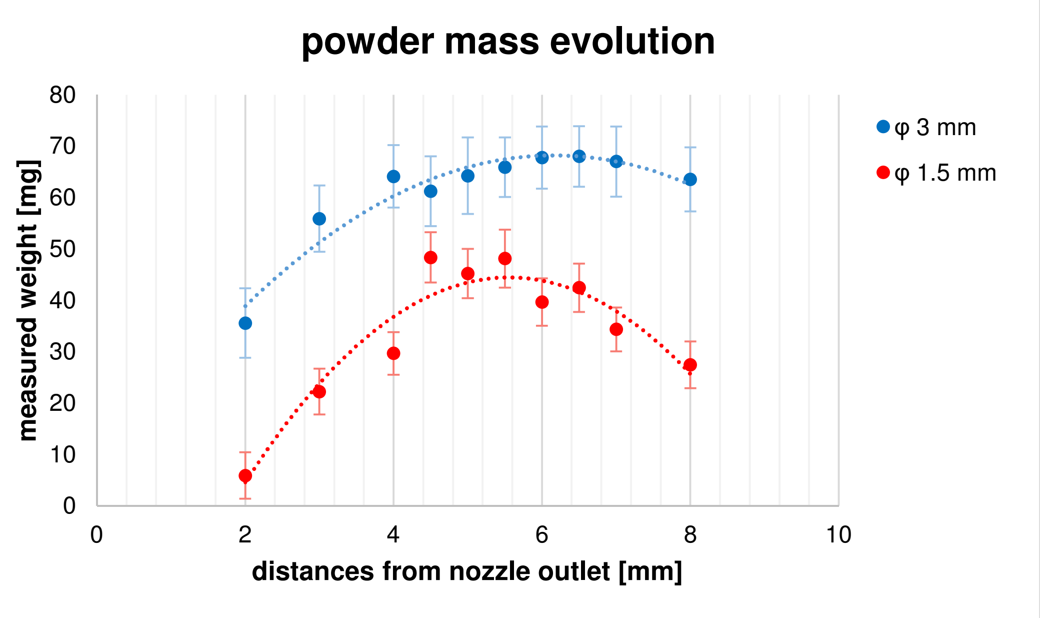

Figure 7.6 Powder mass variation profiles for the two different containers involved in the experimental validation.

7.3.3. Conclusions

In this Sub-chapter the first process step of the experimental procedure was introduced and discussed. The deposition powder cloud was characterized both numerically and experimentally and the optimal working-plane distance was defined. The results related to the CFD analysis showed to be in good agreement with the experimental investigation and the zone of maximum powder particle concentration was identified between 4.5 and 6.5 mm from the nozzle outlet (only 0.5 mm above the area of maximum particle mass concentration resulting by the numerical analysis). Moreover, the provided validation method based on a research work of Tabernero et al. [89] showed to be applicable in micro DLMD and particularly efficient for characterizing the variation of the particle mass concentration and powder distribution inside the deposition cloud, without the employment of thermal sources (as previously done in the Chapter §3). Moreover, the working-plane distance for the substrate was set at 5.5 mm from the nozzle and it was kept constant during the following experimental tests.

7.4. Monolayer micro-features

The second process step of the empirical procedure dealt with the evaluation and the choice of micro DLMD process parameters affecting the deposition of continuous and geometrically well-defined single-layer micro-features. The objective of this analysis was to define the best combinations of process factors in terms of laser power (P) and specific energy (I) to use as process parameters for the realization of 3D bulk micro-PINs. As done in the Chapter §5, the influence of P and I on the continuity and integrity of circular deposited tracks was analysed, and the best micro-features in terms of geometrical and dimensional accuracy were chosen as reference points for the successive third process step of the empirical procedure.

7.4.1. Material & methods

7.4.1.1. Experimental procedure

Table 7.4 summarizes the ranges and the levels of P and I taken into account during the experimental campaign. The analysis mainly focused on this two experimental factors because in the previous investigations laser power and specific energy demonstrated to be the most important process parameters affecting the formation, integrity, and final geometric characteristics of the deposited track (see Chapter §5). Ten passes per layer were employed, assuming the MPL building approach introduced in the Chapter §4. As shown in Table 7.4, the chosen experimental plan required three levels for P, three for I, and three repetitions for each combination of process parameters. The main effects of the evaluated factors and their interaction were analysed trough a full factorial Design of Experiments (DOE) for an overall of 81 realized single-layer micro-features.

process parameters	min value	max value	step	levels
laser power (P) [W]	18	24	3	3
specific energy (I) [J/mm^2]	300	400	50	3

Table 7.4 Evaluated factors of the experimental plan.

process parameter	value
laser scan speed (F) [mm/s]	F = P / (I*d)
Argon flow rate [l/min]	0.7
powder feed rate [mg/s]	1.723
working-plane distance [mm]	5.5
laser spot diameter (d) [mm]	0.03
laser defocusing [mm]	+0.2
preheating temperature of the substrate [°C]	T_A, 200, 400

Table 7.5 Constant process parameters.

Concerning the laser scan speed (F), it was adapted depending on the combination of P and I employed in the single experimental test, following the Equation 5.1 introduced in the Chapter §5. The substrate was located at 5.5 mm from the nozzle outlet (as find in the first process step of the experimental procedure, see Chapter §7.3), keeping a constant Argon flow rate of 0.7 l/min and a powder feed rate of

1.723 mg/s. The 30 µm laser spot was focused at 0.2 mm above the working-plane distance, enabling a positive laser defocusing of +200 µm (see Table 7.5).
All the 81 micro-features were realized with a substrate temperature equal to the ambient temperature (T_A). To better characterize the size of the deposited micro-features in terms of track width and height, the significant and well-defined features resulting from the experimental campaign at ambient temperature were repeated with a substrate temperature of 200° and 400° C. These additional depositions were required in order to improve the control on the successive micro-PINs deposition and realization, because:

- the micro-PINs realization and analysis that will be discussed in the following Chapter will take into account two different pre-heating substrate temperatures of 200° and 400° C;
- the track size was supposed to depend on the substrate temperature since it affected the molten pool formation [86].

Before running with the deposition process, the substrates were polished by a Metkon ® Forcipol planar polsher-grinder to improve and level out the starting surface condition. A paper abrasive discs with progressive grit sizes of 800, 1000, and 1200 followed by mirror finishing with a diamond paste grain size of 3 µm and 6 µm were employed. This preliminary preparation of the metal substrate was required and strongly recommended since the analysis conducted in the Chapter §5 showed the high influence of the starting surface condition of the substrate on the molten pool formation and integrity when the DLMD process is applied at the micro-scale.

7.4.1.2. Micro-features considerations

Due to the cylindrical geometry of the micro-PIN cross section, the single-layer micro-features were thin micro-circles with a diameter of 2mm (see Fig. 7.7). As happened in the analysis carried out in the Chapter §5, the circular geometry of the artefact allowed a constant motion of the laser beam on the surface of the substrate during the deposition process. The absence of geometrical sharp angle or sudden direction changes in the motion of the laser beam was advantageous to keep a constant velocity during the part realization, avoiding uncontrolled acceleration or deceleration of the moving table of the Manudirect ® MSL50 system (see Chapter §5.2.2).

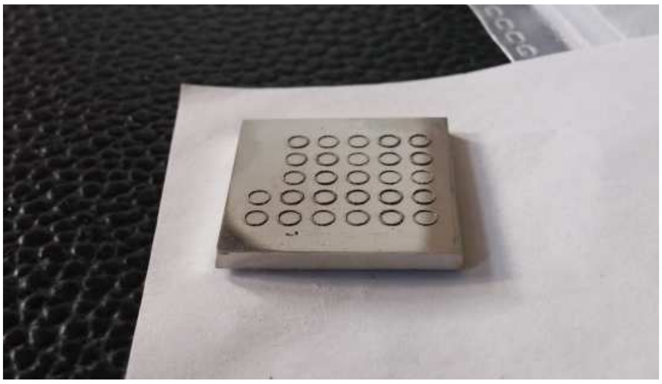

Figure 7.7 Single-layer micro-features realized in the experimental plan.

7.4.1.3. Micro-features characterization

The realized single-layer micro-features were characterized in terms of deposited track continuity, integrity, and presence of powder agglomeration along the edges of the deposited track. A preliminary and qualitative evaluation of the realized artefacts was carried out through FEI Quanta ® 400 Scanning Electron Microscopy (SEM) with ETD detector (see Chapter §2.3.1).

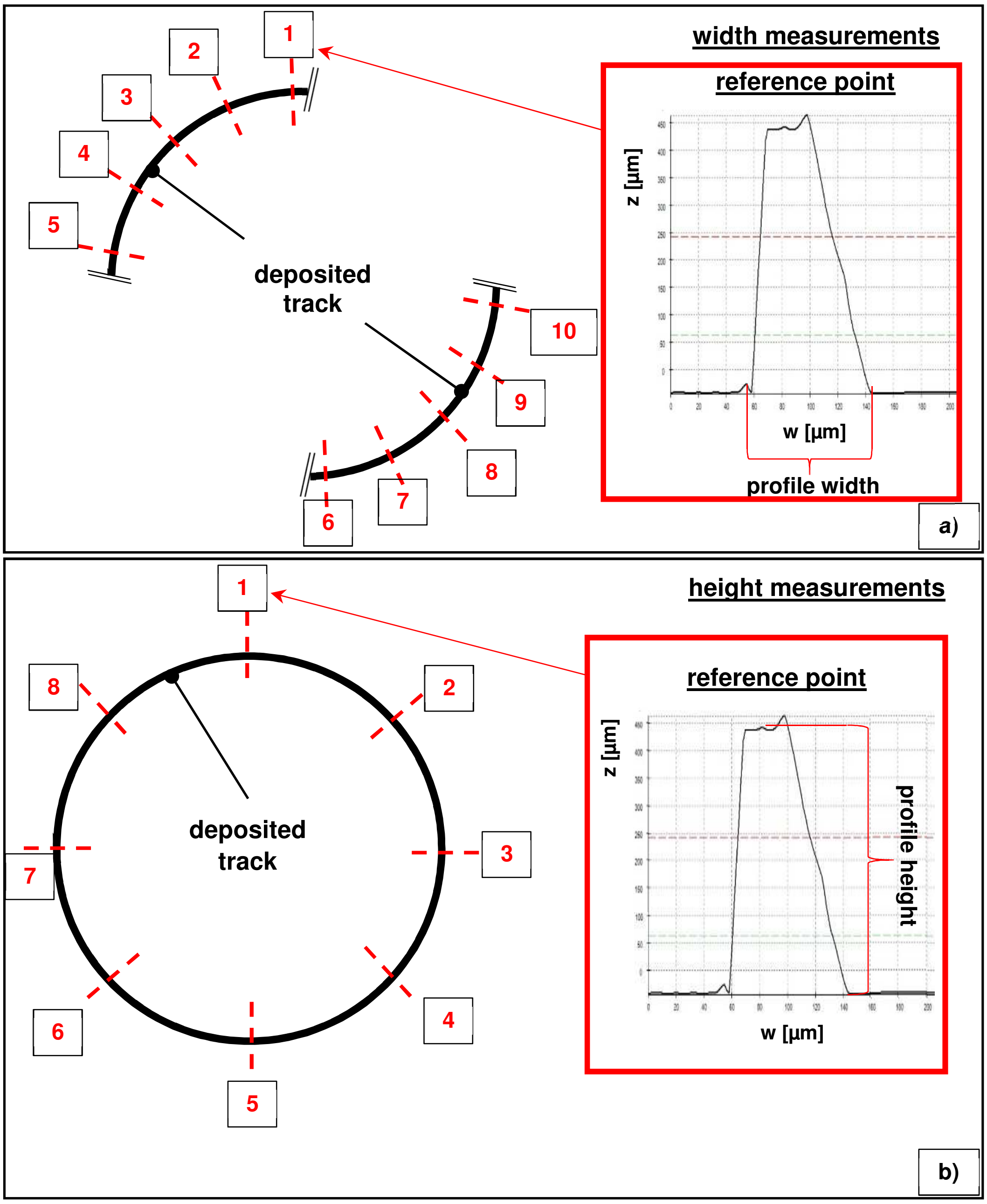

Figure 7.8 a) schematic representation of track width measurements; b) schematic representation of track height measurements.

The thin single-layer circles showing a good continuity and integrity of the deposited track were quantitatively characterized in terms of average track width and height through SEM and Optical profilometer measurements respectively. The average width of each micro-feature was detected averaging ten measurements of the track width taken along ten reference point of the metal bead extension (see Fig. 7.8 a), whereas the average height was detected averaging eight measurements as shown in the Figure 7.8 b.

7.4.2. Results

The experimental results obtained from this experimental investigation are listed in the Table 7.6 and represented in the Figures 7.9, 7.10, and 7.11. In Table 7.6, the words “discontinuous”, “acceptable”, and “poor” characterized the quality and the integrity of the deposited track qualitatively. The meaning of each term was:

- “discontinuous” stayed for a deposited track with points of discontinuities and interruptions along the extension of the track bead (see Fig. 7.9 a, 7.10 a, 7.11 a);
- “acceptable” stayed for a continuous deposited track without the presence of powder agglomerations along the track edge, that might deteriorate the integrity of the realized micro-feature and compromise the deposition of successive layers (see Fig. 7.9 b, 7.10 b, 7.11 b and c) ;
- “poor” stayed for a continuous deposited track but with a dimensional accuracy deteriorated by the presence of powder agglomeration along the track edges (see Fig. 7.9 c and 7.10 c).

The micro-artefacts realized with the lower value for the laser power (18 W) showed a discontinuous deposited track for every level of the specific energy taken into account during the experimental campaign. Figure 7.12 shows evident interruptions of the metal track bead independently from the specific energy employed. The presence of such discontinuities along the track extension deteriorated the quality of the micro-features and weakened the integrity of the part. For this reason, all the combinations of process parameters showing local interruptions on the continuity of the deposited layer were rejected and not taken into account in the future experimental analysis.

Increasing the laser power (from 18 to 24 W), the integrity of the realized micro-features improved, getting more continuous deposited tracks for every value of specific energy employed. Nevertheless, 24 W combined with 300 and 350 J/mm^2 deteriorated the dimensional accuracy of the artefact, causing both a strong formation of powder agglomerations adhered along the track edges and a large deposition of partially-melted powder particles close to the metal track bead (see Fig. 7.13). The presence of these accumulations of powder adhered to or close to the metal bead might negatively affect the successive deposition of new layers, growing in size with the progress of the process. In particular the main consequences derived by these defects were:

- powder agglomerations locally modified the height and the uniformity of growth of the deposited track, prejudicing the deposition of a new layer on the top of the previous one and deteriorating the final quality of the micro-part in terms of dimensional and geometrical accuracy (see Chapter §5.3.1);

- powder attached along the deposited track affected the cooling behaviour of the molten pool, modifying the cross sectional shape of the solid metal bead (see Chapter §5.3.2);
- a high presence of powder particles close to the deposited track might compromise the deposition of successive layer near the previous one, screening the surface of the substrate off from the laser beam and impeding the formation a stable molten pool.

These three undesired effects given by the presence of the aforementioned powder agglomerations were supposed to compromise the manufacture of the part, prejudicing the DLMD process in terms of loss of control in the deposition of new layers and internal porosity generation. For this reasons, all the combinations of process parameters showing the generation of these defects were rejected and not taken into account in the future experimental analysis.

		specific energy [J/mm^2]		
		300	350	400
laser power [W]	18	discontinuous	discontinuous	discontinuous
	21	acceptable	acceptable	acceptable
	24	poor	poor	acceptable

Table 7.6 Preliminary characterization of the single-layer micro-features.

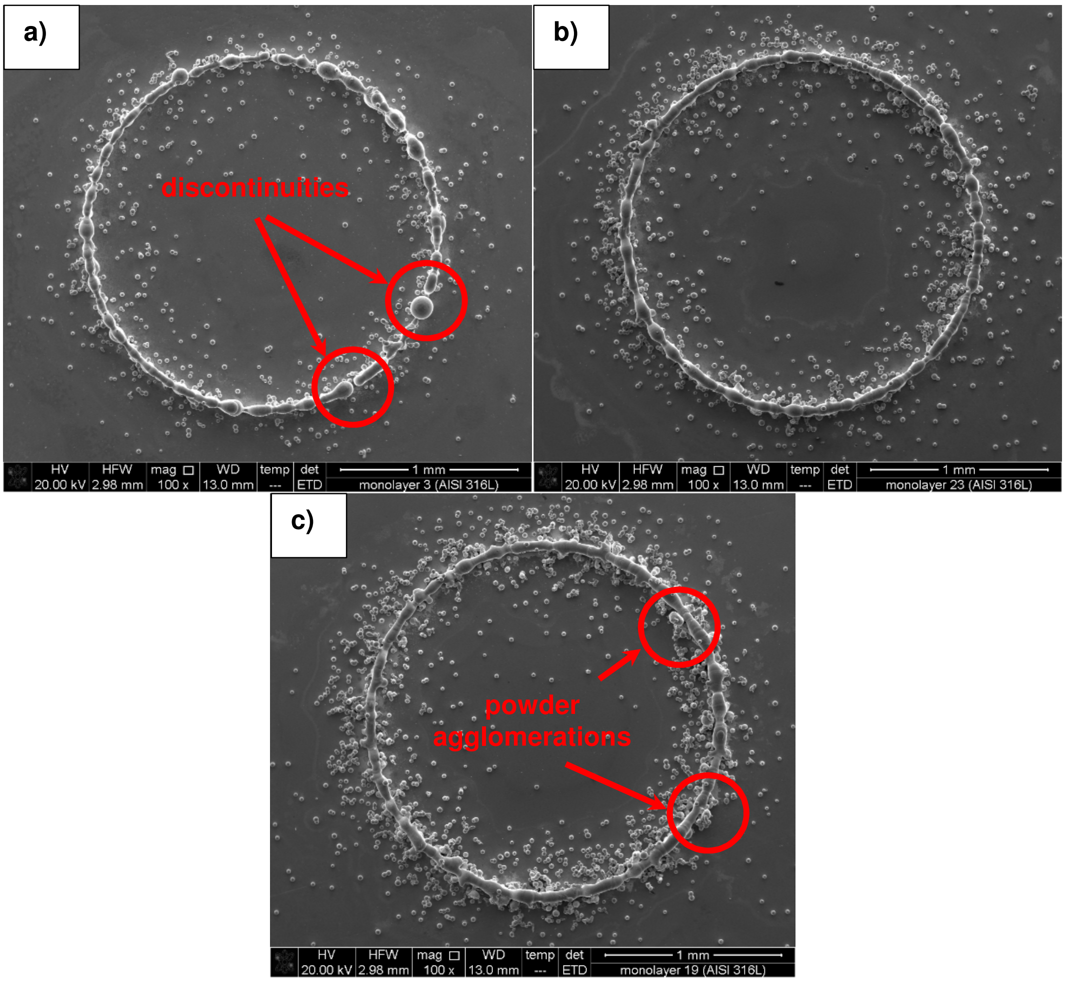

Figure 7.9 Single-layer micro-features realized with I = 300 J/mm^2: a) P = 18 W; b) P = 21 W; c) P = 24 W.

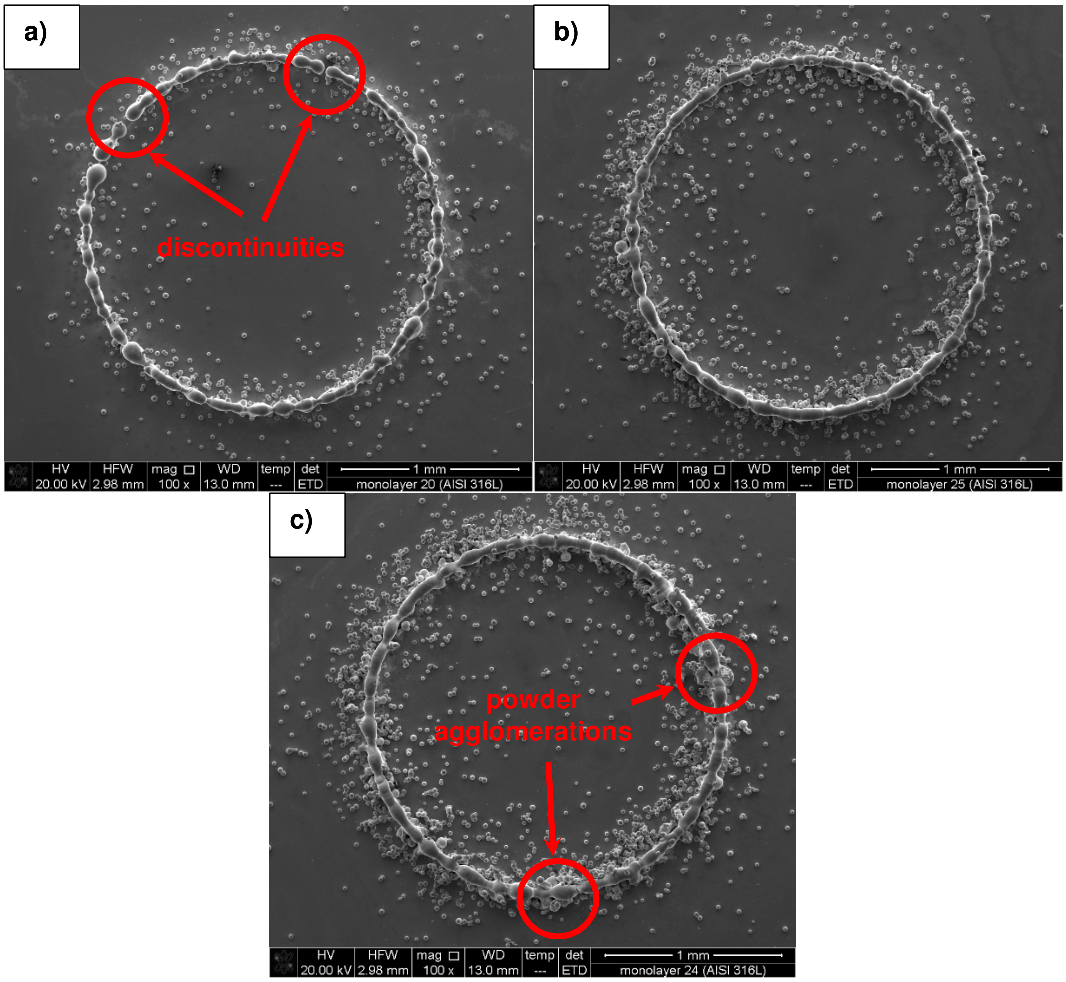

Figure 7.10 Single-layer micro-features realized with I = 350 J/mm^2: a) P = 18 W; b) P = 21 W; c) P = 24 W.

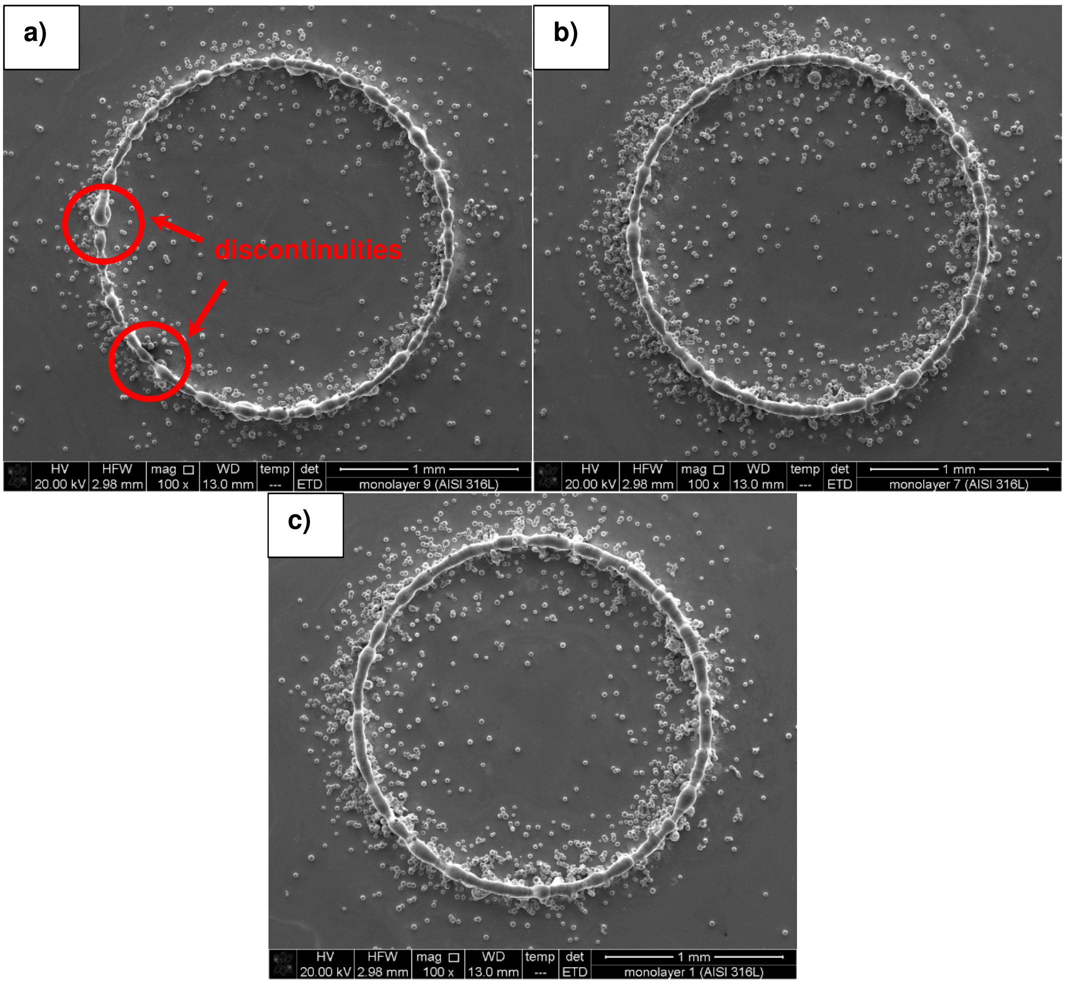

Figure 7.11 Single-layer micro-features realized with I = 400 J/mm^2: a) P = 18 W; b) P = 21 W; c) P = 24 W.

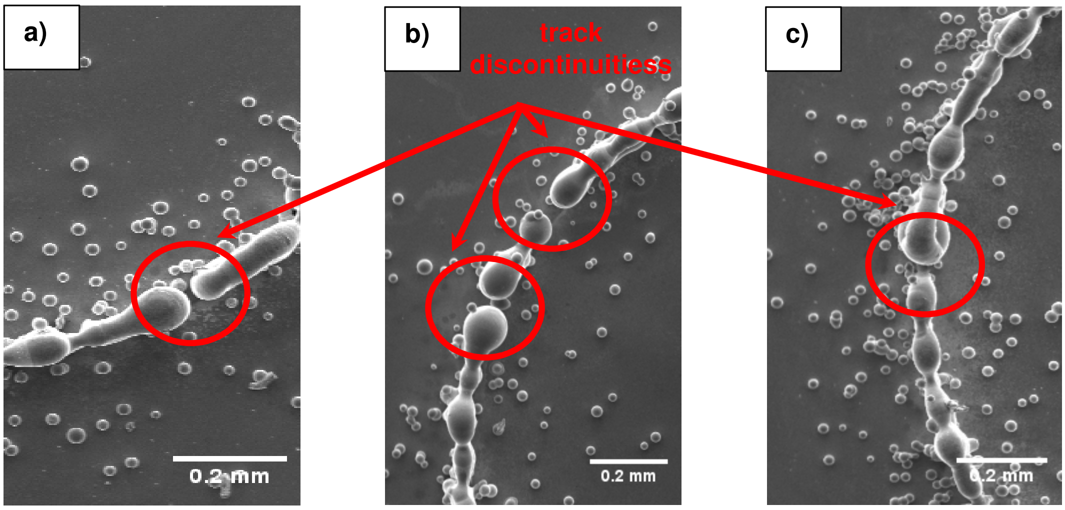

Figure 7.12 Discontinuities along the metal bead extension for P = 18 W: a) 300 J/mm^2; a) 350 J/mm^2; a) 400 J/mm^2.

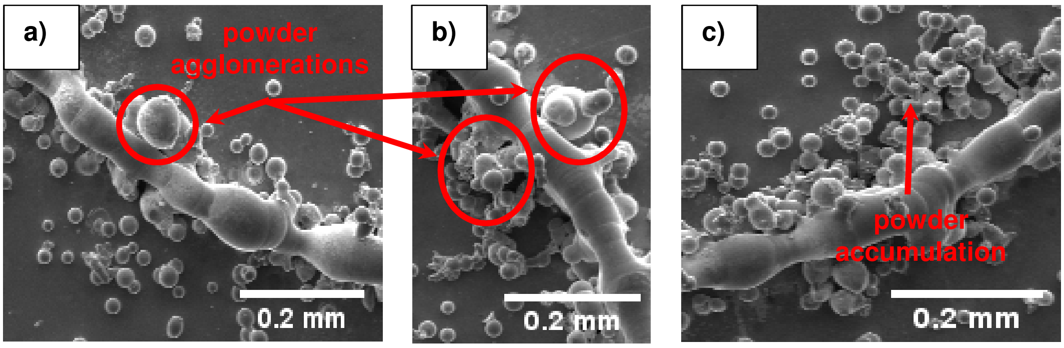

Figure 7.13 a)-b) powder agglomerations attached along the track edges; c) powder accumulations covering the surface of the substrate.

Good results in terms of track continuity and powder agglomerations-free layer were obtained for a laser power of 21 W combined with every value for I, and a laser power of 24 W combined with a specific energy of 400 J/mm^2 (see Table 7.6). The average width of the “acceptable” tracks was detected by SEM measurements as shown in the Figure 7.14.

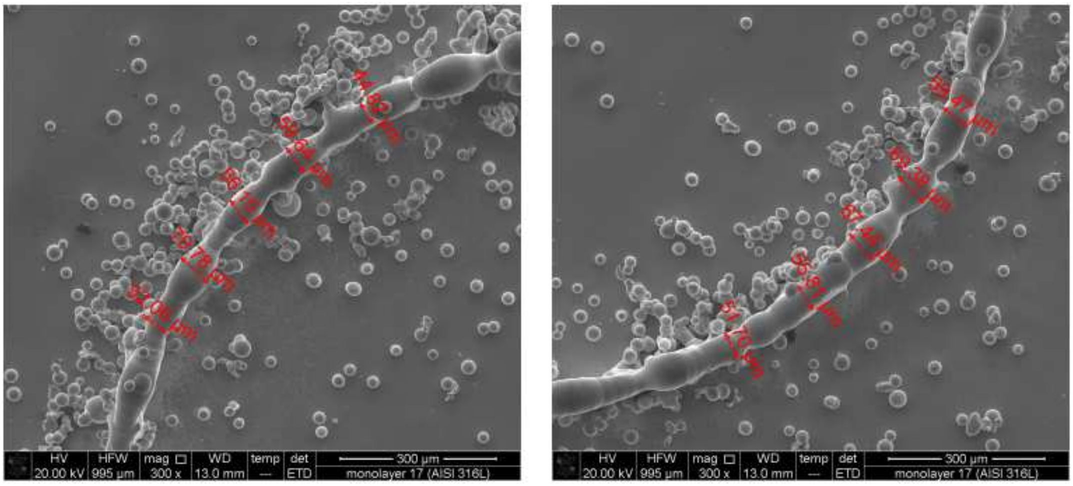

Figure 7.14 Example of width measurements through SEM characterization (I = 400 J/mm^2, P = 21 W).

Table 7.7 summarizes the outputs in terms of average track width and corresponding standard deviation for the deposited layer evaluated “acceptable” during the qualitative analysis through SEM imaging. The results showed an average track width ranging between 55 and 60 µm with the highest standard deviations for high laser power (11.66 µm for a specific energy of 350 J/mm^2 and 10.13 µm for a specific energy of 400 J/mm^2). Based on this observations, parameter combinations with medium value of laser power (21 W) combined with both the lowest and highest specific energy (300, 400J/mm^2 respectively) exhibited less fluctuation in width with lower standard deviation (9.34 and 9.41 µm respectively).

process parameters		average width [µm]	standard deviation [µm]
P [W]	*I [J/mm²]*		
21	300	55.14	9.34
21	350	53.49	11.66
21	400	58.41	9.41
24	400	60.78	10.13

Table 7.7 Width measurements of the good deposited tracks.

These two combinations of process parameters resulting in "acceptable" deposited layer with low fluctuation in track width were chosen to proceed with the experimental investigation and realize the bulk micro-PINs.

Before going on with the empirical procedure and starting with the PIN manufacture, 12 additional single-layer micro-features were realized to analyse the effect of different pre-heating temperatures of the substrate on the final geometry of the track metal bead. In this case, the evaluated process parameters were a constant laser power of 21 W, two levels for the specific energy (300 and 400 respectively), and two values for the pre-heating temperature (200° and 400° C). The outputs in terms of average track width and height are listed in Table 7.8.

process parameters			width_{AVG} [µm]	std dev [µm]	height_{AVG} [µm]	std dev [µm]
P [W]	*I [J/mm²]*	*T [°C]*				
21	300	T_A	55.14	9.34	95.48	18.13
21	300	200	57.12	9.76	89.97	18.20
21	300	400	58.28	10.03	75.86	19.3
21	400	T_A	58.41	9.41	134.09	25.65
21	400	200	59.44	8.55	101.91	21.34
21	400	400	62.63	10.06	92.27	22.19

Table 7.8 Width and height measurements of the chosen single-layer micro-features.

The experimental results showed a decrease in the average layer height with the increase of the pre-heating temperature. For a constant laser power of 21 W and a constant specific energy of 300 J/mm^2, the average finale height of the layer decreased from 95.48 up to 75.86 µm. This reduction was more visible for I equal to 400 J/mm^2 since the average height of the track reduced from 134.09 to 92.27 µm. At the same time, an increment of the pre-heating temperature of the substrate corresponded to a slight increase in the track width (see Table 7.8). The reason of this phenomenon might be explained taking into account the fluid-dynamics involved in the molten pool formation. Indeed, for a pre-heated substrate, less laser energy was dispersed to locally increase the temperature of the substrate, encouraging the formation of a warmer molten pool with a lower viscosity and leading to a smaller and wider track.

7.4.3. Conclusions

In this second process step, the influence of the laser power and specific energy on the continuity and powder agglomeration-free AISI 316L single-layers micro-features was analysed with the aim to determine the best combination of process parameters to employed for the micro-PIN manufacture.

A laser power of 21 W and a specific energy of 300 and 400 J/mm^2 were found to be the best combinations of process parameter ensuring a good quality and continuity of the deposited layer (“acceptable” tracks) with no formation of powder adhesion along the track edges and with the lowest standard deviation concerning the track width variation.

The increase of the pre-heating temperature of the substrate affected the shape of the deposited layer, causing an evident decrease in the average track height and a light increase in the layer width due to the reduction in viscosity of the melted material for the higher temperatures of the substrate.

$P = 21$ W combined with $I = 400$ J/mm^2 and $I = 300$ J/mm^2 respectively were chosen be the combinations of process parameters to employed during the micro-PIN manufacture.

7.5. Micro-PIN realization

The third and last process step of the empirical procedure dealt with the manufacture of bulk micro-PIN, analysing how the deposition strategy and the pre-heating temperature of the substrate affected the final quality of the micro-parts in terms of dimensional and geometrical accuracy, internal porosity, and final surface roughness.

In this experimental investigation, the process parameters such as working-plane distance, laser power, and specific energy were set equal to those found in the previous process steps (see Chapter §7.3 and §7.4). The objective of this experimental analysis was to demonstrate the feasibility of DLMD process in manufacturing 3D bulk micro-parts (i.e. micro-PINs), characterizing the artefacts in terms of structural and surface integrity.

7.5.1. Material and methods

7.5.1.1. Experimental plan

Table 7.9 summarizes the DLMD process parameters kept constant during the experimental investigation, whereas Table 7.10 shows the process parameters evaluated as factors of the experimental plan.

The main effects of the evaluated process parameters and their interactions were analysed through a full factorial Design of Experiments (DOE), taking into account two levels for each factor. Moreover, three repetitions for each combination of process parameters were realized to have scientific reliability for an overall of 24 realized micro-PINs.

process parameter	value
Argon flow rate [l/min]	0.7
powder feed rate [mg/s]	1.723
working-plane distance [mm]	5.5
laser spot diameter (d) [mm]	0.03
laser defocusing [mm]	+0.2
laser power [W]	21

Table 7.9 Process parameters kept constant during the experimental plan.

process parameters	min value	max value	step	levels
preheating temperature of the substrate (T) [°C]	200	400	200	2
deposition strategies	A	B	-	2
specific energy (I) [J/mm^2]	300	400	100	2

Table 7.10 Evaluated factors of the experimental plan.

In order to easily handle for future characterizations, each micro-PIN was manufactured over a small AISI 316L Stainless Steel cylindrical substrate with a height of 2 mm and a diameter of 5 mm. The cylindrical substrates were placed in a bigger AISI 316L Stainless Steel drilled substrate with a size of 20x20 mm and a thickness of 2 mm that was directly fixed into the clamping system of the MSL50 machine (see Fig. 7.15).

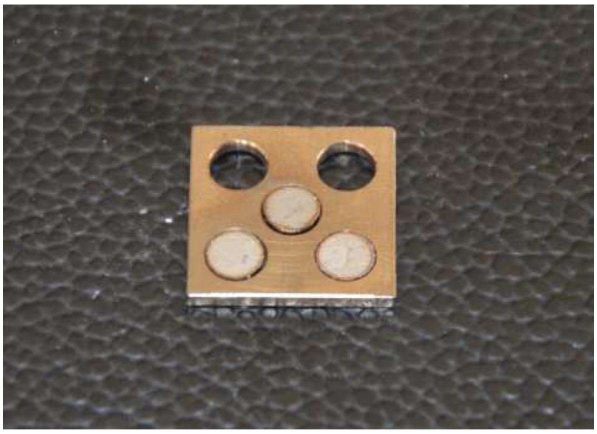

Figure 7.15 Small cylindrical substrates in the holder square support.

In order to improve the clamping in the MSL50 machine, the small substrates were fixed with adhesive tape on the back side.

Contrary to what happened with the realization of thin micro-artefact (see Chapter §6), for the manufacture of a 3D bulk part through DLMD, one more process parameter was required, that was the hatching distance between successive tracks. The hatching distance was defined as the relative gap between the axis of successive tracks. In particular, if this distance was smaller than the track width, an overlapping between tracks happened. On the contrary, for hatching distances larger than the track width, the deposition layer was deposited without overlapping between tracks. This was an important parameter since it affected the free space between successive track depositions and consequently the intra-layer porosity of the realized part.

In this specific case, the hatching distance was set equal to 60 µm and kept constant for all the manufactured micro-PINs. The value of 60 µm was chosen because it was a good compromise between the average width of 58.28 and 62.63 µm resulted for 21 W combined with 300 J/mm^2 and 21 W combined with 400 J/mm^2 respectively.

Regarding the displacement of the substrate along the z direction after the complete realization of each layer (i.e. the nominal height of the deposited layer) it was set equal to the approximation of the average track height detected for each combination of process parameters to use in the micro-PIN manufacture. Table 7.11 summarizes the hatching distances and the Δz displacements for each combination of process parameters employed during the experimental tests.

process parameters			**hatching distance [µm]**	**Δz displacement [µm]**
P [W]	*I [J/mm^2]*	*T [°C]*		
21	300	200	60	90
21	300	400	60	76
21	400	200	60	102
21	400	400	60	92

Table 7.11 Hatching distance and z displacement employed during the experimental plan for each combination of process parameters.

After deposition, the micro-PINs were cleaned in Acetone and deionized water solution using an ultrasonic cleaner.

7.5.1.2. Micro-features considerations

The micro-PINs were cylindrical micro-parts with a nominal diameter of 0.4 mm and a nominal height of 2 mm (see Fig. 7.16).

For an AM technology point of view, a 3D bulk part was equivalent to a collage of layers with a predefined shape and thickness. Moreover, the technological nature of the DLMD process intrinsically identified each single layer as a sum of successive tracks deposited close to each other (see Fig. 7.16 b). This meant that, under a deposition point of view, the DLMD process was very similar to the Fused

Deposition Modeling (FDM), where the metal deposited tracks were replaced by warm polymeric filament. Therefore, for a DLMD process, whatever bulk part to manufacture appeared as a composition of successive layers which, in turn, were built up by several deposited tracks close to each other.

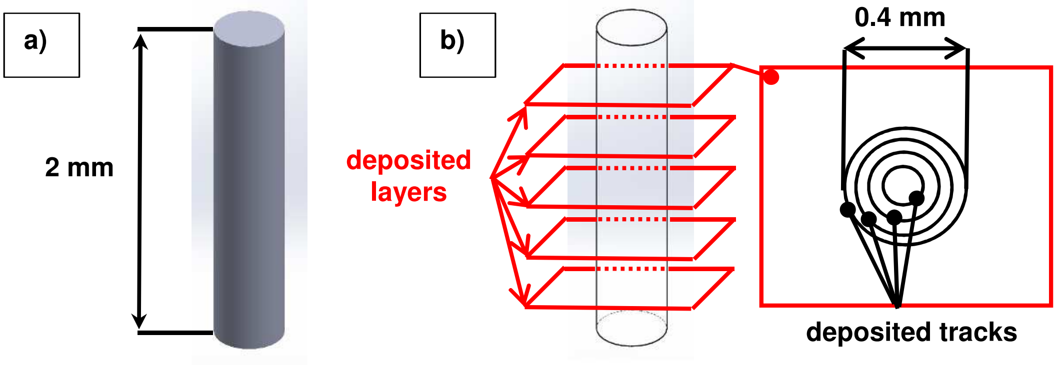

Figure 7.16 a) nominal size of the micro-PIN; b) slicing and deposited tracks.

Concerning the specific case of the micro-PIN realization, the cross-section of the micro-part was composed by three concentric circular tracks with a diameter (referred to the track axis) of 0.160, 0.280, and 0.400 mm respectively (see Fig. 7.17).

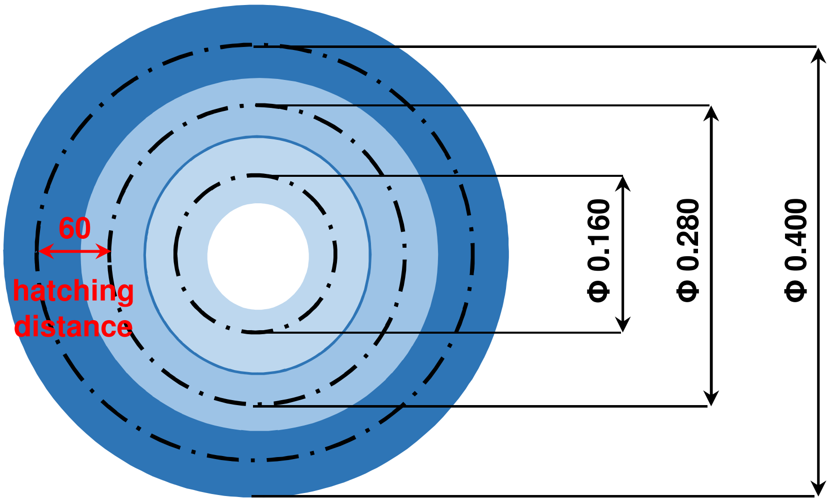

Figure 7.17 Track distribution for each deposited layer (mm).

The track arrangement represented in Figure 7.17 was called offset track deposition. For this offset configuration, DLMD process showed to be thermally critical at the centre of the layer due to the high thermal gradient involved. Moreover, in this zone the temperature of the molten pool could rise up due to the multiple passes per layer required by the MPL approach, causing a conspicuous enlargement of the molten pool and an uncontrollable growth of the deposition track. For this reason, the geometrical shape of circular layer was specifically designed to generate a central free-space large enough to avoid not-controlled heat accumulations at the centre of the part and an instable growth of the deposition track during the deposition process.

7.5.1.3. Deposition strategies considerations

Two different deposition strategies were designed to evaluate the influence of the inter-layer idle time on the final quality of the realized micro-parts in terms of structural integrity and lateral surface roughness. The idle time was defined as the timing between successive track depositions and it was one of the most important process parameters affecting the thermal gradient and local heat accumulations involved during the DLMD process. In this specific case, the two designed strategies did not differ in the geometry or location of the deposited tracks, but in the timing of deposition between the three concentric circular tracks forming the deposited layer. They were defined as follows:

- *deposition strategy A*. Three micro-PINs representing the three repetitions for each combination of process parameters were manufactured together. In this case, the inner circular track with a nominal diameter of 0.160 mm was realized first for all the three micro-PIN repetitions (blue line in the Figure 7.18). Successively, the middle track (green line) and the external one (orange line) were realized according to the deposition order represented in the Figure 7.18.

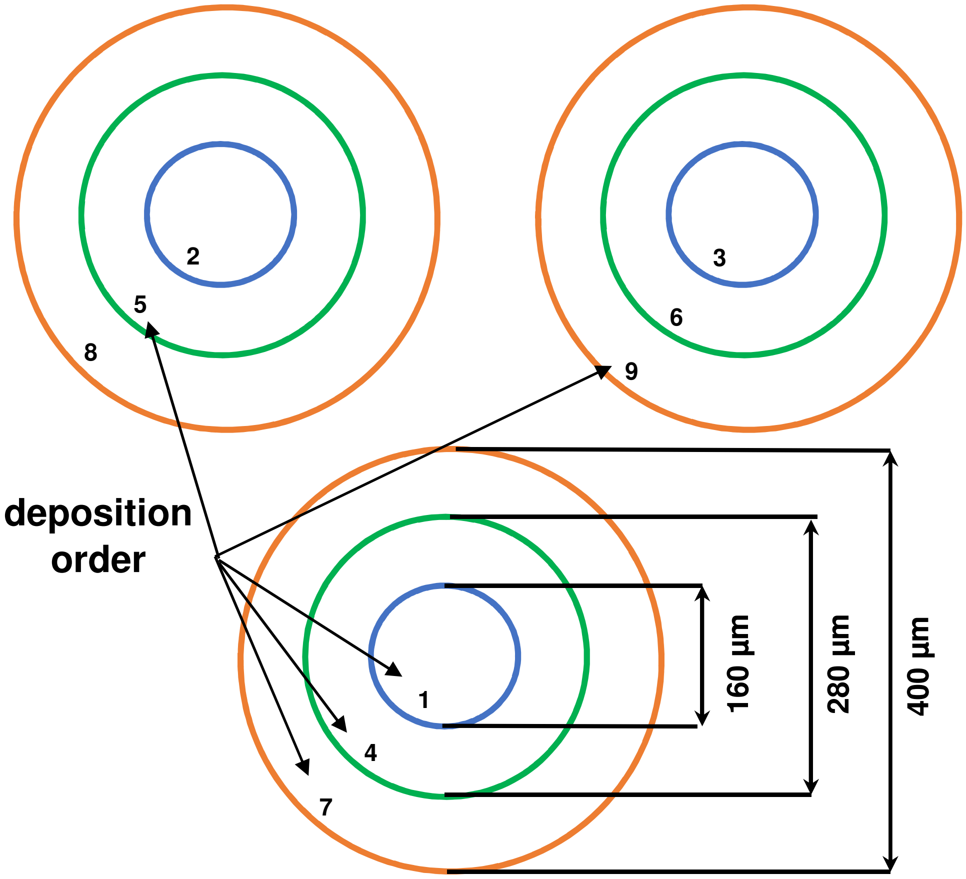

Figure 7.18 Deposition strategy A.

The objective of this strategy was to realize each layer alternatively, reducing the heat accumulations between successive depositions of tracks belonging to the same layer. Moving from a micro-Pin repetition to another for each deposited track, the idle time was long enough to disperse the accumulated heat through the metal substrate. After the realization of the entire layer, the metal substrate moved down of a gap equal to the track height defined in the Table 7.11 and the deposition process continued as previously introduced;

- *deposition strategy B*. Three micro-PINs representing the three repetitions for each combination of process parameters were manufactured together. In this case, the inner, the middle, and the external circular tracks were realized sequentially on the same repetition. After that, the deposition process moved on the second and third repetition respectively following the order represented in the Figure 7.19.

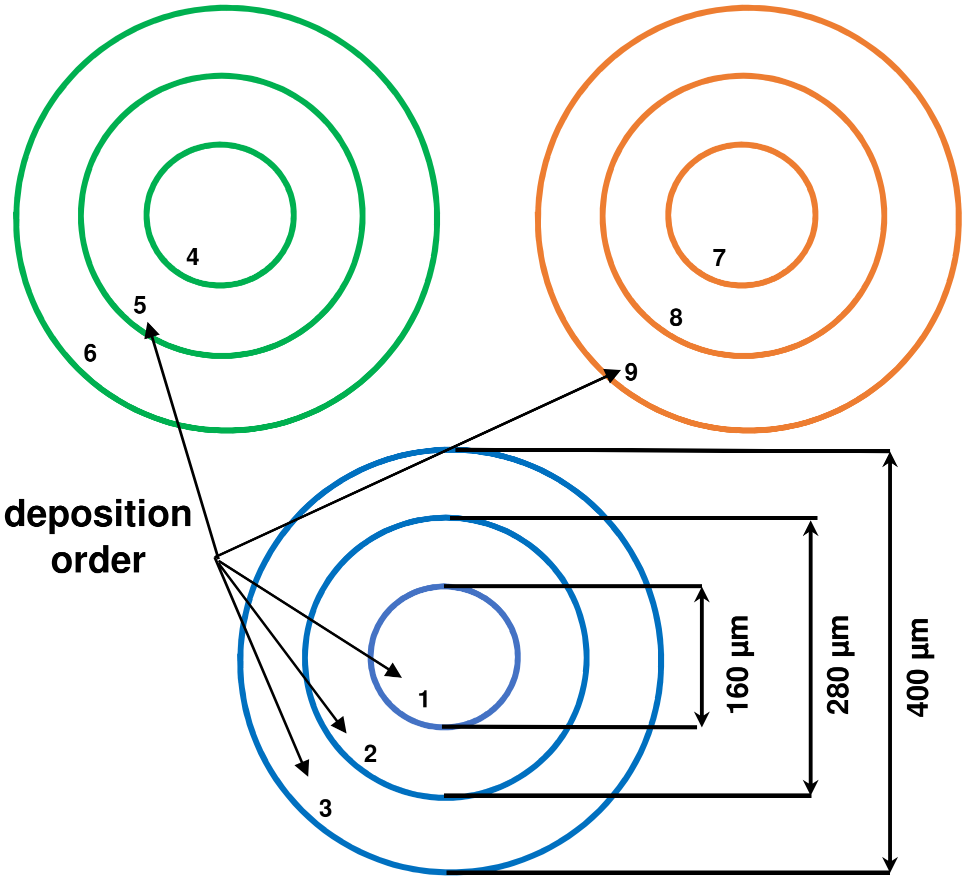

Figure 7.19 Deposition strategy B.

Contrary to deposition strategy A, here the layer was realized continuously, incrementing the heat accumulations and thermal gradient involved during the deposition process. After the realization of the entire layer, the metal substrate moved down of a gap equal to the track height defined in the Table 7.11 and the deposition process continued as previously introduced.

7.5.1.4. Micro-PIN characterization

After deposition process, the realized micro-PINs were characterized though three different instruments of analysis:

- FEI Quanta 450 ® Scanning Electron Microscope (SEM) with ETD detector (see Chapter §2.3.1) to qualitatively evaluate the topography and surface condition of the micro-parts, providing also some dimensional measurements of the artefact;
- Sensofar Plus Neox 3D ® Optical Profilometer (see Chapter §2.3.2) to detect and quantitatively analyse the surface conditions of the realized micro-PINs in terms of lateral surface roughness, “stepwise” effect”, and presence of partially-melted powder particles along the vertical sides of the PINs;
- Nikon Metrology X-Tek MCT225 ® metrological X-ray Computed Tomography (see Chapter §2.3.3) to evaluate the structural integrity of the micro-parts and the internal porosity distribution along the bulk of the micro-PIN.

The methodology followed to detect the surface roughness variation is explained in detailed in the Appendix B.

7.5.2. Results

The results obtained from the experimental campaign were in part unexpectedly surprising and in part unsatisfying which suggested the need of further investigations to improve the final quality of the artefact and the control of the DLMD process applied at the micro-scale.

7.5.2.1. Dimensional accuracy and integrity of the micro-PINs

Independently from the employed combination of process parameters, all the 24 micro-PINs where characterized by a particular external morphology characterized by two distinctive zones (see Fig. 7.20):

- in the lower side of the micro-PINs, a necking zone appeared. Here, the cylindrical shape of the micro-artefact was not well defined, but a strong deterioration with a high presence of defects (e.g. powder accumulations) was evident. In this zone the structural and superficial integrity of the artefact was strongly compromised, showing a strong reduction of the micro-PIN width compare to the designed nominal width of 400 µm. (see Fig. 7.20);
- in the upper side of the micro-PINs, the integrity and dimensional accuracy of the micro-artefact improved. Here, the cylindrical shape of the micro-PIN was complied and the number of partially-melted powder particles stuck on the PIN surface decreased. No necking was detected, but the width of the micro-part showed to be more uniform.

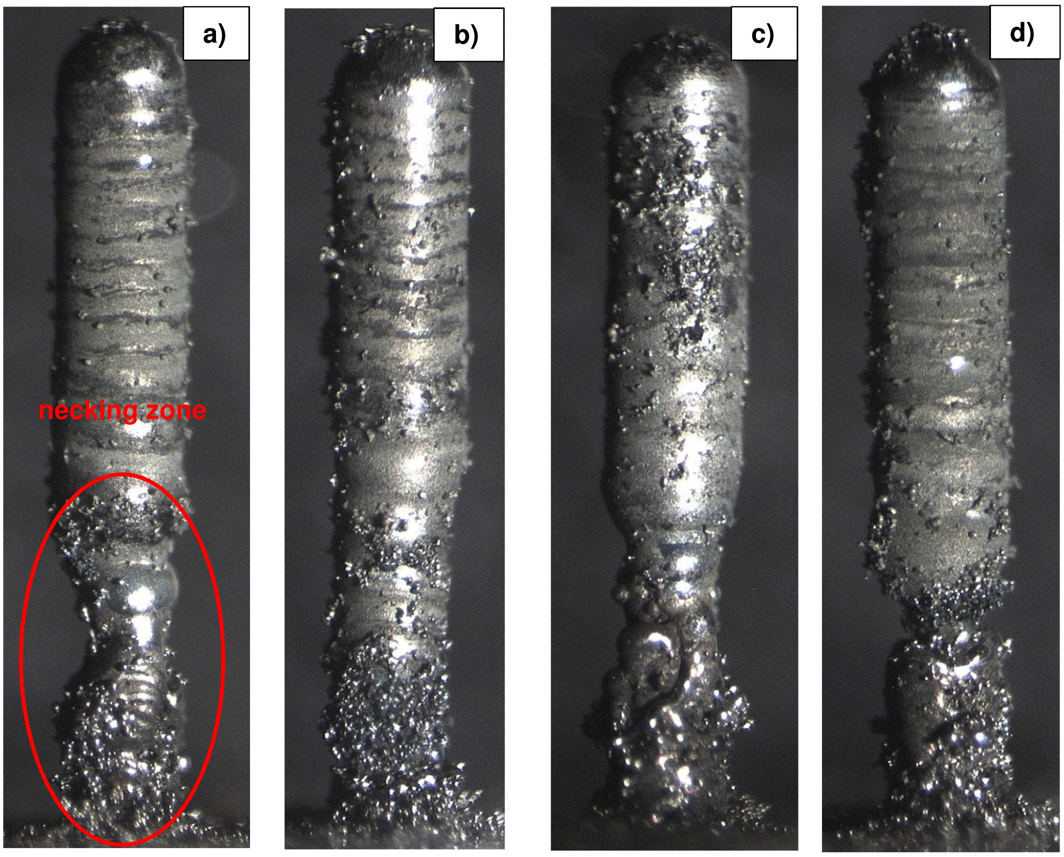

Figure 7.20 Micro-PINs image at the optical microscope: a) I = 400 J/mm^2, T = 400° C, deposition strategy A; b) I = 300 J/mm^2, T = 200° C, deposition strategy A; c) I = 300 J/mm^2, T = 400° C, deposition strategy A; d) I = 400 J/mm^2, T = 400° C, deposition strategy B.

Figure 7.21 represents two images derived by the CT scan analysis and shows one of the 24 micro-PINs realized during the experimental plan. As supposed by the previous external analysis carried out though optical microscope, the lower side of the micro-PIN showed a necking zone with a strong presence of voids and internal porosity with an evident deterioration and weakening of the structure. Figure 7.22 represents the necking zone in detail. As we can observe, in the lower side of the micro-part, the reduction in width of the micro-parts was because the growth of the middle and external tracks was suddenly interrupted. The reasons of this phenomenon were not well understood, but it could be explained by the concomitance of two effects:

- the excessive and uncontrolled growth of the inner circular tracks compared to the middle and external tracks;
- the influence of the metal substrate on the metal particles trajectories and consequently on the distribution of the powder coming out from the nozzle during the deposition process.

Figure 7.22 b shows a prevalent growth of the inner circular track compared to the middle and external tracks belonging to the deposition layer clearly. The reason of such phenomenon could be explained by the high thermal fluxes involved during the inner track deposition. Keeping constant P, I, and the number of passes per layer for each concentric circular tracks, the track with the shortest length was subjected to the highest heat accumulations and thermal gradients during the deposition process. As a consequence, the resulting molten pool was warmer and with a larger size which entrapped a bigger number of powder particles, causing a faster growth of the metal bead compared to the middle and external track belonging to the same deposition layer.

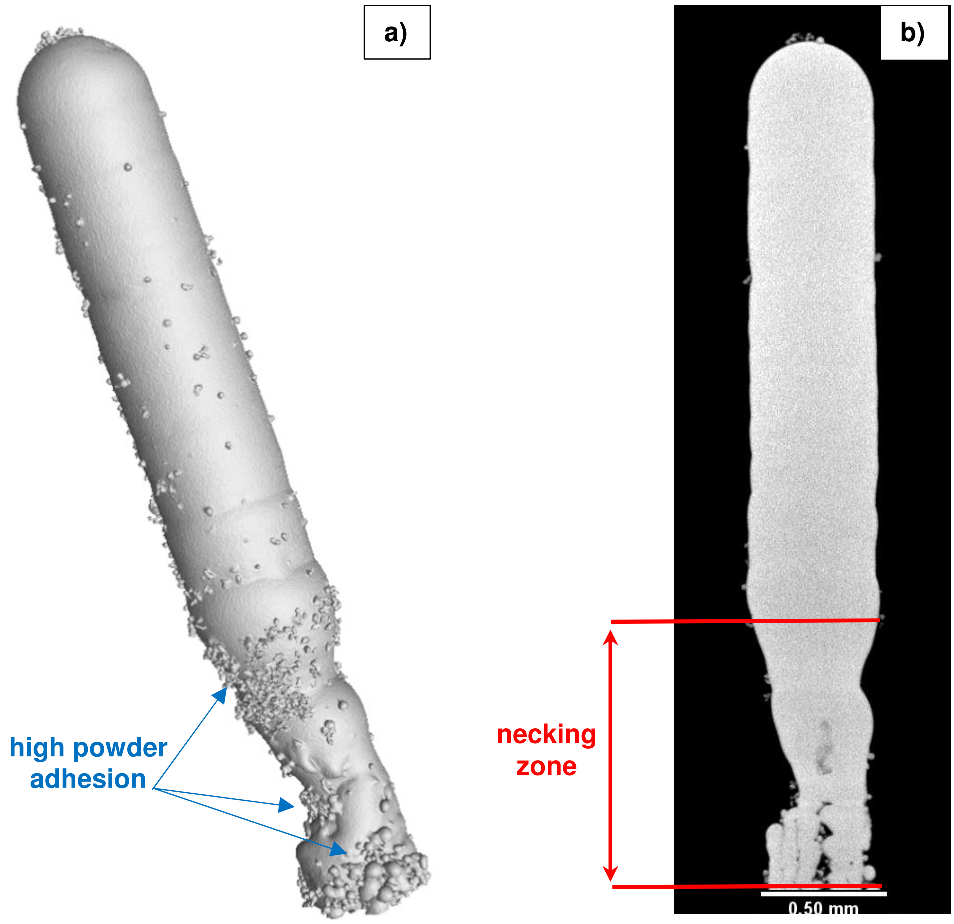

Figure 7.21 Micro-PIN realized with I = 400 J/mm^2, T = 400° C, deposition strategy A: a) 3D CT scan image of the analysed micro-PIN; b) internal CT scan analysis.

The high thermal fluxes generated in correspondence to the inner track were supported by the presence of the *Balling phenomenon* that caused an uncontrolled width extension and track growth during the deposition of the first layers (see Fig. 7.22 a and d). As analysed in the Chapter §5, *Balling* was a consequence of the high temperature and thermal gradients involved during the deposition process and was responsible of a strong deterioration of the artefact. In this specific case, the *Balling* confirmed the development of high heat accumulations during the inner track formation, deteriorating the micro-artefact in terms of structural integrity and dimensional accuracy.

Close to the substrate, the micro-PIN showed a high number of voids between the tracks, indicating a high internal porosity (see Fig. 7.22 b and d). In particular, the number of powder particles partially-melted and adhered to the external side of the micro-artefact is high (see Fig. 7.21 a).

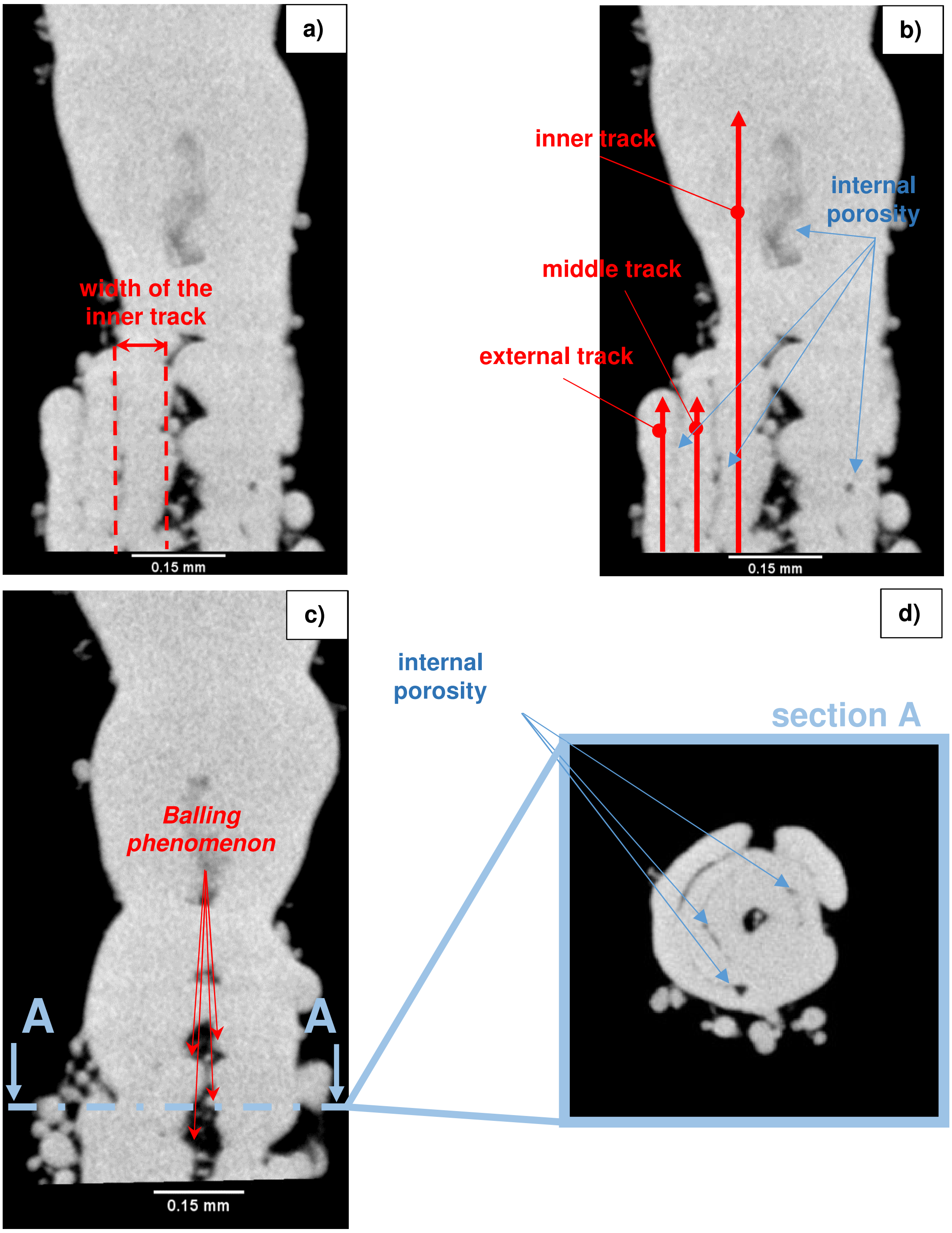

Figure 7.22 Details of the necking zone: I = 400 J/mm^2, T = 400° C, deposition strategy A.

The sudden and uncontrolled growth of the inner circular track caused a progressive changing of the relative distance between the optics of the laser and the surface where the molten pool formed. Indeed, being the growth rate of the inner track higher than the nominal layer height designed in the experimental plan, the starting laser defocusing of +0.2 mm gradually decreased with the increase of the deposition, causing an increase in the laser spot. The increase of the laser spot caused an increment of the size of the molten pool with a consequent increase of the deposited track. At the top of the necking zone, the laser spot was so large to fill the designed internal free space at the centre of the micro-PIN completely (see Fig. 7.22). The gradual enlargement of micro-part width on the top of the necking zone acted as screen for the middle and external tracks which did not receive the supply of fresh powder and interrupted their growth (see Fig. 7.23).

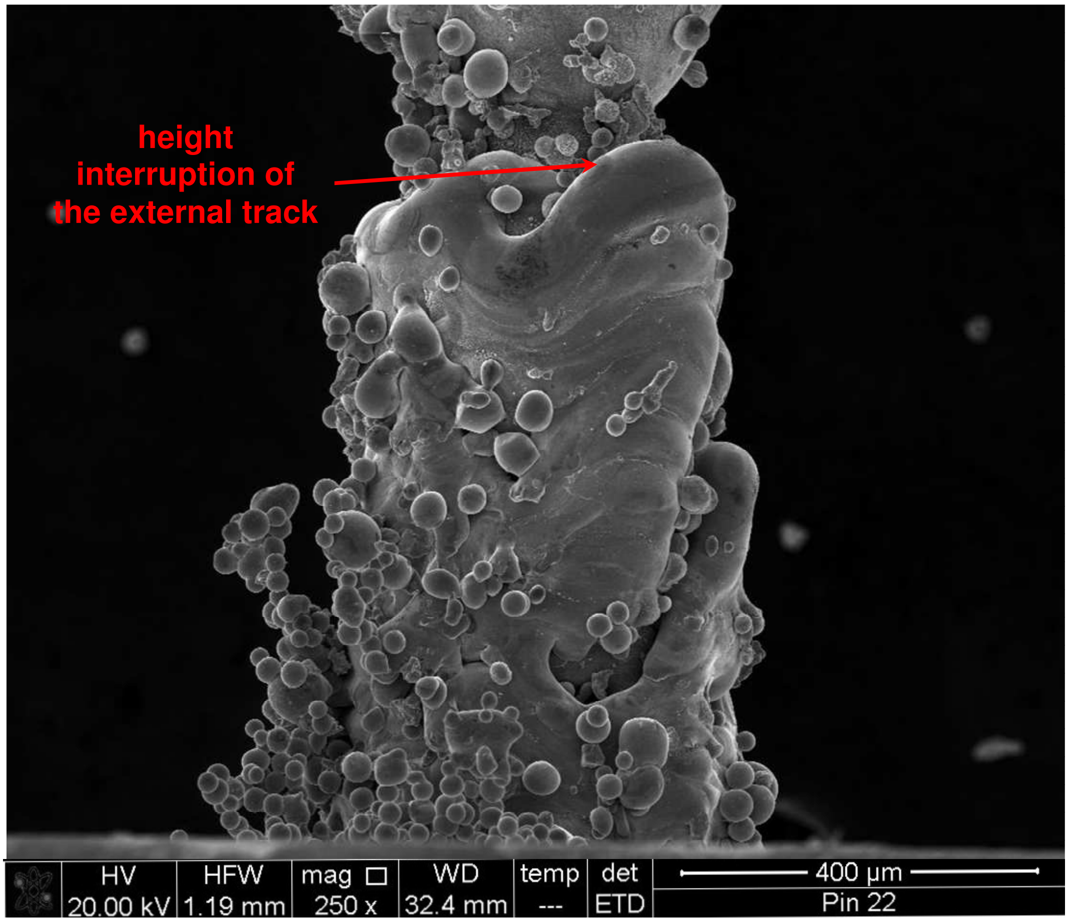

Figure 7.23 First layers of deposition: I = 300 J/mm^2; T = 400° C; deposition strategy B.

Moreover, the influence of the heat accumulation on the uncontrolled growth of the inner track was supposed to be aggravated by the distortion of the fluid-dynamic behaviour of the metal particles due to the presence of the metal substrate. To have a preliminary response on this hypothesis, some CFD analysis were carried out to evaluate the influence of the metal substrate on the particle trajectories and powder distribution during the deposition process numerically. The theoretical model and assumptions assumed in these analyses were the same introduced in the previous Chapter §3. As solid boundary, two different substrates were taken into account:

- one flat substrate with no presence of micro-PINs on the surface and located at 5.5 mm from the nozzle outlet;
- one substrate located at 5.8 mm from the nozzle outlet and having a micro-PIN 0.3 mm tall at the top of its surface;

Figure 7.24 graphically compares the new CFD results with those obtained in the Subchapter §7.3.1.1 where no substrate was taken into account.

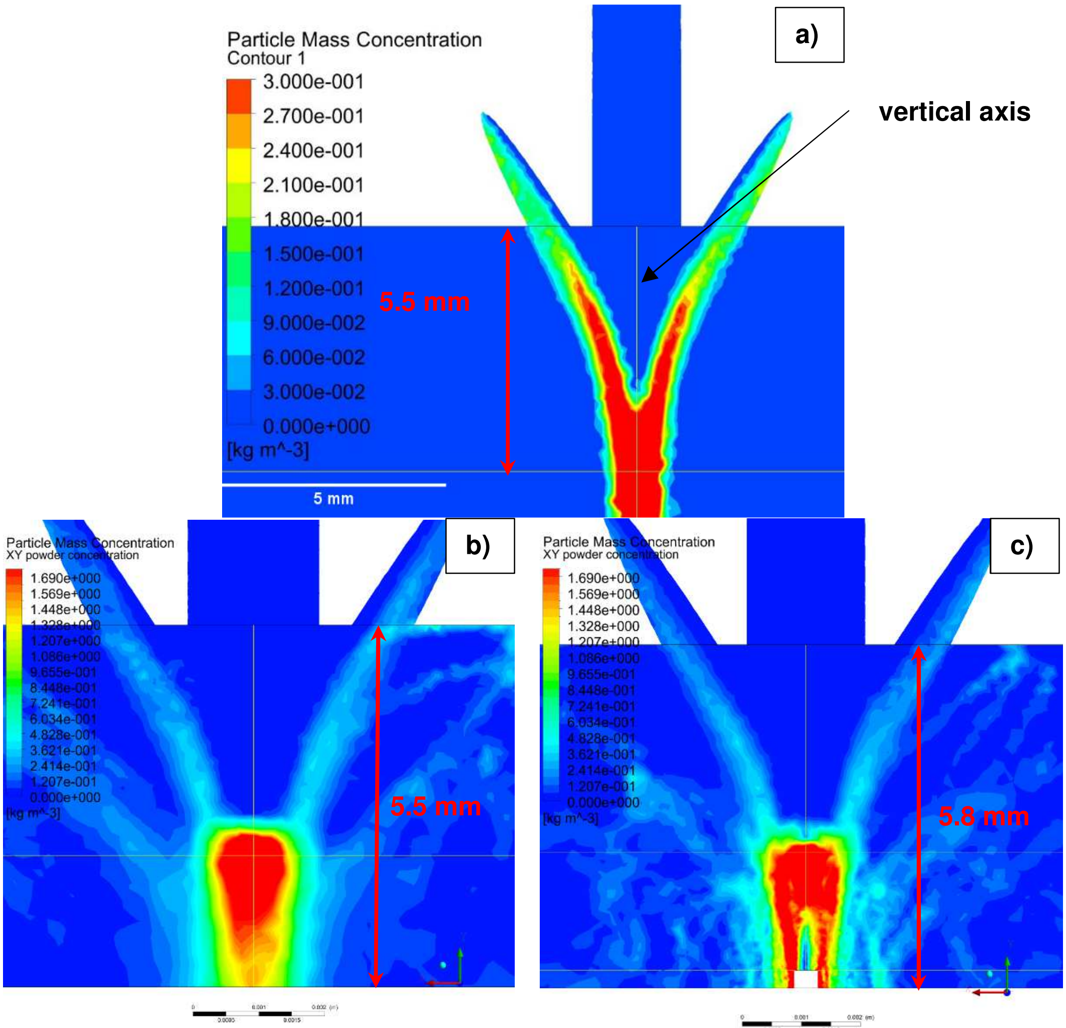

Figure 7.24 a) CFD analysis without the substrate presence; b) CFD analysis with the presence of a flat substrate; c) CFD analysis with the presence of a substrate with a micro-PIN 0.3 mm tall.

The presence of the substrate strongly affected the powder distribution in proximity to the metal plain surface. Figure 7.24 b and c shows that the maximum particle mass concentration was not at 5.5 mm as demonstrated in the Figure 7.24 a, but it shifted some millimetres above, probably due to the rebound of the powder particles on the metal substrate. Moreover, in the cases b and c the maximum of particle mass concentration is one order of magnitude bigger than in the case a. The particle mass concentration was more critical when a micro-PIN started to form. Figure 7.24 c shows a powder distribution not homogeneous on the top of the micro-part, but strongly concentrated along the edges of the artefact and some millimetres above the micro-part. The CFD results underlined a possible process issue in the powder deposition when a substrate was present below the nozzle. Further experimental investigation were required to analyse how acting on the Argon flow rate to increase the particle mass concentration in correspondence to the molten pool, but, unfortunately, no more tests were possible to carry out in time due to an important breakdown of the MSL50 system, causing a forced stop of more 5 months.

Table 7.12 summarizes the results in terms of final height. All the 24 micro-PINs reached an average final height taller than the nominal one designed in the experimental plan. The reason was mainly related to the presence of the necking zone at the starting layers of deposition. The vertical extension of this zone is considerable high and it was ranging between 1 and 1.6 mm in average.

process parameters			**final height [mm]**
I [J/mm²]	*T [°C]*	*deposition strategy*	
300	200	A	3.536
300	400	A	3.525
400	200	A	3.767
400	400	A	3.776
300	200	B	3.48
300	400	B	3.429
400	200	B	3.542
400	400	B	3.557

Table 7.12 Final height of the realized micro-PINs.

The upper side of the micro-PINs showed a better internal integrity and a more uniform width (see Fig. 7.25 and 7.26). CT scan analysis did not detect internal porosity. The reason probably was related to the increase in the laser spot due to the excessive growth of the artefact in the first layers of deposition. Independently from the employed combination of process parameters, in this zone the CT images showed a “stepwise” effect surprising reduced with the lateral sides of the micro-artefact almost straight. Nevertheless, the deposition layer are clearly visible since they were defined by horizontal stripes (see Fig. 7.26 a). Table 7.13 summarizes the average width detected by SEM measuring. The experimental results showed a nominal width larger than the nominal one designed by the experimental plan. The evaluated process parameters did not show a considerable influence on the width variation of the upper side of the micro-PINs which generally ranged between 490 and 500 µm roughly (respectively 30 and 40 µm larger than the nominal designed width of 460 µm). The reason of this enlargement is probably related to the increased in the molten pool size due to the widening of the laser spot. The author believed it was the cause of limited stepwise effect detected in this case, but no robust bases supported this hypothesis and further experimental investigation were required to deeply analyse this phenomenon.

Unfortunately, and important breakdown of the MSL50 system made impossible further experimental test required to analyse the phenomenon detected during the micro-Pin characterization specifically and to improve the final quality of the micro-artefacts.

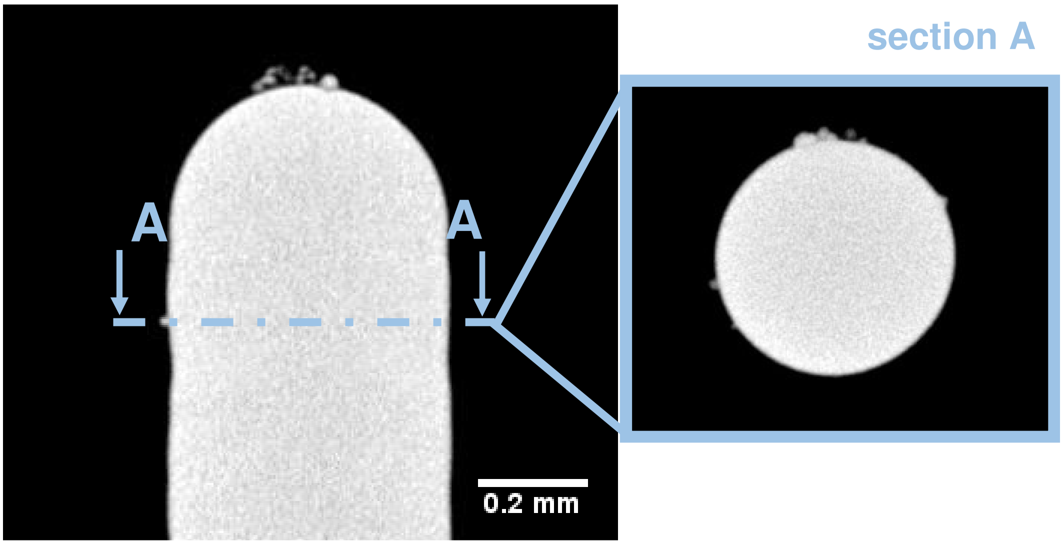

Figure 7.25 CT scan image of the upper side of the micro-PIN (I = 400 J/mm^2, T = 400° C, deposition strategy A).

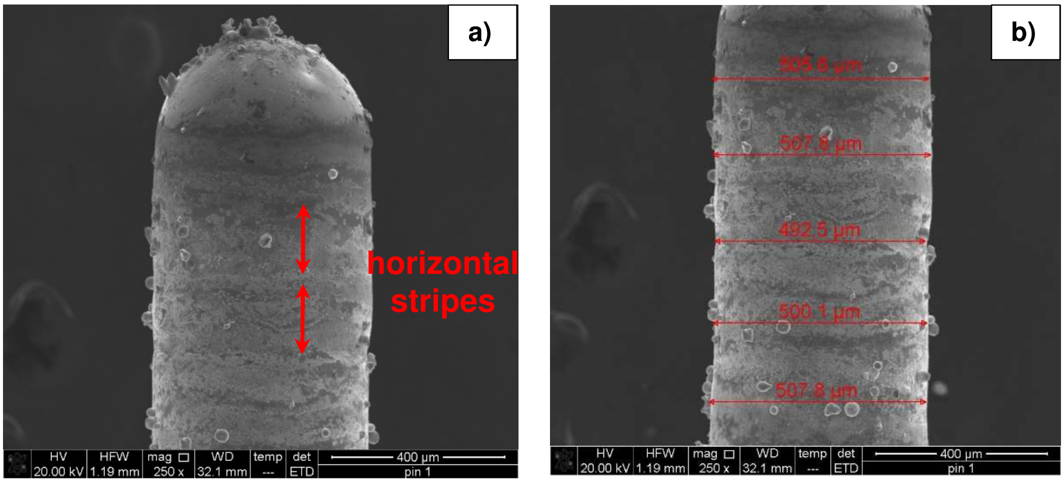

Figure 7.26 SEM image of the upper side of the micro-PIN (I = 400 J/mm^2, T = 400° C, deposition strategy A): a) horizontal stripes; b) width evaluation.

process parameters			**average width [µm]**
I [J/mm²]	*T [°C]*	*deposition strategy*	
300	200	A	495.19
300	400	A	493.46
400	200	A	487.02
400	400	A	505.35
300	200	B	493.04
300	400	B	490.45
400	200	B	490.82
400	400	B	497.52

Table 7.13 Average width of the upper side of the micro-PINs.

7.5.2.2. Micro-PIN final surface conditions

To completely characterize the final quality of the realized micro-PINs, a further analysis was carried out to investigate the influence of the evaluated process parameters on the final surface condition of the micro-artefact.

This analysis focused on the upper side of the micro-PINs since it was the part of the artefact with a good structural integrity. The surface condition was carried out detecting:

- the lateral surface roughness of the cylindrical artefact;
- the presence of powder particles adhered to the micro-PIN surface.

The surface roughness was evaluated along an evaluation length of 1.2 mm (see Fig. 7.27) following the measurement procedure discussed in the Appendix B. In this way it was defined an evaluation area where roughness parameters could be evaluated (see Fig. 7.27 b). To separate the roughness analysis from the presence of powder particles adhered to the micro-PIN surface, it was measured the percentage of observed area occupied by powder particles, locating them by a threshold height imposed equal to 15 µm, considered more than the expected roughness crests. Table 7.14 and 7.15 summarize the results in terms of S_i and R_i obtained by the surface investigation.

The performed ANOVA analysis showed a strong influence of the preheating temperature of the substrate on the final surface roughness of the micro-PIN (see Table 7.16). Indeed, the influence of this process parameter was significant, showing a *p-value* lower than the maximum acceptable value of 0.05. Table 7.14 and 7.15 report how the surface roughness improved increasing the preheating substrate temperature from 200 to 400° C. Concerning S_a, it decreased with the increase of T from a value of 3.43 to 1.87 µm. The specific energy and the deposition strategy had no influence on the final surface roughness in the evaluated process range. Nevertheless, the interaction between I and deposition strategy had a *p-value* very close to the maximum acceptable value of 0.05 (i.e.

0.069). This fact could imply a very small influence of these two parameters on the evaluated output even if there was no statistical support. If the main- and interaction-plots were taken into account, the interaction between the aforementioned factors was more evident (see Fig. 7.27 and 7.28). Figure 7.28 a underlines that an important interaction between the specific energy and the deposition strategy occurred. In particular, the surface roughness improved if high values for the specific energy were combined with the deposition strategy B (i.e. low idle time), or low values for I were combined with the deposition strategy A (i.e. high idle time). Nevertheless, the reason of this experimental behaviour was not easy to formulate and understand due to the formation of the necking zone (transient zone) that changed the starting process condition (e.g. laser defocusing, layer height, etc.) and affected the micro-DLMD process in an uncontrolled way.

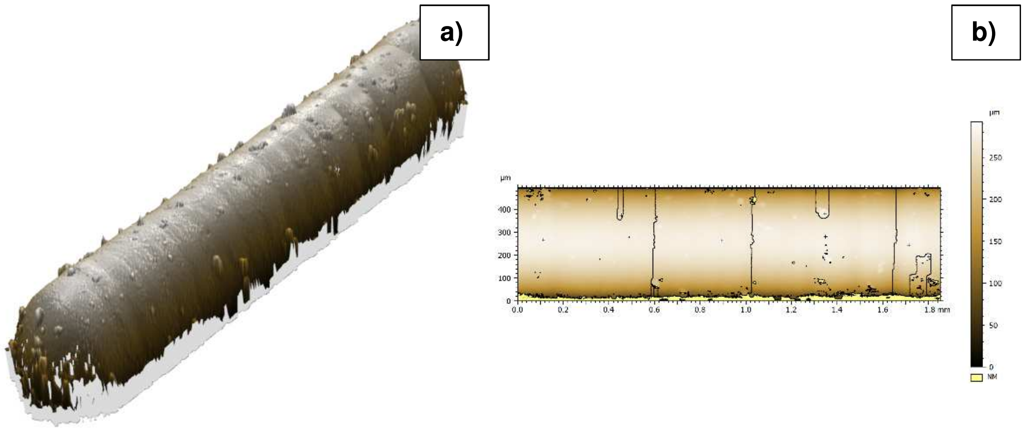

Figure 7.27 a) example of micro PIN measurement through optical profilometer; b) example of roughness evaluation area.

process parameters			S_a [µm]	S_q [µm]	S_z [µm]
I [J/mm^2]	*T*	*strategy*			
400	400	A	2.23	3.47	29.17
400	200	A	3.57	5.47	36.3
300	400	A	1.66	2.42	18.8
300	200	A	2.99	4.15	29.33
400	400	B	1.4	1.82	14.49
400	200	B	2.86	4.38	32.73
300	400	B	2.2	3.05	25.9
300	200	B	4.28	5.56	36.27

Table 7.14 Lateral surface roughness, S_i coefficients.

process parameters			R_a [µm]	R_q [µm]	R_z [µm]
I [J/mm^2]	*T*	*strategy*			
400	400	A	1.22	1.8	8.69
400	200	A	1.83	2.53	11.77
300	400	A	0.9	1.23	5.62
300	200	A	1.54	2.25	11.09
400	400	B	0.62	0.8	3.56
400	200	B	1.3	1.89	8.69
300	400	B	0.95	1.37	6.89
300	200	B	1.6	2.18	10.1

Table 7.15 Lateral surface roughness, R_i coefficients.

source	DF	Adj SS	Adj MS	F-Value	P-Value
linear					
strategy	1	0.02	0.02	0.02	0.897
I [J/mm^2]	1	0.496	0.496	0.43	0.522
T [°C]	1	14.711	14.711	12.73	0.003
interactions					
strategy*I	1	4.395	4.395	3.8	0.069
strategy*T	1	0.32	0.32	0.28	0.606
I*T	1	0.113	0.113	0.1	0.758
strategy*I*T	1	0.122	0.122	0.11	0.75
error	16	18.487	1.155		
total	23	38.663			

Table 7.16 ANOVA of the surface roughness S_a.

Looking to R_z, its high values reflected the presence of very big powder particles on external surface. It was about an half of powder particle diameter, because they had to be in a semi melt state in order to adhere to the micro-PIN lateral surface.
Furthermore confronting R_a with R_q their values were similar. So could be concluded that adhered powder particles covered a small percentage of surface, confirming what observed by SEM analysis.
Analysing surface parameters reported in tab. 10.2 could be done similar observation to the profile one. S_z values were about an order of magnitude bigger

than S_a that was generally very close to S_q, reporting the presence of restricted zone where superficial height was elevated.

The adhesion of the powder particles on the lateral side of the micro-artefacts was quite high for all the 24 micro-PINs and affected the final quality of the surface negatively. None of the considered parameters or interactions were estimated influential since the influence of each single parameters on this phenomenon was not clearly visible. Indeed, all of them had a *p-value* above the supposed maximum acceptable value of 0.05. This fact was linked to the high variability of stuck powder area percentage between repetitions using the same parameters. Hence, it was not possible to suggest any direction of parameter optimization assuming an reasonable risk.

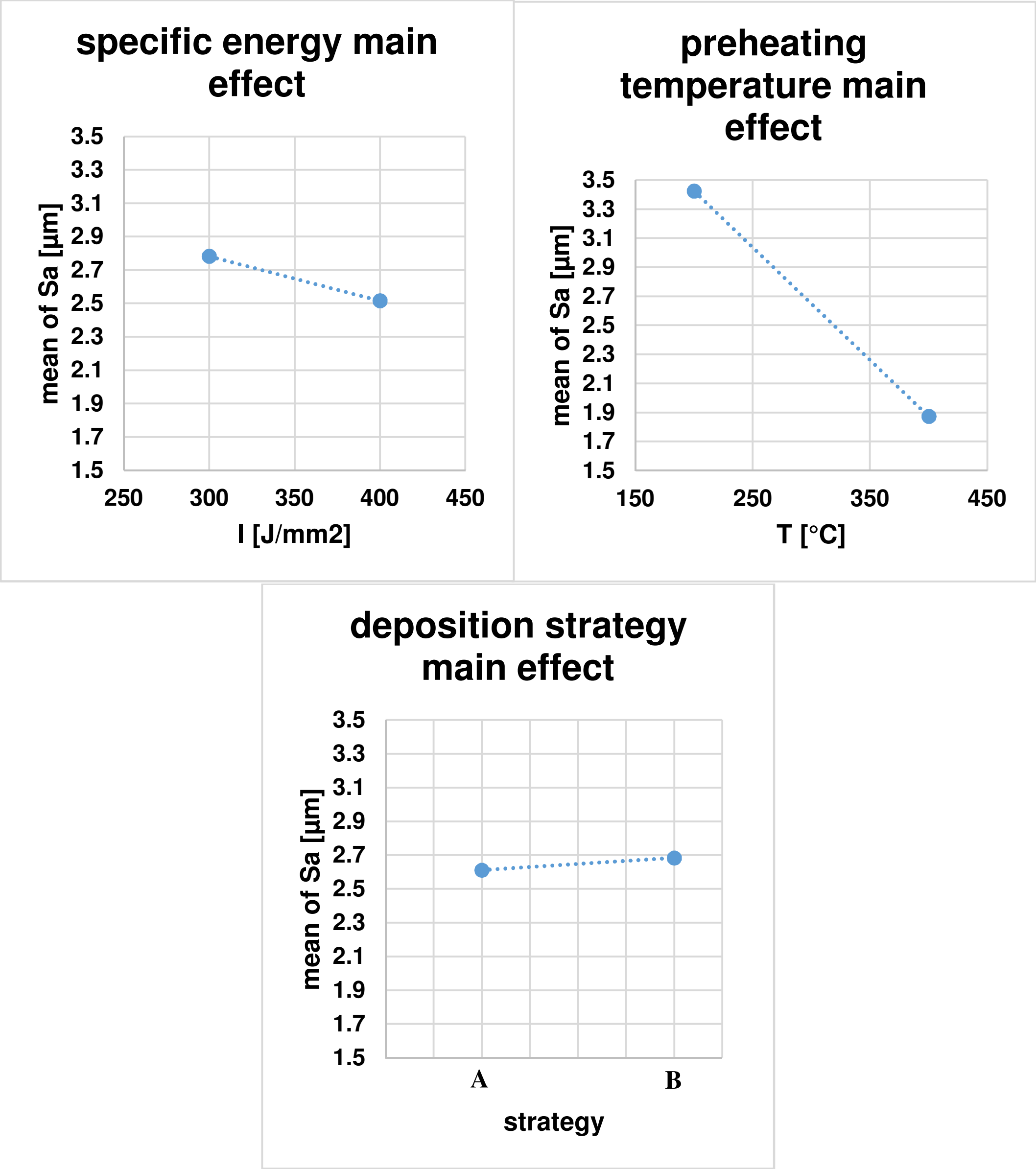

Figure 7.28 Main effect of the evaluated process parameters.

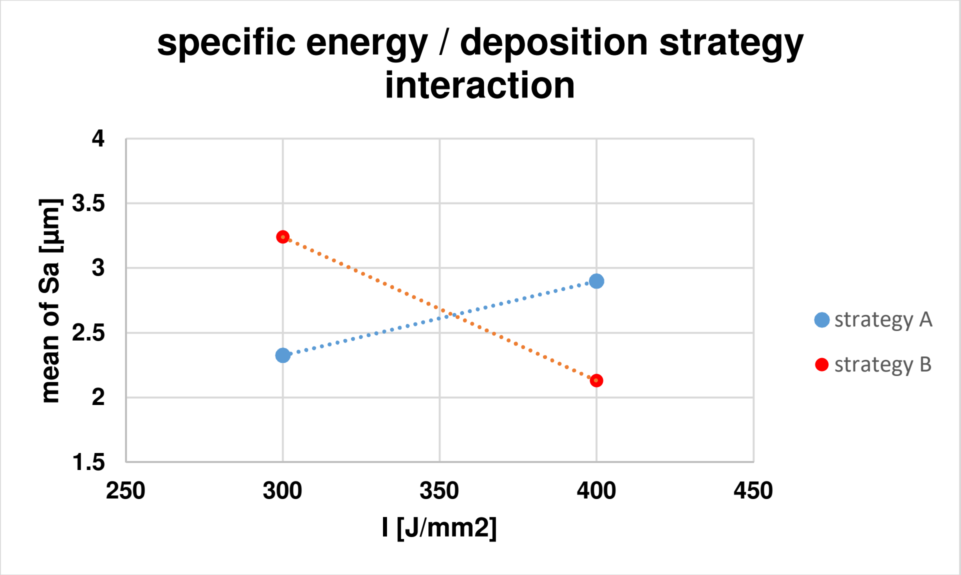

Figure 7.29 Interaction effect between specific energy [J/mm^2] and deposition strategy.

7.5.3. Conclusions

In this third process step of the suggested experimental procedure, the influence of inter-track idle time, preheating temperature of the substrate, and specific energy on the manufacture of 3D bulk PINs through micro DLMD process was investigated. The effect of each experimental factor on the final quality of the micro-artefacts in terms of structural integrity and final surface roughness was analysed through a 2^2 Full Factorial Design.

The results demonstrated the feasibility in applying the DLMD technology at the micro-scale to realized component with unexpected surface finishing, reduced “stepwise effect”, and almost absence of internal porosity. Nevertheless, the knowledge and the control of the process under these critical conditions had to be improved with further experimental investigations and analyses.

The main findings could be summarized as follows:

- the realized micro-PINs showed two different morphological zone independently by the combination of process parameters employed;
- the structural integrity and dimensional accuracy of the lower part of the micro-artefacts were strongly damaged and deteriorated by the presence of internal porosity and powder particle agglomerations adhered on the PIN surface;
- the high heat accumulations and thermal gradients generated at the centre of the micro-artefact caused an uncontrolled growth of the internal track which gradually reduced the laser defocusing, increasing the laser spot diameter;
- an starting uncontrolled growth and enlargement of the internal bead screened the supply of metal powder at the middle and external track, interrupting the deposition process for the external part of the layer temporarily;
- CFD simulations demonstrated that the presence of the substrate affected the particle trajectories and the powder distribution on the deposition powder cloud

probably. Nevertheless it was no possible to verify this hypothesis experimentally due to a serious malfunction of the MSL50 system;

- the structural integrity and final surface roughness of the upper side of the micro-artefacts was surprising with no internal voids and a “stepwise effect” strongly reduced;
- the lateral surface roughness improved with the increase of the preheating temperature of the substrate. An increment of T from 200° C to 400° C determined a decrease of S_a from 3.43 to 1.87 µm in average;
- S_z values were about an order of magnitude bigger than S_a indicating the presence of restricted zones with particle adhesion on the micro-artefact surface;
- the presence of un-melted powder particles stuck along the vertical walls of the micro-parts decreased with both low (deposition strategy A combined with low specific energy) and high (deposition strategy B combined with high specific energy) thermal fluxes;
- all the realized micro-PINs exceeded the nominal size designed by the experimental plan, showing a diameter between 490/500 µm and a final height of 3.6 mm in average;

These preliminary experimental results were promising. Nevertheless, further analysis and hypothesis have to be verified to improve the final quality of the micro-artefact in terms of dimensional accuracy, surface conditions, and structural integrity.

7.6. Conclusions

In this Chapter the manufacture of cylindrical 3D bulk PINs through DLMD applied at the micro-scale was introduced and discussed.

An empirical procedure was suggested to guide step by step the choice of the best combination of process parameters needed to realized the 3D micro-part. The main outputs coming out from this analysis were:

- the CFD simulations investigating the fluid-dynamic behaviour of the powder particles coming out from the deposition nozzle had to take into account the solid boundary condition of the substrate to correctly predict the distribution of the metal particles into the deposition powder cloud;
- the choice of the DLMD process parameters had to depend on the geometry of the deposition layer and on the track length in order to reduce or avoid high local heat accumulations;
- the realization of full-dense parts was possible through DLMD applied at the micro-scale, but the control on the thermal distribution involved during the process had to be improved to ensure a better structural integrity of the realized micro-artefact;
- the final surface roughness was surprising low if compared to that commonly obtained in DLMD. Nevertheless, the presence of powder particles adhered on the lateral surface was still high;
- high preheating temperature of the substrate improved the final surface roughness and reduced the “stepwise effect”.

Chapter 8

New developments in micro DLMD

This Chapter deals with a research work that is the natural continuation of the previous research activities introduced in the Chapter §7.
The influence of a modular laser power and specific energy on the final dimensional accuracy and structural integrity of 3D bulk circular micro-PINs is investigated. Due to the serious damage of the MSL50 system, the experiments are carried out on a new prototyping system for micro DLMD adopting a new deposition nozzle design and located at the Manudirect company.
The obtained results demonstrate the feasibility to manufacture very accurate free-necking circular micro-PINs at the micro-scale additively. It is remarkable that no adaptive control was employed during the experimentation. Nevertheless, the experimental investigation demonstrates the importance in limiting the thermal gradient and local heat accumulation to realized micro-artefacts with a remarkable finale surface roughness and a restricted “stepwise effect”.

8.1. Introduction

In the Chapter §7 the need in adjusting the DLMD process parameters depending on the layer geometry and deposition track length was clear. Indeed, keeping constant the number of passes per layer and the specific energy for all the tracks constituting the layer caused the generation of high heat accumulations on the centre of the micro-artefact, loosing the control on the inner track deposition and metal bead formation. The larger molten pool here formed produced a rapid and uncontrolled growth of the inner part of the micro-artefact, compromising the structural integrity of the 3D bulk micro-component and generating the formation of a necking zone that weakened the micro-PIN.

Taking into account the experimental results and consideration coming from the previous analysis, the aim of this research work was to fabricate circular micro-PINs with a variable laser power and specific energy depending on both the length of the deposited track and the position of the actual deposition layer.

In this way, each single track was deposited with a different combination of process parameters, modulating the laser power and the specific energy in order to limit the heat accumulation in correspondence to the centre of the micro-part.

8.2. Material & methods

8.2.1. DLMD technology

The micro DLMD system employed during this experimental plan was a prototyping system designed and manufactured by Manudirect ® company and born from the development of the MSL50 machine and the collaboration with the university of Padua. It had a new and compact design with an internal and safe system to clean the realized artefact from the un-melted powder particles automatically.

Moreover, it presented a new concept of coaxial deposition nozzle designed to provide a bigger powder particle amount in correspondence to the molten-pool.

The AM system was equipped with a new and flexible software that allowed a dynamic control on the DLMD parameters during the process with a redesigned user-friendly interface.

No more information concerning the micro-DLMD system can be provided by the author due to the confidential terms related to the actual development of this new system.

8.2.1.1. The new deposition nozzle concept

The deposition nozzle installed in the new system was a different and developed solution in compared to that mounted in the MSL50 machine.

This new solution kept the conical shape of the previous nozzle but with a reduced number of outlet holes (from 11 to 3). The laser beam came out from the centre of the nozzle (as happened for the MSL50 machine) but without a central shielding gas (see Fig. 8.1). The choice to do not employ a central shielding gas allowed a higher powder particle concentration on the interaction zone between the laser spot and the melted metal surface.

Moreover, this new nozzle solution reduced the Argon consumption during the deposition process, preventing the oxide formation during the DLMD process even with an Argon flow rate of 0.2 l/min.

Figure 8.1 Concept of the new deposition nozzle: domain of the Argon-powder mixture inside the feeding pipes and sintering chamber of the micro DLMD-machine.

No more information are available due to the industrial confidentially.

8.2.2. Metal powder and micro-artefacts

The material employed during this experimental plan was AISI 316L Stainless Steel powder with a grain size between 20 and 25 µm. The characteristics and chemical composition of this metal powder were introduced in the Chapter §2.1.
The micro-artefacts were circular PINs with a nominal diameter and height of 0.4 mm and 2 mm respectively. Contrary to the micro-PINs realized in the previous Chapter §7, in this case the cross sections of the artefacts were composed by only 2 concentric circles with a diameter of 200 µm and 400 µm respectively (see Fig. 8.2).

Three reasons brought to this choice:

- the low quantity of AISI 316L powder available for the experimental tests;
- the low time available to carry out and complete the experimental campaign;
- the need to increase the length of the inner track to reduce the heat fluxes and the heat accumulation in the centre of the micro-PIN.

As happened for the experimental tests introduced in the previous Chapter §7, each micro-PIN was realized on a cylindrical AISI 316L substrate with a diameter of 5 mm and an height of 2 mm. Each small substrate was fixed on the clamping system of the machine through a drilled square AISI 316L substrate.

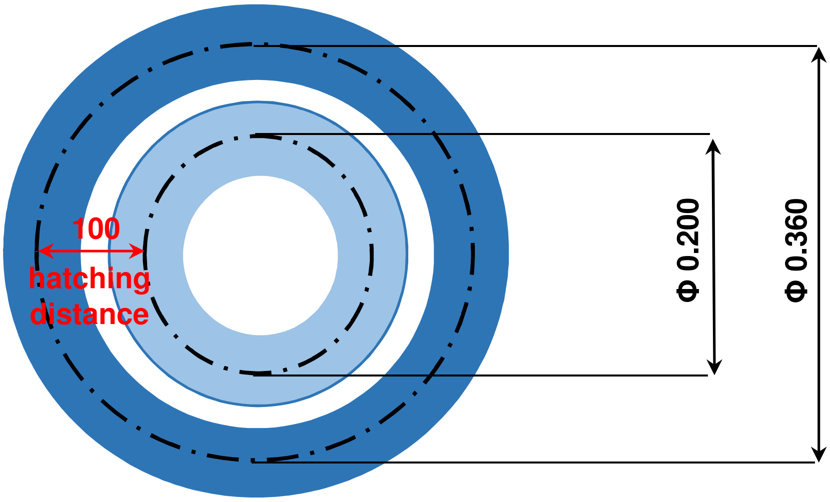

Figure 8.2 Geometrical configuration of the deposited tracks for each layer.

8.2.3. Experimental plan

The experimental factors taken into account during this analysis were the laser power and the specific energy. Nevertheless, the experimental procedure provided in this investigation was slightly different from the procedures followed in the previous experimental analysis. In this case, the experimental factors was not kept constant during the manufacturing of each single micro-PIN, but they were varied during the deposition process. Indeed, to reduce the heat accumulations on the centre of the micro-artefact and get more control on the track growth, the laser power and the specific energy were modulated for each track and for each layer.

Concerning the laser power, it was modulated following an empirical equation based on the manufacturer experience, that is:

$$P = P_f - [(P_f - P_i)e^{-\frac{i_{layer}\Delta z}{\tau}}]$$

Equation 8.1

where P (W) was the actual laser power, P_i and P_f were the laser power of the starting and final layer respectively, i_{layer} corresponded to the actual layer, Δz (mm) was the nominal layer height, and τ (mm) was an empirical constant.

To reduce the number of variables, only P_f was considered as an experimental factor whereas P_i, Δz, and τ were kept constant for all the realized micro-PINs. The specific energy was defined in the equation 5.1 that is reported below:

$$I = \frac{P}{Fd}$$

Equation 5.1

where *F* is the laser scan speed (mm/s) and d (mm) is the laser spot diameter. Since the laser spot was kept constant during the experimental tests and the laser power was defined following the equation 8.1, the specific energy depended on the laser scan speed employed during the experimental investigation. Two different F were employed for the two concentric circular tracks forming the deposition layer. The value of the two different laser scan speed was defined by a factor k equal to:

$$k = {}^{v_1}\!/_{v_2}$$

Equation 8.2

where v_1 is the laser scan speed employed for the external deposited track and v_2 is the laser scan speed for the internal one.
The factor k was the second experimental factors taken into account during the experimental plan. Two levels for each evaluated process parameter were chosen and their effects were analysed through a full factorial Design of Experiments (DOE) The values of k and P_f are summarized in the Table 8.1.

process parameters	**min value**	**max value**
final laser power [W]	18	20
k factor	0.7	0.74

Table 8.1 Evaluated factors of the experimental plan.

Three repetitions for each combination of process parameters were carried out to have scientific reliability for an overall of 12 realized circular micro-PINs.
The micro-artefacts were realized with an initial laser power (P_i) of 50 W, employing the deposition strategy B introduced and discussed in the Chapter §7.5.1.3. No pre-heating of the substrate was employed during this experimental campaign since the heating system was not implemented in the new prototyping machine yet. The laser was a continuous fibre laser YLM-100-WC IPG with a wavelength of 1030 nm and a constant spot diameter of 30 µm. The laser beam was focused at 7.3 mm from the nozzle outlet, whereas the working-plane distance was of 7.5 mm, causing a positive laser defocus of +0.2 mm.
The other relevant DLMD process parameters kept constant during the experimental tests are summarized in the Table 8.2.

process parameter	value
Argon flow rate [l/min]	0.6
powder feed rate [mg/s]	1.723
working-plane distance [mm]	7.5
laser spot diameter (d) [mm]	0.03
laser defocusing [mm]	+0.2
substrate pre-heating [° C]	0
hatching distance [mm]	0.1
P_i [W]	50
v_1 [mm/min]	90
empirical constant τ [mm]	0.4
laser spot [mm]	0.03
layer height Δz [mm]	0.105
nominal track width [mm]	0.06
deposition strategy	B
number of passes	10

Table 8.2 Process parameters kept constant during the experimental plan.

All samples were cleaned after the deposition process in Acetone and deionized water solution using an ultrasonic cleaner.

All the micro-PINs were characterized through SEM imaging to have a preliminary evaluation of the final dimensional accuracy and surface integrity. Moreover, the final surface roughness along the later side of the artefact was provided by surface measurements through optical profilometer. Finally, the structural integrity characterization was carried out through CT analysis.

8.3. Results

All the 12 realized micro-PINs showed an improved dimensional accuracy and structural integrity for all their height extension. As done in the Chapter §7.5.2, the discussion of the experimental results was divided in two parts: one concerning the dimensional accuracy and structural integrity, and one concerning the evaluation of the final surface roughness and presence of powder particles adhered along the vertical sides of the micro-PINs.

8.3.1. Dimensional accuracy and integrity of the micro-PINs

Contrary to the first micro-PINs realized during the experimental tests discussed in the previous Chapter §7, in this case the micro-artefacts did not present the necking zone that weakened the structural integrity of the micro-parts (see Fig. 8.3).

All the realized samples showed an almost uniform width along their height extension with no presence of sudden shrinkage and a final height very close to the nominal value of 2 mm (see Fig.8.4).

The absence of a necking zone and an improved control on the growth of the micro-artefact probably was a consequence of the application of modular laser power and specific energy during the DLMD process. Higher laser scan speed applied to the central track allowed lower heat fluxes and heat accumulation in the centre of the artefact, with a consequent metal bead formation more dimensionally stable and controllable.

Moreover, the gradually reduction in the laser power layer upon layer allowed to reduce the heat concentration and thermal gradient along the vertical extension of the micro-PIN, ensuring more constant heat fluxes along the vertical axes of the artefact during its realization.

The effect of this combination of modular process parameters resulted in micro-PINs with improved dimensional accuracy and a low presence of powder particle adhesion along the vertical side of the micro-artefact.

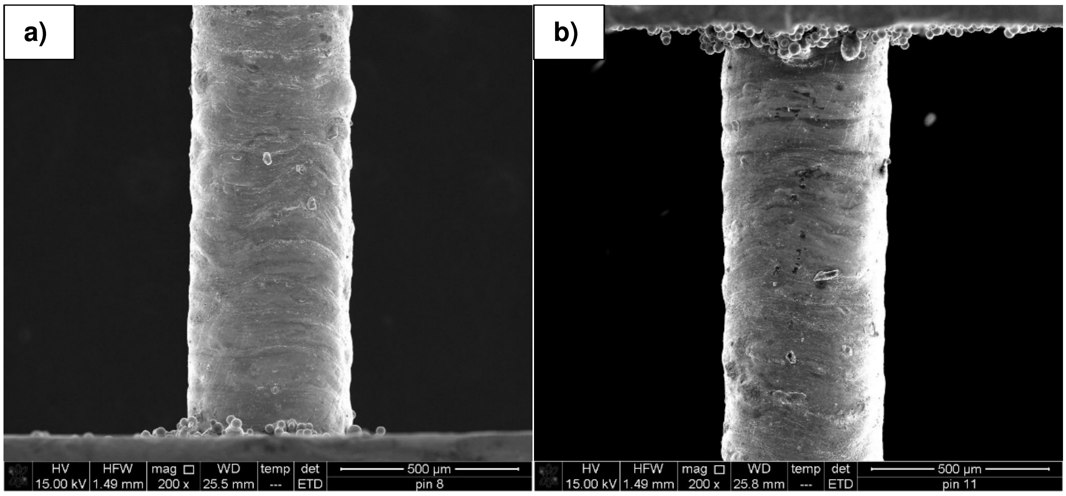

Figure 8.3 Detail of the first layers deposited during the experimental plan: a) P_f = 18, k = 0.74; b) P_f = 20, k = 0.74.

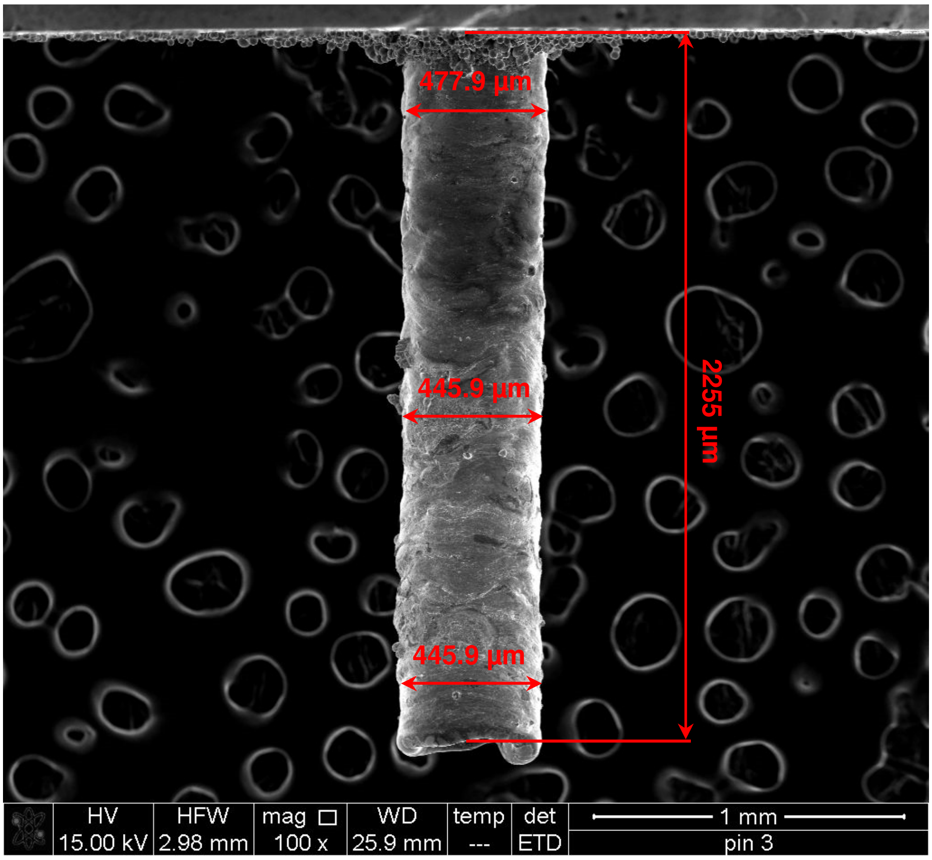

Figure 8.4 Micro-PINs realized with: $P_f = 18$, $k = 0.7$.

The effectiveness in applying variable process parameter for the realization of micro-component in DLMD was well visible at the top of the manufactured parts. In fact, at the top side of the micro-PINs, the circular deposited track were well visible (see Fig. 8.5). This phenomenon was expected since in this case the designed hatching distance of 100 µm was bigger than the nominal track width of 60 µm, but it was only possible with a stronger dimensional stability of the deposited track during the process. Indeed, contrary to the micro-PINs realized in the previous experimental analysis explained in the Chapter §7, here the positive laser defocus of +0.2 mm did not change with the height of the micro-artefact thanks to the improve controlled on the track formation for the reduction in the heat accumulations.

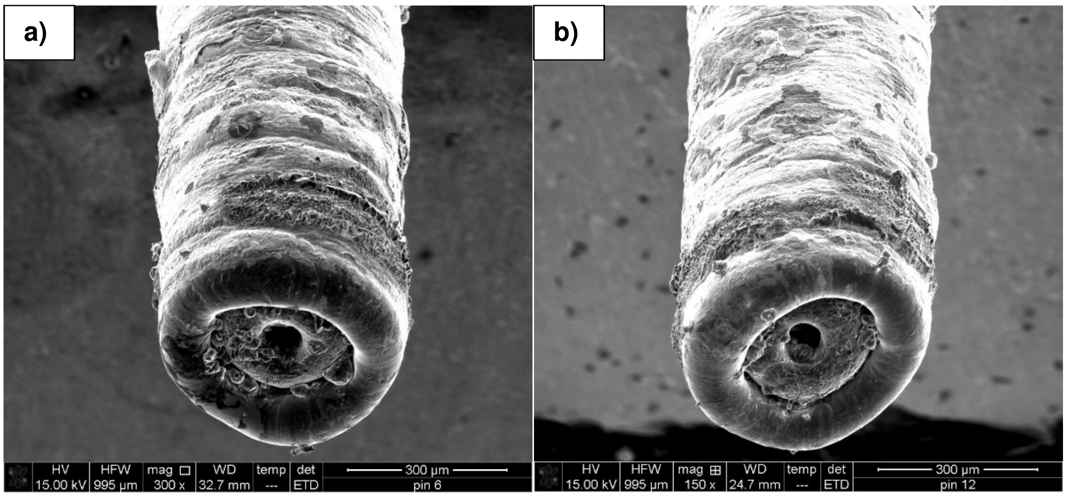

Figure 8.5 Detail of the top side of the micro-PINs: a) $P_f = 20$, $k = 0.7$; b) $P_f = 20$, $k = 0.74$.

Then, the visibility of the deposited tracks on the top of the micro-PINs underlined the positive effect when the DLMD process parameters were modulated depending on both the size of the manufacturing micro-part and the zone where the track had to be deposited.

Table 8.3 summarizes the results in terms of average micro-PIN width and height obtained from the experimental investigation.

process parameters		**average height [µm]**	**average width [µm]**
P_f [W]	*k*		
18	0.7	2275	455
20	0.7	2289	459
18	0.74	2200	460
20	0.74	2222	462

Table 8.3 Average final width and height of the micro-PINs realized by micro-DLMD.

As reported in the Table above, the average final height reached by the micro-PINs was very close to the nominal one of 2 mm. This indicated a good correspondence between the nominal designed value and the real measured height, with a consequent very good control in the layer growth during the process.

Concerning the average final width, all the micro-PINs showed an average width larger than the nominal one designed by the experimental part. In particular, the ANOVA analysis demonstrated that the final laser power was significant in determining the final width of the micro-artefact (see Fig. 8.6).

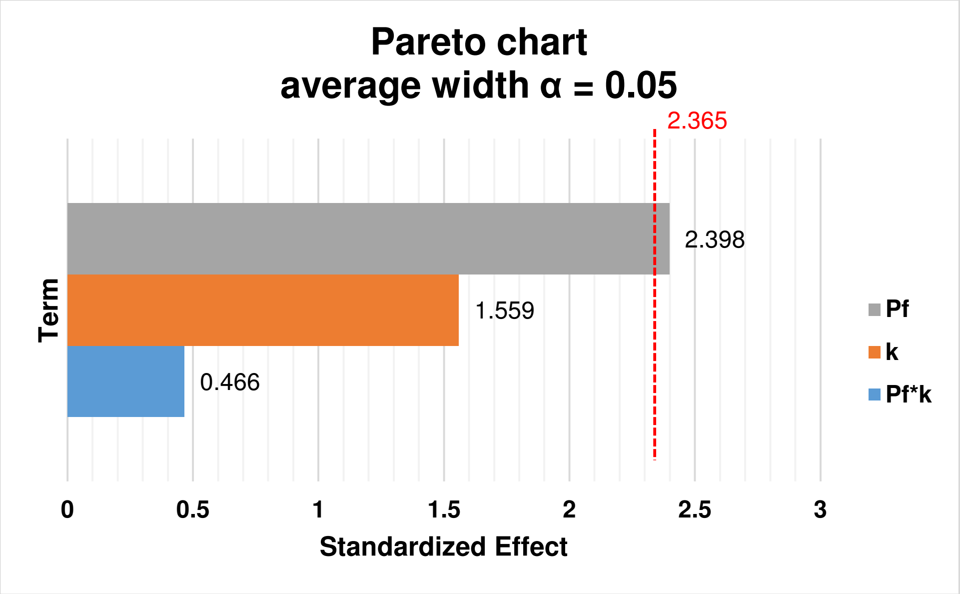

Figure 8.6 Pareto chart for the average final width of the realized micro-PINs.

Figure 8.7 shows the main effect of P_f. An increase of the final laser power from 18 to 20 W caused an increase of the final average width from 451.153 to 460.239 µm.

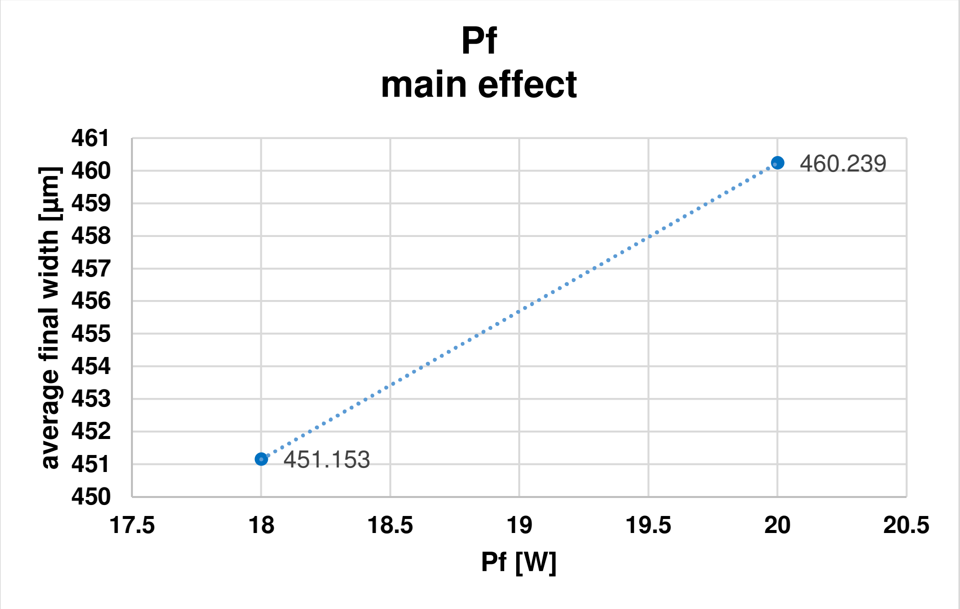

Figure 8.7 Influence of the final laser power on the average final width of the realized micro-PINs.

The reason of this behaviour could be attributed to the heat fluxes generated along the vertical extension of the micro-PIN during its fabrication. In fact, following the equation 8.1, the reduction of P layer upon layer was slower when P_f is 20 W than

18 W. This meant that the intermediate layers forming the micro-PINs were deposited at a higher temperature, causing a molten pool wormer, with a lower viscosity and consequently with a larger metal bead. This happened for both the tracks forming the deposition layer, determining both an enlargement of the micro-PIN width and a reduction of the free space between the concentric tracks (see Fig. 8.8).

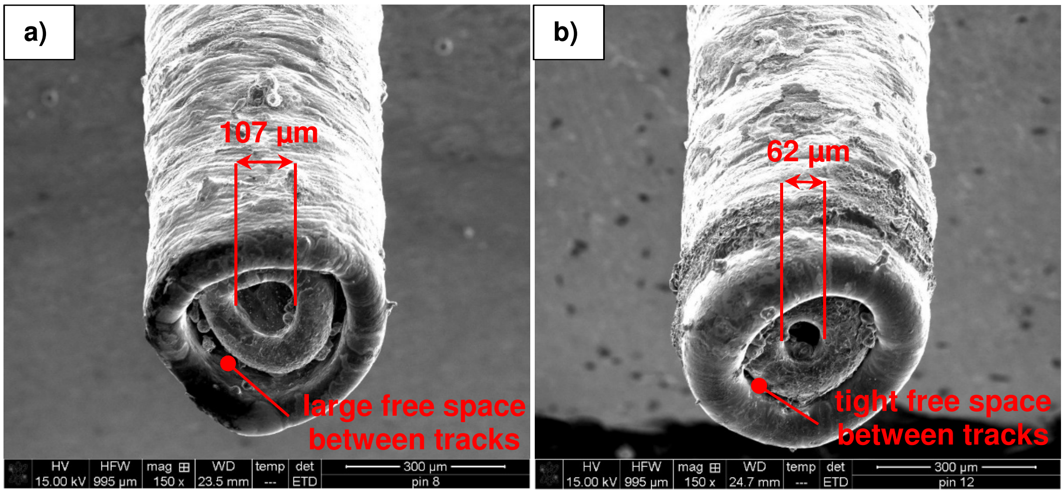

Figure 8.8 Top side of the micro-PINs: a) P_f = 18, k = 0.74; b) P_f = 20, k = 0.74.

ANOVA analysis showed the no significance of the k factor and interaction P_f*k on the final width variation of the micro-PINs. Nevertheless, SEM images demonstrated the positive effect in increasing the laser scan speed for the internal deposited track (see Fig. 8.5 and 8.8) since the inner track growth was almost equivalent to the growth of the external one.

As happened in the Chapter §7, the micro-PINs were also investigated through CT analysis to characterize the internal structure of the realized artefacts. Figure 8.9 shows the internal structure of two micro-PINs realized with different P_f and constant k. As it was supposed by the external analysis of the micro-artefacts carried out by SEM imaging, the realized micro-parts did not have a full dense structure due to the employed hatching distance that was larger than the nominal width of the deposited track. Nevertheless, the edges of the two concentric tracks were well defined, indicating that no necking zone and uncontrolled growth of the inner metal bead occurred during the deposition process.

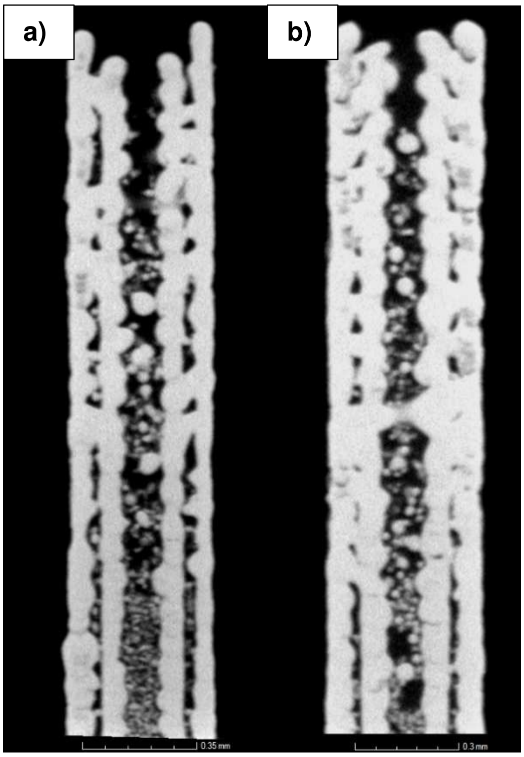

Figure 8.9 CT image of micro-PIN internal structure: a) P_f = 18, k = 0.74; b) P_f = 20, k = 0.74.

Concerning each deposited track, the CT analysis showed an average increment in the track width increasing the final laser power used to realized the micro-artefact, moving the track edges closer and justifying what observed in Figure 8.8 (see Fig. 8.10).

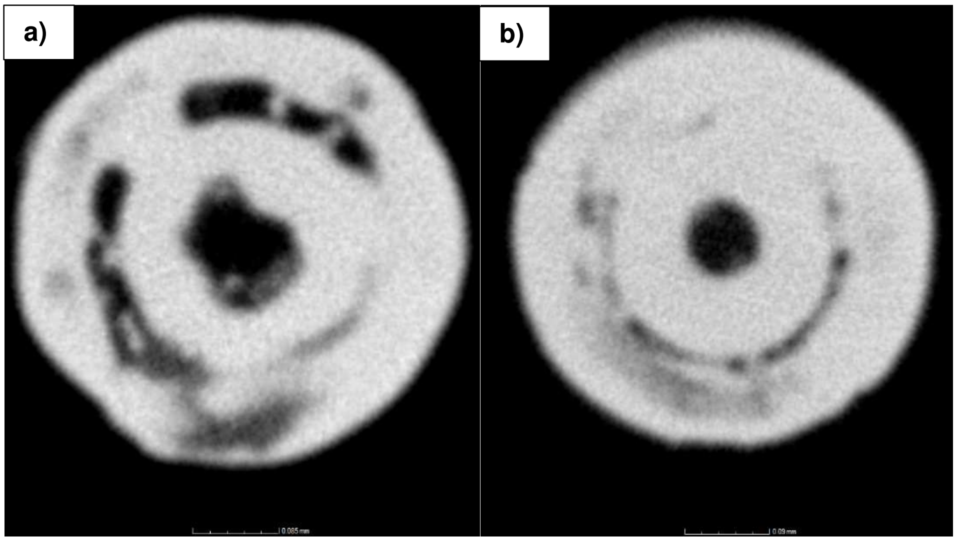

Figure 8.10 CT image of micro-PIN internal structure: a) P_f = 18, k = 0.74; b) P_f = 20, k = 0.74.

8.3.2. Micro-PIN final surface conditions

Compare to the micro-Pins realized with the MSL50 machine during the experimental plan discussed in the Chapter §7, in this case the lateral side of the cylindrical micro-artefacts exhibited a more evident "stepwise effect". Figure 8.11 shows a later side with and evident undulation that identified each deposited layer. Nevertheless, the results concerning the final lateral roughness are in good agreement with the previous results obtained in the Chapter §7.
Similarly as done in the previous Chapter §7, the micro-PIN lateral surfaces were analyzed by profilometer following the procedure reported in Appendix B with a comparative area length of 2 mm starting from the top side of the artefact. First of all it was measured the percentage of observed area occupied by powder particles, locating them by a threshold height imposed equal to 15 µm above the average surface plane, considered more than the expected roughness crests but enough to highlight powder particle presence. As reported in section 7.5, it had to be noted that R_a was obtained from low-pass filtered data instead S_a from no filtered one, just the lowest and highest 0.5% of the values were discharged.

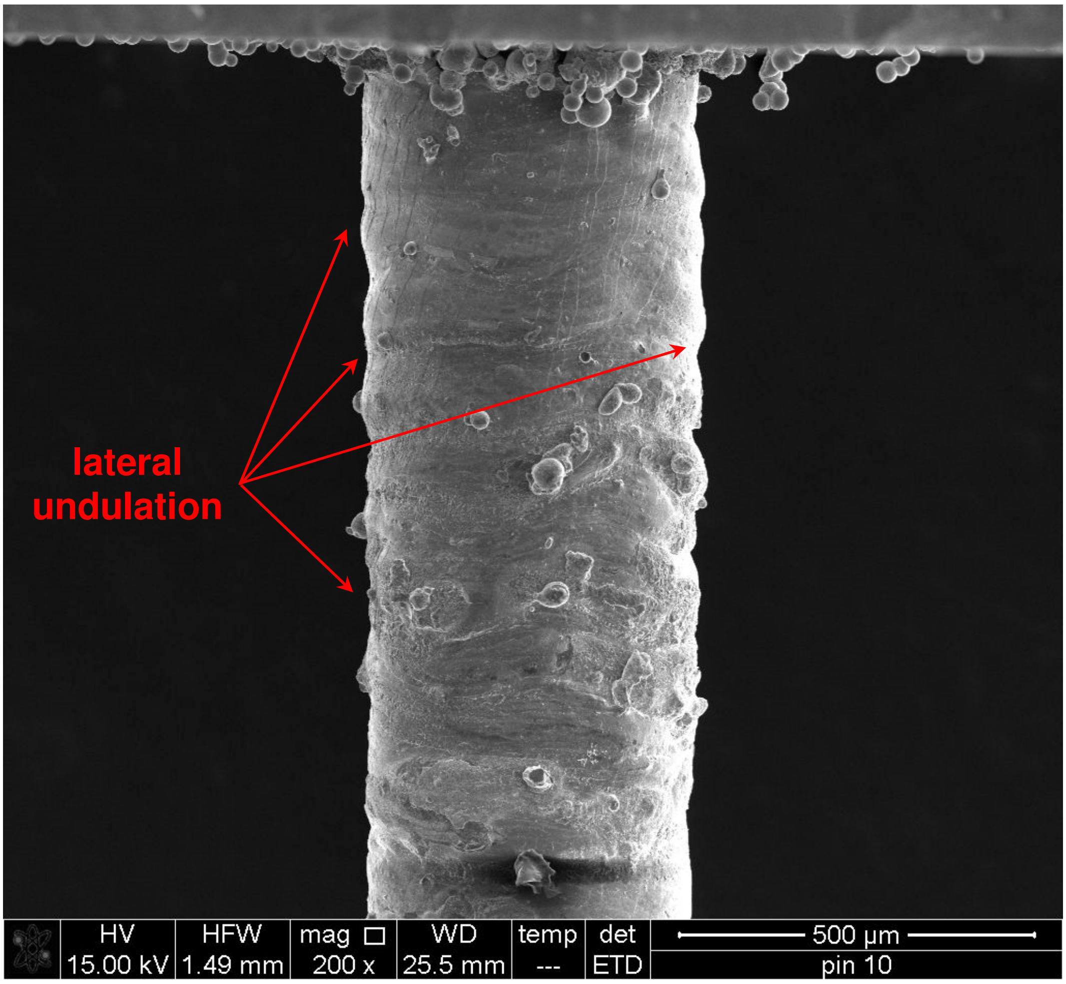

Figure 8.11 Micro-Pin realized with a P_f = 20 and k = 0.74.

process parameters		S_a [µm]	S_q [µm]	S_z [µm]
P_f [W]	k			
18	0.7	3.27	4.17	23.4
20	0.7	3.54	4.65	28.7
18	0.74	3.11	3.99	22.3
20	0.74	2.81	3.71	23.73

Table 8.4 Lateral surface roughness, S_i coefficients.

process parameters		R_a [µm]	R_q [µm]	R_z [µm]
P_f [W]	k			
18	0.7	1.44	1.79	8.05
20	0.7	1.84	2.27	9.31
18	0.74	1.59	1.59	9.14
20	0.74	1.54	1.92	8.17

Table 8.5 Lateral surface roughness, R_i coefficients.

Table 8.4 and 8.5 summarize the results in terms of R_i and S_i obtained at the end of this experimental analysis.

The ANOVA analysis carried out to characterize the influence of the evaluated process parameters on the roughness variation showed no statistical significance of the considered experimental factors on the analysed output. In fact, both for the P_f and k effect, the corresponding p-values were higher than 0.05 (statistical confidence interval of 95%).

Nevertheless, concerning S_a, if the main effects were taken into account, the best results were obtain when the highest levels for P_f (20 W) and k (0,74) were taken into account (see Fig. 8.12).

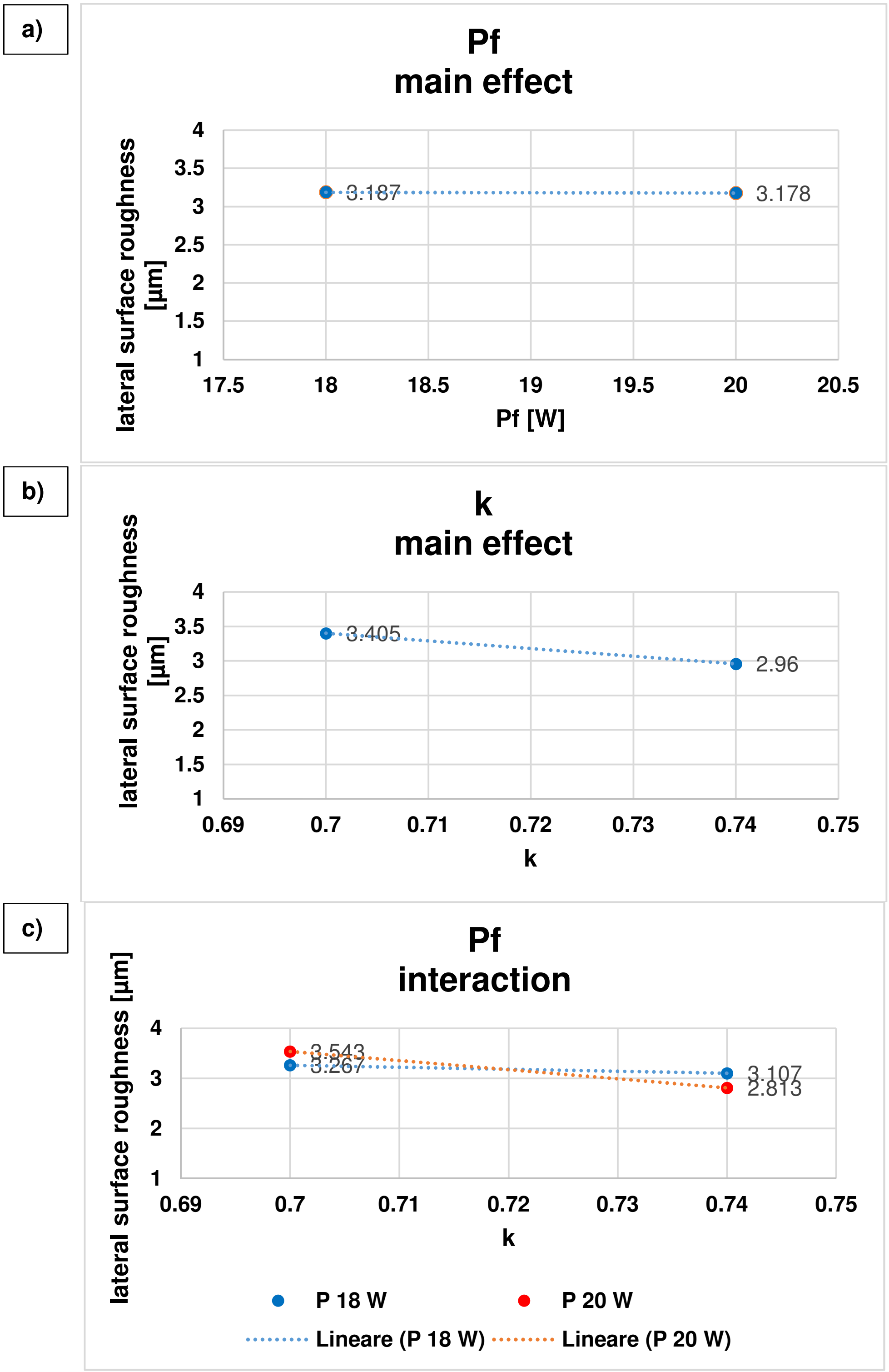

Figure 8.12 a) main effect of P_f; b) main effect of k; c) interaction effect between P_f and k.

It was noteworthy that the results shown in the Figure 8.12 did not have a statistical significance due to their high p-value. Anyway, they could be useful in order to choose the parameters to use in further tests.

Observing the profile parameters reported in Table 8.5, all the linear coefficients R_a, R_q, and R_z are similar to those obtained in the Chapter §7, so the considerations done in Chapter 7.5.2.2 were still valid. The high value of R_z (between 9.31 µm and 8.05 µm in average) was a good index of the presence of metal particles stuck on the external surface of the micro-PINs. On the contrary, R_a and R_q values were similar, so adhered powder particles covered just a small percentage of surface, confirming what observed by SEM analysis.

Analysing surface parameters reported in Table 8.4 could be noted that S_a values were similar to the obtained ones during the first test campaign, instead S_q and S_z were lower. This fact reflected the lower percentage of powder adhesion obtained in the second test campaign.

8.4. Conclusions

In this experimental investigation, the influence of modular process parameters on the final dimensional accuracy and structural integrity of AISI 316L Stainless Steel micro-PINs was investigated.

The evaluated process parameters were a variable final laser power and a velocity ratio k that allowed different specific energy depending on the deposited track.

The results showed an improved dimensional accuracy and structural integrity of the realized micro-artefacts when the DLMD process parameters were adopted to the designed geometry correctly.

The main achievements were:

- the laser power variation given by the equation 8.1 showed to be a good solution to modulate the laser energy correctly during the micro DLMD process, allowing the realization of micro-PINs with a uniform width along their vertical extension;
- higher laser scan speed for the deposition of the inner track of the layer was needed to reduce the heat accumulation at the centre of the cylindrical micro-artefact and improve a more controllable growth of the artefact;
- a modular variation of the process parameters in conjunction with a new concept of deposition nozzle allowed to increase the flux of powder in correspondence of the molten pool and to get a more accurate micro-artefacts in comparison to those realized in the Chapter §7;
- increasing P_f from 18 to 20 W, the average width of the micro-PINs increased from 451.153 to 460.239 µm in average;
- concerning the superficial surface roughness variation, the evaluated process parameters were no significant in the considered evaluation range;
- high values for k (i.e. 0.74) combined with high values of P_f (i.e. 20 W) reduced the final surface roughness along the vertical sides of the micro-PINs, even if there was no statistical significance;
- the micro-artefacts showed a more evident stepwise effect;
- S_q and S_z were lower than those obtained in the Chapter §7, indicating a lower presence of powder particles adhered along the vertical surface of the micro-PINs.

Chapter 9

Conclusions & future works

This chapter deals with the main research achievements obtained during this Ph.D. project concerning the application a DLMD system at the micro-scale. The main differences and technological findings concerning the downscaling of this AM technology are also provided, underlying the feasibility of micro DLMD system in manufacture micro-artefacts with good dimensional accuracy.

Moreover, some considerations concerning future research activities needed to improve the process control and the development of the Manudirect ® MSL50 system are provided.

9.1 Conclusions

In this Ph.D. research work, for the first time the DLMD technology was applied at the micro-scale and the feasibility of the process under this critical process conditions was explored and analysed. The technological issues concerning the downscaling of this AM system from macro to micro are recognized, discussed, and analysed in detail to increase the knowledge of this process and improve the system performance.
The main DLMD process parameters such as laser power, laser scan speed, specific energy, and deposition strategies critically affect the final quality of the realized micro-part in terms of dimensional accuracy, deposited track degradation, surface finish, and porosity formation into a bulk micro- artefact. The main findings obtained in this research investigation can be summarized as follows:

- the deposition powder cloud is characterized by three well defined zones: an initial convergent zone, an intermediate zone with ah high particle mass concentration, and a final divergent zone;
- the Argon flow rate is the most important process parameter affecting the extension and the position of the intermediate zone of the deposition powder cloud;
- increasing the Argon flow rate up to 2.7 l/min, the intermediate zone becomes wider and moves near the nozzle, decreasing the powder deposition efficiency and increasing the risk of clogging in correspondence to the nozzle outlet;
- for low values of the carrier gas (0.7 l/min), the intermediate zone moves away from the nozzle outlet, but the powder density increases in correspondence to the vertical axis of the powder cloud;
- the metal substrate should be located in the intermediate zone of the powder cloud to ensure the higher powder supply during the DLMD process. Nevertheless, the physical presence of the solid substrate could affect the motion of the metal particles and the powder distribution along the powder cloud extension;
- a positive laser defocusing encourages the formation of a continuous track and an uniform growth of the realizing micro-artefact, preheating the powder involved in the deposition process and increasing the size of the molten pool;
- laser defocusing ranging between +0.2 and +0.5 mm decreases the unevenness of thin wall top surface and improves the final surface roughness (from 28.9 µm to 16.8 µm);
- in micro DLMD process, the deposition efficiency is very low due to both the ineffectiveness of the common employed nozzles and the dimension of the powder particles very close to the molten pool size;
- Multi Passes per Layer (MPL) is a new building approach that works well for DLMD applied at the micro-scale;
- One Pass per Layer (OPL) building approach is less efficient than MPL and it does not ensure a good control on the layer formation;
- increasing the number of passes per layer, the continuity of the deposited track increases;

- at constant specific energy, increasing the laser power (from 18 to 30 W) the deposited track becomes wider and more continuous;
- bead cross-section shape strongly depends on the initial surface conditions of the metal surface and on the presence of partially melted particles stuck along the edges of the sintered track;
- continuous and significant sintered track s show an average width between 54 and 95 µm with an average height between 20 and 63 µm;
- accurate AISI 316L Stainless Steel micro-square ribs with an average width of 50 µm are possible;
- the laser power is the main process parameters affecting the onset and the extension of the *Balling phenomenon*;
- high laser powers (42 W) negatively affect the track accuracy due to the formation of large drops (up to 500 µm) along the edges of the deposited track, which strong deteriorate the dimensional and geometrical accuracy of the micro-artefact;
- higher laser scan speed (up to 500 mm/min) limits the *Balling* extension, but can introduce instability in the molten pool formation, deteriorating the structural integrity of the realized micro-artefact;
- in the MPL approach, laser power, laser scan speed, and powder feed rate do not affect the uniformity of growth in micro DLMD process;
- an experimental procedure is provided to realized 3D micro bulk part step by step, which helps in select the working-plane distance for the substrate and the best combination of process parameters to ensure the formation of continuous metal bead;
- for AISI 316L Stainless Steel micro-PINs, higher preheating of the metal substrate (up to 400° C) improves the final surface roughness along the lateral sides of the deposited PIN, reducing the “stepwise” effect visibly;
- very high (low idle time combined with high specific energy) or very low heat fluxes (high idle time combined with low specific energy) reduce the number of powder particles adhered to the surface of the realized micro-artefacts;
- high local heat accumulations and elevated thermal gradient negatively affect the structural integrity and dimensional accuracy of the realized part, causing an uncontrolled growth of the deposited track;
- a modular variation of the DLMD process parameters depending on the layer geometry and track length is needed to improve the final quality of the micro-artefact and the control on the process;
- equation 8.1 showed to be a good solution to modulate the laser energy correctly during the micro DLMD process, allowing the realization of micro-PINs with a uniform width along their vertical extension;
- increasing P_f from 18 to 20 W, the average width of the micro-PINs increased from 451.153 to 460.239 µm in average;
- during this Ph.D. project, the Manudirect ® MSL50 system has been improved installing a module to heat and control the substrate temperature during the micro DLMD process, a more powerful cooling system and a more efficient sintering chamber in terms of Argon consumption.

- in the next future, the MSL50 system should be equipped with precise sensors suitable to accurately detect the thermal distribution and molten pool temperature during the execution of the micro DLMD process. This will allow a deeper characterization and analysis of the AM process, laying the groundwork for a closed loop control system.

9.2 Future works

This Ph.D. research work demonstrated the feasibility of DLMD process applied at the micro-scale. Nevertheless, more efforts have to be carried out to improve the final quality of the realized parts and the efficiency of the micro DLMD process. Future research activities should be focused on:

- a new concept and design for the deposition nozzle, decreasing the powder waste and improving the mass particle concentration in correspondence to the molten pool, increasing the deposition efficiency;
- to optimize the Argon mass flow depending on the kind of nozzle and substrate employed;
- to equip the micro DLMD system with performing instruments suitable to characterize and control the DLMD process applied at the micro-scale;
- the design of a closed loop control system suitable to adjust the process parameters during the part realization, reducing the heat accumulations and enhancing the performance of the Manudirect ® MSL50 machine;
- to analyse the effect of track overlapping in order to realize full-dense micro-artefacts;
- the development of new metal powders specifically designed to take advantage of the capabilities and potentialities the DLMD process;
- to increase the system degrees of freedom up to 5 to allow the realization of component with very high complex geometrical shapes;
- the investigation of the influence of the DLMD process parameters on the manufacture of Functionally Graded Structures (FGS).

References

[1] ASTM-International, ASTM Standard F2792-12a: Standard Terminology for Additive Manufacturing Technologies, 2012.

[2] C.L. Weber et al., “The Role of the National Science Foundation in the Origin and Evaluation of Additive Manufacturing in the United State”, 2013.

[3] W. Gao et al., “The status, challenges, and future of additive manufacturing in engineering”, Comput Aided Des, 2015, 69, 65-89.

[4] K. Karunakaran et al., “Rapid manufacturing of metallic objects”, Rapid Prototyp J, 2012, 18, 264-280.

[5] D. Bak, “Rapid prototyping or rapid production? 3D printing processes move industry towards the latter”, Assem Autom, 2003, 23, 340-345.

[6] Brice CA, Taminger KM, Additive manufacturing workshop, Commonwealth Scientific and Industrial Research Organisation, Melbourne, Australia, 2011. http://amcrc.com.au/wp-content/uploads/2013/03/CSIRO-NASA-additive-manufacturing-workshop.pfd.

[7] M. Lee et al., “Toward nanoscale three-dimensional printing: Nanowalls built of electrospun nanofibers, Langmuir, 2014, 30, 1210-1214.

[8] K.M. Taminger, “Evolution and control of 2219 aluminium microstructural features through electron beam freeform fabrication, Trans Tech Publ, 2006, 519, 1297-1302.

[9] Y. Pan, “Smooth surface fabrication in mask projection based stereolithography “, J Manuf Processes, 2012, 14, 460-470.

[10] S.M. Thompson, “An overview of Direct Laser Deposition for additive manufacturing; Part I: Transport phenomena, modeling and diagnostics”, Addit Manuf, 2015, 8, 36-62.

[11] A.J. Pinkerton et al., “Component repair using laser direct metal deposition”, Proc Inst Mech Eng B J Eng Manuf, 2008, 222, 827-836.

[12] P.S. Korinko et al., “Laser engineered net shaping for repair and hydrogen compatibility”, Weld J, 2011, 90, 171s-181s.

[13] V. Fallah et al., “Process optimization of Ti-Nb alloy coatings on a Ti-6Al-4V plate using a fibre laser and blended elemental powders”, J Mater Process Technol, 2010, 210, 2081-2087.

[14] W.U.H. Syed et al., “Combining wire and coaxial powder feeding in laser direct metal deposition for rapid prototyping”, App Surf Sci, 2006, 252, 4803-4808.

[15] F. Wang et al., “Compositionally graded Ti-6Al-4V + TiC made by direct laser fabrication using powder and wire”, Mater Des, 2007, 28, 2040-2046.

[16] S. Kaierle et al., “Review on Laser Deposition Welding: From Micro to Macro”, Phys Procedia, 2012, 39, 336-345.

[17] P. Farahmand et al., “An experimental-numerical investigation of heat distribution and stress field in single- and multi-track laser cladding by a high-power direct diode laser”, Opt Laser Technol, 2014, 63, 154-168.

[18] D. Salehi et al., “Melt pool temperature control using LabVIEW in Nd: YAG laser blown powder cladding process”, Int J Adv Manuf Technol, 2006, 29, 273-278.

[19] I. Smurov et al., “Comprehensive analysis of laser cladding by means of optical diagnostics and numerical simulation”, Surf Coat Technol, 2013, 220, 112-121.

[20] Y. Tadjdeh, “Navy Beefs Up 3D Printing Efforts with New Print the Fleet Program”, Natl Def, 2014, 24-26.

[21] W. Hofmeister et al., “Investigating solidification with the laser-engineered net shaping (LENS) process”, JOM, 1999, 51, 6-11.

[22] M. Grujicic et al., “Computer simulations of the evolution of solidification microstructure in the LENS rapid fabrication process”, Appl Surf Sci, 2001, 183, 43-57.

[23] Z.L. Lu et al., “The prediction of the building precision in the laser engineering net shaping process using advanced networks”, Opt Lasers Eng, 2010, 48, 519-525.

[24] T. Hua et al., “Research on molten pool temperature in the process of laser rapid forming”, J Mater Process Technolg, 2008, 198, 454-462.

[25] T.A. Davis, “The Effect of Process Parameters on Laser Deposited Ti-6Al-4V”, University of Louisville, 2004.

[26] D. Srivastava et al. “The effect of process parameters and heat treatment on the microstructure of direct laser fabricated TiAl alloy samples”, Intermetallics, 2001, 9, 1003-1013.

[27] A. Birnbaum et al., “Process scaling and transient melt pool size control in laser-based additive manufacturing processes”, Proc 14th Solid Free Fabr Symp Austin, USA, 2003, 328-339.

[28] X. He et al., “Transport phenomena during direct metal deposition”, J Appl Phys, 2007, 101, 053113.

[29] R.R. Unocic et al., “Process efficiency measurements in the laser engineered net shaping process”, Metall Mater Trans B, 2004, 35, 143-152.

[30] P. Peyre et al., “Analytical and numerical modelling of the direct metal deposition process”, J Phys D Appl Phys, 2008, 41, 025403.

[31] W.M. Steen, “Laser material processing – an overview”, J Opt A Pure Appl Opt, 2003, 5, 3-7.

[32] F.P. Jeantette et al., “Method and System for Producing Complex-Shape Objects”, 2000, Patent: US006046426A.

[33] L. Han et al., “Thermal behavior and geometry model of melt pool in laser material process”, ASME J Heat Transfer, 2005, 127, 1005.

[34] H. Yin et al., “Fluid flow, heat and mass transfer in the molten pool of the LENS process, Met Mater Soc, 2008, 261-270.

[35] L. Wang et al., “Process modeling in laser deposition of multilayer SS410 steel”, J Manuf Sci Eng, 2007, 129, 1028-1034.

[36] K.I. Schwendner et al., “Direct Laser deposition of alloys from elemental powder blends”, Scr Mater, 2001, 45, 1123-1129.

[37] V. Neela et al., “Three-dimensional heat transfer analysis of LENS process using finite element method”, Int J Adv Manuf Technol, 2009, 45, 935-943.

[38] M.L. Griffith et al., “Multi-material processing by LENSTM”, Proc 8th Solid Free Fabr Symp, Austin, USA, 1997, 387-394.

[39] B. Zheng et al., “Thermal behavior and microstructural evolution during laser deposition with laser-engineered net shaping: part I. Numerical calculations”, Metall Mater Trans A, 2008, 39 2228-2236.

[40] W. Kurz et al., “Columnar to equiazed transition in solidification processing”, Sci Technol Adv Mater 2, 2001, 2, 185-191.

[41] M.R. Boddu, “Control of laser cladding for rapid prototyping – a review”, University of Missouri – Rolla, MO 65409.

[42] M.N. Ahsan et al., “A comparative study of laser direct metal deposition characteristics using gas and plasma-atomized Ti-6Al-4V powders”, Mat Sci Eng A, 2011, 528, 7648-7657.

[43] J. Tomas, “Particles on Surfaces 8: Detection, Adhesion and Removal”, KL Mittal (Ed), 2003, 183-229.

[44] P. Balu et al., “Parametric study on a coaxial multi-material powder flow in laser-based powder deposition process”, J Mater Process Tech, 2012, 212, 1598-1610.

[45] I. Kovaleva et al., “Numerical simulation and comparison of powder jet profiles for different types of coaxial nozzles in direct material deposition”, Physics Procedia, 2013, 41, 870-872.

[46] J. Liu et al., “Effects of powder concentration distribution on fabrication of thin-wall parts in coaxial laser cladding”, Opt Laser Technol, 2005, 37, 287-292.

[47] V. Giuliani et al., “Particle velocity detection in laser deposition processing”, Rapid Prototyping J, 2008, 14, 141-148.

[48] Y. Huang et al., “A comprehensive analytical model for laser powder-fed additive manufacturing”, Addit Manuf, 2016, 12, 90-99.

[49] G. Zhu et al., “Numerical simulation of metallic powder flow in a coaxial nozzle in laser direct metal deposition”, Opt Laser Technol, 2011, 43, 106-113.

[50] S. Zekovic et al., “Numerical simulation and experimental investigation of gas-powder flow from radially symmetrical nozzles in laser-based direct metal deposition”, Int J Mach Tools Manuf, 2007, 47, 112-123.

[51] O.S. Fatoba et al., “Computational Dynamics of Anti-Corrosion Performance of Laser Alloyed Metallic Materials”, INTECH, 2016, 345-366.

[52] Z. Fan et al., “Numerical Modeling of the Additive Manufacturing (AM) Processes of Titanium Alloy”, INTECH, 20016, 3-28.

[53] G. Zhu et al., “The influence of laser and powder defocusing characteristics on the surface quality in laser direct metal deposition”, Opt Laser Technol, 2012, 44, 349-356.

[54] M. Gharbi et al., “Influence of various process conditions on surface finishes induced by the direct metal deposition laser technique on a Ti-6Al-4V alloy”, J Mater Process Tech, 2013, 213, 791-800.

[55] A.J. Pinkerton et al., “The significance of deposition point standoff variations in multiple-layer coaxial laser cladding (coaxial cladding standoff effects)”, Int J Mach Tools Manuf, 2004, 44, 573-584.

[56] E. Nyoni et al., “Process parameters interaction effect on the evolving properties of laser metal deposited titanium for biomedical application”, Thin Solid Films, 2016.

[57] O.B. Kovalev et al., “Multivortex convection of metal in molten pool with dispersed impurity induced by laser radiation”, Int J Heat Mass Transfer, 2014, 68, 269-277.

[58] S. Wen et al., “Modeling of transport phenomena in direct laser deposition of metal matrix composite”, Int J Heat Mass Transfer, 2011, 54, 5319-5326.

[59] J. Yu et al., “Mechanics and energy analysis on molten pool spreading during laser solid forming”, Appl Surf Sci, 2010, 256, 4612-4620.

[60] T. Hua et al., “Research on molten pool temperature in the process of laser rapid forming”, J Mater Process Technol, 2008, 198, 454-462.
[61] T. Amine et al., “An investigation of the effect of direct metal deposition parameters on the characteristics of the deposited layers”, Case Stud Therm Eng, 2014, 3, 21-34.
[62] J.S. Keist et al., “Role of geometry on properties of additively manufactured Ti-6Al-4V structures fabricated using laser based directed energy deposition”, Mater Design, 2016, 106, 482-494.
[63] L. Ri-Sheng et al., “The influence of scanning methods on the cracking failure of thin-wall metal parts fabricated by laser direct deposition shaping”, Eng Fail Anal, 2016, 59, 269-278.
[64] Y. Zhang et al., “Numerical and experimental investigation of multilayer SS410 thin wall built by laser direct metal deposition”, J Mater Process Tech, 2012, 212,106-112.
[65] S.K. Ghosh et al., “Development of an in-situ multi-component reinforced Al-based metal matrix composite by direct metal laser sintering technique-Optimization of process parameters”, Mater Charact, 2014, 93, 68-78.
[66] T. Amine et al., “Investigation of effect of process parameters on multilayer builds by direct metal deposition”, Appl Therm Eng, 2014, 73, 500-511.
[67] S. Ocylok et al., “Correlations of Melt Pool Geometry and Process Parameters During Laser Metal Deposition by Coaxial Process Monitoring”, Phys Procedia, 2014, 56, 228-238.
[68] Z.L. Lu et al., “Investigation into the direct laser forming process of steam turbine blade”, Opt Laser Eng, 2011, 49, 1101-1110.
[69] I. Yadroitsev et al., “Single track formation in selective laser melting of metal powders”, J Mat Process Tech, 2010, 210, 1624-1631.
[70] D. Gu et al., “Balling phenomena in direct laser sintering of stainless steel powder: metallurgical mechanisms and control methods”, Mater Design, 2009, 30, 2903-2910.
[71] S.H. Nikam et al., “Thermal modeling of geometry of single-track deposition in micro-plasma transferred arc deposition process”, J Mater Process Tech, 2016, 230, 121-130.
[72] N.K. Tolochko et al., “Balling processes during selective laser treatment of powders”, Rapid Prototyp J, 2004, 10, 78-87.
[73] K. Bartkowiak, “Direct laser deposition process within spectrographic analysis in situ”, Phys Procedia, 2010, 5, 623-629.
[74] H. Sahasrabudhe et al., “Stainless steel to titanium bimetallic structure using LENS^{TM}”, Addit Manuf, 2015, 5, 1-8.
[75] M. Ma et al., “Control of shape and performance for direct laser fabrication of precision large-scale metal parts with 316L Stainless Steel”, Opt Laser Technol, 2013, 45, 209-216.
[76] K. Zhang et al., “Characterization of Stainless Steel Parts by Laser Metal Deposition Shaping”, Mater Des, 2014, 55, 104-119.
[77] C. Qiu et al., “Fabrication of large Ti-6Al-4V structures by direct laser deposition”, J Alloys Compd, 2015, 629, 351-361.

[78] D. Gu et al., “Balling phenomena during direct laser sintering of multi-component Cu-based matal powder”, J Alloys Compd, 2007, 432, 163-166.

[79] K. Kempen et al., “Dimensional accuracy of internal channels in SLM produced parts”, 2014, ASPE Spring Topical Meeting, 76-79.

[80] M.B. Bauza et al., “Study of accuracy of parts produced using additive manufacturing”, 2014, ASPE Spring Topical Meeting, 86-91.

[81] D. Boisselier et al., “Improvement of the laser direct metal deposition process in 5-axis configuration”, Physics Procedia, 2014, 56, 239-249.

[82] P. Muller et al., “Modeling and control of a direct laser powder deposition process for Functionally Graded Materials (FGM) parts manufacturing”, J Mater Process Tech, 2013, 213, 685-692.

[83] I. Shishkovsky, et al., “Diret metal deposition of functional graded structures in Ti-Al system", Physics Procedia, 2012, 39, 382-391.

[84] N. Shamsaei et al., “An overview of Direct Laser Deposition for additive manufacturing; Part II: Mechanical behavior, process parameter optimization and control”, Addit Manuf, 2015, 8, 12-35.

[85] X. Wang et al., “Influences of deposition strategies and oblique angle on properties of AISI 316L stainless steel oblique thin-walled part by direct laser fabrication”, Opt Laser Technol, 2016, 80, 138-144.

[86] V. Fallah et al., “Impact of localized surface preheating on the microstructure and crack formation in laser deposition of Stellite 1 on AISI 4340 steel”, Appl Surf Sci, 2010, 257, 1716-1723.

[87] A. Yadollahi et al., “Effects of process time interval and heat treatment on the mechanical and microstructural properties of direct laser deposited 316L stainless steel”, Mater Sci Eng A, 2015, 644, 171-183.

[88] L. Costa et al., “Rapid tooling by laser powder deposition: Process simulation using finite element analysis”, Acta Mater, 2005, 53, 3987-3999.

[89] I. Tabernero et al., “Numerical simulation and experimental validation of powder flux distribution in coaxial laser cladding”, J Mater Process Tech, 2010, 210, 2125-2134.

APPENDIX A

Powder feeding and handling

Introduction

Feeding of powders and bulk solids is a process step which occurs in many technical processes and economic branches. Some examples are:

- powder coating (polymer coatings);
- thermal spraying (ceramic or metal coatings);
- food industry;
- pharmaceutical industry;
- cement industry;
- discharging of ships.

We are not interested in transporting the powder by shovel, buckets and other tools which may allow the transport of any kind of powder. We are interested in a continuous flow process realised by a pneumatic feeding process. The powder shall be dispersed in stream of gas.

There are different pneumatic powder feeder designs available on the market. Some examples are shown in Figure 1.A. In all cases, at the beginning of the feeding process, gravity is an important driving force, usually combined with another mechanical process (e.g. rotating wheel, vibration) which enhances homogenous dosing. Further, most feeding processes are supported by a stream of gas to transport the powder to its place of application.

Figure 1.A a shows a pure gravity-based powder feeder. The dosing principle is the same as for a sand clock. The mass flow of the powder is determined by the width of an orifice. The principle requires very good flow behaviour of the powder. Figure 1.A b shows a vibrating feeder. The powder is stored in a tray which is vibrated to control the powder feed rate into the process. A vibratory-based powder feeder can feed most powders from at least 8 g/min to 2000 g/ min, where homogeneous powder flow is facilitated by mechanical vibrations. In Figure 1.A c, a rotating disk is used to control the feed rate of the powder. The powder is falling from a tank into a slot of a rotating disk by gravity. This step may be facilitated by a stirring device within the tank. At another position of the rotation path, the powder is entrained by a stream of gas. The powder feed rate is controlled by the speed of the disk and the width of the slot. Figure 1.A d sows another metering principle for the powder based on a rotating wheel.

None of the powder feeders shown in Figure 1.A fulfils the demands of the laser micro sintering process for which much lower powder feed rates are required. The minimum powder flow of these systems is much too high for micro laser sintering.

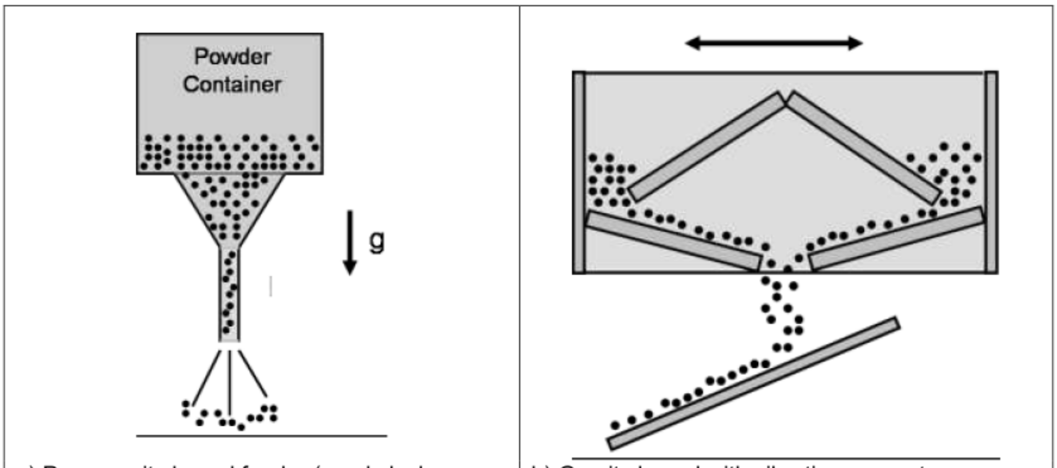

a) Pure gravity based feeder (sand clock principle).

b) Gravity based with vibration support.

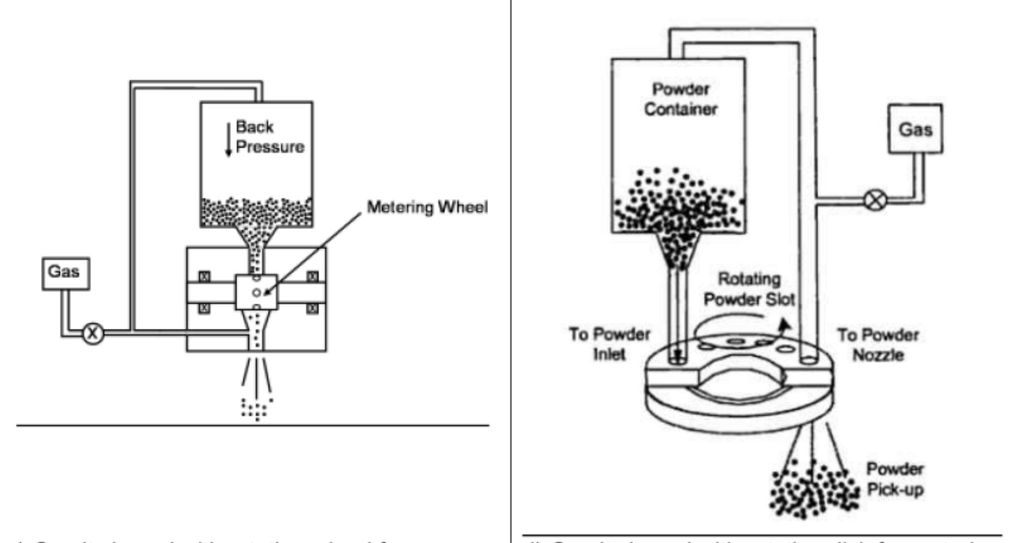

c) Gravity based with rotating wheel for metering.

d) Gravity based with rotating disk for metering.

Figure 1.A. Gravity based powder feeders with different mechanical supporting devices.

Micro-LS powder feeder

The micro-LS powder feeder is especially designed for homogeneously providing low powder quantities. It based on a technology for the generation of particle aerosols which are used in calibration of particle measurement systems. Existing technology was modified in order to reduce the gas stream required for dispersing the particles. Figure 2.A shows the principle of the powder feeder.

The powder is stored in a powder cartridge, which is pressed against the housing of a rotating brush. The powder is pressed against the brush by a piston inside the cartridge. The piston is driven by an electric motor with very high accuracy (down to 0.1 µm/s). The powder is entrained by a rotating brush and released into the feeder outlet. Fine dispersing is enhanced by the mechanical deformation and relaxation of the bristles of the brush at a specifically designed edge of the outlet.

The chamber of the rotating brush is connected to a gas supply, and the feeding gas is passed through the chamber to the outlet. Due to the combination of rotating brush and gas flow, the powder should now be in a state of a fine solid-gas dispersion which is fed into a pipe from which it is guided towards the laser process head.

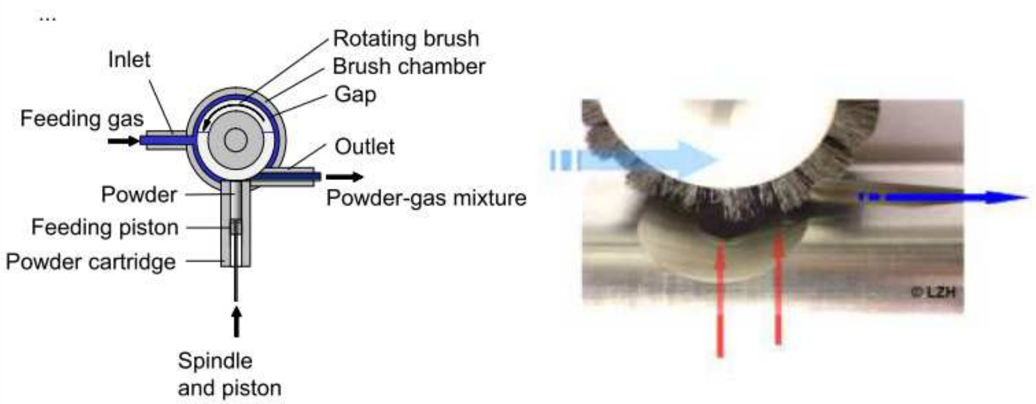

Figure 2.A. Sketch of the micro-LS powder feeder.

Figure 3.A shows the components of the whole feeding system. The feeder outlet is connected to a pipe which guides the powder-gas dispersion to a distributor. In the distributor the stream is guided into 11 pipes which direct the powder-gas dispersion to the laser head from which it is coaxially fed into the process. The distributor may be connected to an ultrasonic vibrating device to lower the risk of sedimentation within the distributor.

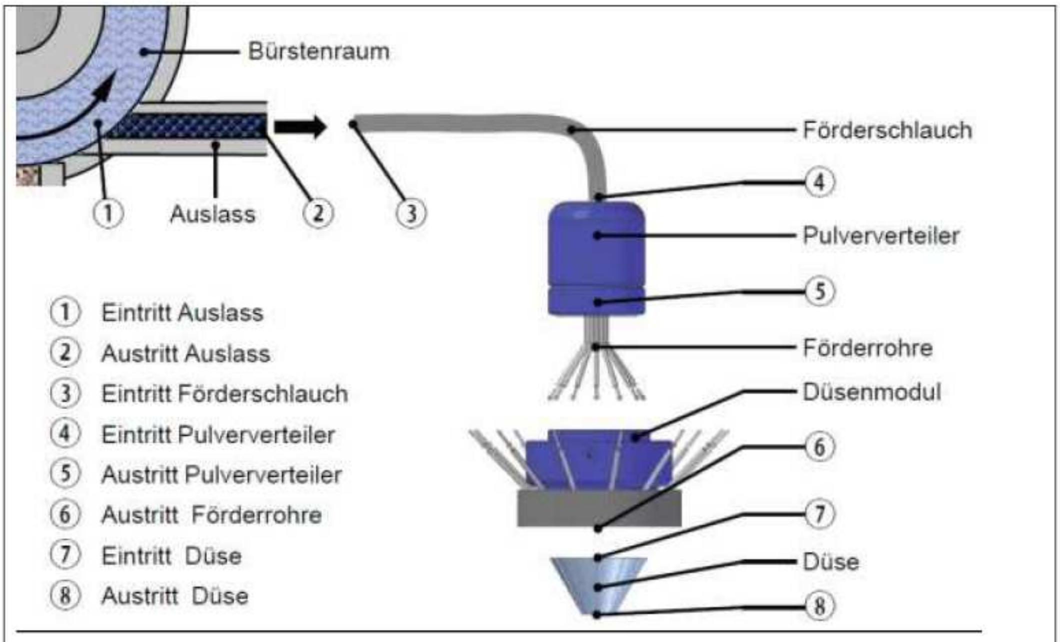

Figure 3.A. Sketch of the whole feeding system.

Photos of the feeding components installed at a laboratory set-up at LZH are shown in Figure 4.A.

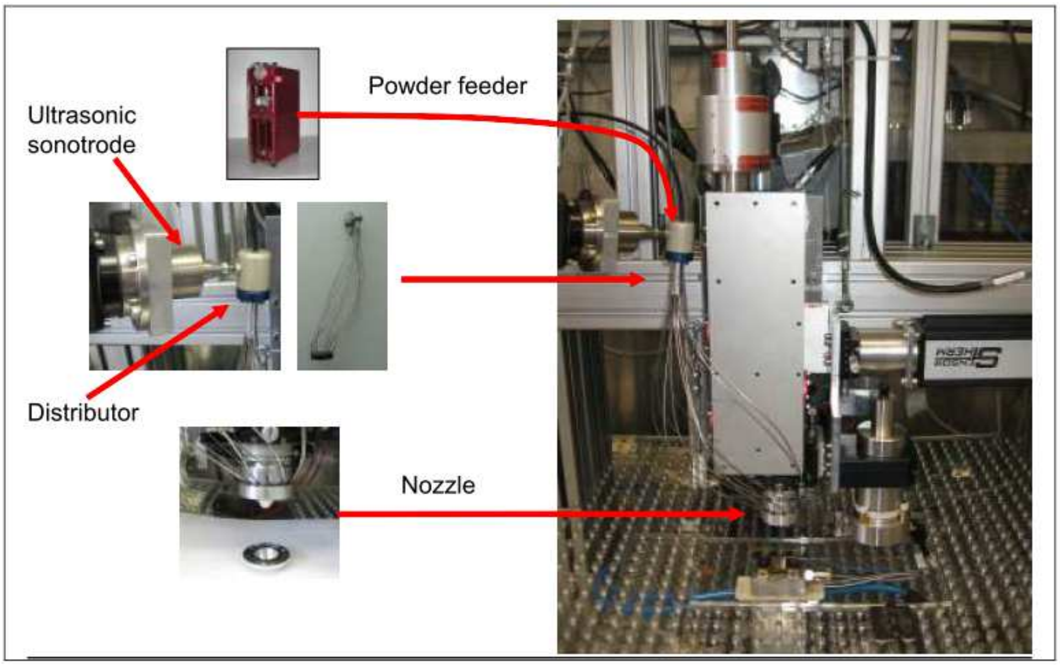

Figure 4.A. Photo of laboratory micro laser sintering set-up.

Within the frame of the Manudirect project, the micro-LS powder feeder was designed in a modular way as shown in Figure 5.A. One important design criterion was to give the user easy access to the brush chamber for the purpose of cleaning. However the disadvantage is that exchange of the powder cartouche always requires a removal of the brush chamber, and for powders sensitive to oxidation an exchange of the cartouche within a glove box under protective atmosphere would be necessary.

For this reason, FPT has made some modifications to the micro-LS powder feeder design. The current powder feeder is shown in Figure 6.A. Removal of the brush chamber for exchanging the powder cartouche is not necessary any more. Further, the cartouche can be inserted into the feeder without lifting the cap. The cap is removed automatically, and the cartouche is positioned automatically towards the brush. This way exchange of the powder cartouche is realised in a very comfortable way.

Switching between different powders is an important feature of the laser sintering machine. The principle of powder switching is shown in Figure 7.A. Each powder to be used in a sintering process requires an own powder feeder. For fast switching, both powder streams must be available at the same time, in order to keep the time of process interruption at a minimum. For a certain time interval around the switching moment, both powder streams must be active.

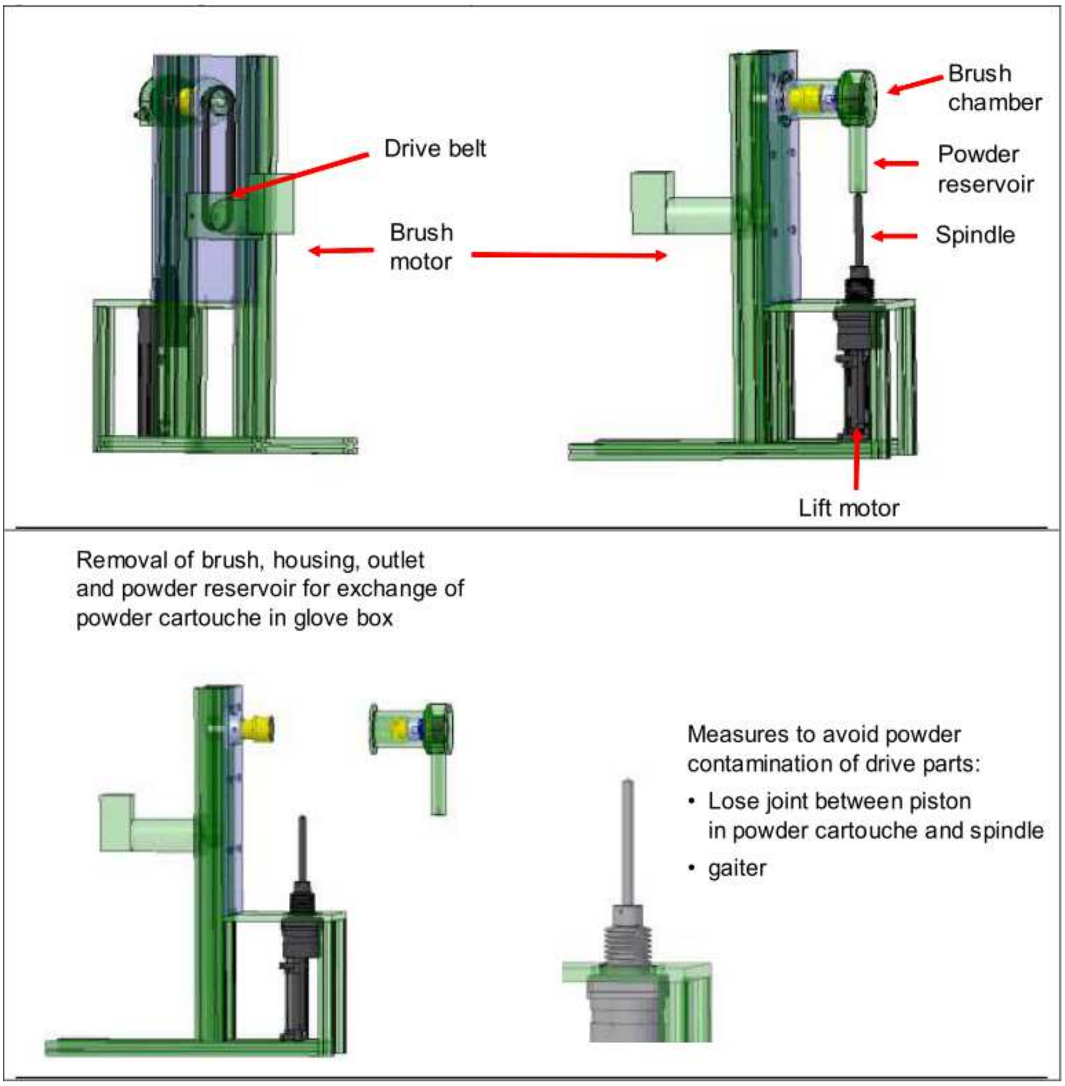

Figure 5.A. Original micro-LS powder feeder design.

One is directed to the process head, the other one is directed to an exhaust. On switching, the destinations (process or exhaust) of both powder streams are exchanged. A second path for each switch is not necessary, if there is not the requirement of fast switching. In this case, the work piece would be removed from the process zone, the first powder flow would be stopped and the second one would be started. After a certain time needed for homogenisation of powder flow, the work piece would be positioned again in the process zone, and the process would be continued.

Micro-LS has designed two types of powder switches, which can be implemented into the sintering machine, shown in Figure 8.A and Figure 9.A. The first design avoids dead volumes where powders may deposit, however it shows leakage problems. The second design is much simpler with respect to the switching mechanism and thus it avoids leakage. However, there are dead volumes which may cause sedimentation problems.

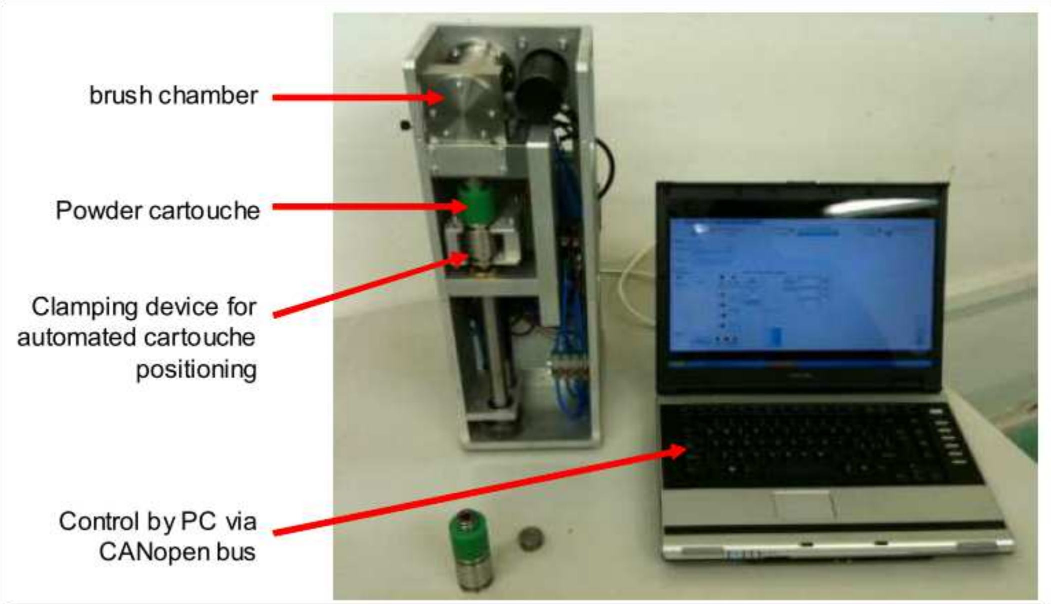

Figure 6.A. Photo of the MANUDIRECT powder feeder, as built by FPT. Stand alone system.

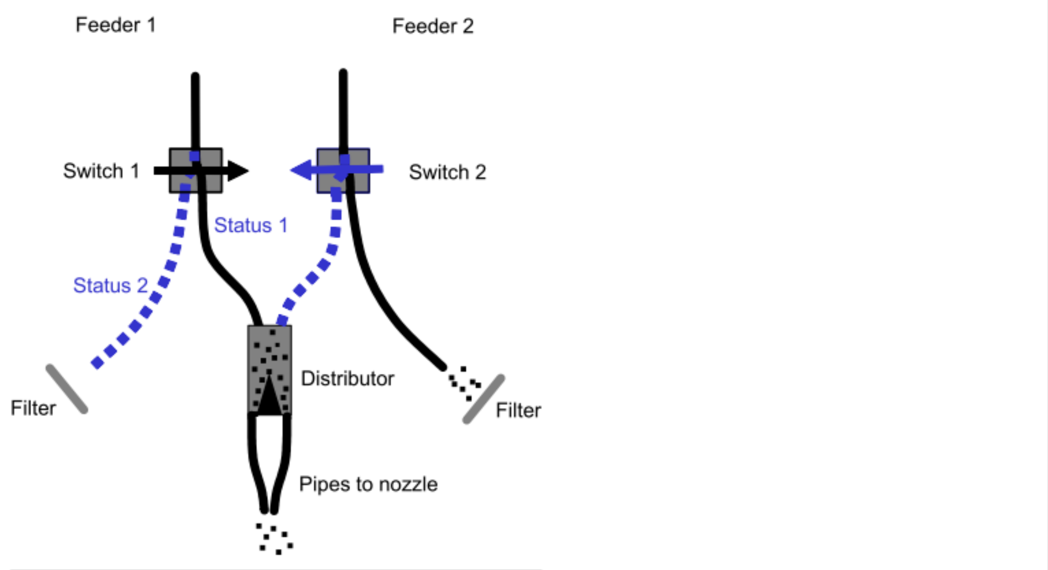

Figure 7.A. Principle of powder switching.

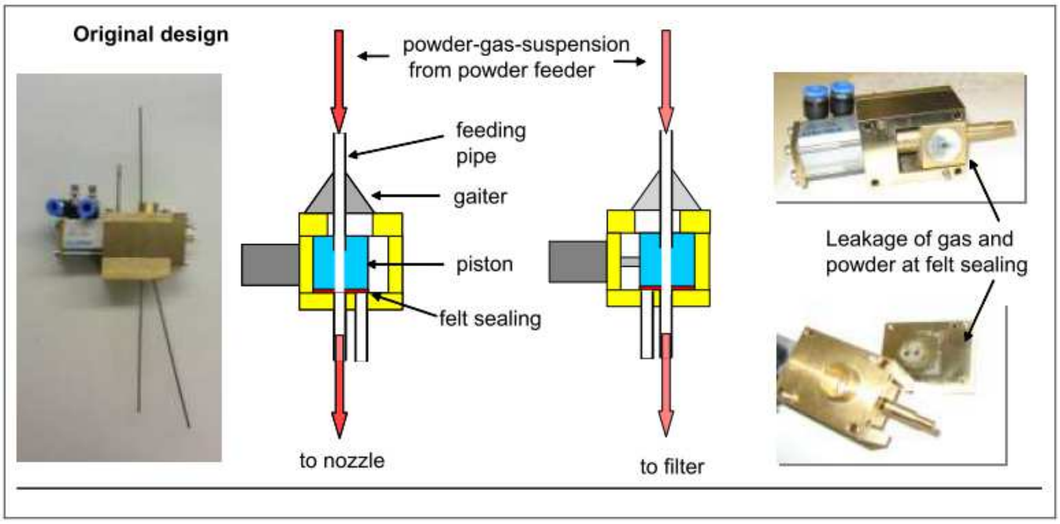

Figure 8.A. Powder switching by piston with channel.

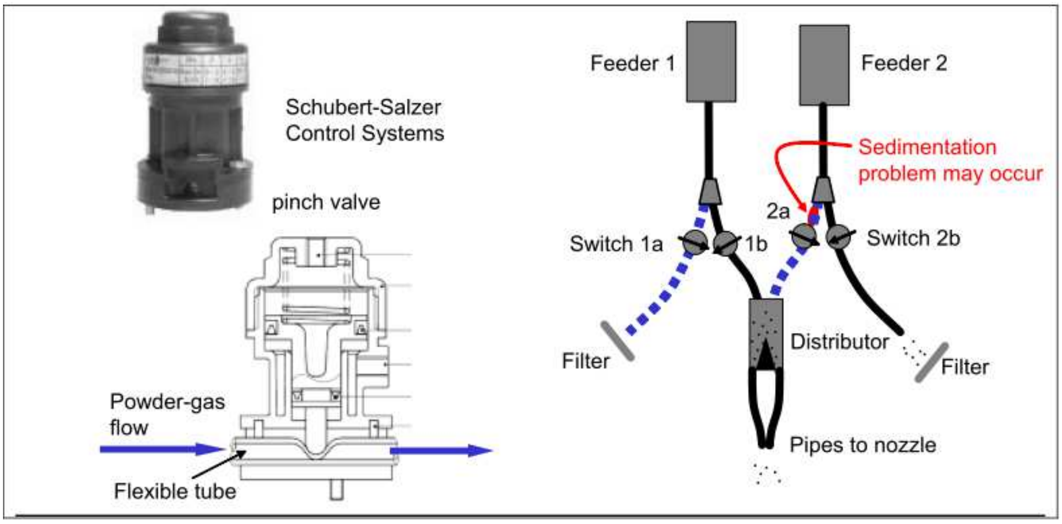

Figure 9.A. Switching alternative: punch valve.

Theoretic considerations of pneumatic feeding process

Powder flow

We will now perform some physical considerations to better understand the pneumatic feeding process. An understanding of the feeding process is helpful to understand the reasons for potential feeding and focussing problems and to find solutions. Pneumatic feeding is possible because the gas stream exerts drag forces on the particles. Due to the influence of gravity on the powder particles the flow characteristics strongly depend on the flow direction (upward, downward, horizontal). In upward flow (Figure 10.A), the drag forces on the powder must overcome the gravity force on the particles to achieve powder any flow at all. If gravity is overcome, the powder flows upward with a speed lower than the gas speed. As a rule of thumb for rough orientation, the gas speed should be 3 times higher than the sinking speed of a powder in free fall conditions. In downward direction, due to gravity, the speed of the particles is higher than the gas speed, if no clogging occurs. In horizontal flow, the flow behaviour is completely different, because drag forces do not compensate the gravitational force. Depending on the powder properties, the mass flow and the gas speed, the powder may settle and typical flow patterns may arise as shown in Figure 11.A.

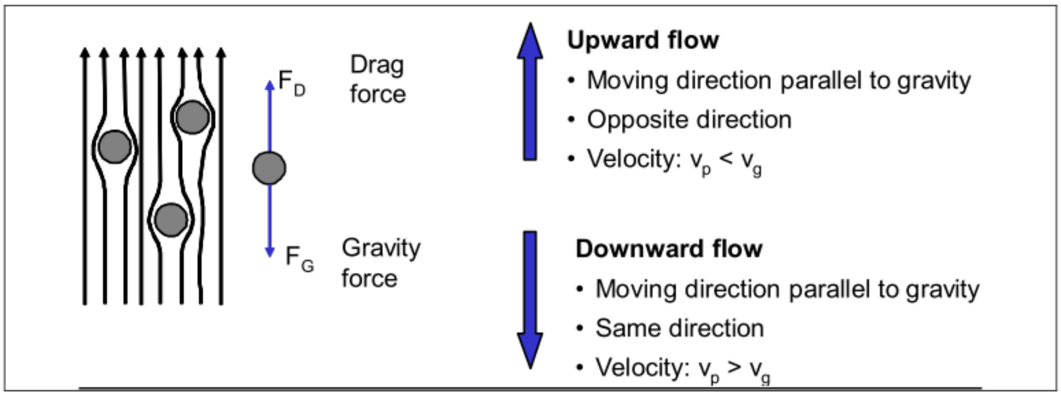

Figure 10.A. Drag forces in vertical flow.

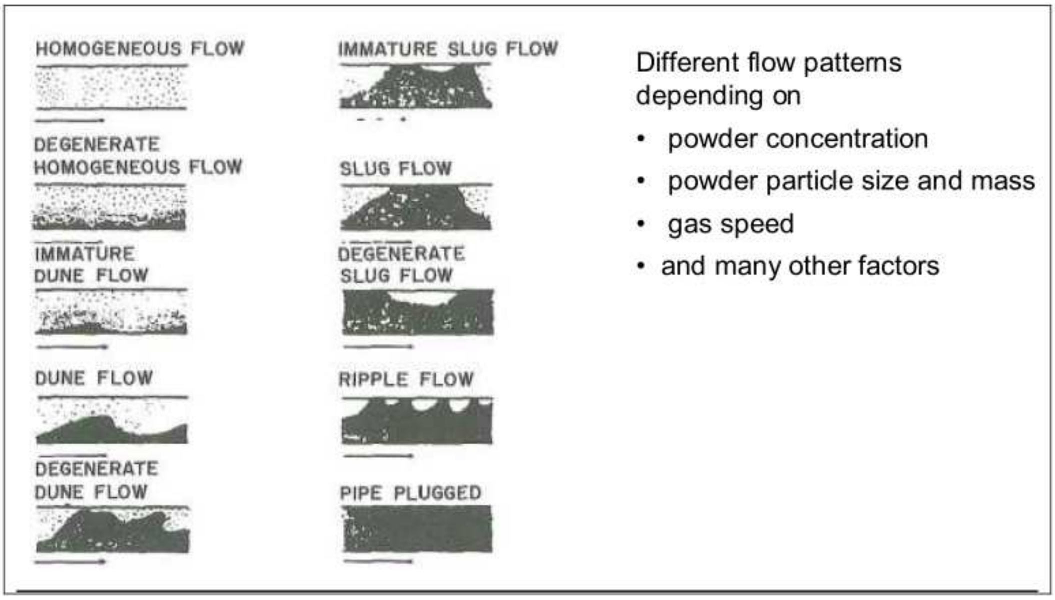

Figure 11.A. Horizontal flow patterns.

The most important states are homogenous flow, dune flow, slug flow ripple flow and plugged pipe. The other states are transition patterns. Depending on the parameters, the powder is more or less flying within the gas stream. Depending on the particle concentration in the gas stream, two categories of feeding situations can be roughly distinguished:

- dilute phase systems;
- dense phase systems.

Dilute phase systems are characterised by a uniform powder distribution over the cross section of the pipe. According to /i/, the mass flow ratio in dilute phase systems is between 0 and 15.
The mass flow ratio is the ratio between the mass of the powder and the mass of the carrier gas streaming through a cross-section of the pipe per time unit:

$$mass\ flow\ ratio = \frac{\dot{m}_p}{\dot{m}_g} = \frac{\dot{m}_p}{\rho_g \dot{V}_g} \cong \frac{RT\dot{m}_p}{Mp\dot{V}_g}$$

Where: $\dot{m}_p = mass\ flow\ of\ the\ particles\ [kg/s]$
$\dot{m}_g = mass\ flow\ of\ the\ carrier\ gas\ [kg/s]$
$\dot{V}_g = volume\ flow\ of\ the\ carrier\ gas\ [m^3/s]$
$\rho_g = mass\ density\ of\ the\ carrier\ gas\ [kg/m^3]$
$R = universal\ gas\ constant\ [8.314\ J/(mol\ K)]$
$T = absolute\ temperature\ [K]$
$M = molar\ mass\ [kg/mol]$
$p = gas\ pressure$

Equation 1.A.

It is clear that for the micro-LS feeding process, in which low quantities of powder shall be transported in homogenous way, the homogenous flow pattern is the first choice to be achieved. For other feeding processes, e.g. when a ship shall discharged another flow pattern may result, because high mass flow is most important. It will be shown below, that the micro-LS powder feeder will strongly favour homogenous flow in the pipes. However, there are locations in the feeding way, where sedimentation may take place and may cause a dune flow pattern.
In the following, we will analyse the feeding situation for the laser sintering machine for a typical set of parameters listed in Table 1.A. We will present the results for some theoretical considerations assuming some ideal conditions, which are not given in reality. These considerations shall provide a better process understanding and answer the following questions:

- How dense is the powder flow?
- Are there collisions between particles?
- Is powder flow laminar or turbulent?
- What is the minimum flow speed of the gas?
- What is the particle speed at the nozzle exit?
- How much time is needed for the particles to react on a change in gas flow?
- What is the corresponding path length?
- May curvatures in the feeding path influence the focussing behaviour?

carrier gas (Argon)	M = 0.040 kg/mol
density of the gas	ρ_g = 0.61 kg/m^3
dynamic viscosity of the gas	η = 21 * 10^{-6} Ns/m^2
gas pressure	p = 1 bar
gas temperature	T = 293 K
gas flow rate	$\dot{V}_g$= 1.5 l/min
diameter of the pipe	d = 10 mm
number of pipes	11
steel powder density	$\rho_p = 7800\ kg/m^3$
particle mass transportation rate	$\dot{V}_p$= 3 g/h

Table 1.A. Parameters for a typical feeding situation

Let´s first calculate the mass flow ratio:

$$mass\ flow\ ratio = \frac{8.314\frac{J}{mol\ K}\ 298\ K\frac{0.003\ kg}{3600\ s}}{0.040\frac{kg}{mol}\ 10^5 Pa\frac{0.0015\ m^3}{60s}} = 0.021$$

Equation 2.A.

As said before, the dilute phase region extends from mass flow ratio 0 to 15. It thus can be concluded that the micro-LS powder feeder operates in the (very) dilute phase regime where homogenous flow can be expected. The dilute situation becomes even more apparent, if one compares the volume of powder particles compared to the volume of the feeding pipes. Assuming the same feeding situation as in Eq. 2, the volume of gas transported in relation to the volume of powder transported per unit time is:

$$\frac{\dot{V}_g}{\dot{V}_p} = \frac{\dot{V}_g \rho_p}{\dot{m}_p} = 234$$

Equation 3.A.

Lets assume a medium particle diameter of d_p=50 µm. The number of particles per unit time fed to the process is:

$$\dot{N}_{50\mu} = \frac{\dot{V}_p}{1/6\pi d_p^3} = \frac{6\dot{m}_p}{\rho_p \pi d_p^3} = 1632\frac{particles}{s}$$

Equation 4.A.

Distributed over the 11 tubes to the laser head, the number of particles per unit time in each tube is 136 particles/s. The absolute velocity v_g of the gas is

$$v_g = \frac{\dot{V}_g}{11\pi(d/2)^2} = 2.5\, m/s$$

Equation 5.A.

The average distance of the particles to each other in the pipes is

$$\lambda_p = \frac{\dot{N}_{50\mu}}{v_p} \cong \frac{\dot{N}_{50\mu}}{v_g} = 18\, mm$$

Equation 6.A.

which is 360 times the diameter of each particle. Conclusion: Under typical conditions, collisions between particles are extremely rare and can be neglected for the overall flow behaviour.

One requirement for powder feeding against the direction of gravity in vertical tubes is that the gas flow speed is higher than the falling speed of the particles in the field of gravity. There is rule of thumb that the gas speed should be 3 times higher than the free fall speed in the gas. In order to get a rough estimate of the free fall speed of the powder, we consider the fall speed of a single particle. In our situation of high dilution, the single particle assumption is well justified. However in case of agglomerates, the free fall speed of the agglomerate would be essential for the minimum gas speed required. When a particle is submitted to free fall, the ambient gas exerts a drag force on the particle according to its aerodynamic resistance. The particle is accelerated until the drag force is equal to the gravity force of the particle.

$$-F_D = F_G$$

Equation 7.A.

$$C_D \frac{\rho_g}{2} w^2 A_p = m_p g$$

Equation 8.A.

C_D is the drag coefficient. A_p is the aerodynamic cross section of the particle and w is the difference velocity between the particle and the gas. As w has an opposite direction to the drag force, the negative sign of F_D in Eq. 7.A disappears in Eq. 8.A. Assuming a spherical particle, the cross section area A_p can be substituted using the diameter of the sphere.

$$F_D = C_D \frac{\rho_g}{2} w^2 \frac{\pi d_p^2}{4}$$

Equation 9.A.

The drag coefficient is not a constant but a function of the particle´s Reynolds number (see Fig. 12.A)

$$Re_p = \frac{w d_p \rho_g}{\eta}$$

Equation 10.A.

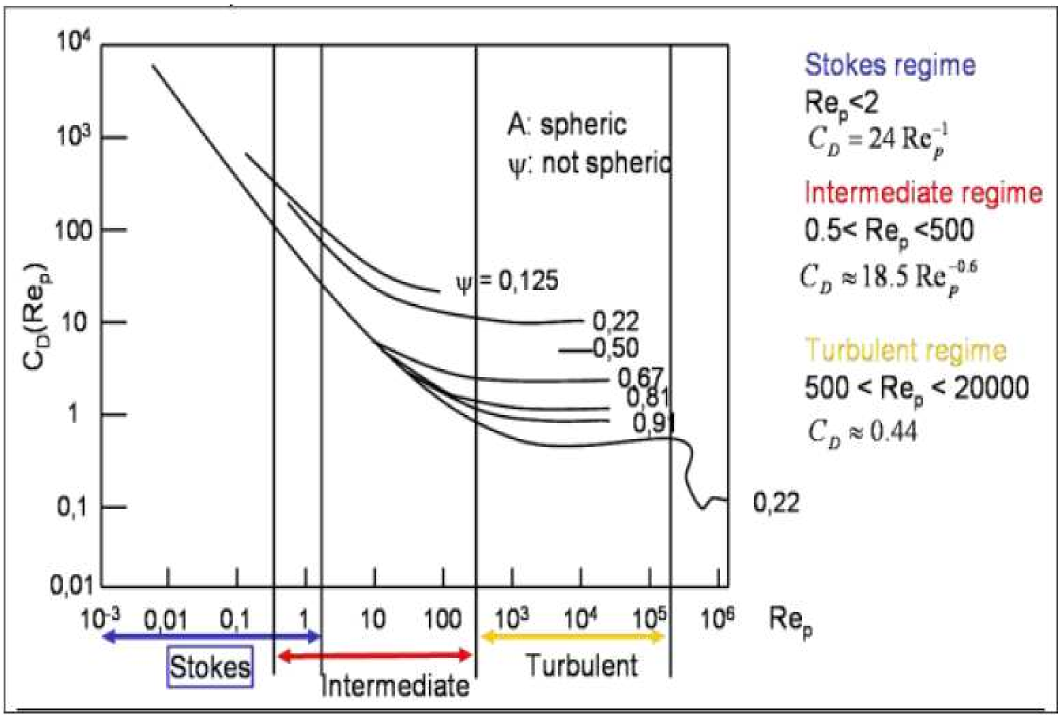

Figure 12.A. Dependence of drag coefficient of a powder particle on the Reynolds number of that particle in a stream of gas.

The relation between drag coefficient and Reynolds number is complex. Usually, the drag coefficient is approximated by different equations, depending on the height of the Reynolds number. The following regimes can be distinguished.

1. Stokes´ law region (creeping flow region) with $Re_p < 2.0$

$$C_D = 24Re_p^{-1}$$

Equation 11.A.

2. Intermediate region with $0.5 < Re_p > 500$

$$C_D \cong 18.5Re_p^{-0.6}$$

Equation 12.A.

3. Fully developed turbulence regime (Newton´s law region) with $500 < Re_p < 200{,}000$

$$C_D \cong 0.44$$

Equation 13.A.

The calculation of the free fall speed of a circular spherical particle from equation Eq. 9.A depends on the regime of the Reynolds number for that particle, which itself is a function of the falling speed. The easiest way to calculate the free fall speed is to assume a flow regime, calculate the velocity, then calculate the Reynolds number of the particle and finally check if the assumption of the flow regime was correct. If the assumption on the flow regime was not justified, try the same procedure with another flow regime.
We will calculate the falling speed using the equations of both regimes Stokes and intermediate, according to Eq. 11.A and Eq. 12.A. In these cases, Eq. 9.A can be transformed into the following expressions:

1. Stokes regime

$$w = \frac{gd^2\rho_p}{18\eta}$$

Equation 14.A.

2. Intermediate regime

$$w = \frac{0.153g^{0.71}d^{1.14}\rho_p^{0.71}}{\rho^{0.29}\eta^{0.43}}$$

Equation 15.A.

Using the following parameters and material data of Table 1, the following free fall speeds can be obtained for circular particles of different sizes:

	stoke regime		**intermediate regime**	
d_p [µm]	w [m/s]	Re_p	w [m/s]	Re_p
10	0.11	0.031	0.02	0.00058
25	0.30	0.21	0.13	0.094
50	0.66	0.97	0.51	0.74
75	1.1	2.4	1.1	2.4
100	1.5	4.3	2.0	

Table 2.A. Calculated free fall speeds of spherical steel particles of different diameters in Argon

For particles smaller than 50 µm, particle flow is in the Stokes regime, i.e. the Argon gas is flowing smoothly around the particles without turbulences. Above 50 µm, the flow is at the beginning of the intermediate regime, and slight tendencies of turbulence appear. However all particles are far away from the fully turbulent region. Conclusion: The particles show a smooth flow in the gas stream and turbulences can be neglected. The particles will follow a parallel flow, if the gas stream itself within the tube is smooth (laminar). Let´s now calculate if the gas stream in the tube is laminar or turbulent. The appropriate quantity is the Reynolds number in the tube. The flow would be turbulent for Re tube > 2300.

Under the conditions of Table 1, the Reynolds number is:

$$Re_p = \frac{w d_p \rho_g}{\eta} = 72$$

Equation 16.A.

Conclusion: The flow of the gas in the feeding pipes is laminar.
Let´s now consider the acceleration of a single particle. Knowledge on the acceleration behaviour of particles is essential to avoid errors in the design of the powder focussing device.
We neglect gravitational forces and take only inertia force and drag force into account. We assume that at the beginning, the particle has a certain velocity difference to the gas stream, w_0. The particle is then accelerated by the drag forces of the gas stream until it reaches the velocity of the gas stream, i.e. $w_f = 0$.
The equation of force equilibrium is

$$F_a = -F_D$$

Equation 17.A.

$$m_p \frac{dw}{dt} = -C_D \frac{\rho_g}{2} w^2 A_p$$

Equation 18.A.

$$\frac{dw}{dt} = -\frac{3}{4} C_D \frac{\rho_g}{\rho_p d_p} w^2$$

Equation 19.A.

In the Stokes regime (smooth flow) C_D can be substituted by Eq. 10.A und Eq. 11.A and the following linear differential equation is obtained.

$$\frac{dw}{dt} = -\frac{18\eta}{\rho_p d_p^2} w$$

Equation 20.A.

This differential equation has an analytical solution which under the given boundary conditions is:

$$w(t) = w_o e^{-\frac{t}{\tau}}$$

Equation 21.A.

and

$$\tau = \frac{\rho_p d_p^2}{18\eta}$$

Equation 22.A.

The relaxation time τ is the time needed to reduce the velocity difference to 37 % (1/e) of the initial difference. It is a quite popular quantity in dust handling literature. Its relevance for powder focussing is as follows:
It is essential for powder focussing, that the powder particles flow parallel to each other at the exit of the nozzle. This is only possible, if they are in parallel with the laminar gas stream within the feeding pipes. If the transport path of the powder changes its direction (e.g. by bent feeding pipes or surface curvatures inside the nozzle), collisions with the wall occur and the powder particles change their direction. The powder then needs some time to get aligned again in the laminar flow of the gas stream, and the time needed is strongly related to the relaxation time. Depending on the gas velocity, the relaxation time is associated with a length of a path and during this distance to the nozzle exit, curvatures should be avoided. For the intermediate flow region, C_D in Eq. 19.A has to be replaced by Eq. 12.A. Now the following differential equation results:

$$\frac{dw}{dt} = \frac{13.9\rho^{0.4}\eta^{0.6}}{\rho_p d_p^{1.6}} w^{1.4}$$

Equation 23.A.

and the solution is:

$$w(t) = (w_0^{-0.4} + \frac{5.56\rho^{0.4}\eta^{0.6}}{\rho_p d_p^{1.6}} t)^{2.5}$$

Equation 24.A.

In the intermediate flow region, the time to reach 37% of the initial velocity difference is not a constant, and it depends on the velocity of the gas stream. Table 3 lists the relaxation times and associated relaxation path lengths for the typical feeding parameters listed in Table 1.

	stoke regime		**intermediate regime**	
d_p [µm]	Relaxation time/s	Associated length in cm at v=2.5 m/s	Relaxation time/s	Associated length in cm at v=2.5 m/s
10	0.0021	0.53		
25	0.013	3.3		
50	0.052 (0.15)	13	0.049	12
75	0.12	30	0.094	24
100	0.21	53	0.15	38

Table 3.A Relaxation times and associated relaxation path lengths.

It can be easily seen from the table that relaxation lengths are so long that constructive measures to bend the particle beam within the nozzle deteriorate the focussing behaviour. Feeding pipes should be collinear to the channels within the nozzle for a sufficiently long distance.

Adhesion of powder to walls

Surface forces between powder particles and between particles and the wall may strongly affect the feeding process. Adhesion forces between particles are called cohesive forces. Depending on the size of the particles, cohesive forces may cause agglomerates. Humidity in the powder, even at low level, may cause agglomeration due to the formation of liquid bridges between particles.

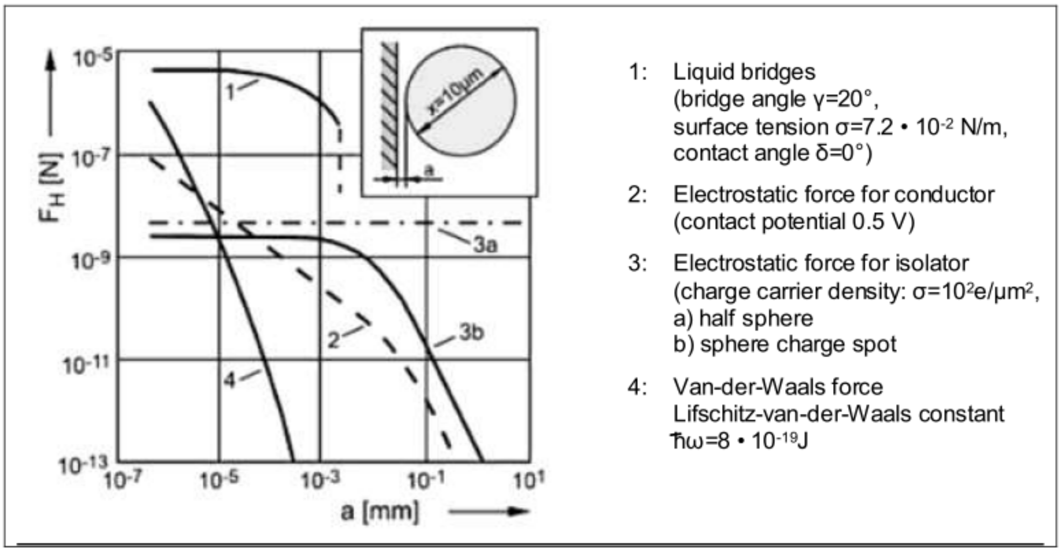

Figure 13.A. Adhesion forces depending on distance to wall.

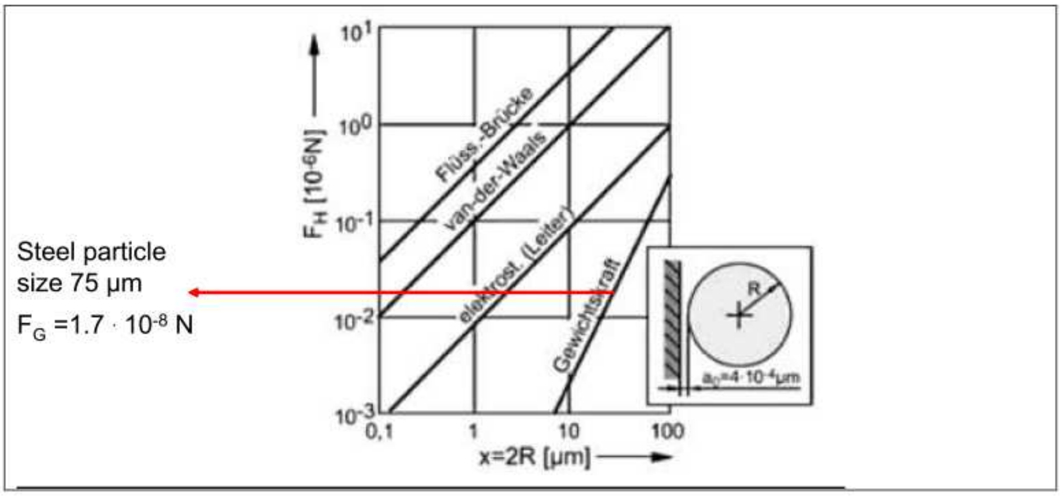

Figure 14.A. Adhesion forces depending on the size of the particle.

Figure 13.A shows the dependence of different adhesion forces of a spherical particle to a wall on the distance between the particle and the wall /2/. The diagram is based on theoretical calculations. Liquid bridges represent the strongest adhesion mechanism. In case of dry powders (which is the relevant case for MANUDIRECT powders), electrostatic and van-der-Waals force have to be considered. At short distance much lower than a micron, van-der-Waals represent the strongest adhesion mechanism.

Figure 14.A shows the effect of particle size on the adhesion force at an atomic distance to the wall. In the whole particle size range (up to 100 µm), the adhesion forces are much stronger than the gravitational force of the particle. For this reason, one would expect the particles to adhere tightly to all surfaces of the feeding path (outlet ramp, feeding pipes, distributor, etc.), and feeding should not be possible. However, in reality adhesion forces are much lower than those calculated shown in Figure 13.A and Figure 14.A. The adhesion behaviour of different powders has been investigated experimentally. The powder was deposited loosely on a flat and polished steel surface (spatula). The surface was then turn moved into a vertical position, and finally a stream of compressed air was guided over the surface to blow away the powder. The result is shown in Figure 15.A. If the powders particles did not adhere to the steel surface, they already fell down on vertical inclination of the spatula. In case they adhered to the steel surface, there was no significant difference between mere inclination of the spatula and application of a gas stream.

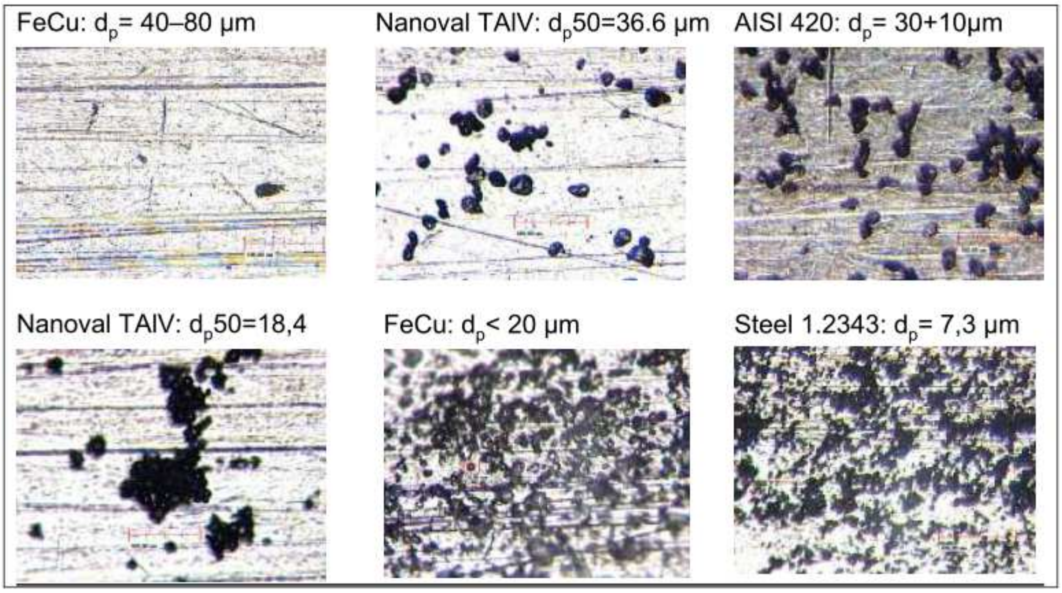

FeCu: d_p= 40–80 µm

Nanoval TAIV: d_p50=36.6 µm

AISI 420: d_p= 30+10µm

Nanoval TAIV: d_p50=18,4

FeCu: d_p< 20 µm

Steel 1.2343: d_p= 7,3 µm

Figure 15.A. Adhesion behaviour of different powders to steel surface.

Powders exceeding a certain size of about 40 µm in diameter did not adhere to the steel surface. Powders below about 40 µm showed adhesion behaviour. The lower the particle size the higher is the degree of covering the surface, i.e. the adhesion behaviour. Particles below 20 µm showed a strong tendency of forming agglomerates. Though there is a tendency for small powders to adhere to a flat steel surface, this does not necessarily mean that clogging of the feeding pipes occurs. The adhesions shown in Figure 15.A are all mono-layers - in case of agglomerates, the height of the monolayer is the height of the agglomerate. Clogging of a feeding pipe would involve the formation of multilayer adhesions, for which at the moment there is no evidence. It can be concluded the adhesion behaviour of real powders to a flat surface is much lower than expected by the theoretical calculations represented Figure 13.A and Figure 14.A. This observation can be explained by the surface roughness of the surface. Surface roughness increases the effective distance between particle and the wall as shown in Figure 16.A.

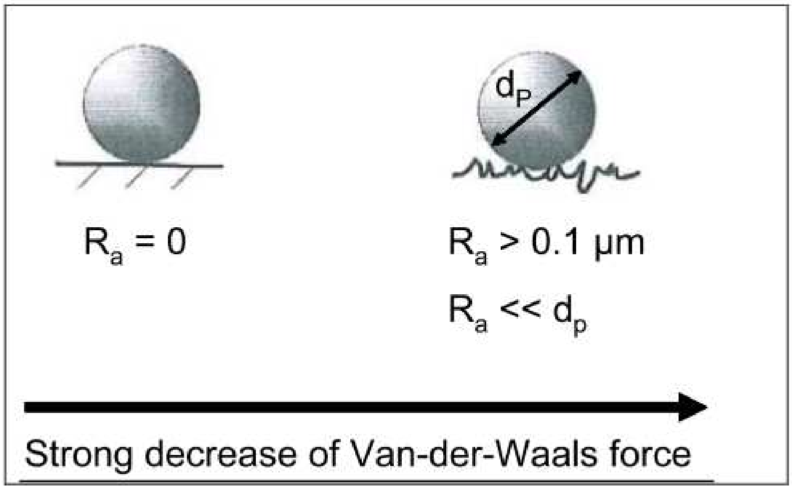

Figure 16.A. Decrease of Van-der-Waals force due to surface roughness

Operating the powder feeder

The operation of the powder feeder is fully integrated into the operation of the MANUDIRECT laser sintering machine. Figure 17.A gives an overview on the most important process steps for operating the powder feeder.

1. Before the feeding process is started it should be verified that the powder cartouche is inserted and that the edge of the powder column is at the edge of the cartouche. Otherwise, if the cartouche is only partially filled and the edge of the powder is below the edge of the cartouche, the powder feeder would not supply powder to the process until the powder column reaches the edge of the cartouche.
2. Feeding parameters should be adjusted before starting the feeding process, though a correction of these parameters is still possible during the process. The feeding parameters are: gas volume rate, rotating speed of the brush and translational speed of the powder lifting piston.
3. The gas flow should not be switched on in form of a sudden rise. Instead it should be switched on smoothly by a pressure ramp. gas pressure
4. Rotating brush and powder lift motor may be started at the same time. Before the process is started there should be inserted a delay time for the powder flow to get homogeneous.
5. Then the working table is moved to the start position of the part to be manufactured.
6. Without delay, the laser is switched on without delay and

7. Without delay, the movement of the working table is started

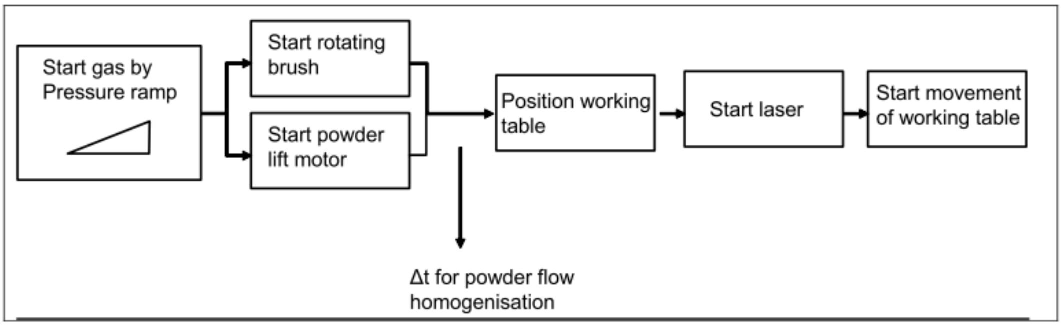

Figure 17.A. Powder feeder operating steps.

Potential disturbances of the feeding process

In ideal case powder flow should be homogenous. However it has been observed in the past that the following disturbances may occur under unfavourable conditions:

- seizing (locking) of the piston in the powder cartouche;
- pulsating powder flow (few Hz);
- sudden release of powder;
- plugging of feeding pipes;
- sudden release of powder plug.

In the following potential sources for disturbances in the feeding process shall be identified:

<u>powder reservoir</u>

It is not a matter of fact that the powder is lifted by the piston without problems. Due to friction with the wall and cohesive forces within the powder, the pressure exerted by the piston is (partially) "absorbed" by the walls of the cartouche (see Fig. 18.A). Depending on the height of the piston force or the properties of the powder, the pressure reaches the powder layer at the top of the cartouche where the brush is acting. The phenomenon is similar to a well known phenomenon which may be observed in silos Figure 19.A.

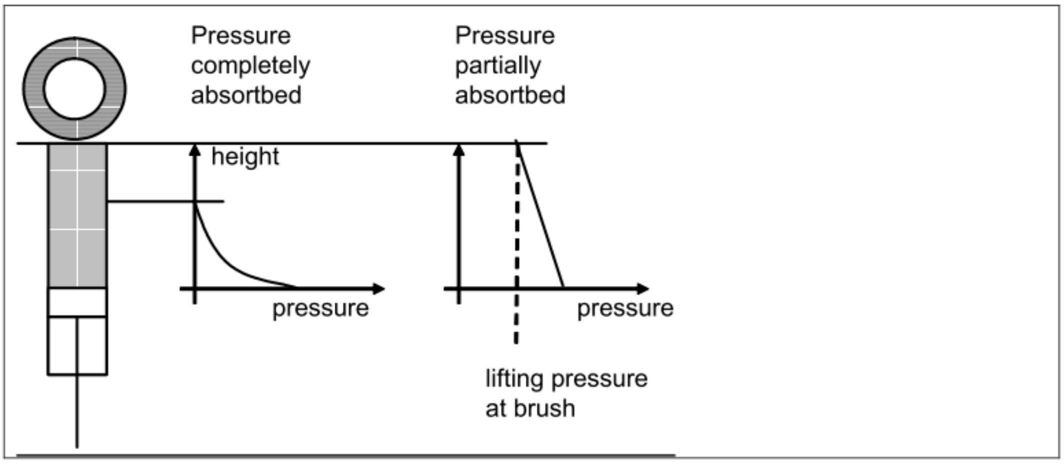

Figure 18.A. Pressure decay in the powder cartouche

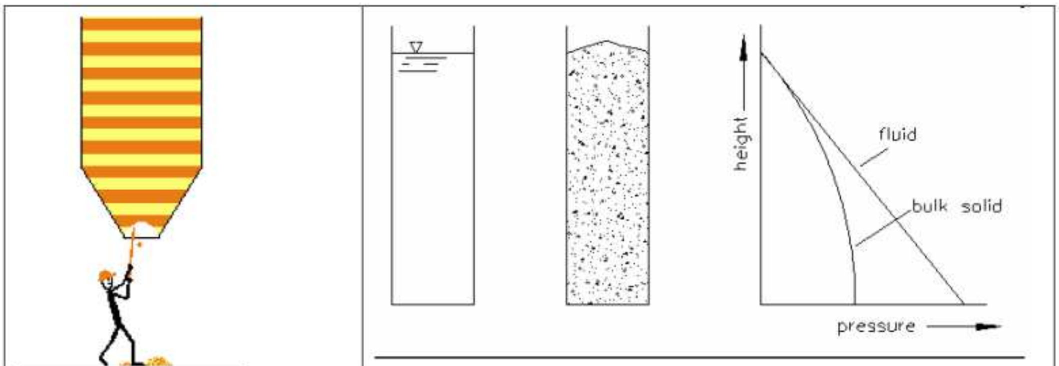

a) Bridge building

b) Pressure in dependence of the filling height for liquid and bulk solid

Figure 19.A. Phenomena of bulk solids (powders) in a silo.

In a previous version of the powder feeder, lockage of the piston was a real problem in some cases which required the fill level of the cartouche to be reduced. The current version of the powder feeder has a much stronger motor, and so far, locking of the piston has not been observed.

Another friction problem may arise, if powder particles enter into space between the piston and the cartouche wall. This may happen if the powder particles damage the flatness of the cartouche walls due to abrasion.

Friction between the cartridge wall and the powder may also be responsible for the pulsating of the powder stream due to the slip-stick effect explained in Fig. 20. The slip stick effect may occur if static friction is higher than dynamic friction.

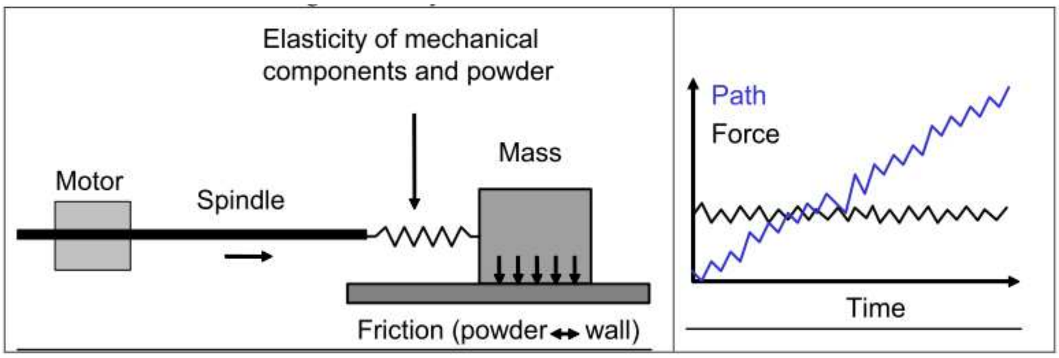

Figure 20.A. Model of the slip-stick effect

Outlet ramp

The geometrical dimensions of the powder transport path significantly change between the outlet of the brush chamber and the entrance into the feeding pipe to the powder distributor. At the beginning of the outlet ramp, the cross section is rectangular with a large width to height ratio while the feeding pipe connected to the exit of the outlet ramp has a circular cross section of 1.6 mm inner diameter. In previous versions of the powder feeder, the cross section at the entrance of the powder ramp was higher than at the exit of this ramp, thus leading to a much lower gas velocity at the beginning of the outlet ramp compared to the gas velocity within the tube. In consequence powder deposition may occur at the ramp (see Fig. 21.A) which in some cases clogs the feeder. In the recent version the design of the ramp was modified providing a constant cross section over the whole ramp which equals the cross section of the pipe. According to feedback from the developer of the laser sintering machine, powder depositions at the outlet ramp do not occur to an unacceptable extent. However, in case of inhomogeneous powder flow at the laser head, the outlet ramp should be taken into account as a potential source of disturbances, and it should be investigated for potential depositions. It cannot be excluded that powder depositions on the outlet ramp may be responsible for pulsating effects because dune flow might occur.

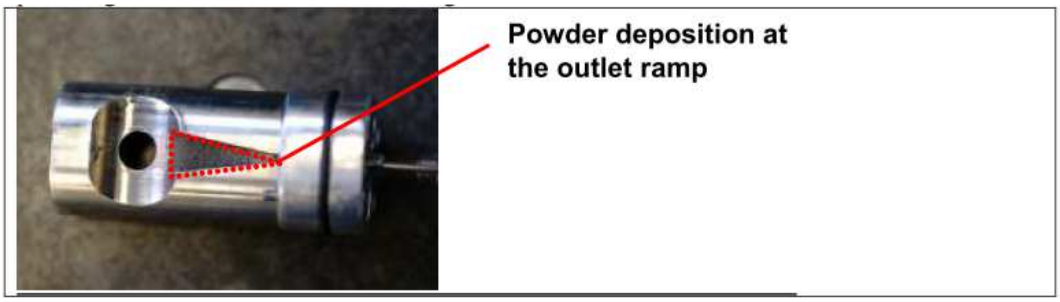

Figure 21.A. Powder depositions at the outlet ramp

Distributor

The distributor is connected to 1 inlet tube at the top and 11 outlet tubes at the bottom. Within the distributor, the cross-section is much bigger than the cross section of the inlet tube or the sum of cross sections of the outlet tubes. Thus, the gas velocity in the distributor is lower than in the tubes and powder deposition may occur. Even with powder depositions in the distributor, the feeding process may appear to work well. However a sudden release of accumulated powder, either by accident or by knocking against the distributor, may strongly disturb the laser sintering process. It cannot be excluded that powder depositions in the distributor on the outlet ramp may be responsible for pulsating effects because dune flow might occur.

Powder depositions in the tubes

The tubes from the distributor to the powder nozzle have an inner diameter each of 1.0 mm. The tube from the powder feeder outlet to the distributor has an inner diameter of 1.6 mm. Compared to the diameter, the tubes are very long and it cannot be excluded that powder depositions may occur. However, according to the experimental investigations on powder adhesion shown in Figure 15.A, there is no experimental evidence that clogging of the feeding pipes really occurs in vertical sections. However, if the gas speed is too low, in horizontal sections of the tubes, depositions may occur due to gravity and the flow may follow one of the patterns sketched in Fig. 11.A.

Powder handling

Correct handling of the powder is important

- to ensure good flow behaviour of the powder;
- to achieve good manufacturing results;
- to avoid incinerations (in case of highly reactive powders);
- and to avoid health risks for the operator.

The powder flow may react very sensitively to slight changes in the powder caused. Even small amount of humidity may cause the formation of liquid bridges between particles and oxidation may change the adhesion forces between particles. Both effects increase the tendency for agglomeration and thus affect the flow behaviour of the powder. Further the material properties of the laser sintered part may be affected.
As a consequence the following handling rules are recommended:

- be aware of limited storage time some of some powders;
- perform filling processes of cartouche in glove box with appropriate inert gas atmosphere;
- close and seal opened storage containers and feeding cartouches.

Some powder materials such as Mg and Ti are very reactive when they get into contact with air. They may cause incineration or explosions. Handling these powders under inert gas atmosphere is not just an issue of good process behaviour but of safety. Rests of oxygen in the laser sintering machine may lead to incineration within the machine. In case of exposition to powder aerosols, technical regulations apply and may require protective measures, such as a filter mask. Powder exposition may occur in powder filling operations and cleaning operations of the machine. In these cases, filter masks should be used. Pay attention that the filter type is appropriate for the particle size.

APPENDIX B

Profilometer data elaboration

During this Ph.D. research work an optical confocal profilometer called Sensofar Plu Neox was used. The measurement procedure is carried out firstly positioning the specimen in the desired orientation by some tape and eventually a support. Then appropriate scanning parameters are chosen, that include scanning range, focusing and light level. In order to do that, the sample is moved on the x/y plane in the objective position, then using confocal mode is set the starting and finishing z value of the scan. If the observed area is bigger than that can be observed from a single position, it is possible to stitch several single scansion in a wider one, increasing the efficacy of the instrument, but uncertainty too. Data collected by this instrument is then elaborated in order to obtain information about surface roughness and waviness. This is possible using the instrument software SensoSCAN neox 3.2.3 or other dedicated program as Digital Surf MountainsMap. Analysing a pin geometry, as requested in this study, a particular post processing was necessary after the acquisition. Firstly, it is necessary to eliminate the cylindrical shape of the nominal pin surface in order to characterize only its surface. In this work it was chosen to use a polynomial surface of fifth grade calculated by a ordinary least squares method, removing the shape influence. Then it is extract a sufficient wide portion of surface and it is eliminate eventually erroneous peaks. From the data can be obtained parameters about areal, profile morphology and information about the amount or powder stick on the external surface. This latter evaluation is done highlighting and measuring the percentage of the observed area that have a height above 15 µm from the average plane. That value it is used because it is smaller than the particle diameter but bigger than the expected value of roughness. In order to get numerical values about the other two morphology characteristics it is necessary to filter the acquired data, distinguish roughness, waviness from nominal surface. This passage is critical. Looking at measurement literature and normative it is not well defined as treat a additive manufacturing part. Regarding linear measurements, several works consider a low-pass Gaussian filter with a λ = 0.8 mm, but it is usually impossible to have the prescript evaluation length of 4 mm (according to ISO 25178). So during this work it was considered a low-pass Gaussian filter with a λ = 0.4 mm, that require an evaluation length of just 1.25 mm. Nevertheless the influence of the powder presence remained, because the diameter of the particles used was between 20 µm and 25 µm. Areal measurements were also considered, without any filter. In this way their numeral value take in account all the amount of defects present on surface. In this case, it is very important to remove correctly the cylindrical shape of the nominal surface. Furthermore in order to reduce the influence of erroneous peaks and valley that generated a small amount of value very distant from the average plane, the lowest and highest 5% of the values were rejected.

Several parameters can be are calculated from profilometer analyses. Their definitions are similar between linear and areal ones, so the more important ones are reported by couples.

- S_a and R_a: arithmetic mean height in its absolute value. This is strongly correlated with the following S_q and R_q value. They are defined as:

$$S_a = \int \int_A |Z(x,y)|\, dx\, dy \qquad R_a = \frac{1}{L}\int_0^L |y|\, dx$$

- S_q and R_q: root mean square height, defined as the root mean square value of the surface Z(x,y) or profile Z(x). It has a more statistical significance than S_a because it is the standard deviation and often has a more physical grounding. It is defined as

$$S_q = \sqrt{\frac{1}{A}\iint_A (Z(x,y))^2\,dx\,dy} \qquad R_q = \sqrt{\frac{1}{L}\int_o^L Z^2\,(x)\,dx}$$

- S_z and R_z: are the maximum height of the surface on the considered area or profile. In order to decrease the influence of erroneous values, it is calculated as the difference between the average values of the five highest peaks (ppi) and lowest valleys (pvi):

$$S_z = R_z = \frac{\sum_{i=1}^{5} y_{pi} - \sum_{j=1}^{5} y_{vi}}{5}$$

- S_{sk} and R_{sk}: areal and profile Skewness. It describes the shape of the surface height distribution measuring the surface or profile symmetry about the mean line. The sign of S_{sk} indicates the presence of fairly high spikes that protrude above a flatter average ($S_{sk} > 0$) or on the contrary the presence of fairly deep valleys in a smoother plateau ($S_{sk} < 0$). Its value is strongly influenced by isolated peaks or valleys and is unit-less because it is normalized by S_q. A topography with a random or Gaussian height distribution, the skewness is zero. It is defined as

$$S_{sk} = \frac{1}{S_q^3}\int\int_a (Z(x,y))^3\,dx\,dy \qquad R_{sk} = \frac{1}{LRq^3}\int_0^L Z^3(x)\,dx$$

- S_{ku} and S_{ku}: Areal and profile Kurtosis. This parameter indicates the sharpness of the surface height distribution of the surface. Unlike S_{sk} and R_{sk}, which detects only whether the profile spikes are evenly distributed, the S_{ku} and R_{ku} parameters also provide a measure of the spikiness of the area or profile. A spiky surface will have a high kurtosis and a bumpy surface will have a low one. This parameter is strictly positive and unit-less, and characterizes the spread of the height distribution. A surface with a Gaussian height distribution has a kurtosis value of 3. They are defined as

$$S_{ku} = \frac{1}{S_q^4}\int\int_a (Z(x,y))^4\,dx\,dy \qquad R_{ku} = \frac{1}{LRq^4}\int_0^L Z^4(x)\,dx$$

Furthermore another graphical representation is given from the acquired data. It is based on the Material Ratio (mr), that is the ratio of the intersecting area of a plane (parallel to the mean plane) passing through the surface at a given height. The Areal Material Ratio Curve (Abbot Firestone Curve) is established by evaluating mr at various levels from the highest peak to the lowest valley. S_k, S_{pk} and S_{vk} can be graphically expressed looking at the Areal Material Ratio Curve, as the distances reported in Figure 1.B.

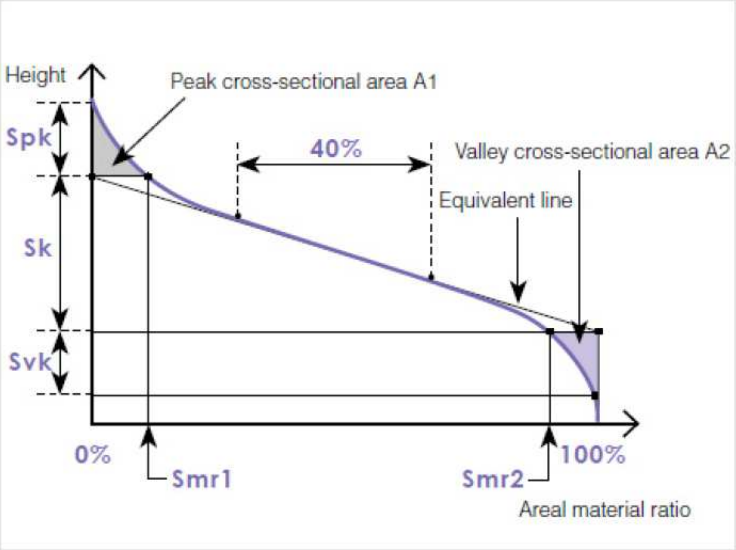

Figure 1.B. Graphical construction of collected parameters by Abbot Firestone Curve.

Information about height distribution in the acquired area can be evaluated comparing these curves as well as using the above exposed parameters.